Epitaxial thin films of the noncollinear antiferromagnets Mn_3Ir and Mn_3Sn for topological spintronic applications

Dissertation

zur Erlangung des
Doktorgrades der Naturwissenschaften
(Dr. rer. nat.)

der Naturwissenschaftlichen Fakultät II
- Chemie, Physik und Mathematik

der Martin-Luther-Universität Halle-Wittenberg

vorgelegt von Herrn

James Mark Taylor

geboren am 08.12.1990 in Sheffield (UK)

Gutachter:
Prof. Dr. Stuart S. P. Parkin
Prof. Dr. Ingrid Mertig
Prof. Dr. Günter Reiss

Tag der öffentlichen Verteidigung:
30.09.2020

Contents

Zusammenfassung

In dieser Arbeit werden epitaktische Dünnschichten aus nicht-kollinearen Antiferromagneten Mn_3Ir und Mn_3Sn mittels Magnetronsputtern hergestellt. Deren Kristallstruktur wird durch XRD und TEM charakterisiert. Messungen ihrer magnetischen Eigenschaften mittels VSM und XMCD zeigen die wichtige Rolle des nicht-kompensierten Mn-Moments.

Um die Nützlichkeit der Dünnschichten für Spintronik einzuschätzen, wird der magnetische Transport in lithographisch hergestellten Bauelementen untersucht.

Im Fall von Mn_3Sn messen wir bei 300 K einen anormalen Hall-Effekt in der Größenordnung von $\sigma_{\mathrm{xy}}(\mu_0 H = 0\,\mathrm{T}) = 21\,\Omega^{-1}\,\mathrm{cm}^{-1}$ in Dünnschichten von bis 30 nm, der durch Berry-Krümmung hervorgerufenen wird. Beim nachfolgenden Kühlen - unter den Übergang zum gläsernen ferromagnetischen Zustand - beobachten wir einen Wechsel in den topologischen Hall-Effekt. Wir ordnen diesen Effekt zu der Entstehung von chiralen Domänenwänden in Mn_3Sn und zeigen, dass die Spin-Konfiguration vom Magnetfeldkühlen abhängt.

Abstract

In this thesis, we prepare epitaxial thin films of the noncollinear antiferromagnets Mn_3Ir and Mn_3Sn, via magnetron sputtering. Their crystal structure is characterized by x-ray diffraction and transmission electron microscopy. Measurements of their magnetic properties, using vibrating sample magnetometry and x-ray magnetic circular dichroism, reveal the important role of uncompensated Mn moments.

To assess the thin films' suitability for topological spintronic applications, we study magnetotransport in lithographically fabricated devices.

In the case of Mn_3Sn, we measure Berry curvature driven anomalous Hall effect at 300 K, with a magnitude of $\sigma_{\mathrm{xy}}(\mu_0 H = 0\,\mathrm{T}) = 21\,\Omega^{-1}\,\mathrm{cm}^{-1}$, in thin films down to 30 nm. On subsequent cooling to below its transition into a glassy ferromagnetic state, we observe a change to a topological Hall effect. We attribute this to chiral domain walls in our Mn_3Sn films, and observe that their spin configuration depends on magnetic-field cooling condition.

List of figures

List of tables

List of abbreviations

AF	Antiferromagnet(ic)
AFM	Atomic force microscopy
AHE	Anomalous Hall effect
DMI	Dzyaloshinskii–Moriya interaction
EB	Exchange bias
EDXS	Energy dispersive x-ray spectroscopy
FM	Ferromagnet(ic)
GMR	Giant magnetoresistance
IP	In-plane
MCA	Magnetocrystalline anisotropy
MOKE	Magneto-optical Kerr effect
MR	Magnetoresistance
MRAM	Magnetoresistive random access memory
MTJ	Magnetic tunnel junction
OP	Out-of-plane
SAED	Selected area electron diffraction
SHE	Spin Hall effect
SOC	Spin-orbit coupling
SOT	Spin-orbit torque
SQUID	Superconducting quantum interference device
TEM	Transmission electron microscopy
THE	Topological Hall effect
TMR	Tunnel magnetoresistance
VSM	Vibrating sample magnetometer
X-PEEM	XMC(L)D - Photoemission Electron Microscopy
XMCD	X-ray magnetic circular dichroism
XMLD	X-ray magnetic linear dichroism
XRD	X-ray diffraction
XRR	X-ray reflectivity

1 Introduction

1.1 Lead In

Antiferromagnetic spintronics aims to replace the ferromagnetism used in conventional spintronic devices with the antiferromagnetic order parameter. Doing so offers a number of advantages, such as improved stability, reduction in stray fields and increased speed of dynamics. However, changes in the orientation of typical antiferromagnets' Néel vectors do not produce read-out signals of the size required for applications. Topological antiferromagnets may offer the solution. Here topologically non-trivial band structures can generate large magnetotransport effects.

In particular, the noncollinear antiferromagnets of the type Mn_3X have been predicted to show large intrinsic anomalous and spin Hall effects, driven by a fictitious magnetic field that is generated by the momentum-space Berry curvature arising from symmetry breaking by the materials' chiral spin textures. In certain cases these phenomena have been experimentally verified, but with the majority of studies confined to single-crystal bulk samples.

Instead, in this thesis, we progress towards the utilization of these Berry curvature driven magnetotransport properties in antiferromagnetic spintronic applications, by preparing two distinct varieties of noncollinear antiferromagnet in the thin film form required to realize devices. Specifically, we deposit films of $\mathrm{Mn}_3\mathrm{Ir}$, with a cubic structure, and $\mathrm{Mn}_3\mathrm{Sn}$, with a hexagonal structure. We use the flexible technique of magnetron sputtering, optimizing growth parameters, substrate choice and buffer layer texture to achieve the high structural quality necessary to observe topological transport phenomena. The crystal structure of the films is characterized using a combination of x-ray diffraction and transmission electron microscopy, including the different orientations of each material, their respective epitaxial relationships, and specific microstructural properties.

Measurements of the films' magnetism, using magnetometry and x-ray magnetic circular dichroism, reveal important differences between $\mathrm{Mn}_3\mathrm{Ir}$, with a triangular antiferromagnetic order, and $\mathrm{Mn}_3\mathrm{Sn}$, with an inverse triangular spin texture. In parallel, we illuminate the important role played by uncompensated moments in both materials, exploring how these are affected by sample microstructure and how, in turn, they effect antiferromagnetic domain distribution. The link between crystal structure, uncompensated moments and noncollinear antiferromagnetic domains emerges as a common theme throughout this thesis (with such chiral domains also governing, for example, the exchange bias measured in bilayer samples of $\mathrm{Mn}_3\mathrm{Ir(Sn)}$ coupled to ferromagnetic permalloy).

Furthermore, the chirality of different antiferromagnetic domains plays a key role in governing topological magnetotransport in these compounds. We elucidate this by measuring the Hall effect in lithographically patterned samples of both $\mathrm{Mn_3Ir}$ and $\mathrm{Mn_3Sn}$, and find very different behavior in both cases. Whilst $\mathrm{Mn_3Ir}$ shows a small conventional anomalous Hall effect, driven by uncompensated Mn moments in the film, it shows no evidence of a Berry curvature driven anomalous Hall effect. We attribute this to the large internal anisotropies of this cubic material causing it to remain in a multi-domain state, even in a strong magnetic field.

On the other hand, we succeed in measuring Berry curvature driven anomalous Hall effect in $\mathrm{Mn_3Sn}$ thin films. In this case, magnetocrystalline anisotropy arising from the hexagonal structure generates an uncompensated moment coupled to the inverse triangular antiferromagnetic order, allowing the momentum-space Berry curvature generated anomalous Hall effect to be observed when $\mathrm{Mn_3Sn}$ is driven into a single chiral domain state via a mechanism of domain wall nucleation and propagation.

Following cooling of $\mathrm{Mn_3Sn}$ below its transition temperature into a glassy ferromagnetic state, we identify a change in transport behavior from anomalous to topological Hall effects. We attribute this to chiral domain walls in our $\mathrm{Mn_3Sn}$ thin films, and identify that their spin configuration depends on sample magnetic history. The thesis therefore concludes by discussing the potential applications of this large, room temperature, Berry curvature driven anomalous Hall effect, and of this chiral domain wall memory phenomenon, and therefore how the $\mathrm{Mn_3Sn}$ thin films presented here may be advantageous to topological antiferromagnetic spintronics.

However, before we elucidate the specific objectives of this thesis, and explore in detail the results outlined above, we introduce the thesis with an overview of its conceptual foundations (Section 1.2). Here we give a brief history of the field of spintronics and a summary of the different phenomena currently utilized in state-of-the-art FM-based spintronic devices. We answer the questions what are AFs, how can they improve spintronic performance and what are their limitations?

We then discuss how noncollinear AFs, of the form Mn_3X, may address these problems, at the same time giving an overview of how topology generates Berry curvature in these materials. Finally, we introduce the magnetotransport properties that are driven by this Berry curvature and how these may find applications in topological AFs spintronics.

1.2 Conceptual foundations

1.2.1 Spintronics

Spintronics (‘spin’ & ‘electronics’) aims to utilize the spin angular momentum of electrons, instead of their charge, to perform useful electronic operations. Examples of spintronic technologies include magnetic field sensors and nonvolatile computer memories [1].

Controlling the spin of electrons in a current can be achieved through their interaction with atomic magnetic moments. Therefore, research in the field of spintronics revolves around the study of electrical transport in devices fabricated (see Section 1.3.9) of magnetic (and other supporting) materials (and correlation with their, often novel, magnetic properties, measured as described in Sections 1.3.7).

Spintronic components offer the potential advantages of [1]:

- Scalability - magnetic bits could be made just a few atoms in size, whilst avoiding the leakage current inherent in charge-based transistors.
- Energy efficiency - a flow of spin angular momentum in a metal, unlike electronic charge in a semiconductor, wastes little energy as heat.
- Non-volatility - when power is removed, a component will retain its magnetic state, whilst also avoiding the need for continual recharging of transistors.

Magnetic materials hosting long-range exchange interactions possess an order parameter that is stable in the absence of magnetic field and against moderate external perturbations, making them ideal for nonvolatile memory devices. A magnetic bit, with its magnetic order parameter aligned in different directions, can represent a ‘0’ or ‘1’ in a binary data system [I]. Such a system is currently used to save data in computer hard drives [1].

The first requirement of any computer system is a method to *read-out* the stored data electrically (with sufficient contrast between its different states). This same problem is present in magnetic field sensors, where small changes in the magnetism of the sensing component, caused by the external magnetic

---

[I] In addition, spintronic components have been shown to achieve multiple stable and distinguishable resistance levels in between ‘0’ and ‘1’. This memristive property is reminiscent of synaptic behavior in animal brains. As such, it may offer a way to efficiently implement artificial intelligence learning algorithms in dedicated spintronic-based hardware. Examples of systems where such neuromorphic computing has been demonstrated are: progressive SOT-switching of a FM layer stabilized by exchange bias [2]; a series of spin-transfer torque driven MTJs switching stochastically [3]; and the Néel-order torque switching of consecutive domains in an antiferromagnet [4].

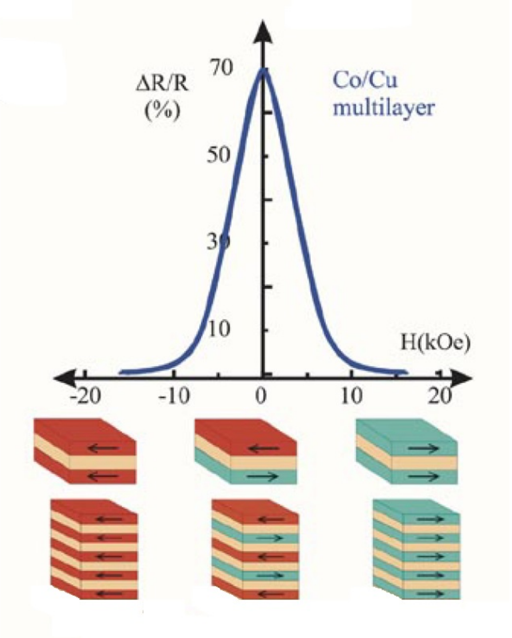

Figure 1: Plot of magnetoresistance ratio against magnetic field for a Co/Cu multilayer, demonstrating the GMR effect. The illustrations below the figure show the configuration of magnetic electrodes at different fields, in either a superlattice stack (lower) or spin valve structure (upper), with AF indirect exchange coupling. Adapted from [5].

field to be measured, must be detected electrically. (Such sensors are also used as the reading mechanism in the aforementioned hard drives).

Historically, the observed changes in a material's electrical resistance with magnetization have been very small. Therefore, the field of spintronics truly began with the development of a technique for the high-fidelity read-out of the orientation of a magnetic material, **giant magnetoresistance** [5].

GMR occurs in two thin films of magnetic material, separated by a layer of nonmagnetic conductor. It relies on three phenomena, described in more detail later in this thesis. The first, is the spin polarization of $4s$ delocalized electrons in itinerant ferromagnets, explained in Section 1.2.2. Here, the conduction electrons in the magnetic layers, which are metallic materials with long-range ordering of atomic moments generated by localized $3d$ electrons, align their spins parallel with the layer's magnetization.

The second, are the $s-d$ scattering events explained in Section 1.2.8. The $3d$ electron sub-shells which generate the atomic moments in the magnetic layer will have only a partially occupied density of states with spins aligned antiparallel to the magnetization. The third, is that the probability of $4s$ conduction electrons whose spins are aligned with these unoccupied states have a higher probability to scatter into them (as dictated by Fermi's golden rule, explained in Section 1.3.8). However, since most electrons have spins polarized parallel to the orientation of the magnetic moments, few scattering events occur in each individual layer.

Considering now the thin film stack, some spin-polarized electrons will flow from the first magnetic electrode, through the spacer layer, into the second magnetic layer, and vice versa. The spin polarization of these itinerant electrons is predominantly determined by the orientation of atomic moments localized *close to the interface* between the first magnetic electrode and the spacer layer [6].

As the spin-polarized $4s$ electrons cross the spacer layer into the second magnetic electrode, their scattering rate depends on the density of states of atomic moments **at the interface** [6].If the magnetization of the two layers are parallel, the likelihood of electrons from one layer undergoing $s-d$ scattering at the interface to the other layer is still suppressed.

However, if the magnetizations of the two electrodes are antiparallel, then spin polarized conduction electrons crossing the spacer layer will encounter a large, unoccupied $3d$ density of states aligned with their spin at the interface. *There is an increased probability the itinerant electrons will scatter into these states.* Hence their mean free path is reduced, and the resistivity of each electrode to conduction electrons from the other electrode is increased. This therefore increases the resistance of the entire multilayer device.

Thus, a GMR device shows two resistance states: a low-resistance state where the electrodes' magnetizations are aligned parallel, and a high-resistance state where they are aligned antiparallel [7, 8].

Early GMR observations focused on thin-films stacks comprising multiple repeats of Fe/Cr, Co/Cr or Co/Ru layers (known as superlattices) [9]. In this case, the magnetic electrodes indirectly exchange couple through the spacer layer. By increasing the thickness of the spacer, the sign of the indirect exchange interaction changes from negative to positive and back again, leading to alternating AF and FM coupling of the magnetic electrodes [9].

By selecting the correct thickness of spacer layer, antiparallel alignment of the two electrodes' magnetization can be favored. We now call this a *synthetic antiferromagnet* [10], and it results in a high-resistance state at zero external magnetic field.

However, when sufficient magnetic field is applied to force the electrodes' magnetizations to align, the resistance of the stack drops [9]. A plot of the GMR in such a thin-film multilayer is shown in Fig. 1.

Importantly, similar *oscillatory coupling* was discovered when using free-electron-like transition metal Cu spacer layers with thicknesses up to 5 nm [11]. If the thickness of the Cu spacer is kept $<$ 1 nm, and superlattices

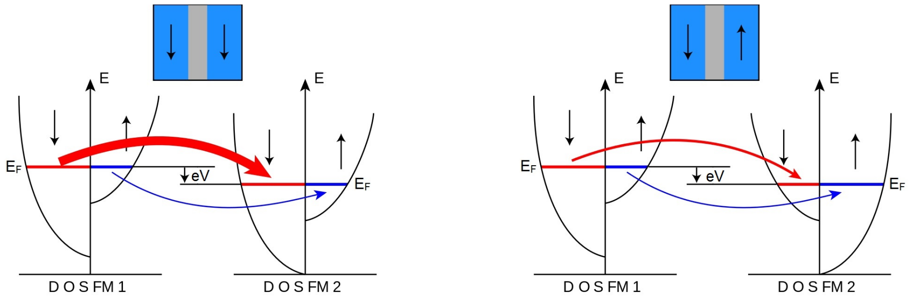

Figure 2: Density of $4s$ sub-band states (DOS) around the Fermi level (E_F) in the reference (FM 1) and free (FM 2) layers of an MTJ in both parallel (left) and antiparallel (right) configurations. In the parallel case, a majority of states are spin-down in both the reference and free electrodes, resulting in a large tunneling current of spin-down polarized itinerant electrons (thick red arrow). Meanwhile, a minority of states are spin-up in both the reference and free electrodes, resulting in a small current of spin-up polarized itinerant electrons (thin blue arrow). In the antiparallel case, the density of states in the free electrode is reversed. A majority of available states are now spin-up polarized, maintaining a small current of spin-up conduction electrons (thin blue arrow). Meanwhile, a minority of available states are now spin-down polarized, blocking tunneling of some spin-down conduction electrons (thin red arrow). eV is the drop in chemical potential across the tunnel barrier. Adapted from [14].

formed with Co electrodes, then (as shown in Fig. 1) GMR ratios of 60 % can be achieved.

If instead the Cu spacer is made thicker, the two magnetic electrodes decouple and their magnetizations can be aligned independently [11]. Due to the long spin diffusion length in Cu, GMR was also found in this case, even when using soft magnetic electrodes (for example $\mathrm{Ni}_{80}\mathrm{Fe}_{20}$) [12]. These discoveries allowed for the practical implementation of GMR in a device called a **spin valve**.

In this case, the magnetization of one electrode, called the *reference layer*, is pinned in one direction by introducing a unidirectional anisotropy using exchange bias (see Section 1.2.5). The magnetization of the other magnetically soft electrode, called the *free layer*, follows the direction of even a weak external magnetic field, resulting in a resistance change (originally of the order 5 % at room temperature) [12].

Whilst these changes in resistance achievable with spin valves are sufficient for the purposes of magnetic sensors, a larger difference between the two states is required for error-free computational bits. This was provided by a phenomena first predicted in 1975, **tunnel magnetoresistance** [13].

TMR occurs in a device called a **magnetic tunnel junction**, which is similar to a spin valve but with the nonmagnetic space layer replaced by a barrier of insulating material. Again, an MTJ is a device that can only be engineered using thin film deposition technology, since the insulating barrier must be thin enough for electrons to quantum mechanically tunnel through.

If we apply a bias voltage (V) across an MTJ, a current of delocalized conduction electrons begins to move through the reference magnetic electrode, across the tunnel barrier and out of the free magnetic electrode on the other side. Fig. 2 shows the $4s$ density of states in each layer of the MTJ. The bias voltage shifts the chemical potential of one electrode with respect to the other, creating a difference between their two Fermi levels.

For a fixed bias voltage, the size of this tunneling current (hence giving the measured device resistance) again depends on three physical phenomena that are key to the operation of spintronic devices. The $4s$ conduction electrons moving through the reference layer become spin polarized in a direction parallel to its magnetization, because of itinerant FM (see Section 1.2.2). The probability of these electrons tunneling through the barrier depends on Fermi's golden rule, partially determined by the density of states in the free layer (see Section 1.3.8). This density of states is spontaneously spin split, by exchange interactions combined with the Pauli exclusion principle, depending on the magnetization of the free layer (see Section 1.2.8).

However, the tunneling process involves conduction electrons transitioning from $4s$ delocalized orbitals in the reference layer, to $4s$ delocalized orbitals in the free layer. These itinerant electrons are continually moving into and out of such orbitals close to the Fermi level, because the drop in chemical potential across the MTJ encourages current flow. Therefore, the tunneling probability depends directly on the relative densities of spin-split $4s$ electron states at the Fermi level.

There will be a high density of itinerant electron states with spins aligned parallel to the free layer magnetization. Hence, if the magnetizations of both electrodes are aligned parallel, there will be plenty of states available for itinerant $4s$ electrons to move through; tunneling probability will therefore be high and the resistance of the MTJ will be low. Conversely, if the magnetizations of the two layers are antiparallel, then the majority of spin-polarized $4s$ electrons will have few states available to tunnel into, and the resistance of the MTJ will be high [15]. Fig. 2 illustrates this tunneling process.

The difference in resistance between these two states can be large. The first MTJs, fabricated using Al_2O_3 tunnel barriers [16], reported TMR ratios of 10 to 20 % at room temperature (already higher than spin valves) [17]. However, much higher TMR ratios ($> 100\,\%$) were discovered in MTJs with (001) oriented, body-centered cubic MgO tunnel barriers and Fe [18] or CoFe [19] or CoFeB [20] magnetic electrodes grown epitaxially (see Section 1.3.2).

This is because such crystalline MgO tunnel barriers suppress the tunneling

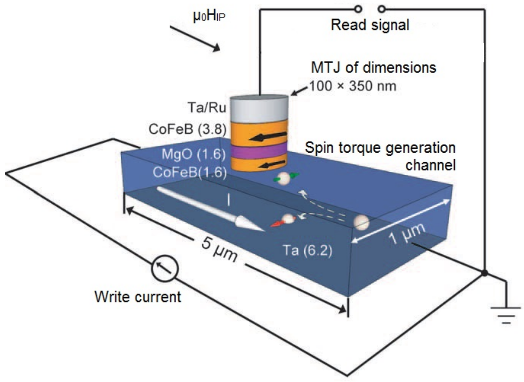

Figure 3: Illustration of the SOT switching process for a CoFeB / MgO / CoFeB MTJ nanopillar fabricated on top of a Ta spin torque generation channel. The white arrow represents the direction of switching current flow, and the white balls represent electrons moving in the opposite direction. The SHE in Ta deflects left-spin electrons towards the bottom of the channel, and right-spin electrons towards the top of the channel. With the application of an IP magnetic field ($\mu_0 H_{\mathrm{IP}}$), the SOT generated by the SHE will reverse the magnetization of the bottom MTJ electrode. Adapted from [23].

transition matrix elements of all but a certain set of Bloch wavefunction symmetries [21]. Electrons with these Bloch wavefunction symmetries occupy specific bands in the metallic electrodes, which, in the case of body-centered cubic Fe (001) and CoFe (001) thin films, are strongly spin polarized [22].

The high MR ratios obtained in CoFeB / MgO MTJs make these good candidates for the basic building blocks of non-volatile spintronic-based bits, a technology called **magnetoresistive random access memory** [24].

Through TMR, we have an efficient read-out mechanism for MRAM bits. However, the second requirement in any computer memory is a method to quickly write new data to each bit. Spintronics also offers a unique possibility to do this, using the reverse of the process utilized thus far [1]. By injecting a current of spin-polarized electrons across the interface to a magnetic film, the resulting transfer of angular momentum exerts a torque on the atomic moments, manipulating their direction.

Originally, this was achieved by passing a current through either the reference electrode, or through an oppositely magnetized polarizing layer deposited on the other end of the MTJ. The electrons in the charge current become spin polarized by one of the two layers, according to the direction of current flow, and so exert a torque in one of two directions on the free electrode, in order to switch its magnetization [25, 26]. We call this the *spin-transfer torque* switching mechanism; however, it has the disadvantage of requiring a large current to pass through the fragile tunnel barrier [27].

Instead, a second mechanism utilizes a three-terminal device to achieve **spin-orbit torque** switching. Here, an accumulation of spin-polarized electrons at the top of a spin torque generation channel, in the region where it interfaces with a perpendicularly magnetized film, will result in a transfer of angular momentum [28]. When combined with a small IP magnetic field, to provide a preferential direction around which the magnetization can precess during switching, the resulting spin torque will reverse magnetization direction[29].

Fig. 3 shows how this SOT mechanism is used to switch an MRAM bit [23]. A large current can be passed through the spin torque generation channel in either a positive or negative direction, to deterministically switch the MTJ free layer. Meanwhile, a much smaller read current flowing vertically through the device will measure the parallel/antiparallel alignment of the MTJ, without damaging the tunnel barrier.

In Fig. 3, spin-polarized electrons moving in the vertical direction, with their spins directed IP and orthogonal to the charge current, exert the SOT that switches the MTJ free layer [23]. This charge-current to spin-current conversion mechanism is the **spin Hall effect**.

If a material exhibits the spin Hall effect, the paths of some electrons in the charge current will bend depending on their spin orientation; spin-up electrons will be deflected in a direction transverse to both their charge current and their spin orientation, whilst spin-down electrons will be deflected in the opposite transverse direction.

The transverse-deflection mechanisms that cause the SHE are comparable to those responsible for the AHE (as explained in Section 1.2.9).

The extrinsic transverse-deflection mechanisms are identical to those causing AHE; these spin-dependently deflect conduction electrons transversely during scattering events.

Specifically, these are *skew-scattering* (where coupling of an electron's spin and orbital angular momenta means it has a higher probability of scattering in a direction given by the vector product of its propagation direction and spin) and *side-jump* (where coupling between an electron's spin and the orbital angular momentum of impurity atoms introduces a transverse component to the electron's momentum with sign depending on its spin) [30].

The intrinsic transverse-deflection mechanism is similar to that causing AHE; but is instead driven by momentum-space spin Berry curvature. This generates a emergent spin-orbit field, which exerts a force on electrons in a transverse direction depending on their spin (rather than their charge) [30].

The intrinsic contribution to SHE depends only on the bandstructure of the material, therefore can be large in metals where SOC modifies bandstructure around the Fermi level to show avoided crossing (for example Pt or Ta) [30]. We explain the intrinsic-SHE in detail in Section 1.2.6.

Since all of these transverse-deflection mechanisms rely on strong SOC, large SHE has been discovered in heavy elements such as Pt [28], Ta [23] or W [31]. An illustration of the SHE in such a nonmagnetic metal is outlined in Fig. 13 (see Section 1.2.6).

When a charge current of electrons flows in these nonmagnetic metals, there is an equal distribution of spin-up and spin-down electrons. This means identical numbers of electrons will be deflected in each direction, resulting in a net difference in spin, but no net difference in charge, in the transverse direction across a SHE device [30]. We call this a pure spin current, which (due to the lack of net charge current in the direction of the spin current) can provide a very energy efficient means of transmitting information in spintronic applications, or reversing the magnetization of thin films.

Field-free switching of magnetic layers has been achieved by combining SOTs with the effective field induced by exchange bias (see Section 1.2.6). In addition, spin currents play a key role in driving domain wall motion in *racetrack memory* [32, 33], and *charge-spin conversion in noncollinear AFs* by the SHE is an area of active research (see Section 1.2.6).

The discovery and development of these two phenomena, first GMR and subsequently TMR, form the basis of the discipline now known as spintronics. This field continues to advance, incorporating new physical effects and solid-state materials to enable improved performance and novel functionalities (see Section 1.2.3). However, GMR and TMR are still the state-of-art for technological applications of spintronics, with GMR devices forming the basis of many modern magnetic sensors, whilst SOT-switched MTJs are being commercialized in MRAM [34].

1.2.2 Ferromagnetism

Atoms of an element, or atoms of specific elements within a compound, host magnetic moments (m). The atom's electrons generate these magnetic moments. Consequently, atomic magnetic moment has two contributions, orbital magnetic moment and spin magnetic moment [35]. These stem from the orbital and spin angular momenta, respectively, of the electrons arranged in shells around the atomic nucleus.

In many materials, the net combination of spin and orbital angular momenta will almost cancel out and their atoms show no magnetic moment. An external magnetic field will induce orbital currents in the sample, which generate a small magnetic moment counter to the applied field [36]. The specimen adopts a small magnetization ($M = m({}^{N}\!/_{V})$, where ${}^{N}\!/_{V}$ =number of atoms per unit volume) opposite to the applied magnetic field (that increases linearly with it); an effect we call **diamagnetism**.

In other materials, atoms have a net magnetic moment. The total angular momentum operator ($\hat{\boldsymbol{J}}$) gives the size of this magnetic moment, which in turn comprises of contributions from the orbital ($\hat{\boldsymbol{L}}$) and spin ($\hat{\boldsymbol{S}}$) angular momentum operators [35]. Choosing our axis of quantization as the z direction, these operators ($\hat{L}_\mathrm{z}$ and $\hat{S}_\mathrm{z}$) can only adopt certain discrete quantized values: $m_\mathrm{orbital} = 0, \pm 1, \pm 2, \ldots, \pm L$ and $m_\mathrm{spin} = -S, -S+1, \ldots, S-1, S$.

The total angular momentum operator ($\hat{J}_\mathrm{z}$) therefore has eigenvalues $m_\mathrm{J} = -J, -J+1, \ldots, J-1, J$, where J represents different possible combinations of orbital and spin angular momentum eigenvalues L and S [37].

These different allowed combinations of L and S depend on the specific arrangement of electrons in atomic orbitals. Using Hund's rules, electrons are placed in available states according the Pauli exclusion principle, and the values of J can be determined [38]. In the case of the transition metal elements, which are of interest for spintronics, the magnetic moment of the atoms is generated by electrons in the $3d$ sub-shell. The orbital moments of these $3d$ electrons are quenched [35]. Therefore, for the $3d$ transition metals, atomic magnetic moment is dominated by spin contribution.

Atomic magnetic moment is thus also quantized and given by,

$$m = -g\mu_\mathrm{B} m_\mathrm{J} \tag{1}$$

where μ_B is the Bohr magnetron,

$$\mu_\mathrm{B} = \frac{e\hbar}{2m_\mathrm{e}} \tag{2}$$

where e is electron charge, $\hbar$ is reduced Planck's constant, and m_e is electron rest mass [38]. In addition, g is known as the Landé g-factor,

$$g = 1 + \frac{J(J+1) + S(S+1) - L(L-1)}{2J(J+1)} \tag{3}$$

For a pure orbital contribution to total angular momentum, $g = 1$, whilst for a pure spin contribution, $g = 2$ [35].

For $3d$ transition metals, g takes a value close to 2, because their magnetic moment is dominated by electron spin. The actual eigenvalues of the spin angular momentum result from the specific electron sub-shell filling for the given valencey of an element in a compound. However, suppose we have an atom where only a single electron contributes to magnetic moment, as was the case in the Stern-Gerlach experiment [39].

Here $m_\mathrm{spin} = \pm 1/2$, because an electron is a spin-$1/2$ particle. Therefore $S = 1/2$, so $J = 1/2$, so $m_\mathrm{J} = \pm 1/2$, and $g = 2$. The electron (and, in turn,

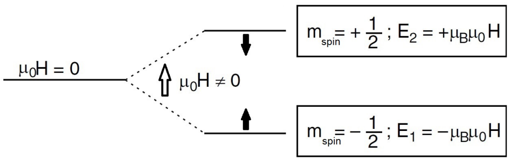

Figure 4: Energy level diagram for an atomic moment, with spin angular momentum given by a single electron, in a magnetic field pointing along the positive z direction. The resulting energy levels are E_1 for the spin-up configuration ($m_{\mathrm{spin}} = -1/2$) and E_2 for the spin down configuration ($m_{\mathrm{spin}} = +1/2$). Adapted from [35].

atom) therefore has two allowed values of magnetic moment, which we denote as spin-up ($m_{\mathrm{J}} = m_{\mathrm{spin}} = -1/2$) and spin-down ($m_{\mathrm{J}} = m_{\mathrm{spin}} = +1/2$) [36],

$$m = -g\mu_{\mathrm{B}} m_{\mathrm{J}} = -2\mu_{\mathrm{B}} \pm \frac{1}{2} = \mp \frac{e\hbar}{2m_{\mathrm{e}}} \tag{4}$$

When such an atomic moment is placed in a magnetic field, $\mu_0 H$, there arises a magnetostatic energy, E,

$$E = -\boldsymbol{m} \cdot \mu_0 \boldsymbol{H} = -m\mu_0 H \cos\theta = -m\mu_0 H = - \mp \mu_{\mathrm{B}}\mu_0 H = \pm \frac{e\hbar}{2m_{\mathrm{e}}} \mu_0 H \tag{5}$$

if simplified for the case of a magnetic field along the positive z direction (same direction as the spin-up electron) [36].

The magnetic field lifts degeneracy, and the magnetic atom can occupy one of two energy levels as illustrated in Fig. 4 [35]. The lower level, $E_1 = -\mu_{\mathrm{B}}\mu_0 H$, is the energy of the spin-up electron (which is parallel with the field) [36]. The upper level, $E_2 = +\mu_{\mathrm{B}}\mu_0 H$, is the energy of the spin-down electron (which is antiparallel with the field) [36].

The relative occupation of each energy level will therefore determine the net magnetization of the material. This occupation is, in turn, governed by the balance between magnetostatic energy and thermal excitation ($k_{\mathrm{B}}T$) for the ensemble of atoms, according to a Boltzmann distribution [35]. This can be generalized in the form of a Brillouin function, $\mathrm{Br}(\alpha)$, which relates to magnetization as follows,

$$M = \frac{N}{V} g\mu_{\mathrm{B}} S \mathrm{Br}(\alpha) \tag{6}$$

where α incorporates the field dependence according to (for a spin-1/2 electron) [35],

$$\alpha = \frac{g\mu_B S \mu_0 H}{k_{\mathrm{B}}T} = \frac{\mu_{\mathrm{B}}\mu_0 H}{k_{\mathrm{B}}T} \tag{7}$$

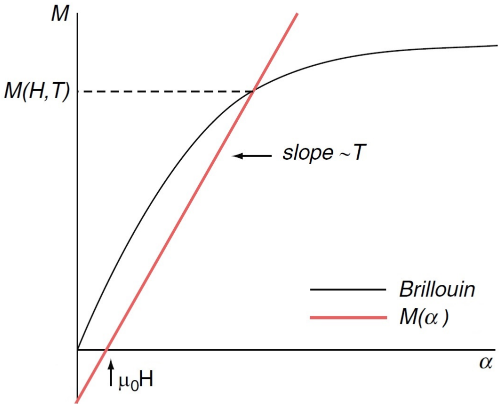

Figure 5: Magnetization plotted against α-parameter (incorporating applied magnetic field and temperature), with dependencies determined by both a Brillouin function (Equation 6) and linear relation extracted from the mean-field approximation (Equation 10). The slope and x intercept of the linear function reflect the temperature and external magnetic field dependencies of a FM, respectively. The resulting intercept with the Brillouin function represents the distribution of atomic moments among different energy levels, and hence yields the net magnetization of the material. Adapted from [35].

Plotting Equation 6, as shown in Fig. 5, we see that magnetization initially increases linearly in response to magnetic field. This is because energy in the system is lowered by more atoms moving into the lower energy state, thus aligning their magnetic moment with the applied field[36]. Once external field is removed, however, thermal fluctuations will scatter the aligned atomic moments, and magnetization decreases again [36]. We call this behavior **paramagnetism**.

However, for spintronic applications (for example nonvolatile computer memories) we look to FMs, such as the $3d$ transition metals mentioned above. These materials demonstrate large net magnetization even in the absence of a magnetic field. What makes such a spontaneous, long-range ordering of atomic moments energetically favorable?

The answer is an apparent field that acts within the material to align individual magnetic moments parallel to one another, against their otherwise random disruption by thermal motion. This *molecular field* is a result of coupling between the magnetic moment of one atom and its neighbors, as quantified by a parameter, λ_{ex} [35]. Therefore, the total field felt by a given atom will be a combination of any external magnetic field and the internal molecular field,

$$\mu_0 H \Rightarrow \left(\mu_0 H - \frac{\lambda_{\text{ex}} n \langle S \rangle}{g \mu_{\text{B}}} \right) \tag{8}$$

where n is each atom's number of nearest neighbors. Here we have calculated the expectation value for atomic moment using the thermal mean of the spin angular momentum eigenvalue ($\langle S\rangle$), in an approach called the *mean field approximation* [35].

Substituting this effective field into the expression for α (Equation 7), defining the external field and temperature dependence of magnetization,

$$\alpha = \frac{g\mu_\mathrm{B} S \mu_0}{k_\mathrm{B} T}\left(H - \frac{\lambda_\mathrm{ex} n \langle S\rangle}{g\mu_\mathrm{B}\mu_0}\right) \tag{9}$$

and hence

$$M = \frac{N}{V}\left[\left(\frac{k_\mathrm{B} T g\mu_\mathrm{B}}{\lambda_\mathrm{ex} n S}\right)\alpha - \frac{(g\mu_\mathrm{B})^2\mu_0 H}{\lambda_\mathrm{ex} n}\right] \tag{10}$$

Equation 10 is linear in α [35]. If we solve it, together with the Brillouin function (Equation 6), graphically, as plotted in Fig. 5, we obtain three distinct regimes [40]:

- High temperature: Here the gradient of Equation 10 is steep. For $\mu_0 H = 0$, the only solution is $M = 0$, and the material is nonmagnetic. If $\mu_0 H$ is increased at constant high temperature, then M will increase linearly, i.e. paramagnetic behavior.
- Equation 10 is a tangent to Equation 6: Here there is no analytic solution for M. This indicates a phase change; specifically, from the paramagnetic regime at high temperature (see above) to the FM regime at low temperature (see below). The temperature at which this phase change occurs is called the **Curie temperature**, T_c. It can be determined by equating the slope of the Brillouin function in the linear region ($\alpha \to 0$) with the gradient of the linear function at $\mu_0 H = 0$,

  $$\frac{N}{V} g S \mu_\mathrm{B} \frac{\mathrm{dBr}(\alpha \to 0)}{\mathrm{d}\alpha} = \frac{N}{V}\frac{k_\mathrm{B} T_\mathrm{c} g\mu_\mathrm{B}}{\lambda_\mathrm{ex} n S} \tag{11}$$

  which yields,

  $$T_\mathrm{c} = \frac{\lambda_\mathrm{ex} n S(S+1)}{3k_\mathrm{B}} \tag{12}$$

  by making the approximation that $\mathrm{Br}(\alpha \to 0) = {}^{(S+1)\alpha}/_{3S}$ [35].
- Low temperature: Here the gradient of Equation 10 is shallow, and its intercept with Equation 6 will yield non-zero magnetization, even when $\mu_0 H = 0$. The material is therefore FM. As the temperature

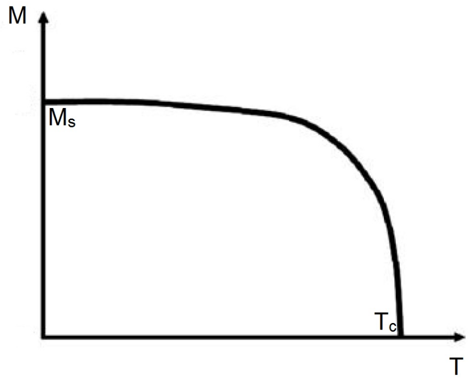

Figure 6: Temperature dependence of magnetization in a FM, extracted by sweeping the gradient of Equation 10 in Fig. 5. Magnetization tends to saturation at low temperatures, whilst above the Curie temperature the FM undergoes a phase transition to the paramagnetic regime. Adapted from [35].

is decreased below Curie temperature (i.e. the gradient of the line is further decreased) the intercept sweeps along the Brillouin curve, and magnetization increases towards saturation. This gives the Curie-Weiss behavior expected for an FM, as shown in Fig. 6 [35].

Alternatively, for a fixed temperature below Curie temperature, sweeping magnetic field (translating the linear function along the x axis in Fig. 5) will increase magnetization nonlinearly towards **saturation** (M_s) [35]. This results in the hysteresis loop response of magnetization to applied magnetic field that is typical of FMs [40]. We show such a loop in Fig. 7.

The energy associated with aligning magnetization and external field determines the shape of this hysteresis loop. This energy varies along different directions in the material, an effect called *magnetic anisotropy.* Two key contributions which govern the hysteresis loop response, and that can be exploited when engineering spintronic devices, are [35]:

- **Magnetocrystalline anisotropy.** Electron orbitals in atoms are coupled to the material's crystal lattice. For example, they may elongate along a particular crystallographic direction. The resulting overlap of wavefunctions makes it easier for electrons to delocalize (see below), making this an energetically preferable situation. The spin angular momentum of electrons is, in turn, coupled to the atomic orbitals they occupy. Therefore, a preferred orientation of electron spin also emerges; a direction in which it is easier to magnetize the material. We call this a *magnetic easy axis* [37].

- **Shape anisotropy.** In a magnetized material, the local dipolar field generated by each atomic moment will act on the magnetic moments of neighboring atoms. The net effect of all these dipolar fields is to create an additional field opposing the magnetization of the material. This field is given by $\boldsymbol{H}_\mathrm{d} = -N_\mathrm{d}\boldsymbol{M}$, where the coefficient N_d depends on the shape of the sample. We call the field $\mu_0 H_\mathrm{d}$ the *demagnetizing field*, and the magnetostatic energy associated with it the *demagnetization energy* [37].

The dependence of a 3d electron's spin orientation on the orbital angular momentum of the sub-shell it occupies is an example of a fundamental phenomenon that is important to several other physical mechanisms explored in this thesis; spin-orbit coupling (SOC)[II].

Given these anisotropies, a balance of different energy contributions determines the response of a FM to an applied magnetic field. The molecular field favors aligning all atomic moments in a sample. However, this produces the largest possible demagnetizing field. In order to lower demagnetization energy, it is favorable to form regions where magnetization is locally aligned, but with the magnetization of neighboring regions opposing one another [37]. We call such regions *magnetic domains.* Fig. 8 shows possible domain configuration for a FM [42].

The magnetization of opposite domains will still preferably orientate along a magnetic easy axis (especially in highly-crystalline materials such as epitaxial thin films). Alternatively, in a polycrystal, consisting of many crystallites of mixed orientation, the relative magnetization of neighboring domains will be randomly oriented in the unmagnetized state [42].

Again, a balance of energies determines the exact domain configuration. It becomes energetically favorable to create a region of opposite magnetization orientation when the increase in molecular field and anisotropy energies

---

[II] **SOC** describes the interaction between the spin and orbital magnetic moments of electrons [35]. *Its physical origin is the influence of the magnetic dipole created by orbital angular momentum upon the direction of electron spins* [41]. This may be, for example, the orientation dependence of an electron's spin angular momentum on its occupation of particular orbitals around an atom (which, in nature, leads to spin-split sub-shells and a plethora of possible MCAs). Alternatively, it may describe the coupling between conduction electron spins in metals, typically delocalized from the *s* band, and the orbital angular momentum of localized *d* sub-shell electrons (in atoms of the lattice). This results in magnetotransport phenomena such as the AHE and SHE (see Sections 1.2.9 and 1.2.1 respectively). This interaction can be reversed, such that a delocalized electron's orbital motion is influenced by the localized spins moments on atoms (causing the anisotropic magnetoresistance explained in Section 1.2.8). Finally, SOC can connect an electron's orbital angular momentum to its own spin direction (as is the case with the Rashba and Dresselhaus spin-orbit interactions introduced in Section 1.2.3).

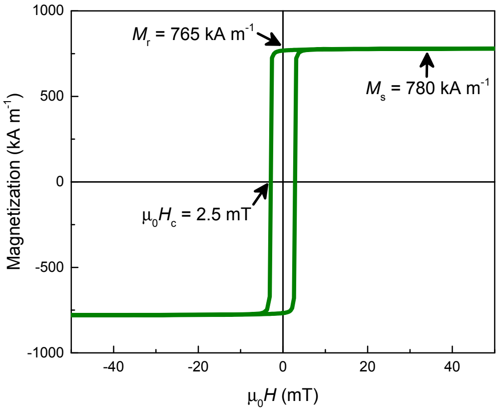

Figure 7: Magnetization variation as a function of external magnetic field plots out a typical hysteresis loop for a FM. Saturation magnetization, remnant magnetization and coercive field are labeled. The behavior of these quantities reflects the rich physics of FM systems, in particular the response of magnetic domains to magnetic field. Measured for a 5 nm $Ni_{80}Fe_{20}$ film.

associated with inserting a boundary between the new domains (a *domain wall*) is exceeded by the demagnetization energy saving [37].

As external magnetic field is applied, the magnetostatic energy of domains not aligned to the magnetic field increases, such that domains aligned with the field grow in order to reduce overall energy. This process occurs by a movement of the domain wall, to increase the size of domains aligned parallel to the magnetic field at the expense of those aligned antiparallel. This continues until the sample approaches a dominant domain state. At this point, any final domains not aligned with the field will rotate, to saturate magnetization [42].

The rate at which magnetization changes with magnetic field depends on the ease with which domain walls move. Sample microstructure limits this through pinning. *Pinning sites* provide a region of lower energy for a domain wall, thus encouraging it to stay there [35]. Magnetic field must increase further, until it overcomes the activation energy barrier necessary to drive the domain wall past the pinning site.

However, once a domain wall has passed a pinning site, this same energy barrier makes it energetically unfavorable for the domain wall to relax back (even if we remove external magnetic field) [42]. In other words, pinning sites ‘trap’ the increase in net magnetization; FMs retain their net magnetization when magnetic field is decreased back to zero. Nevertheless, some

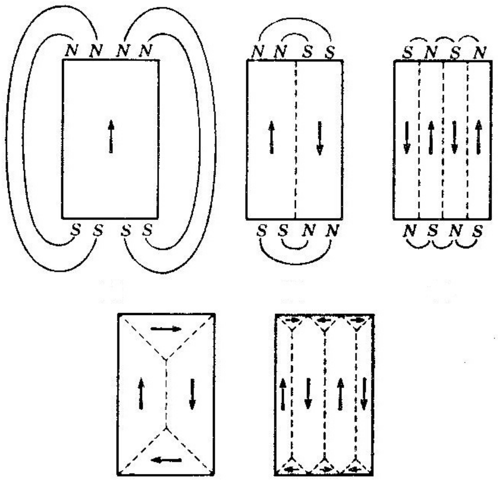

Figure 8: Illustration of a series of simplified domain configurations for a FM. Magnetic poles indicate the strength of the demagnetizing field in each case. The materials have a uniaxial easy axis along the vertical direction, encouraging the formation of domains (of opposite magnetization but) aligned along this direction. Adapted from [42].

rotated or weakly pinned domains will relax and randomize their orientation, slightly lowering magnetization. The resulting 'left-over' magnetization at zero magnetic field is called **remanence** (M_r), as shown in Fig. 7.

If magnetic field is now reversed, domains with their magnetization opposite to the existing dominant domain state begin to *nucleate*. This occurs preferentially at pinning sites, where anisotropies are weakened [35]. As we increase magnetic field in the reverse direction, these new domains will grow. At a certain field, the size of oppositely aligned domains will be such that magnetization totally cancels [42]. We call this the **coercive field** ($\mu_0 H_\mathrm{c}$). The size of the coercive field depends on pinning strength in the sample; for stronger pinning, higher field is required to move domain walls and so coercivity is larger.

As we increase reversed magnetic field further beyond coercivity, saturation in this reverse direction is achieved [42]. This process is typical of magnetization response to an external magnetic field in FMs, and sketches out the hysteresis loop shown in Fig. 7. In Sections 2.2 and 3.2, we discuss how this situation compares in AFs, and we will see that domain wall pinning is a very important parameter to consider when designing materials for spintronic applications. Two main types of pinning site are important [38]:

- Impurity or inclusion atoms within a magnetic matrix significantly increase the magnetostatic energy in their vicinity. Domain walls, where neighboring atomic moments are misaligned, therefore reduce this energy, meaning it is favorable for the domain wall to stay at this position. Since spatial variations in energy landscape surrounding such inclusions can be large, such pinning sites disproportionately effect wider domain walls, 10 to 100 nm, which are associated with high-moment, low anisotropy materials. Such materials are therefore often easy to saturate and reverse (*magnetically soft*), because of the typically low densities of such impurities. On the other hand, inclusions could be engineered in a material, for example through ion beam irradiation, to act as artificial pinning sites and so increase coercive field [35].
- Dislocations and other structural defects are surrounded by a strain field in the crystal lattice. These are very small, typically encompassing only a few atoms, but there may be many of them (especially in imperfectly grown thin films of novel materials), and as such can cause large coercivity increases in low-moment materials with strong internal anisotropies (for example AFs) that show narrow domain walls. This is because of *magnetostriction*; lattice strains modify the spacing between atomic magnetic moments, thus changing the strength of the molecular field coupling, λ_{ex}, between them (and so modifying the magnetic energy landscape of the material) [35].

What then, is the origin of this molecular field, λ_{ex}, which determines the long-range order in FMs? An atom's electrons experience Coulomb repulsion from the electrons of its nearest-neighbor atoms in a crystal lattice. At the same time, the wavefunctions of the atoms' electron clouds will overlap. The resulting expectation value for the separation distance between these two electron clouds will therefore depend on the relative spins of electrons, according to the Pauli exclusion principle [38].

This dictates that two fermions of opposite spin can occupy the same atomic orbital (which causes, for example, covalent chemical bonding). Conversely, two fermions with the same spin cannot occupy the same atomic orbital. Since such orbitals are distributed spatially, two spins aligned parallel must (occupy different orbitals within a sub-shell and, hence) move further apart. This, in turn, reduces the electrostatic energy of the two electron clouds. This saving in energy is called the exchange energy, and depends on the value of λ_{ex} [35].

The value of λ_{ex} is given by the Heisenberg Hamiltonian (H_{Heis}) describing the interaction of two spin-dominated atomic magnetic moments, $\hat{\boldsymbol{S}}_{\text{i}}$ and $\hat{\boldsymbol{S}}_{\text{j}}$, which can be simplified to [35],

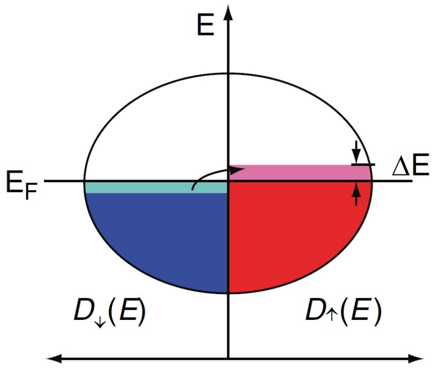

Figure 9: Density of states ($D_{\uparrow\downarrow}(E)$) as a function of energy (E) around the Fermi level in a FM metal. Application of a magnetic field in the positive z direction will align atomic moments and, via the exchange interaction, encourage delocalized s electrons to occupy spin-up states. If the increase in energy (ΔE) associated with electrons occupy spatially separated states (as dictated by the Pauli exclusion principle) is less than the exchange energy saving, then the itinerant electrons will contribute to FM. In addition, the difference in occupation of spin-up and spin-down states close to the Fermi level results in a net spin polarization of charge carriers, leading to spin-polarized currents. Adapted from [35].

$$H_{\text{Heisenberg}} = -\lambda_{\text{ex}} \sum_{\text{i}\neq\text{j}}^{\text{nn}} \hat{\boldsymbol{S}}_{\text{i}} \cdot \hat{\boldsymbol{S}}_{\text{j}} \tag{13}$$

We call this interaction the *exchange interaction*, and λ_{ex} quantifies its strength. The exchange interaction is a result of coulomb repulsion combined with the Pauli exclusion principle, and is a spin-spin coupling occurring between atoms whose wavefunctions overlap (nearest neighbors, denoted nn) [35].

If $\lambda_{\text{ex}} > 0$, then the exchange energy resulting from the Heisenberg Hamiltonian will be negative. It is, therefore, favorable to locate the (sub-shell electrons governing the) magnetic moments of neighboring atoms in states with parallel spin [38]. This means that the magnetic moments of adjacent atoms will align, and our material will show net magnetization.

For certain materials (see below), the value of λ_{ex} is comparatively large. This indicates that the exchange interaction is a very strong effect, sufficient to overcome thermal perturbations that would otherwise randomize the direction of atomic moments [42]. Therefore, the atomic moments of such materials will spontaneously align, even at temperatures up to the (typically relatively high) Curie temperature and in an absence of external magnetic field. This is the origin of **ferromagnetism**.

(In reality, an external magnetic field is initially required to orientate the domains in real magnetic materials. But within each domain, strong exchange interactions are responsible for magnetic order even in zero-field. Once any applied field is removed, each domain retains magnetic order. This is different to paramagnets, where thermal excitations randomize atomic moments as soon the magnetic field is removed [42]).

However, a positive value of λ_{ex} alone is insufficient condition for FM in transition metals. In such materials (of interest for spintronics), conduction electrons also play a role. Whilst their $3d$ electrons are localized and responsible for atomic magnetic moment, the $4s$ band electrons are delocalized and cause conduction [38]. These electrons are *itinerant and can move into unoccupied atomic orbitals* around the Fermi level [35]. According to the exchange interaction, there will be an energy saving associated with moving these electrons into states aligned parallel to the atomic moments in the crystal. In other words, the bands occupied by conduction electrons are spontaneously spin split [38]. Fig. 9 illustrates this process [35].

However, the itinerant electrons with parallel spin must still obey the Pauli exclusion principle, and so move into spatially separated unoccupied atomic orbitals. This increases the energy of the system by ΔE, as indicated in Fig. 9, which will depend on the density of states close to the Fermi level, $D_{\uparrow\downarrow}(E_{\text{F}})$ [35]. For a broad Fermi surface, $D_{\uparrow\downarrow}(E_{\text{F}})$ is larger and electrons can move into parallel states without a large ΔE. For a narrower Fermi surface, the increase in energy will be higher.

If the exchange energy $> \Delta E$, it is favorable for the conduction electrons to move into states aligned with the atomic moments, and both contribute to long range magnetic order. We call this **itinerant ferromagnetism** [35].

A majority of conduction electrons now occupy states of a particular spin direction (occupy one of the spin-split sub-bands). This is the origin of spin-polarized currents in metallic FMs. Such spin-polarized currents are key to a number of physical phenomena utilized in spintronics [38].

Specifically, they cause the GMR and TMR phenomena detailed in Section 1.2.1, affect the $s-d$ scattering processes responsible for the anisotropic-MR described in Section 1.2.8 and play an important role in the AHE discussed in Section 1.2.9.

Thus a combination of exchange energy and the density of states close to the Fermi level determine whether itinerant electrons can establish long range magnetic order in a transition metal. This condition is summarized by the Stoner criterion [38],

$$\lambda_{\text{ex}} D_{\uparrow\downarrow}(E_{\text{F}}) > 1 \tag{14}$$

Element	**Cr**	**Mn**	**Fe**	**Co**	**Ni**	**Pd**
$\lambda_{\text{ex}} D_{\uparrow\downarrow}(E_{\text{F}})$	0.27	0.63	1.43	1.70	2.04	0.78
λ_{ex}	< 0	< 0	> 0	> 0	> 0	> 0

Table 1: The Stoner criterion ($\lambda_{\text{ex}} D_{\uparrow\downarrow}(E_{\text{F}})$) and exchange coupling strength (λ_{ex}) for some transition metals of interest for spintronic applications. The first five elements run across the first transition metal period of the periodic table. Pd is located below Ni in group ten. Fe, Co and Ni are FMs.

Table 1 shows some typical values of the Stoner criterion for magnetic metals [35]. The transition metal FMs (Fe, Co, Ni) all satisfy the *Stoner criterion*, resulting in long-range magnetic order. At the same time, they have $\lambda_{\text{ex}} > 0$, meaning this order will be FM. We also see that Pd, located below Ni in the periodic table, is close to fulfilling the Stoner criterion with $\lambda_{\text{ex}} > 0$. Along with Pt (in the same periodic table group), this material is therefore close to being FM.

1.2.3 Antiferromagnetism

In Table 1 (of Section 1.2.2) we see the Stoner criterion is fulfilled for three common FMs in the transition metal series. At the other end of the transition metal series, Mn is again close to fulfilling the Stoner criterion. When alloyed with other metals, it can thus show itinerant long-range magnetic order. However, in this case $\lambda_{\text{ex}} < 0$ [38]. This means that its *long-range magnetic ordering is opposite* to that of a FM. The moments on neighboring Mn atoms are aligned antiparallel to one another. This is **antiferromagnetism** [37].

Fig. 10 (a) shows an example of AF ordering in CuMnAs [43]. The moments on Mn atoms in adjacent planes are oppositely aligned (this results from a difference in intra- and inter-plane exchange interactions). The moments are all oriented along the *same axis*; we therefore call this material a **collinear** AF. Because the moments fully compensate, such materials have no net magnetization and no external magnetic field projects from their surface [37]. Nevertheless, they possess a stable magnetic order internally.

This long-range antiferromagnetism therefore forms a stable order parameter that could be used to store spin information in a non-volatile manner. Therefore, AFs are also an interesting class of materials to utilize for spintronic applications. We call this contemporary field of research **antiferromagnetic spintronics** [44].

In principle, we could substitute FM order parameter (aligned at 0 versus 180° with respect to probe-current direction) with AF order parameter (aligned at 0 versus 90° with respect to probe-current direction)[III]in order to code for a '0' or '1' in a binary data system. This replacement offers a number of potential advantages in terms of device performance [45]:

- Miniaturization: A key problem for FM-based spintronics, such as MRAM based on MTJs (see Section 1.2.1) is that the stray magnetic field produced by the FM layers can interfere with neighboring bits. For spintronic devices utilizing AFs, the net zero magnetization of the AF results in *no stray fields*, meaning elements could be packed together for higher density memory devices. In addition, when FM components are shrunk to nanometer sizes, demagnetizing field causes their long-range magnetic order to change configuration (mentioned in Section 1.3.9), for example forming vortex cores [46]. In AFs, where *demagnetizing fields from antiparallel moments cancel*, there is no such problem, potentially allowing the fabrication of bits on a nanometer scale.
- High-speed dynamics: The SOT switching of FMs (as introduced in Section 1.2.1), occurs via a precessional motion of magnetization. However, such FM resonance occurs in the 10s GHz frequency regime. This limits the switching time of FM-based spintronic devices to the order of nanoseconds [47]. The resonances of AFs, however, are found closer to *terahertz frequencies* [48]. This offers an avenue for much faster switching of AF spintronic devices in the future [49].
- Stability: A final disadvantage of FM spintronic devices is that they are sensitive to environmental perturbations, such as ionizing radiation or magnetic fields, which could disrupt the information they store [48]. Not only is AF order more resistant to radiation damage (potentially giving AF spintronics applications in *space technology*) but there is no energy saving to made by aligning one (or neither) of its antiparallel moments with an external magnetic field. Thus, AFs can typically only be manipulated by strong (order of several Tesla) magnetic fields.

[III] The state of a spintronic device based on a collinear AF will appear symmetric when reversing the order parameter by 180°. However, for read current flowing in a given direction, rotating the AF order by 90°, such that it is parallel or perpendicular to current flow, can produce a resistivity change in some materials [50]. Fig. 10 shows this for the example of CuMnAs. The resistivity change arises because of an anisotropic MR mechanism (discussed in Section 1.2.8) that can be detected in both longitudinal and transverse voltage channels (the latter is also known as the planar Hall effect).

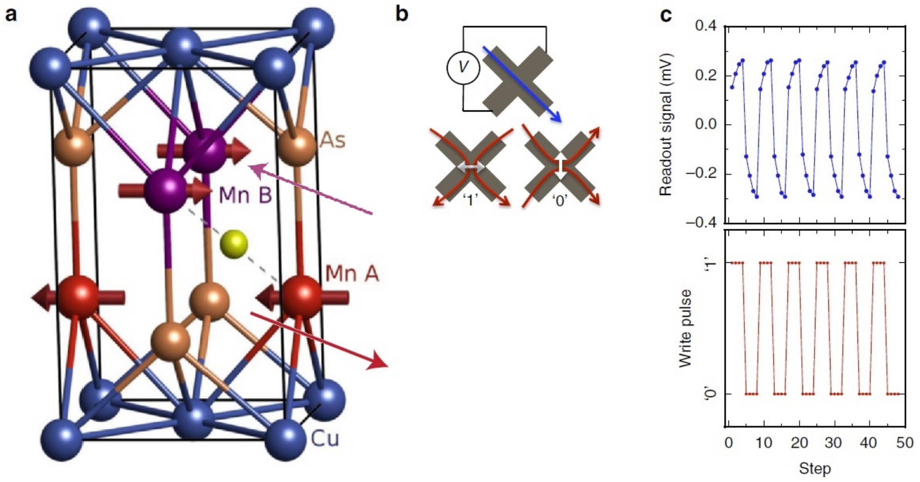

Figure 10: (a) Crystal lattice and magnetic structure of CuMnAs. The two colors of Mn atoms represent different sub-lattices (A and B) and the direction of their atomic moments. Intra-sub-lattice coupling is FM, whilst inter-sub-lattice coupling is AF, resulting in opposite magnetic moments in adjacent planes and creating a collinear AF. Thin arrows represent the direction of the torque that rotates each sub-lattice in the same direction (A out of page, B into page) as a result of the Néel-order switching mechanism. (b and c) Experimental configuration for switching CuMnAs. Current pulses are passed from top-to-bottom, or from left-to-write, as plotted in the lower panel of (c). The inverse spin galvanic effect creates a spin polarization orthogonal to the current flow, thus rotating the collinear AF order perpendicular to the current direction (as shown). This writes a '1' or '0' respectively. The resulting state of the CuMnAs is read-out by applying a smaller read-current and measuring transverse-anisotropic-MR, the value of which is plotted after consecutive current pulses in the upper panel of (c). Adapted from [4] and [43].

Whilst this last point makes AFs attractive as a stable alternative to FMs for spintronic devices, it also introduces problems when it comes to writing information to AF-based bits. Experiments have tested use of the *SHE to exert an SOT on an AF* [51]. However, because it is an interface effect, this encounters problems due to the short spin diffusion length in AFs (order of nanometers) and the often rough surfaces of epitaxial grown AF films [45]. The exertion of SOT on AFs is thus an *ongoing area of research* [52].

Instead, AF spintronics really took off after the discovery of a bulk-originating technique (that is not sensitive to interfacial disorder) to switch the AF CuMnAs [43]. This mechanism requires a crystal structure that is locally noncentrosymmetric, and has subsequently been demonstrated in the AFs MnTe [53] and $\mathrm{Mn_2Au}$ [54]. This effect is known as Néel-order switching, and is based on the **inverse spin galvanic** (or Edelstein) effect [48].

Here, SOC splits the spin-up and spin-down charge carrier sub-bands in a material, and at the same time the two bands are shifted in momentum space due to inversion symmetry breaking [30]. The combined effect of the sub-band splitting and shift in momentum space is called the Rashba effect (if resulting from structural or interfacial inversion symmetry breaking) or the Dresselhaus effect (if resulting from bulk inversion symmetry breaking in semiconductor lattices) [55].

If we apply a voltage across the device, the chemical potential of the sub-bands shifts up and down relative to one another. Charge carrier momentum is thus changed and they are scattered from one sub-band to the other. In the process, they must undergo a spin-flip. This results in an unequal number of electrons occupying spin-up and spin-down bands, and hence a non-equilibrium spin density of charge carriers. If the spin-polarized carriers are exchange coupled to atomic moments, a SOT is induced [30].

In antiferromagnets, such as CuMnAs, the inversion symmetry breaking that induces the inverse spin galvanic effect is local, due to the magnetic moments on each Mn sub-lattice [56]. Fig. 10 (a) shows the inversion center about which centrosymmetry is broken. This results in a local variation in the sign of the inverse spin galvanic effect and, hence, charge carriers with opposite spin-polarization build up at each sub-lattice [56].

However, because the atomic moments on either sub-lattice are aligned antiparallel, the resulting torque exerted on either sub-lattice will be in the same direction. This staggered torque rotates the Mn magnetic moments on both sub-lattices in the same direction, thus maintaining their collinear antiparallel configuration[56]. Because the spin-polarization orientation generated by the inverse spin galvanic effect is perpendicular to current direction, the result is the rotation of the entire collinear AF order by 90°.

The experimental process by which this can be used to write ‘0’ and ‘1’ states into a CuMnAs-based AF spintronic memory element, using **Néel-order switching** to align the collinear Mn atomic moments into orthogonal orientations, is described in Fig. 10 (b).

With this mechanism, we have solved half the problem in realizing a spintronic component based on antiferromagnets; namely, we can *write* a particular configuration to them electrically. However, it is still necessary to *read-out* the state of our device. The electrical signal measured in Fig. 10 (c) corresponds to a magnetoresistance change of $\approx 4\,\%$ between the two orientations of CuMnAs (of the same order as anisotropic-MR in FMs; much less than that typically obtained from TMR) [57].

Therefore, a new mechanism for electrically reading-out the orientation of the AF order parameter is required. A solution to this problem is proposed, through the use of topological antiferromagnets that can generate large magnetotransport signatures [58], in the next Section 1.2.4.

1.2.4 Noncollinear antiferromagnets

In Section 1.2.3, we considered the application of collinear antiferromagnets to spintronics, but found that the magnetotransport effects in such materials are too small to provide a reliable read-out signal. In collinear AFs, neighboring moments align antiparallel, but all pointing along the same axis.

However, now consider the case of AF-coupled ($\lambda_{\text{ex}} < 1$) atomic magnetic moments arranged in the basal plane of a hexagonal crystal structure, or in the (111) plane of a face-centered cubic crystal structure. Here the atomic moments are arranged in sets of three at the vertices of triangles, in turn positioned along the edges of a hexagon in an orientation known as a kagome lattice [38]. If the first two moments couple antiparallel and collinear, in which direction should the third moment point?

It is equally unfavorable to couple the third moment parallel to the first and antiparallel to the second, or vice versa [38]. Thus, there are two possible ground states for this system, a problem we call geometric frustration.

The geometric frustration can be relieved, and a lower energy arrangement of moments achieved, by instead orienting the moments at angles of 120° from one another. The moments still compensate, but are no longer aligned along one axis, so we call such magnetic order **noncollinear antiferromagnetism**. The specific crystal structures of Mn_3Ir (introduced in Section 1.2.6) and Mn_3Sn (introduced in Section 1.2.7) both result in ground state noncollinear AF orders, each with slightly different properties.

Furthermore, MCA will play a role in determining the specific noncollinear magnetic order exhibited by a particular crystal structure, by introducing preferable axes for atomic moments to follow. This, in competition with FM versus AF exchange coupling, geometric frustration and DMI can stabilize a plethora of complex noncollinear magnetic textures in different crystals, including helical spin structures [59] and (anti)skyrmions [60].

Fig. 11 shows the crystal structure of Mn_3Ir, and its noncollinear AF order in the (111) kagome plane. Hopping between the Mn atoms forming each triangle in the *clockwise* direction, we see that each consecutive magnetic moment rotates by 120° (with respect to the previous moment) also in a *clockwise* direction. Hopping anticlockwise, the atomic moments are rotated 120° anticlockwise. We call this **triangular spin texture** [61].

On the other hand, the crystal structure and noncollinear AF order in the (0001) basal plane of Mn_3Sn are shown in Fig. 14 (see Section 1.2.7). Hopping between the Mn atoms forming each triangle in the *clockwise* direction, we see that each consecutive magnetic moment rotates by 120° in an *anticlockwise* direction. Hopping anticlockwise, the atomic moments are rotated 120° clockwise. We call this **inverse triangular spin texture** [62].

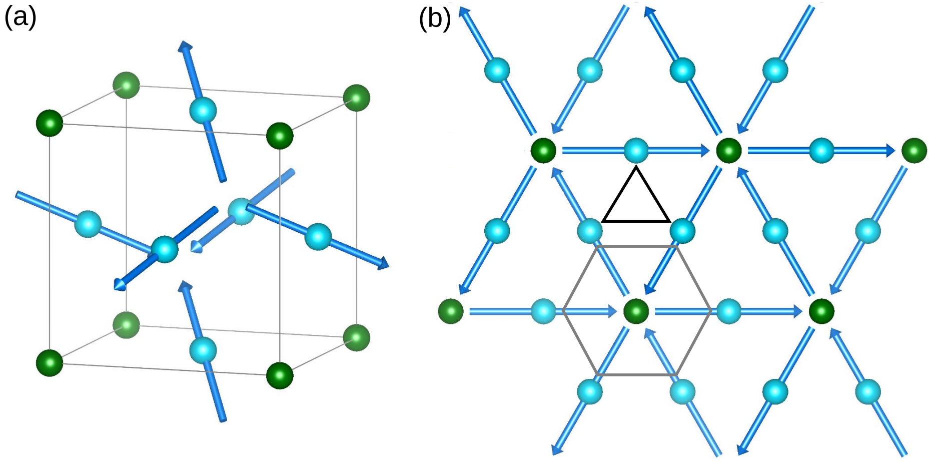

Figure 11: (a) Crystallographic unit cell of Mn_3Ir. Mn atoms shown in blue (with arrows indicating magnetic moments) and Ir atoms shown in green. (b) Noncollinear AF order of Mn_3Ir in the (111) plane. The triangular and hexagonal tiles of the kagome lattice are indicated. Sets of three (AF-exchange-coupled and geometrically-frustrated with DMI-induced-chirality) Mn moments projected along [111] direction form a triangular spin texture.

Whilst the magnetic structures of Mn_3Ir and Mn_3Sn are different, both exhibit **chirality** or *handedness*. This means that a left-hand rotation in one direction through the spin texture encounters different magnetic properties to a right-hand rotation.

For example, for the chirality shown in Fig. 11, a clockwise rotation around the upper triangle sees the Mn moments running tail-to-head, whilst an anticlockwise rotation sees them running head-to-tail. If the direction of all the magnetic moments in the structure is switched, the anticlockwise rotation now see the moments running tail-to-head and vice versa. By flipping the direction of the Mn moments, the *chirality has been reversed.*

Within a particular geometrically frustrated noncollinear AF order, the chirality stabilized in the ground state depends on the energy landscape of the magnetic structure. Specifically, the chirality is determined by the **Dzyaloshinskii–Moriya interaction**. DMI is an example of a superexchange interaction [38]. This means that it couples two atomic moments, as mediated by the overlap of their wavefunctions with that of a third site in the crystal lattice [63]. For this reason, a net DMI only plays a role in a crystal structure with **broken inversion symmetry**.

Furthermore, DMI is an antisymmetric exchange interaction. DMI introduced an additional term to the Heisenberg hamiltonian (see Equation 13), which describes how the coupling between two atomic moments ($\boldsymbol{S}_1$) and $\boldsymbol{S}_2$) effects the energy of the magnetic system [64],

$$H_{\mathrm{DMI}} = -\boldsymbol{D}_{12} \cdot (\boldsymbol{S}_1 \times \boldsymbol{S}_2) \tag{15}$$

Here $\boldsymbol{D}_{12}$ is the DMI vector, whose length describes the strength of the DMI and whose direction points out of the plane containing moments $\boldsymbol{S}_1$ and $\boldsymbol{S}_2$, as shown in Fig. 18 (a) (see Section 1.2.10) [38]. The DMI can introduce a negative contribution to the hamiltonian (i.e. lower the energy of the two coupled atomic moments) if moment $\boldsymbol{S}_1$ forms an angle with moment $\boldsymbol{S}_2$ [63]. This means that the presence of a DMI tends to lead to the canting of moments in a magnetic material (detailed further in Section 1.2.10).

However, this energy saving only arises if moment $\boldsymbol{S}_1$ is rotated to form an angle in a particular direction with respect to moment $\boldsymbol{S}_2$. If $\boldsymbol{S}_1$ tilts in the opposite direction with respect to $\boldsymbol{S}_2$, there will, in fact, be an energy penalty. This means that the DMI energetically favors a certain direction of rotation from one moment to the next [63]. In other words, it introduces a **chirality** to our magnetic system.

This is opposed to the case of the Heisenberg exchange interaction (see Equation 13) given by the scalar product of two magnetic moments, which therefore favors the (anti)parallel alignment of these moments, but whose sign stays the same regardless of whether moment $\boldsymbol{S}_1$ is aligned (anti)parallel to moment $\boldsymbol{S}_2$ or vice versa (and hence is symmetric).

Mn_3Ir and Mn_3Sn are examples of globally centrosymmetric crystal structures. However, the introduction of moments on the Mn atoms, which are geometrically frustrated to form a noncollinear AF order, *breaks inversion symmetry locally* (discussed in Sections 1.2.6 and 1.2.7 respectively). This therefore introduces DMI, which defines a particular chirality for the noncollinear AF order and stabilizes the (inverse) triangular spin texture [65, 66].

The long-range ordering of both the triangular spin texture of Mn_3Ir and inverse triangular spin texture of Mn_3Sn **break time reversal symmetry**. A time reversal operation flips the direction of all the atomic moments, and so the magnetic structure is not reproduced afterwards [67].

An additional mirror symmetry operation might act to switch the magnetic moments back to their original configuration. However, the chirality of both noncollinear AF orders means this is not the case; the mirror image of an object with a certain handedness does not recover the original structure. Thus, *chirality prevents mirror symmetry from rectifying time-reversal symmetry breaking* [67].

By selecting one particular chirality of the (inverse) triangular spin texture, therefore, both mirror and time reversal symmetries are broken [67]. This symmetry breaking caused by localized atomic moments has the effect of modifying the potential generated by the magnetic material's crystal lattice. Specifically, breaking symmetries tends to lift degeneracies in a material's energy-momentum dispersion relation, creating band crossings [58].

Where an itinerant magnet also exhibits **strong SOC**, interactions of these $3d$ atomic moments with $4s$ electrons will lead to a modification of the band structure around the Fermi level [67]. In particular, it can create a band gap at the crossing points, splitting the valence and conduction bands to opposite sides of the Fermi surface [30]. In Mn_3Ir and Mn_3Sn, the strong SOC of the heavy Ir and Sn atoms will be transferred to the Mn moments through hybridization [67].

Such avoided crossings are sources of **momentum-space Berry curvature** [68]. Berry curvature acts as an effective field in reciprocal space [41]. As conduction electrons move across the Fermi surface of the itinerant magnet, this momentum-space Berry curvature will modify their magnetotransport properties (described in Section 1.2.8). We explain this in the context of the intrinsic AHE in Section 1.2.9. Momentum-space Berry curvature is also the origin of intrinsic SHE (introduced in Section 1.2.1).

Whilst the effect on magnetotransport depends on the integral of Berry curvature over the material's Brillouin zone (see Equation 30), the Berry curvature will be concentrated around 'hot spots' in reciprocal space [IV]. We describe band structure features inducing Berry curvature as **topological** [68].

In the case of the noncollinear AFs $Mn_3Ir(Sn)$, it is therefore the chirality of their (inverse) triangular spin texture that breaks time reversal symmetry and generates momentum-space Berry curvature [73]. We can *represent this symmetry breaking through the introduction of an order parameter.* This defines the handedness of the noncollinear AF order, and is called the cluster octupole magnetic moment order parameter [74].

Performing either a time-reversal or mirror-symmetry operation on the noncollinear AF structure *transforms the (inverse) triangular spin texture into its chiral image* [75].

[IV] It has been theoretically proposed that the momentum-space Berry curvature 'hot spots' in Mn_3Sn are the projection of buried **Weyl points** onto the Fermi surface [69, 70]. Weyl points arise when the spin degeneracy of a Dirac point (region of linear dispersion in the bandstructure) is lifted by time- (or inversion-) symmetry breaking [71]. This creates a pair of chiral quasiparticles, which act as *monopole sources/sinks of Berry curvature.* Experimental evidence of these buried Weyl points has been discovered in Mn_3Sn single crystals [72]. That Mn_3Sn is a Weyl antiferromagnet opens up a range of new topological physics that could be explored in this material.

Switching from one chirality (flipping the direction of the magnetic moments) to the other reverses the sign of Berry curvature. This will therefore change the polarity of any magnetotransport effects that are odd with respect to net Berry curvature (whilst leaving those that are even in Berry curvature unchanged) [75].

As we will discuss further in Section 1.2.6, noncollinear AFs, like any long range ordered magnetic material, with have an energetic preference to break up into domains. In the case of $Mn_3Ir(Sn)$ with an (inverse) triangular spin texture, this will result in multiple domains with chirality alternating between them [75]. Manipulating this **chiral domain** structure, in order to control the chirality within the noncollinear AF, is therefore key to realizing topological magnetotransport properties and utilizing them for spintronic applications. In particular, in Section 1.2.6 we see that this is an obstacle for Mn_3Ir, whilst in Section 1.2.7 we see how the unique MCA in Mn_3Sn can be used to drive this material into a single chiral domain state [76].

The noncollinear AFs are therefore a fascinating category of materials in which to study electrical transport, both from the perspective of unraveling the mysteries of topological magnetism, and from the point of view of potential spintronic applications. This is because the large magnitude predicted for such Berry curvature driven magnetotransport phenomena, and the fact that they will switch sign as the chirality of the noncollinear AF is reversed, could provide *the large read signals of AF state* required for spintronics [58]. This developing field is known as **topological spintronics**.

1.2.5 Exchange bias

The first implementation of AF materials (see Section 1.2.3) in spintronics was for the establishing of **exchange bias**. EB is a phenomenon, whereby an AF in contact with a FM introduces an additional *unidirectional anisotropy* to the FM material [77]. This is particularly prominent in thin films, where FM layers can be deposited (see Section 1.3.1) onto AF films, resulting in strong coupling arising at their interface.

For this reason, EB has found applications in spintronic devices such as spin valves or MTJs (see Section 1.2.1). An AF film is deposited adjacent to the reference electrode, with the ensuing unidirectional anisotropy *pinning the magnetization* of the reference layer in a given direction [78]. An external magnetic field or SOT can then switch the free layer, allowing stabilization of parallel and antiparallel states in the device [13].

An exchange-biased FM is characterized by a *shift in its hysteresis loop* along the magnetic field axis when the field ($\mu_0 H$) is applied parallel to the EB-setting direction (discussed with Fig. 12), or a hard axis response (when field is applied perpendicular) [77]. Fig. 12 (a) illustrates this behavior (measured as in Section 1.3.7). An increase in coercive field ($\mu_0 H_\mathrm{c}$) may also accompany the loop shift, due to enhanced pinning of FM domain walls at the interface with the AF [77].

We call this shift in the hysteresis loop the **EB field** ($\mu_0 H_\mathrm{EB}$). Fig 12 (a) indicates the EB field. It is defined as the difference between the points where magnetization (M) crosses the magnetic field axis at both positive ($\mu_0 H_+$) and negative ($\mu_0 H_-$) applied fields,

$$\mu_0 H_\mathrm{EB} = \frac{1}{2}(\mu_0 H_+ - \mu_0 H_-) \tag{16}$$

whilst average coercive field is defined by their sum,

$$\mu_0 H_\mathrm{c} = \frac{1}{2}(\mu_0 H_+ + \mu_0 H_-) \tag{17}$$

The shift in hysteresis loop arises because, when external magnetic field is applied antiparallel to the induced unidirectional anisotropy, more energy (and hence a stronger field) is required to reverse the magnetization. The (cost) saving in energy per unit area by aligning the saturated FM magnetization (M_s) (anti)parallel with the unidirectional anisotropy is related to the EB field by,

$$J_\mathrm{EB} = M_\mathrm{s} d_\mathrm{FM} \mu_0 H_\mathrm{EB}. \tag{18}$$

where d_FM is the thickness of the FM layer [79].

In optimized AF/FM bilayers used for spintronic devices, with a large EB field but minimal increase in coercivity, the hysteresis loop may completely reverse before magnetic field direction is flipped. This is the case in Fig. 12 (a) where, at weak negative fields (on negative to positive field sweeps), it already becomes energetically favorable to reverse the magnetization due to the **interfacial anisotropy energy** saving that results (J_EB).

The interface between the AF and FM dominates the microscopic origin of EB. *Uncompensated magnetic moments arise at the surface of the AF.* These will exchange couple across the interface to the long-range-ordered moments of the FM [80]. Whether this coupling is parallel or antiparallel depends on the sign of the exchange interaction between the AF and FM atomic moments; in the case of the Mn and Ni moments dominating EB in Fig. 12 (a), the coupling is FM [81]. Therefore, the uncompensated Mn moments align parallel with the magnetization of the $\mathrm{Ni_{80}Fe_{20}}$ (ultimately causing the negative shift of the hysteresis loop).

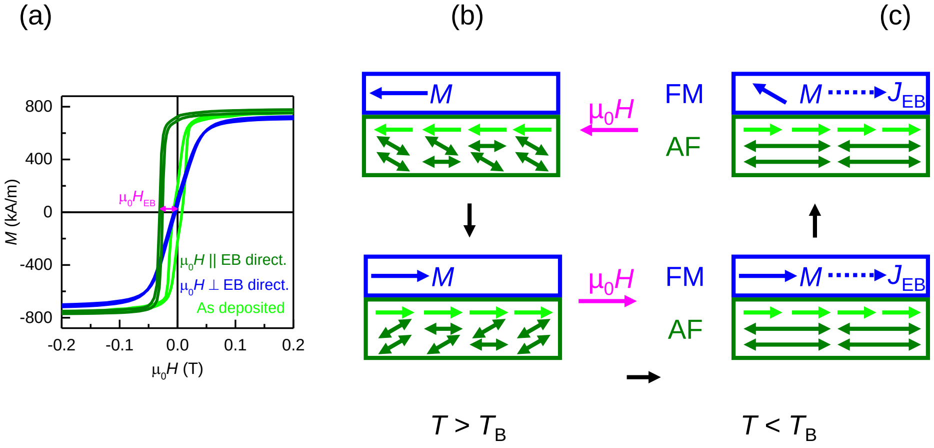

Figure 12: (a) Magnetic hysteresis loops for a 10 nm Mn_3Ir (001) / 5 nm $Ni_{80}Fe_{20}$ bilayer in the as-deposited state and after EB has been set by the procedure illustrated in (b) and (c). With external magnetic field applied perpendicular to the setting direction of unidirectional anisotropy (denoted 'EB direction'), we observe a hard axis response. With external magnetic field applied parallel to the setting direction of unidirectional anisotropy, a large EB field ($\mu_0 H_{\mathrm{EB}}$) shifts the hysteresis loop entirely to negative fields. For spintronic devices such as MTJs, this would allow a free layer to be switched by a small magnetic field, whilst the reference electrode stays pinned, illustrating the applicability of the thin films prepared in this thesis to technological applications. (b) and (c) Exchange coupled AF/FM bilayer; FM magnetization (blue) is coupled FM to uncompensated interfacial moments (light green) which are coupled AF to bulk AF order (dark green). (b) Above T_{B}, the uncompensated interfacial moments follow the FM and AF domain structure is loose. (b → c) When the bilayer is cooled below T_{B} in an external field $\mu_0 H$, the FM magnetization and uncompensated interfacial moments follow the magnetic field, and the corresponding AF domain state becomes fixed. (c) Below T_{B}, the interfacial moments are pinned (by the AF domain structure) in the direction of $\mu_0 H$ applied during cooling, thus setting unidirectional anisotropy (J_{EB}) in the same direction.

The resulting microscopic picture of exchange bias is sketched in Figs. 12 (b) and (c). At high temperatures, the uncompensated AF moments follow the direction of the FM magnetization, if an external magnetic field reverses the latter [82]. However, when cooled below a characteristic temperature (called the **blocking temperature**, T_{B}), the uncompensated interfacial moments become fixed in a certain direction [82]. At this point, the interfacial exchange coupling means that it becomes energetically favorable to keep the FM magnetization aligned with the uncompensated AF moments. Thus, a unidirectional anisotropy is induced.

A generally accepted mechanism as to why the uncompensated moments become pinned below the blocking temperature is the *domain state model of exchange bias*. This posits that, above the blocking temperature of the bilayer system, domains in the AF are loose; the orientation of AF order within them changes, and their AF domain walls move [83, 84]. (The blocking temperature is usually someway below the Néel temperature where the material completely loses its AF character).

The uncompensated AF moments at the interface remain strongly exchanged coupled to the bulk AF order, as well as to the FM magnetization [83, 84]. Thus, above blocking temperature, reorientation of the FM magnetization using an external magnetic field will not only reorientate the uncompensated interfacial moments but, in turn, the entire domain structure of the AF [82]. Fig. 12 (b) illustrates this.

However, as the bilayer is cooled below blocking temperature, the AF domain state is no longer loosened by thermal fluctuations and becomes fixed in place [82]. At this point, the strong AF exchange coupling fixes the uncompensated interfacial moments in a certain direction, and the unidirectional anisotropy sets in [83, 84]. Fig. 12 (c) illustrates this.

The direction in which the uncompensated AF moments become pinned, and hence of the unidirectional anisotropy, can be controlled as described in Figs. 12 (b) and (c) [85].

The AF domains become fixed because of *pinning of the domain walls* separating them [83, 84]. The more robustly these domain walls are pinned in place, the more stable the domain state and the stronger the unidirectional anisotropy. One source of domain wall pinning (as described in Section 1.2.2) are crystallographic grain boundaries in the AF film. Therefore, larger values of EB field are often achieved when using polycrystalline films, where grain boundaries between crystallites pin AF domain walls [86].

The unidirectional anisotropy strength further increases as temperature is reduced below blocking temperature (because thermal fluctuations perturb the AF domain structure less). Therefore, for large EB fields at room temperature, blocking temperature must be as high as possible. A number of factors determine blocking temperature [79, 86–89] [V].

[V] Blocking temperature is affected by: *FM film thickness* (the thicker the FM layer, the lower the blocking temperature, because this parameter, unique to the specific AF/FM system, is an interface effect) [85] versus *AF film thickness* (the thinner the AF layer, the lower the blocking temperature, because the resulting smaller grain size weakens internal anisotropies, due to finite size effects, and lowers Néel temperature) [88] which, in turn, must be balanced against *AF film microstructure* (small grains, defects or impurities, whilst detrimentally affecting blocking temperature, may pin domain walls more strongly, increasing EB field) [86].

In particular, since blocking temperature is located someway below bulk Néel temperature, AFs with high Néel temperature are desirable for EB applications. An example of such an AF (Néel temperature ≈ 700 K), often used to exchange bias spintronic devices, is $\mathrm{Mn_{100\text{-}x}Ir_x}$ [87, 88]. Some of the largest EB fields reported were obtained with polycrystalline $\mathrm{Mn_{80}Ir_{20}}$ thin films [79, 89].

However, epitaxially grown films (see Section 1.3.2) with a stoichiometric 3:1 composition ratio also exhibit a particularly robust EB [90, 91]. These form the ordered phase $\mathrm{Mn_3Ir}$, which is a noncollinear AF and the focus of this thesis [89, 92]. Therefore, in the results chapter 2.1, we delve in much more detail into the EB of epitaxial $\mathrm{Mn_3Ir}$ films. Before that, in the coming Section 1.2.6, we introduce this noncollinear AF and explain why its ordered phase shows particularly large EB.

1.2.6 $\mathrm{Mn_3Ir}$

$\mathrm{Mn_3Ir}$ is a noncollinear AF with a **face-centered-cubic** crystal structure and a lattice parameter $a = c = 0.378\,\mathrm{nm}$ [93]. The unit cell of $\mathrm{Mn_3Ir}$ is shown in Fig. 11 (a) (see Section 1.2.4).

$\mathrm{Mn_3Ir}$ can form in an $L1_2$-ordered phase (where Mn atoms sit on face-center sites and Ir atoms on corner sites), with a Néel temperature of ≈ 960 K [61]. Alternatively, in its γ-disordered phase (where Mn moments are randomly distributed amongst sites), Néel temperature is ≈ 730 K [94].

In a partially-ordered phase, planes of Mn and Ir atoms stack in an ABCA... sequence along the [111] direction (described in Section 1.3.2), projecting a *kagome lattice with triangles of Mn atoms along the edges of hexagons that host Ir atoms* at their center [95]. Each Mn atom has a magnetic moment of $\approx 2.6\mu_\mathrm{B}$ per atom [96].

These Mn atoms are close to fulfilling the Stoner criterion but are exchange coupled with a strength $\lambda_\mathrm{ex} < 1$ (outlined in Section 1.2.2). As explained in Section 1.2.4, this arrangement of Mn atoms therefore produces a **triangular spin texture** [93]. This is illustrated in Fig. 11 (b) [61].

Cubic symmetry is locally broken around the Mn moment on each face-centered lattice site [65]. This local inversion symmetry breaking introduces a DMI between neighboring Mn moments, resulting in the triangular spin texture showing a particular chirality, as detailed in Section 1.2.4.

This local symmetry breaking appears to each Mn moment as an elongation of one crystal axis, yielding a tetragonal symmetry [65]. Tetragonal lattices favor a MCA direction parallel to their elongated axis. This therefore *introduces a uniaxial anisotropy to each Mn moment*, parallel to the $\langle\bar{1}\bar{1}2\rangle$ crystallographic direction [65].

This uniaxial MCA therefore makes it energetically preferable for each Mn moment to align along the $\langle\bar{1}12\rangle$ crystalline direction in closest proximity, as shown in Fig 11 (b). It also introduces a *large energy barrier to rotation of individual Mn moments* around the (111) axis (OP direction in Fig 11 (b)), of $\approx 10\,\mathrm{meV}$ per unit cell [65].

This strong anisotropy results in the **high Néel temperature** of Mn_3Ir ($\approx 1000\,\mathrm{K}$), and makes it a material of choice for introducing large EB to coupled FM layers [65]. This is because (at a given temperature), the preferential axes along which Mn moments lie stabilize the AF order, which in turn strongly pins uncompensated interfacial moments in the direction of unidirectional anisotropy, as explained in Section 1.2.5.

In a real AF sample, however, the magnetic order will break down into domains [97, 98]. Unlike the case of a FM, where domain formation is favorable to reduce demagnetization energy, an **AF domain** forms due to sample microstructure and the resulting magnetostrictive effects [98]. Structural defects in the lattice produce crystalline strain fields, which slightly modify the spacing between atoms. The resulting disruption to the otherwise strong exchange coupling (as well as DMI and MCA) between atomic moments will modify the magnetic structure's energy landscape and favor the formation of domain walls (as explained in Section 1.2.2). In a noncollinear AF, this results in neighboring *domains with alternating chirality.*

Because of the large energy barrier to rotating Mn moments in the triangular spin texture of Mn_3Ir [65], it is very energetically costly to reorientate the chirality of one domain. To achieve this with an external magnetic field would require an extremely strong magnetic field. Furthermore, because each Mn moment within a particular triangular spin texture chirality lies along its preferred $\langle\bar{1}12\rangle$ MCA axis [65], there is *no direction in which we could apply the magnetic field that would favor the growth of a certain domain chirality* at the expense of others. For this reason, Mn_3Ir remains in a **multidomain state**, even in very strong applied magnetic fields. Pinning of the many resulting domain walls also enhances the EB induced by Mn_3Ir [86].

This EB enables the *field-free* current-driven switching of FM layers coupled to Mn_3Ir [99–102]. In this SOT switching process, as described in Section 1.2.1, the unidirectional anisotropy introduced to the FM by EB takes the place of the external magnetic field. At the same time, Mn_3Ir generates the spin current required for switching through the SHE [103–106].

As well as an extrinsic SHE, detailed in Section 1.2.1, Mn_3Ir exhibits an **intrinsic SHE**, also predicted for Mn_3Sn (see Section 1.2.7).

The intrinsic SHE is driven by momentum-space spin Berry curvature; this is generated from topological bandstructure features induced in materials showing certain symmetry breaking [73].

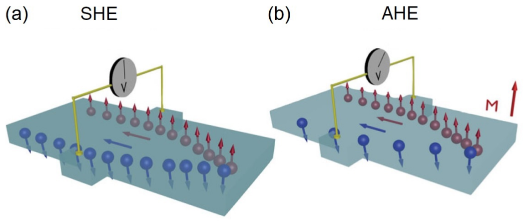

Figure 13: (a) Illustration of the SHE. A current composed of equal numbers of spin-up and spin-down electrons undergo spin-dependent deflection via extrinsic (explained in Section 1.2.1) and intrinsic (discussed in Section 1.2.6) effects. This results in a pure spin current propagating transversely across the device (with no net charge imbalance). (b) Illustration of the AHE. A fictitious magnetic field deflects itinerant charge carriers, giving an intrinsic contribution (introduced in Section 1.2.4). This is combined with an extrinsic contribution from spin-dependent scattering of conduction electrons (detailed in Section 1.2.9), where $4s$ electrons are spin polarized in samples with long-range FM magnetization (M). This results in a net Hall voltage across the sample, and also a spin imbalance (referred to as magnetic SHE).

In parallel with the induced fictitious magnetic field that is the origin of the intrinsic AHE (detailed in Section 1.2.9), this spin Berry curvature leads to the emergence of a *spin-orbit field.* The strength of this spin-orbit field is proportional to the integral of the spin Berry curvature in occupied electron bands around the Fermi level [30].

In a material that also has strong SOC, the emergent spin-orbit field will modify the orbital angular momentum of propagating charge-current carriers depending on their spin [30]. Therefore, interaction with the emergent spin-orbit field exerts *an effective transverse force* on itinerant carriers, with a *sign depending on their spin* orientation. This is comparable to the Lorentz force, which bends the paths of carriers with opposite charge in opposite transverse directions in the ordinary Hall effect (described in Section 1.2.8).

Thus, spin-up electrons are deflected in a certain transverse direction, and the same number of spin-down electrons in the opposite direction [30]. This sets up a pure spin current across a sample, in a direction orthogonal to the charge current.

An intrinsic spin Hall was discovered in Mn_3Ir [75]. This is because its time-reversal symmetry breaking noncollinear AF order introduces corrections to the momentum-space energy dispersion in the form of band crossings (see Section 1.2.4). Combined with **strong SOC**, (see Section 1.2.2), provided by hybridization with the heavy Ir atoms, these crossing points are gapped and act as sources of **momentum-space spin Berry curvature**.

Due to the generation of *spin Berry curvature from the time-reversal symmetry breaking triangular spin texture in kagome* (111) planes, the strength of the emergent spin-orbit field will vary within the crystal structure. This results in an anisotropic SHE, where the spin current generated is of different size along different crystallographic directions [75]. The presence of an intrinsic SHE in Mn_3Ir was indeed confirmed by measuring the ratio of charge-current to spin-current conversion in epitaxial thin films with different crystal orientation, in order to demonstrate this anisotropy through **ST-FMR** measurements [VI].

In Section 1.2.4, we discuss how the opposite chiralities of the noncollinear AF structure show opposite signs of Berry curvature; this also reverses the direction of the emergent spin-orbit field. However, because switching the chirality is equivalent to a time-reversal symmetry-operation, the direction of transverse deflection velocity for each spin-orientation also reverses [75]. The combined effect of switching both spin-orbit field and spin-dependent transverse velocity is that *electrons of a particular spin are deflected in the same transverse direction after chirality reversal.* This is effectively the same as spin Berry curvature being even with chirality [73].

Therefore, intrinsic SHE has the same polarity, regardless of the chirality of the magnetic structure driving it, and the spin current generated will add up over all AF domains [75]. This means that, even though Mn_3Ir breaks down into many small chiral domains, it still exhibits a net SHE that is utilizable in spintronic applications such as field-free SOT switching.

On the other hand, the random distribution of chiralities among AF domains means that the intrinsic AHE (whose polarity is odd with respect to the sign of Berry curvature, as explained in Section 1.2.9) will cancel in Mn_3Ir [67]. With no practical way to use external magnetic field to achieve a dominant chiral domain state (as opposed to the case of Mn_3Sn detailed in Section 1.2.7), AHE has avoided detection even in single crystals of Mn_3Ir.

Whilst there is very recent experimental evidence of a measured AHE in highly-ordered Mn_3Ir films [108], we are motivated to pursue other meth-

---

[VI] One way of measuring SHE is via the modification of the resonance of a FM layer coupled to a spin current generating material [107]. When resonance is excited, e.g. by an external microwave field, two torques are exerted on the FM. The *field-like torque* alters the magnetic energy landscape of the material, changing the precession cone angle in response to excitation frequency, applied magnetic field, and demagnetizing field of the sample. The *damping-like torque* suppresses precession cone angle through the Gilbert damping mechanism. Spin current injection can modify both these torques, contributing either an additional field-like torque, which will modify the resonance field of the FM, or an additional antidamping-like torque, which will act to modulate the Gilbert damping, changing precession cone angle and thus modify resonance linewidth [30]. We call this measurement technique **spin-torque ferromagnetic resonance** (ST-FMR) [Ref: A. Markou et al., “Noncollinear antiferromagnetism and spin Hall effect in cubic Weyl Mn_3Ge thin films”, *Submitted* (2020)].

ods to manipulate the chiral domain structure of Mn_3Ir in order to realize Berry curvature generated magnetotransport effects. This would also prove valuable to potential commercial spintronic devices, where applying external magnetic field is undesirable.

Recently, the application of strain was used to induce AHE in thin films of the related noncollinear AF Mn_3Pt [109]. We therefore aimed to measure intrinsic AHE in epitaxial Mn_3Ir films, in particular those grown strained (see Objectives 1.4). This first required the deposition of Mn_3Ir thin films whose crystal structure could be well controlled through epitaxial engineering (reported in results chapter 2.1). We then proceeded to study the magnetotransport properties of these Mn_3Ir films, on the hunt for topologically driven effects (detailed in results chapter 2.2). These result chapters also discuss more extensively the experimental results of crystal structure, exchange bias and magnetic properties in epitaxial Mn_3Ir thin films.

1.2.7 Mn_3Sn

Mn_3Sn is a noncollinear AF with a **hexagonal** crystal structure and lattice parameters $a = 0.567\,\mathrm{nm}$ and $c = 0.453\,\mathrm{nm}$ [62]. The unit cell of Mn_3Sn is shown in Fig. 14 (a).

Mn_3Sn forms in an $D0_{19}$-ordered phase, with a Néel temperature of $\approx 420\,\mathrm{K}$ [62]. Here basal planes stacked in an ABAB... sequence along the c-axis (described in Section 1.3.2) form a *kagome lattice with triangles of Mn atoms along the edges of hexagons that host Sn atoms* at their center [73]. Each Mn atom has a spin magnetic moment of $\approx 3.0\mu_\mathrm{B}$ per atom [62] (and a smaller orbital moment [64]).

These Mn atoms are close to fulfilling the Stoner criterion but are exchange coupled with a strength $\lambda_\mathrm{ex} < 1$ (outlined in Section 1.2.2). As explained in Section 1.2.4, geometric frustration of Mn atomic moments in this configuration results in a noncollinear AF structure [110].

In addition, MCA plays an important role in forming the ground-state AF order of Mn_3Sn. **Single ion anisotropy** makes it energetically favorable for Mn moments to lie along crystalline directions joining nearest neighbor Sn ions [110]. This results in the $\langle 2\bar{1}\bar{1}0\rangle$ crystallographic directions becoming magnetic easy axes [111].

Therefore, one Mn moment in the triangle lies along a $\langle 2\bar{1}\bar{1}0\rangle$ crystal axis. Furthermore, the MCA competes with exchange coupling and succeeds in canting the other two moments slightly towards this magnetic easy axis [66]. Fig. 14 (b) indicates this canting. It results in the magnetic moments of the three Mn atoms no longer fully compensating [111]; Mn_3Sn therefore shows a *small uncompensated Mn magnetic moment in the basal plane.*

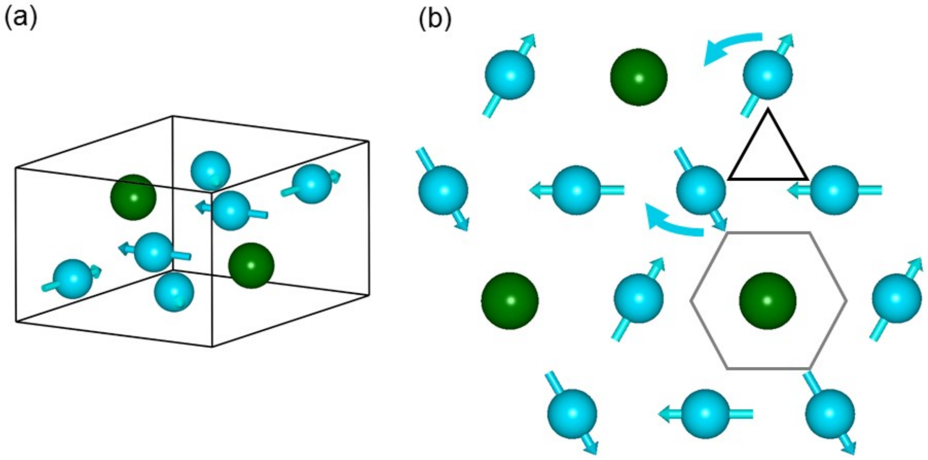

Figure 14: (a) Crystallographic unit cell of Mn_3Sn. Mn atoms shown in blue (with arrows indicating magnetic moments) and Sn atoms shown in green. (b) Noncollinear AF order of Mn_3Sn in the (0001) plane. The triangular and hexagonal tiles of the kagome lattice are indicated. Triangles of Mn moments form an inverse triangular spin texture, with their slight canting towards $\langle 2\bar{1}\bar{1}0 \rangle$ magnetic easy axes highlighted by curved arrows.

This small canting of Mn moments has the additional result of *breaking inversion symmetry locally* [66]. This introduces DMI between Mn moments, which proceeds to further exert a competing influence over the noncollinear AF order [64]. Firstly, because the DMI vector points out of the (0001) plane, parallel to the *c*-axis, the atomic moments are confined in the basal plane (in spite of the significant frustration in the magnetic structure) [66].

Secondly, via the mechanism described in Section 1.2.4, the DMI stabilizes a negative vector chirality in the noncollinear AF order of Mn_3Sn [66]. The resulting **inverse triangular spin texture** is illustrated in Fig. 14 (b) [62].

As temperature is decreased, the balance of interactions acting on the Mn moments changes, and the Mn moments are no longer strongly confined to lie in the kagome plane [112]. The ensuring release of frustration spontaneously tilts magnetic moments out of the basal plane, along the [0001] crystal direction [113]. This results in Mn_3Sn now having a noncollinear, noncoplanar spin texture (whose relevance is detailed in Section 1.2.10) with a small OP FM component of magnetization when magnetic field is applied [113].

It has been proposed that this noncoplanar spin texture may consist of either *two Mn moments canting in the direction of external magnetic field and one canting opposite to it, or all three canting in the field direction* (however, neutron scattering experiments have not conclusively determined which) [112]. This OP canting happens below a transition temperature of

50 K. Due to the spin-glass-type texture of the resulting magnetic structure, we call this the '**glassy-FM**' phase of Mn_3Sn [113].

In the specific case where a sample of Mn_3Sn is prepared with a slight Mn deficiency, such that excess Mn atoms are not occupying Sn sites, the combination of exchange coupling, DMI and MCA stabilizes a third possible magnetic structure [66] (in a temperature range below $\approx 270\,\mathrm{K}$ down to the glassy-FM transition temperature [111]). In this **helical** magnetic phase, Mn moments form a spiral structure propagating along the c-axis [114], whose full rotation occurs over a period of 12 lattice planes [114]. We conjecture that the absence of observation of such a helical magnetic phase in the epitaxial Mn_3Sn films grown in this study is because of a slight excess of Mn (see results chapter 3.2).

Let us focus instead on the inverse triangular spin texture. As explained in Section 1.2.4, the *chirality of this triangular spin texture breaks time reversal symmetry.* This leads to the introduction of topological features to the bandstructure of Mn_3Sn, which act as sources of **momentum-space Berry curvature**, driving novel magnetotransport properties of interest to both fundamental physics and AF spintronic applications [68].

On the other hand, in Section 1.2.6 we discussed how a noncollinear AF will form domains with opposite chirality of the (inverse) triangular spin texture. Berry curvature generated by each chirality will be opposite, meaning that magnetotransport properties that are odd in Berry curvature will cancel across a macroscopic device containing multiple small domains.

The unique magnetic structure of Mn_3Sn, however, gives a mechanism to manipulate chiral domain structure. The **small uncompensated moment** that arises in the basal plane, as a result of the spin canting sketched in Fig. 14 (b) can couple to an external magnetic field. The uncompensated moment can rotate within the (0001) plane, following an applied magnetic field, and can be saturated throughout the sample by magnetic field of moderate strength [112].

Importantly, aligning the weak uncompensated moment, which directly emerges from the noncollinear AF order because of MCA, will rotate all the Mn moments coupled to it via exchange interactions and DMI, in order to maintain the canted inverse triangular spin texture [115]. Since a particular direction of uncompensated moment corresponds to a single chirality of the noncollinear AF order, *by aligning the small uncompensated moment with the external magnetic field, we can orient the entire inverse triangular spin texture into a single chirality.*

This reorientation process occurs via the **motion of domain walls** separating AF domains, growing those domains whose chirality generates an uncompensated moment parallel with the magnetic field, at the expense of others [76]. When the uncompensated moment is saturated (with a theoretical maximum value of $\approx 0.004\mu_{\mathrm{B}}$ per atom [64]) then the $\mathrm{Mn_3Sn}$ is in a single chiral domain state. Use of an external magnetic field to manipulate the weak uncompensated moment therefore gives us a way to saturate, rotate and reverse inverse triangular spin texture, and hence control **topologically driven magnetotransport** properties.

The tiny uncompensated moment, but strong MCA and exchange coupling energies of the noncollinear AF, give narrow domain walls (of the order of nanometers). As discussed in Section 1.2.2, this will result in strong *pinning of the domain walls by structural defects*, producing strain fields that extend over distances comparable to the AF domain wall width. This pinning will play an important role when controlling magnetotransport properties with external magnetic field, and is the origin of the enhanced coercive field observed in epitaxial $\mathrm{Mn_3Sn}$ films, discussed in results chapter 3.2.

The process of chirality reversal via domain wall motion was discovered using **magneto-optical Kerr effect** microscopy, performed on $\mathrm{Mn_3Sn}$ single crystals. Here, significant MOKE contrast arising between domains of opposite chirality allowed their imaging and, hence, observation of their motion in applied magnetic fields [76].

Given that the uncompensated moment is so small, this in itself cannot be the source of the large MOKE contrast observed [115]. In fact, the MOKE (the rotation of the polarization plane during the reflection of linearly polarized light by a magnetic material) measured in (inverse) triangular spin textures is actually a *topological bandstructure effect* [116].

It is driven by momentum-space Berry curvature generated from the time reversal symmetry breaking of the noncollinear AF order in $\mathrm{Mn_3Sn}$ [116].

This also the origin of the **intrinsic AHE** that arises in $\mathrm{Mn_3Sn}$ [68], discussed in Section 1.2.9.

The topological bandstructure induced by the inverse triangular spin texture of $\mathrm{Mn_3Sn}$ will also generate momentum-space spin Berry curvature.

As detailed in Section 1.2.6, $\mathrm{Mn_3Sn}$ is therefore also predicted to demonstrate an **intrinsic SHE** [73].

Finally, in parallel with the comparison between AHE and THE (described in Section 1.2.10), SHE can be complemented by a **topological spin Hall effect**. This is induced by *real-space spin Berry curvature, specifically by spin-rotation symmetry breaking in the real-space chiral AF structure*, and so is predicted to be observable even in the absence of SOC [117].

Finally, charge currents in Mn_3Sn can become spin polarized [VII]. In parallel with the footnote of Section 1.2.9, this causes a **magnetic spin Hall effect** in Mn_3Sn [118].

Up until recently, the majority of these topological magnetotransport phenomena were measured in Mn_3Sn bulk crystals. This was because Mn_3Sn had not been grown in thin film form, despite this being required for any potential spintronic applications.

An important objective, therefore, was the growth of epitaxial Mn_3Sn films (as detailed in Objectives 1.4). The successful deposition of epitaxial Mn_3Sn films is reported in results chapter 3.1. Here, we also give a detailed description of experimentally measured crystal structure and magnetic properties of Mn_3Sn prepared in thin film form.

Subsequently, we aimed to discover topological magnetotransport properties in these epitaxial Mn_3Sn films, starting with the AHE (as the most relevant mechanism for electrically reading-out the state of potential spintronic devices). These measurements are reported in results chapter 3.2.

1.2.8 Magnetotransport and Hall effect

In spintronics, we aim to utilize the electron spin to create functional devices. To do this we use magnetic materials, whose state is written and read using electric currents. Therefore, exploring the interaction between electricity and magnetic order is important. Often this comes in the form of a material's electrical resistivity varying as its magnetic properties change. We call this field of study magnetotransport.

[VII] In the equilibrium state, electrons at the Fermi level of Mn_3Sn occupy states with spin polarization along various directions. When an electric field is applied, these electrons form a longitudinal charge current. Mn_3Sn can be treated as an itinerant magnet [119]. Therefore, $4s$ electrons redistribute into certain states on the Fermi surface, whose spin polarizations are fixed in given directions due to the topological properties of the inverse triangular spin texture [120]. *This is predicted to spin polarize a majority of itinerant electrons in a particular direction, thus forming a longitudinal spin-polarized charge current.* The spin polarization direction is odd under time reversal, so, as with the AHE, the currents will only be prevalent if Mn_3Sn is driven into a dominant chiral domain state [120]. Similar spin-polarized charge currents are predicted for Mn_3Ir [120]. Longitudinal spin-polarized charge currents have yet to be experimentally realized, although open up a new avenue of potential spintronic devices where noncollinear AFs directly substitute $3d$-FMs (for example, the TMR and GMR devices introduced in section 1.2.1). Finally, since charge current electrons are now spin polarized, when they are deflected transversely by intrinsic AHE (see Section 1.2.9), they will also show magnetic SHE, discussed above.

Some magnetotransport effects have been known for over a century, for example AHE (Section 1.2.9); others discovered only recently, such as THE (Section 1.2.10). Magnetotransport in FM thin film heterostructures, e.g. GMR [12] and TMR [13], formed the foundation of spintronics (Section 1.2.1). And magnetotransport measurements are the crux of the results in this thesis.

The electrical transport behavior of a sample under different conditions is characterized through its resistivity. This is, in turn, determined from a measurement of resistance in a specimen of known size. In this section (as in the remainder of the thesis), we discuss the physics of resistance measurements in Hall bars lithographically fabricated (see Section 1.3.9) in thin-film samples. In this case, resistance of the *device-under-test* can be recorded accurately using a four-point resistance measurement. Fig. 15 describes this measurement technique [121].

A current source provides a constant current ($I = I_{\text{source-drain}}$) through the circuit, whilst a high-impendence voltmeter measures a potential drop ($V = V_{\text{Hi}} - V_{\text{Lo}}$) that is almost identical to the potential difference between the voltage terminals of the *device-under-test*. This gives us the resistance, $R = R_{\text{sample}}$, according to Ohm's law,

$$V = IR \tag{19}$$

By measuring voltage as a function of current (an IV curve), the gradient yields the resistance of the *device-under-test*.

We can use this to calculate the (device-size independent) resistivity of the material, ρ,

$$\rho = \frac{RWt}{L} \tag{20}$$

where L is the spacing between voltage contacts, W is the channel width and t is film thickness. We quote such values of resistivity for different samples, as a measure of how reluctant they are to allow electron transport.

Alternatively, if we wish to discuss the ease with which materials propagate current, we quote conductivity, σ,

$$\sigma = \frac{1}{\rho} \tag{21}$$

This is the case, for example, when we discuss the AHE in Section 1.2.9.

Depending on the arrangement of contacts in the *device-under-test*, voltage can be measured parallel to current (giving longitudinal resistivity, ρ_{xx}) or perpendicular to current (giving transverse resistivity, ρ_{xy}).

What insight into material properties can such measurements give? Beginning with the **free-electron** (or Drude) model for carrier (electron or

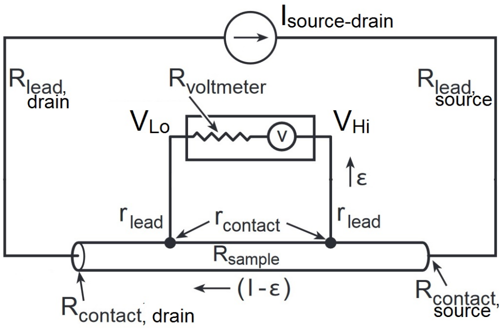

Figure 15: Circuit diagram of a four-probe resistance measurement. Current source applies a current, $I = I_{\text{source-drain}}$. Voltmeter measures potential difference, $V = (V_{\text{Hi}} - V_{\text{Lo}})$. Resistance of *device-under-test*, $R = R_{\text{sample}}$, is determined from Equation 19. Internal resistance of the current source is very large ($1 \times 10^{14}\,\Omega$ for Keithley 6221 utilized in this thesis [122]). It is varied (using a set of transistors and a negative feedback loop) such that a constant current passes through both the *device-under-test*, and source/drain wires and contacts regardless of their resistances ($R_{\text{lead(contact), source(drain)}}$). Internal resistance of the voltmeter is also very large ($1 \times 10^{9}\,\Omega$ for Keithley 2182A utilized in this thesis [123]). Therefore, current flowing into the sense circuit, ϵ, is very small, meaning there is negligible voltage drop across the sense wires and contacts. Thus, the size of their resistance ($r_{\text{lead(contact)}}$) does not impact the measurement and ($V_{\text{Hi}} - V_{\text{Lo}}$) is almost exactly the potential difference between the two voltage terminals on the deivce-under-test. Furthermore, current flowing through the *device-under-test* $(I - \epsilon) \approx I_{\text{source-drain}}$ and its resistance, R_{sample}, can be accurately calculated. Adapted from [121].

hole) transport, which is based on kinetic theory, we can move instead to a semiclassical picture, where electrons are described using Fermi-Dirac statistics (known as the **Drude-Sommerfeld model**) [37]. Extending the model to be fully quantum mechanical, thus introducing the band nature of electronic structure in crystalline solids[VIII], we obtain the following expression for longitudinal resistivity (e is electron charge) [124],

$$\rho_{\text{xx}} = \frac{m^* v_{\text{F}}}{nle^2} \tag{22}$$

Here n is number density of carriers per unit volume, l is carrier mean free path, m^* is carrier **effective mass**, and v_{F} is **Fermi velocity** [37]:

[VIII] In a simple quantum mechanical model, we approximate the carriers as interacting weakly with the crystal lattice, which can be represented as a periodic potential. Bloch's theorem shows us that the carriers encountering this potential will take the form of a superposition of plane waves. Finding steady state solutions to Schrödinger's equation for such wavefunctions, whilst imposing periodic boundary conditions given by the Brillouin zone, yields a quantization of carrier energy. These energy levels extend in bands through reciprocal space, forming the crystal's bandstructure [125].

- n is governed by specific chemical and structural properties. Intentional doping or impurities, as well the actual elements from which the material is made, determine **charge carrier concentration**. In metals, this will be predominant in determining transport behavior. In semiconductors or semimetals, with fewer carriers, other effects play a role. We can measure n using Hall effect, described below.
- l depends on electron scattering rate; how often electrons are deflected by collisions with defects or the vibrating lattice (phonons). Shorter **mean free path** therefore increases the resistivity of thin films with dislocations or stacking faults. Because phonon scattering deceases at lower temperatures, this term is also responsible for the temperature dependence of resistivity in metals.
- m^* is the electron rest mass multiplied by a factor that reflects how carrier motion is modified by the crystal's bandstructure. This may make charge carriers lighter or heavier, as it collects together the ways in which they interact with the potential of the lattice. Because of this, we refer to the theory of *transport incorporating effective mass as the nearly free electron model.*
- v_f is the group *velocity of the carrier wavepacket, determined by the shape of the Fermi surface in its vicinity.* The Fermi surface is the interface between occupied and unoccupied bands, so carriers close to it are responsible for transport. The Fermi surface can lie in the conduction band of metals, or at the boundary between conduction and valence band in semimetals. It can have complex shapes, depending on material properties, especially crystal structure.

Thus, even this simple model can reveal much about the fundamental physics in our materials. What about if we apply a magnetic field?

The change in longitudinal resistivity with magnetic field is called **magnetoresistance**, defined as [38],

$$\mathrm{MR}(\%) = \frac{\rho_{\mathrm{xx}}(\mu_0 H) - \rho_{\mathrm{xx}}(0)}{\rho_{\mathrm{xx}}(0)} \times 100 \tag{23}$$

Magnetic field can affect longitudinal resistivity in two primary ways. Firstly, when a magnetic field penetrates our sample, flowing carriers will experience a Lorentz force (F) perpendicular to both their direction of motion and to the magnetic field,

$$\boldsymbol{F} = e(\boldsymbol{\zeta}_{\mathrm{x}} + \boldsymbol{v}_{\mathrm{F}} \times \boldsymbol{\mu_0 H}) \tag{24}$$

where ζ_{x} is the electric field set up by applying current across the *device-under-test.* This causes carriers to move in helical orbits around the magnetic field lines. Carrier cyclotron frequency (ω_{c}) gives the time taken to complete one orbit [37],

$$\frac{1}{\omega_c} = \frac{m^* c}{\mu_0 H e} \tag{25}$$

When this period is shorter than the time between carrier scattering events ($1/\omega_{\mathrm{c}} < l/v_{\mathrm{F}}$), then the carriers undergo a complete orbit. This requires high magnetic fields, however in this case carriers move through closed loops on the Fermi surface [37]. The shape of the Fermi surface will determine the Fermi velocity, and hence the resistivity measured. Measuring as a function of field strength and direction will change the carrier's closed-loop path on the Fermi surface and thus its Fermi velocity, resulting in a resistance change with magnetic field (in other words, MR). Novel effects can be observed in semimetals whose Fermi surfaces host interesting geometric features or are topologically nontrivial [71]. This effect is known as **geometric, or Lorentz, MR**.

What is current flows through a magnetic material? The resulting physical process relies on three key phenomena detailed elsewhere in this thesis. Firstly, in itinerant FMs, charge carriers comprise of delocalized 4*s* band electrons. These are spin polarized by exchange interactions with atomic magnetic moments, which (due to the quenching of orbital angular momentum) are generated by 3*d* sub-shell electrons (see Section 1.2.2).

SOC within the 3*d sub-shell means electrons of a particular spin can only occupy certain orbitals. Therefore, the* 3*d density of states becomes spin-split; between states that accommodate electrons aligned either parallel or antiparallel with the spin-dominated atomic moment* [126].

The density of states contributing spins to the net atomic moment will be more heavily populated with electrons, whilst some states aligned antiparallel to the net atomic moment will remain unoccupied. In a magnetic transition metal, this effectively shifts the Fermi level up for the split 3*d sub-band aligned parallel with the magnetization, whilst lowering it in the antiparallel* 3*d sub-band* [38].

At the same time, the resistance of such itinerant FMs is dominated by scattering events that transition a delocalized 4*s conduction electron into an localized* 3*d sub-shell state. We call this process* $s - d$ *scattering* [126].

Fermi's golden rule gives the probability of such transition events occuring (the second key phenomenon, explained in Section 1.3.8). The rate of $s - d$ scattering therefore depends on the density of unoccupied states in the 3*d* sub-shell [126]. However, if the 4*s* conduction electrons are spin polarized parallel to the atomic moments, and the majority of states aligned with the atomic moments are fully occupied, then the rate of $s - d$ scattering is suppressed. Thus, if an external magnetic field is applied to align the magnetization of such an itinerant FM, then the mean free path of charge carriers will increase, and its resistivity will decrease [38]. This is one example of a MR effect seen in itinerant FMs.

Furthermore, if we now rotate this magnetic field, to modify atomic moment orientation with respect to current direction, we observe that resistivity is higher when magnetization and current are parallel, and lower when magnetization is dragged perpendicular to current. The origin of this effect is the third key phenomenon, SOC (see Section 1.2.2). Coupling of the $4s$ conduction electron orbital angular momentum to the localized $3d$ atomic moment spin orientation modifies the transition matrix elements that also contribute to determining $s - d$ scattering probability. If the motion of the electrons is parallel to the spin-dominated atomic moment direction, then the $s - d$ scattering rate is higher, and mean free path shorter. If the motion of the electrons is perpendicular to the spin-dominated atomic moment direction, then the scattering rate is lower, and mean free path longer [126]. Therefore, the resistivity of an itinerant FM will vary as we rotate magnetic field, another example of a MR effect.

Finally, SOC of the $3d$ sub-shell spins to the crystal lattice, via their atomic orbitals, causes MCA in highly-crystalline samples. However, it also leads to a dependence of $s-d$ scattering transition matrix elements on crystallographic direction [126]. Combining these effects, we find that the resistivity of a magnetic material depends on the relative orientation of external magnetic field and charge current (and also, in some epitaxial thin films, crystal axes) [38]. This is known as **anisotropic MR**.

Other MR effects have been discovered, for example GMR [12] and TMR [13], that also occur because of the spin polarization of carriers flowing through a ferromagnetic metal (see Section 1.2.2); these form the genesis of the field of spintronics (discussed in Section 1.2.1).

What about transverse resistivity? The variation in transverse resistivity with magnetic field is called the **Hall effect** [127]. Hall effect is measured as explained in Fig. 16.

Again, when magnetic field is applied OP of the thin film, Lorentz forces bend the path of propagating carriers. This causes them to move in a direction perpendicular to the current, therefore setting up a transverse voltage (V_{xy}) across the device under test [127]. A steady state will be established, where the transverse electric field (ζ_{y}) generated by this transverse voltage is equal and opposite to the Lorentz force (from Equation 24),

$$\zeta_{\mathrm{y}} = v_{\mathrm{F}} \mu_0 H \tag{26}$$

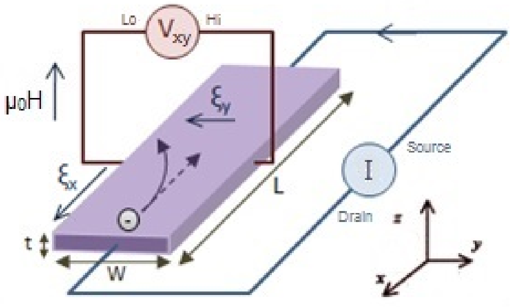

Figure 16: Cartoon summarizing the mechanism of the Hall effect for electrons. Measurement geometry consists of a device (of width, W, length, L and thickness, t) through which a current $I = I_{\text{souce-drain}}$ is passed (along the x direction) whilst measuring transverse voltage $V_{\text{xy}} = (V_{\text{Hi}} - V_{\text{Lo}})$ (along the y direction). This Hall voltage is driven by an electric field, ζ_{y}, and is measured as a function of magnetic field $\mu_0 H$. In a thin film geometry, magnetic field is applied OP (along the z direction), whilst current is sourced and Hall voltage sensed in a device patterned in the film plane. Adapted from [128].

Substituting in the Fermi velocity determined from the **nearly free electron model**, the transverse voltage measured across the *device-under-test* is therefore determined by [127],

$$V_{\text{xy}} = \frac{I}{t}\frac{1}{ne}\mu_0 H \tag{27}$$

In this **ordinary** Hall effect, the *increase in transverse voltage with magnetic field is linear.* Knowing the current through the device and the film thickness, measuring the gradient of transverse voltage as a function of OP applied field allows us to extract a parameter called the Hall coefficient, R_{H},

$$R_{\text{H}} = \frac{1}{nq} \tag{28}$$

where $q = \pm|e|$. The sign of the Hall coefficient is given by carrier charge and indicates whether transport is dominated by electrons (negative) or holes (positive), whilst also allowing us to calculate carrier concentration [127]. Alongside ordinary Hall effect, this same technique can be used to measure anomalous (see Section 1.2.9) and topological (see Section 1.2.10) Hall effects.

In this way, we measured resistivity in Hall-bar devices of noncollinear AF films. A cryostat was utilized for this purpose (details given in Section 1.3.10), enabling studies as a function of temperature down to 2 K and as a function of external magnetic field applied OP. These results of magnetotransport in Mn_3Ir and Mn_3Sn, reported in results chapters 2.2 and 3.2 respectively, are highlights of this thesis.

1.2.9 Anomalous Hall effect

In the previous Section 1.2.8, we explained how an external magnetic field bends the paths of flowing charge carriers, setting up a transverse voltage across a conducting material (Hall effect). In the case of FM metals that are of interest for spintronic applications (discussed in Section 1.2.1) there is an additional, much larger, contribution to the Hall voltage [37]. This is the **anomalous Hall effect**. The AHE has potential uses in spintronics, as the large transverse voltage generated could be used, for example, to read out the orientation of a magnetic component [28].

This is because the AHE tends to follow the magnetization of a FM; the Hall signal increases nonlinearly as magnetic field is applied, reaches a steady value at saturation magnetization, maintains a spontaneous nonzero value as magnetization is reduced through remanence, and changes sign as magnetization direction is reversed through coercivity [38].

This suggests that FM magnetization is responsible for the AHE. This is true, although there are three distinct ways in which the magnetization can generate AHE. We will discuss these in this section. We find that the dominant source of AHE in transition metal FMs is not the magnetization itself, but rather time-reversal symmetry breaking by the FM order [129]. *This opens up the possibility of other materials, which also show time-reversal symmetry breaking long-range magnetic order, also demonstrating AHE.*

We measure AHE in the same way as the ordinary Hall effect (detailed in Section 1.2.8). The transverse voltage across a solid-state sample, or a thin film device, is measured in response to a magnetic field applied OP. The changing voltage (V_{xy}) across the sample, with a constant excitation current (I), corresponds to a proportional change in the material's transverse resistivity (ρ_{xy}). This, in turn, is inversely proportional to a change in conductivity; the Hall conductivity ($\sigma_{\mathrm{xy}} = \rho_{\mathrm{xy}}/(\rho_{\mathrm{xx}})^2$).

The origin of AHE lies in four key phenomena that underpin several of the spintronic effects described in this thesis. They are:

- Spin-splitting of electron orbitals within atoms, for example in the $3d$ sub-shell, and the uneven filling of the resulting density of states to generate magnetic moment (explained in Section 1.2.8).
- Transition, or scattering, probabilities of delocalized electrons depending on how their spin orientation compares with the occupation of localized spin-split density of states (explained in Section 1.3.8).
- The spin polarization of $4s$ conduction electrons in itinerant FMs, in a direction parallel to their magnetization, because of exchange coupling to ordered magnetic moments (explained in Section 1.2.2).

- SOC between spin degree of freedom (of electrons in either $3d$ or $4s$ subshells) and orbital angular momentum (of electrons either in localized or delocalized states) (also explained in Section 1.2.2).

These phenomena, when combined, can cause the *transverse deflection of itinerant electrons* moving through a long-range magnetically ordered material. This *causes an accumulation of charge* at one edge of the sample, *setting up a voltage across the device.* This is similar to the ordinary Hall effect, but with the much stronger *transverse deflection mechanisms* leading to an anomalously-large Hall effect. [129].

The transverse-deflection mechanisms that cause the AHE are comparable to those responsible for the SHE (as explained in Section 1.2.1). These can be divided into two types: **extrinsic** and **intrinsic** [129].

The extrinsic transverse-deflection mechanisms are identical to those causing SHE; these spin-dependently deflect conduction electrons transversely during scattering events [129].

The extrinsic AHE can, in turn, be divided into two contributions [129]:

- **Side jump** contribution arises from *impurity scattering* and is therefore the dominant mechanism in bad metals (where $l \approx$ lattice spacing). Experimentally, its contribution to transverse conductivity ($\sigma_{\mathrm{xy}}^{\mathrm{sj}}$) is found to increase with longitudinal conductivity at a rate faster than linear ($\propto \sigma_{\mathrm{xx}}^{\approx 1.6}$). The spin-dependence of the scattering events requires **strong SOC** between a delocalized electron's spin moment and the orbital angular momentum of localized electrons in impurity atoms. In this case, the *transverse component of momentum* introduced to a conduction electron when scattering off the impurity atom will have a *sign that depends on the conduction electron's spin direction.*
- **Skew scattering** contribution arises from *Mott scattering.* Experimentally, its contribution to transverse conductivity ($\sigma_{\mathrm{xy}}^{\mathrm{skew}}$) is found to increase linearly with longitudinal conductivity ($\propto \sigma_{\mathrm{xx}}$) and it is therefore the dominant mechanism in perfect crystals with long mean free paths. During Mott scattering events, **Fermi's golden rule** gives the probability of a longitudinally propagating electron being scattered in a particular transverse direction. The transition matrix elements governing this dictate that, *in the presence of strong SOC*, an itinerant electron has a *higher probability of being scattered in a transverse direction given by the vector product* of its longitudinal momentum and spin orientation ($\boldsymbol{k}_{\mathrm{x}} \times \boldsymbol{S}_{\uparrow\downarrow}$). This results in a higher proportion of spin-up electrons being scattered in one particular transverse direction, and a higher proportion of spin-down electrons being scattered in the opposite transverse direction.

A majority of $4s$ electrons in an itinerant FM will be spin polarized in a direction parallel to its magnetization. These extrinsic spin-dependent scattering processes will therefore *deflect all these majority-spin-polarized conduction electrons in the same direction*, setting up a transverse voltage across the sample and generating AHE [30].

Fig 13 (see Section 1.2.6) sketches this AHE process and compares it with SHE (in a normal metal where electrons are not spin polarized) [30]. We see that, in materials showing long-range magnetic order where $4s$ electrons are spin polarized, the charge accumulation generating the AHE voltage will also be spin polarized [IX].

The intrinsic AHE contribution, on the other hand, does not depend on spin-dependent scattering (and, hence, is independent of scattering rate and, thus, of longitudinal conductivity).

The intrinsic transverse-deflection mechanism is similar to that causing SHE; but is instead driven by momentum-space Berry curvature. This generates an extremely strong fictitious magnetic field, which deflects charge carriers in a transverse direction just as in the ordinary Hall effect [129].

The intrinsic AHE arises in materials showing **strong SOC**. This is because, the bandstructure of a solid-state material forms as a result of interactions between electrons and the crystal lattice. Where a material has strong SOC, atomic magnetic moments localized to the lattice will modify the bandstructure around the Fermi level inhabited by delocalized conduction electrons [67].

Specifically, long range ordering of $3d$ atomic moments *breaks time reversal symmetry.* Time reversal symmetry breaking introduces **momentum-space Berry curvature** to the band structure [129]. This Berry curvature is a *type of field in reciprocal space.*

As itinerant electrons move across the material's Fermi surface through this Berry-curvature-type field, the Bloch wavefunctions describing these electrons will acquire a phase shift [41]. This is called the momentum-space **Berry phase**. The Berry phase ($\bar{\gamma}$) is given by the integral of Berry curvature (β) over the surface (defined by the normal vector, $\boldsymbol{S}$) across which the electron moves [41],

---

[IX] The intrinsic AHE contribution does not depend on spin-dependent scattering, but rather on a fictitious magnetic field (and, thus, may also be observed in materials not showing spin polarized currents). However, if conduction electrons are spin polarized (as is the case for $4s$ electrons in an itinerant FM, or charge carriers in Mn_3Sn, detailed in Section 1.2.7) then electrons deflected transversely will also be spin polarized. Because of the effective transverse spin current established, we refer to this phenomenon as the magnetic SHE [118].

$$\bar{\gamma} = \int \beta \mathrm{d}\boldsymbol{S} \tag{29}$$

A charged particle will also acquire a Berry phase if it *moves in a magnetic field*. This is known as the Aharonov-Bohm effect, where the particle's energy levels become quantized if it moves on a closed path [39], or, when discussed in the context of electrons in a condensed matter system subject to strong external magnetic field, it is known as the quantum Hall effect [37].

By drawing a parallel with these phenomena, we can equate the Berry phase acquired by electrons in an itinerant FM with *that endowed by an external magnetic field*. In other words, the momentum-space Berry curvature generated by the magnetic material's bandstructure is equivalent to a fictitious magnetic field acting on $4s$ electrons [39].

This **fictitious magnetic field** exerts an effective Lorentz force on the charged electrons, bending their paths as they propagate through the material, in a similar manner to the ordinary Hall effect (explained in Section 1.2.8). However, the fictitious magnetic field generated by the momentum-space Berry curvature can be very strong (of the order 100 T) [58]. Therefore, the paths of the charge carriers are strongly deflected. When the carriers are all electrons, these deflections will all be in the same transverse direction, setting up a large voltage across the sample and thus an intrinsic AHE [129].

The intrinsic contribution to anomalous Hall conductivity induced in the plane of a sample ($\sigma_{\mathrm{xy}}^{\mathrm{intrinsic}}$) can be calculated by integrating the OP component of momentum-space Berry curvature (β_{z}) over the Brillouin zone (BZ),

$$\sigma_{\mathrm{xy}}^{\mathrm{intrinsic}} = \frac{e^2}{\hbar} \int_{\mathrm{BZ}} \frac{\mathrm{d}\boldsymbol{k}}{(2\pi)^3} \sum_{\mathrm{n}} f(\boldsymbol{k}) \beta_{\mathrm{z}}^{\mathrm{n}}(\boldsymbol{k}) \tag{30}$$

where e is electron charge, $\hbar$ is reduced Planck's constant and $\boldsymbol{k}$ is wavevector. $f(\boldsymbol{k})$ is the Fermi-Dirac distribution function, the sum over which adds up the Berry curvature generated by each occupied band (with index, n).

Fig. 17 plots the total anomalous Hall conductivity ($\sigma_{\mathrm{xy}}^{\mathrm{A}} = \sigma_{\mathrm{xy}}^{\mathrm{sj}} + \sigma_{\mathrm{xy}}^{\mathrm{skew}} + \sigma_{\mathrm{xy}}^{\mathrm{intrinsic}}$) measured for various long-range ordered magnetic materials, as a function of the samples' longitudinal conductivity (σ_{xx}, see Equation 21) [130]. Experiments show that the intrinsic mechanism is the dominant contribution to AHE in itinerant FMs [30].

In this case, it is not atomic moments themselves that cause AHE, rather time-reversal symmetry breaking by their long-range magnetic ordering [129].

Therefore, other magnetic materials showing a long-range order that breaks time reversal symmetry would also be expected to show an intrinsic AHE [67, 68]. In Section 1.2.4, we detail how noncollinear AFs break time reversal symmetry. *This introduces topological features to their bandstructure, which act as sources of momentum-space Berry curvature.* Therefore, the noncollinear AFs studied in this thesis, Mn_3Ir [67] and Mn_3Sn [68], are theoretically predicted to show Berry-curvature driven intrinsic AHE [73].

However, for noncollinear spin textures, the sign of the generated Berry curvature is opposite for their two possible chiralities (described in Section 1.2.4). AHE (unlike SHE, discussed in Section 1.2.6) is *odd with respect to Berry curvature*, because the sign of the fictitious magnetic field, and hence the anomalous Hall voltage, is reversed. Therefore, the intrinsic AHE generated by different chiral domains will cancel across a demagnetized sample. In order to exhibit net AHE, a noncollinear AF must obtain a domain state where one chirality is prevelant [73].

As detailed in Section 1.2.6, the large internal anisotropies in a *triangular spin texture* mean there is a large energy barrier to rotating its magnetic moments with an external magnetic field applied in the kagome plane. For this reason, it is hard to obtain a dominant chiral domain state in Mn_3Ir, and thus manipulate its topological magnetotransport properties using magnetic field alone (discussed in more detail in the results chapter 2.2).

On the other hand, in Section 1.2.7, we describe how a combination of DMI and MCA in Mn_3Sn introduces magnetic easy axes within its hexagonal crystal structure. By applying a magnetic field in the basal plane, it becomes energetically favorable to align the **small uncompensated magnetic moment** with the external magnetic field, which in turn acts to coherently rotate the entire inverse triangular spin texture into a single orientation [110].

Therefore, a small external magnetic field can drive Mn_3Sn into a **dominant chiral domain state** (see Section 1.2.7), such that it shows a nonzero net Berry curvature and hence AHE [76]. This mechanism enabled the experimental demonstration of AHE by Nakatsuji et al. in 2015 [131].

This was followed by a number of other observations of AHE in Mn_3Sn bulk samples [115, 132–134] as well as in related hexagonal noncollinear AFs such as Mn_3Ge [135–137]. The ability to control the chirality of the inverse triangular spin texture has also enabled the observation of other **topological phenomena** that emerge as a result of momentum-space Berry curvature in Mn_3Sn, for example MOKE, as detailed in Section 1.2.7.

Whilst these make Mn_3Sn an exciting test-bed for the fundamental physics of topological magnetism (see Section 4), for fully electrical spintronic devices, the AHE will still serve as the key read-out mechanism [X]. Therefore, the further exploration of AHE in thin films of Mn_3Sn is an important goal.

[X] There are also schemes proposed for writing information to devices based on noncollinear AFs [52]. This is an ongoing area of research, described in Section 4.2.

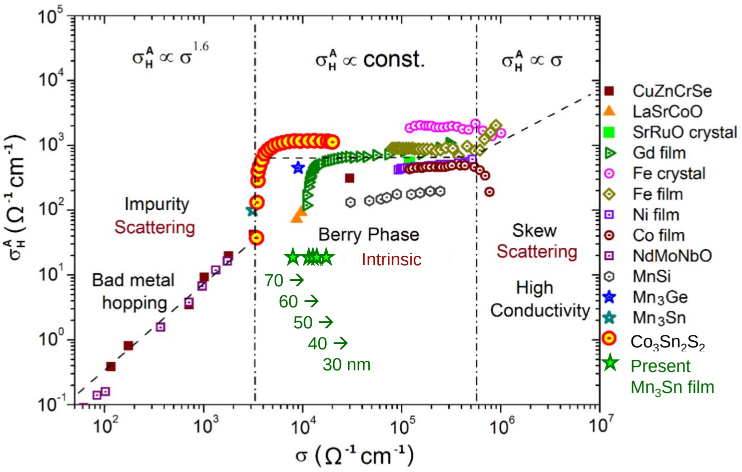

Figure 17: The anomalous Hall conductivity ($\sigma_{\mathrm{xy}}^{\mathrm{A}} = \sigma_{\mathrm{H}}^{\mathrm{A}}$) measured for a variety of materials showing long-range magnetic order, plotted as a function of their longitudinal conductivity ($\sigma_{\mathrm{xx}} = \sigma$). The three conductivity regimes, corresponding to the dominance of each transverse-deflection mechanism, are indicated. The itinerant FMs lie in the intrinsic regime. The results for epitaxial Mn_3Sn films of different thickness measured in this thesis (see Section 3.2) are plotted as green stars. Adapted from [130].

Experimental reports have been made of AHE in polycrystalline Mn_3Sn films [138–141] and also of a planar Hall effect in epitaxial Mn_3Sn films [142]. However, investigation of the momentum-space Berry curvature generated AHE in epitaxial Mn_3Sn films, where high-quality crystal structure may enhance this topological effect (and where epitaxial interfaces may enable spin-coherent switching [45]) remain a key objective (see Section 1.4).

In Section 3.2, we succeed in measuring the AHE in epitaxial Mn_3Sn films; the first demonstration of its kind. The epitaxial Mn_3Sn films show a large anomalous Hall conductivity, which is thickness independent and comparable in magnitude to single crystal samples. We compare this anomalous Hall conductivity with the longitudinal conductivity of the epitaxial Mn_3Sn films in Fig. 17. We thus demonstrate that the AHE of the epitaxial Mn_3Sn films lies in the intrinsic regime. This suggests that the AHE is generated by momentum-space Berry curvature arising from the inverse triangular spin texture, and is the most important finding of this thesis. The results of this thesis therefore pave the way for further studies of topologically driven phenomena in noncollinear AF films and their potential application into functional spintronic devices.

1.2.10 Topological Hall effect

In Section 1.2.4, we described how the antisymmetric exchange DMI can introduce a term to the Hamiltonian describing the energy landscape of a magnetic system, which makes it energetically favorable for magnetic moments to form an angle. The direction of the DMI vector (defined by broken interface or bulk inversion symmetry) determines the preferred direction of this angle (thus introducing a chirality to the magnetic structure) [63].

Let us consider a representative example, presented in Fig. 18 (a) [129]. Three magnetic moments ($\boldsymbol{S}_{1,\,2,\,3}$) in a noncentrosymmetric crystal lattice are exchange coupled with $\lambda_{\text{ex}} > 1$. The three moments align FM, in a direction parallel to $\boldsymbol{S}_3$.

Inversion symmetry breaking now introduces DMI. For coupling between moments $\boldsymbol{S}_1$ and $\boldsymbol{S}_2$, the DMI vector points out of the plane containing the atoms, sketched as a triangle in Fig. 18 (a). The DMI will compete with the exchange interaction, causing moments $\boldsymbol{S}_1$ and $\boldsymbol{S}_2$ to tilt with respect to one another but within the triangular plane. This creates a noncollinear spin texture.

A similar DMI will couple moment $\boldsymbol{S}_3$ to moment $\boldsymbol{S}_1$ and to moment $\boldsymbol{S}_2$ respectively, again causing them to cant with respect to one another, this time out of the triangular plane. The result is a **noncollinear, noncoplanar spin texture**.

Positioning the moments at a single point, as in Fig 18 (b), we see they subtend a certain solid angle [129]. We call this solid angle the scalar spin chirality (κ) of the moments, defined [143],

$$\kappa = \boldsymbol{S}_1 \cdot (\boldsymbol{S}_2 \times \boldsymbol{S}_3) \tag{31}$$

For a noncollinear, noncoplanar spin texture, *scalar spin chirality is nonzero.*

As a 4s electron adiabatically moves through a material containing such magnetic structure, spin-spin exchange interactions will encourage the electron's spin to align parallel to each moment locally [144]. As this delocalized electron spin winds, following the nonzero scalar spin chirality of the magnetic texture, it will acquire a Berry phase that is proportional to the solid angle of the moments [129]. Therefore, if scalar spin chirality is finite, conduction electrons will be imbued with a finite Berry phase [144].

Because the itinerant electrons are moving amongst a magnetic structure in real space, we call this a **real-space Berry phase**, to differentiate it from that endowed by the momentum-space Berry curvature causing AHE (detailed in Section 1.2.9). Another difference from the AHE is that, in this case, *no SOC is required, because the real-space Berry phase is imparted to electrons purely because of spin-spin exchange interactions* [145].

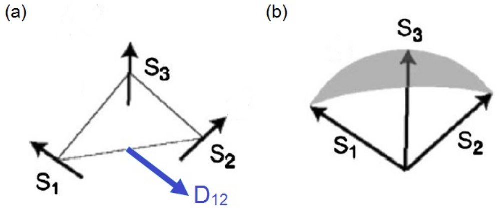

Figure 18: (a) Three magnetic moments, coupled FM by exchange interactions but in a noncentrosymmetric crystal structure. The blue arrow indicates the vector ($\boldsymbol{D}_{12}$) of the DMI which couples moment $\boldsymbol{S}_1$ to $\boldsymbol{S}_2$ and tilts them with respect to one another. Similar DMIs with moment $\boldsymbol{S}_3$ cants them out of the triangular plane, forming a noncollinear, noncoplanar spin texture. (b) Solid angle (shaded area) subtended by the three spins. This is proportional to their scalar spin chirality and, hence, the real-space Berry curvature they induce. Adapted from [129].

Nevertheless, as explained in Section 1.2.9, conduction electrons acquiring a Berry phase will undergo transverse deflection. This will, therefore, create a voltage across the sample; a Hall effect. This Hall effect generated by real-space Berry phase, imbued by a finite scalar spin chirality, is called a **topological Hall effect** [145].

Magnetic materials that show the noncollinear, noncoplanar spin texture required to generate nonzero scalar spin chirality include skyrmions [144] and antiskyrmions [146] [XI]. In such materials, the Hall resistivity ρ_{xy} measured as function of magnetic field ($\mu_0 H$) applied OP can be broken down into [146]:

$$\rho_{\mathrm{xy}} = \rho_{\mathrm{xy}}^{\mathrm{H}} + \rho_{\mathrm{xy}}^{\mathrm{A}} + \rho_{\mathrm{xy}}^{\mathrm{topological}} \tag{32}$$

$$\rho_{\mathrm{xy}} = R_{\mathrm{H}}\mu_0 H + R_{\mathrm{A}} M + \rho_{\mathrm{xy}}^{\mathrm{topological}} \tag{33}$$

[XI] A magnetic skyrmion is a vortex-like ‘knot’ of moments, formed of overlapping helices of magnetic moments, that show a positive winding number (an integer value defining chirality) [63]. Antiskyrmions are similar quasiparticles, but with a different magnetic configuration that has a negative winding number [60]. Both quasiparticles form in regular lattices within noncentrosymmetric crystals or structures with interfacial inversion symmetry breaking, because of competing exchange interactions and DMI. They are topologically protected objects (i.e. cannot be modified without breaking additional symmetries and changing their winding number) and possess nonzero scalar spin chirality, hence serving as a source of THE.

- $\rho_{\mathrm{xy}}^{\mathrm{H}} = R_{\mathrm{H}}\mu_0 H$ represents the ordinary Hall effect. It is linear in magnetic field, with a gradient given by Equation 28.
- $\rho_{\mathrm{xy}}^{\mathrm{A}} = R_{\mathrm{A}}M$ is the AHE contribution. The anomalous Hall coefficient (R_{A}) takes into account the side jump, skew scattering and intrinsic mechanisms which, for a FM, are proportional to magnetization (M).
- $\rho_{\mathrm{xy}}^{\mathrm{topological}}$ represents the remaining contribution to transverse resistivity due to the THE.

By subtracting from measured Hall resistivity both a linear dependence (to account for ordinary Hall effect) and a component proportional to independently measured (for example, using SQUID-VSM explained in Section 1.3.7) sample magnetization (to account for AHE), we can experimentally determine the THE contribution [143]. Typically, we observe this as a *bump in Hall resistivity in a certain magnetic field range. This corresponds to the field range in which the noncollinear, noncoplanar spin texture is stable* (above a certain minimum field strength required to induce the spin texture, but below higher fields that force the FM moments to align collinear) [144].

THE has also been observed in AFs, such as $\mathrm{Mn_5Si_3}$, with a noncollinear, noncoplanar spin texture [143]. Due to the lack of net magnetization, in this case THE manifests itself as a nonlinearity in Hall resistivity in the magnetic field range where the noncollinear, noncoplanar AF order is stabilized.

This raises the question of $\mathrm{Mn_3Sn}$, which hosts a noncollinear AF structure (discussed in Section 1.2.7). By subtracting a contribution proportional to the uncompensated moment (that drives $\mathrm{Mn_3Sn}$ into a single domain state and so can be considered proportional to momentum-space Berry curvature generated AHE), evidence has been discovered of a THE in $\mathrm{Mn_3Sn}$ bulk samples at room temperature [133, 147]. However, because the inverse triangular magnetic structure of $\mathrm{Mn_3Sn}$ is still coplanar, this is instead attributed to the formation of chiral domain walls with more complex spin texture [148].

However, below 50 K $\mathrm{Mn_3Sn}$ transitions into a glassy FM state and its Mn moments cant out of the basal plane. This now forms a noncollinear, noncoplanar spin texture. Evidence has been found of a THE close to the coercive field of polycrystalline bulk $\mathrm{Mn_3Sn}$ samples at low-temperatures [149], suggesting the formation of a finite scalar spin chirality in this region. In results chapter 3.2, we extend this investigation of THE in the glassy FM phase of $\mathrm{Mn_3Sn}$ to thin films, by measuring, for the first time, low-temperature magnetotransport in our epitaxial samples.

1.3 Experimental methods

1.3.1 Magnetron sputtering

The thin films prepared in this work were grown using magnetron sputtering deposition. A number of different techniques can be used to grow materials in thin film form (here referring to layers with thicknesses $<100\,\mathrm{nm}$), such as molecular beam epitaxy or pulsed laser deposition. However, we chose to use magnetron sputtering because of its flexibility when depositing metallic layers in different compositions or configurations, and its speed and efficiency. These advantages also make magnetron sputtering the deposition technique of choice in industrial fabrication of thin film based devices, where metallic layers or heterostructures are grown to prepare spin valves [12] or MTJs [13]. Therefore, use of this technique will help demonstrate the applicability of our Mn_3X films to potential antiferromagnetic spintronic applications.

Sputtering, in common with all thin film preparation techniques, involves removing atoms from a well-controlled **target** material (in this case, a 2 inch or 3 inch disk of elemental metal or a commercially produced alloy) at a controlled rate. The atoms then propagate through a chamber under ultrahigh vacuum until they are *deposited* on a **substrate**. As these so-called adatoms arrive on the substrate surface, they *grow* (via a variety of possible mechanisms) into a thin film [150]. The thin film growth process is discussed in more detail in Section 1.3.2. Here, we shall start with an overview of the physical mechanisms and technological considerations necessary in the sputtering process itself.

The main difference between the various thin film deposition techniques is simply the method used to remove atoms from the target material. In the case of sputtering, this process involves the collision of ionized atoms of a **working gas** with the target. In a traditional sputtering process, an electric field is set up across the sputtering chamber, from a positively charged anode at the substrate, to a negatively charged cathode formed from the target [151]. Electrons are emitted by the cathode. As the working gas, typically inert Ar, is injected into the chamber, collisions between these electrons and Ar will remove an electron from the Ar atom, producing positively charged Ar ions in a plasma [152]. These ions will be accelerated by the electric field towards the target, where they collide with and kick out **adatoms**. We illustrate a traditional sputtering set-up in Fig. 19 [152].

On the other hand, modern sputtering deposition processes use *magnetron-based sources* to generate the plasma. These contain a series of permanent magnets behind the target, which produce a magnetic field parallel to the target surface and directed radially out from its center [152]. Electrons in

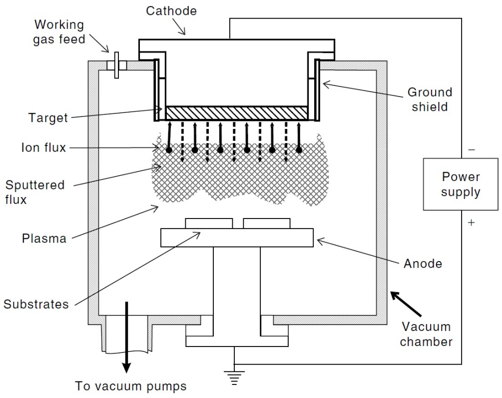

Figure 19: Schematic layout of a traditional sputtering apparatus [152].

the Ar plasma begin to move in cyclotron orbits around these magnetic field lines, trapped in circular paths by Lorentz forces [153]. This confines the electrons close to the target surface. The Ar atoms are, in turn, ionized closer to the target surface, increasing their probability of collision with it [152]. This allows us to stabilize the plasma at a lower working gas pressure, thus reducing possible contamination of the films. Fig. 20 shows a diagram of such a magnetron-sputtering source [154].

In addition, confining the plasma close to the target means it is no longer necessary to bias the substrate; instead a shroud around the magnetron forms the anode and sets-up the electric field to accelerate Ar ions [152]. This enables more precise control of the Ar ion acceleration, which in turn determines sputtering rate. The sputtering power on a magnetron can be set by the user, which involves setting the voltage between target and shroud (whilst simultaneously monitoring ionic current). In this manner, working gas ions are accelerated towards the biased target. These Ar ions are heavy but with a low radius and therefore transfer significant momentum to a limited number of target atoms upon collision. A process begins whereby this momentum is transferred between different atoms in the target, eventually resulting in atoms close to the target surface receiving sufficient energy to be ejected from the target [151]. Higher sputtering power results in faster acceleration of Ar ions, and thus a higher density of more energetic adatom emission that, in turn, increases sputtering rate.

In the experiments reported in this thesis, we controlled the sputtering power on different targets (tuning the voltage between cathode and anode) to yield growth rates encouraging the epitaxial formation of films (see Section 1.3.2) and control the composition of films. For example, Mn_3Sn was co-sputtered from Mn and Sn targets, with the rate on each magnetron varied

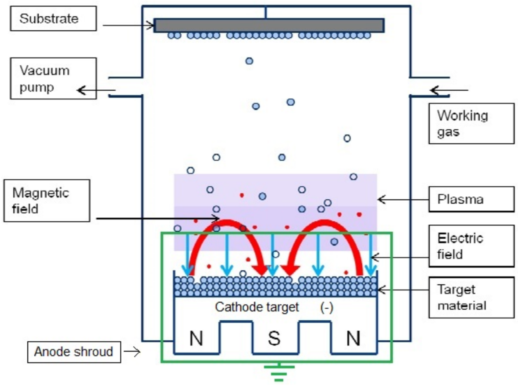

Figure 20: Schematic layout of a magnetron sputtering source. Adapted from [154].

to give the correct stoichiometry. Meanwhile, for Mn_3Ir, which was deposited from an alloy target, we found that varying the sputtering power changed the relative compositions of Mn and Ir in the resulting film. Thus, sputtering power was chosen to give the desired 3:1 stoichiometric ratio.

The magnetron sputtering chamber used to deposit these Mn_3X films is shown in Fig. 21. It contains 13 separate magnetrons, in three clusters of four guns (plus one stand-alone). Each source is fitted with a different target in order to sputter a variety of materials. We then move the substrate laterally, such that it is incident over the desired target. Within each cluster, it is possible to co-sputter from any of the four magnetrons, in order to deposit alloy films.

The sputtered ad-atoms leave the target and travel to the substrate in a plume through a chamber evacuated to ultrahigh vacuum. This ultrahigh vacuum is necessary to minimize contamination of the resulting sample with oxygen, water or other contaminant gases [155]. Such ultrahigh vacuum is created using a combination of rotary vane and turbo molecular pumps.

The roughing pumps use a mechanical piston to extract air from the chamber down to a pressure of approximately 1×10^{-3} mbar. At this point, we switch from measuring pressure using a 'Baratron'-type capacitance manometer, to a highly sensitive cold-cathode gauge [155]. Below such pressures, the remaining gas in the chamber no longer moves with a viscous flow (where inter-atomic collisions dominate), but rather a molecular flow (where collisions with the chamber wall dominate) [156]. This is because the mean-free path of the gas atoms is now longer than the chamber dimensions [156].

Gas atom mean-free path, $\bar{\lambda}$ (in cm) depends on residual gas pressure, p (in mbar) and, at room temperature, can be approximated by [155],

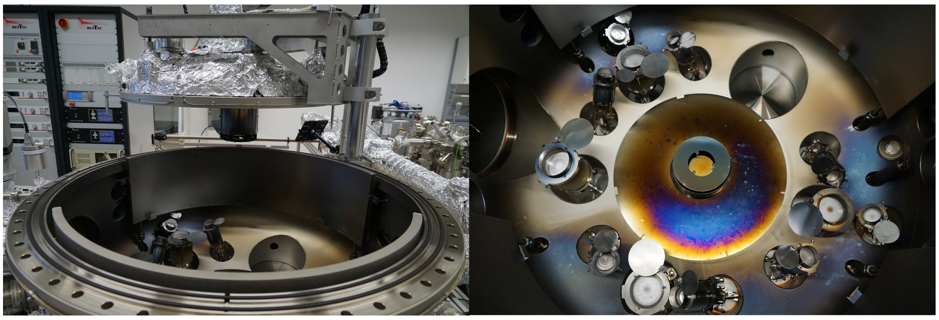

Figure 21: Photographs of the outside (left) and inside (right) of the sputtering system at the Max Planck Institute for Chemical Physics of Solids, Dresden (in 2020).

$$\bar{\lambda} = \frac{6.65 \times 10^{-3}}{p} \tag{34}$$

By comparing mean-free path with a typical chamber length dimension, L, we define Knudsen's number, K_n [156],

$$K_\mathrm{n} = \bar{\lambda}/L \tag{35}$$

In the regime where K_n <1 we observe viscous low, but after the transition to molecular flow K_n >1 [157].

At this point, turbo-molecular pumps take over. These use a series of rapidly rotating (1500 Hz) turbine blades to 'hit' individual molecules away from the chamber flange and out through the pump, lowering the residual pressure inside the chamber much further [157]. We achieve base pressures $<1 \times 10^{-9}$ mbar.

For the sputtering process, the chamber is refilled with highly pure (5N) Ar working gas to 3×10^{-3} mbar. This pressure results in a mean-free path of sputtered atoms of the order cm [155]. We can adjust the vertical target-to-substrate distance with respect to this mean-free path length. For the films grown in this study, target-to-substrate distance was fixed at 15 cm. This means that, by the time the plume of atoms reaches the substrate, adatoms have thermalized through collisions with working-gas atoms [155]. Thus, the adatoms arrive in a diffusive manner, increasing their homogeneity and reducing directional deposition.

In this state, increasing the working gas pressure will also increase the frequency of collisions, which can be used to reduce *growth rate*. In general, a lower rate favors epitaxial film deposition, by allowing more time for adatom recombination on the substrate surface [150]. However, the drop in growth rate as a function of increased pressure can be dramatic, whilst at the same time significantly enhancing Ar inclusion in the thin film. For this reason, in this study we kept Ar pressure as low as possible to form a stable plasma, instead controlling growth rate using sputtering power.

This growth rate is estimated in real time using a quartz crystal microbalance (which measures the subtle alterations in resonance of a vibrating quartz crystal, placed temporarily in front of the substrate, as material is deposited). We subsequently confirm growth rate after-the-fact by measuring the thicknesses of films deposited for a known amount of time (see Section 1.3.4). We optimized growth rates used in this thesis to yield epitaxial film growth with the desired chemical composition. These were typically of the order 0.1 to $1\,\text{Å}\,\text{s}^{-1}$. These are comparatively low on 'human' time scales, meaning film thicknesses can be easily controlled by stopping the deposition after a measured period of time. We discuss the resulting growth mechanisms of thin films in the coming section.

1.3.2 Thin film growth and crystal structure

In the previous Section 1.3.1, we explained how the sputtering process can be used to remove atoms from a target in a measured manner, and propagate them through ultrahigh vacuum to a waiting substrate. As these adatoms are deposited on the substrate at a controlled rate, a thin film begins to grow [158]. The *growth mechanism* favored by the arriving adatoms can be modified by changing the conditions of the substrate [159] (such as its **temperature**, electric potential, applied magnetic field, angle with respect to atomic plume, and rotation speed). In addition, the nature (chemical composition, **crystal structure** and surface preparation) of the substrate plays an important role in seeding the thin film growth [160]. In this Section, we examine the effect of two important substrate parameters (crystal structure and temperature) below, and discuss the different thin film growth mechanisms that can result.

As the first sputtered adatoms arrive at the substrate, they coalesce to form tiny clusters, or nuclei, on the substrate surface [158]. This nucleation is the first stage of the growth process. As more adatoms are deposited, the nuclei enlarge. The process by which this expansion occurs is important in determining the final characteristics of the sputtered sample, in particular whether we achieve high quality epitaxial films, and is what we aim to control through deposition and substrate conditions.

Three basic modes of thin film growth have been identified [150]. These are illustrated diagrammatically in Fig. 22 and arise because of a relative balance of different surface energies (γ) at the interfaces between the film (f), substrate (s) and adatom vapor (v) [150]. Borrowing from the capillary approximation of fluid dynamics, these fulfil Young's equation,

$$\gamma_{\mathrm{sv}} = \gamma_{\mathrm{fs}} + \gamma_{\mathrm{fv}} \cos\theta \tag{36}$$

where θ is the angle between the substrate surface and a tangent to the nucleus' surface [158].

In the first mode, called layer-by-layer (or **Frank-Van der Merwe**), $\theta = 0$ and the surface energy of the film is less than that of the substrate,

$$\gamma_{\mathrm{sv}} \geqslant \gamma_{\mathrm{fs}} + \gamma_{\mathrm{fv}} \tag{37}$$

This is especially true in the case of homoepitaxy, where the substrate and film are chemically similar and the film-substrate interface energy, $\gamma_{\mathrm{fs}} = 0$ [158]. Homoepitaxy is often encountered in the growth of semiconductor-on-semiconductor devices, where the deposition of material one monolayer at a time can enable the preparation of almost defect free laser diodes and quantum wells [161].

In the case of metal film deposition (in particular on oxide substrates) the surface energy of the film nucleus, combined with that of the film-substrate interface, is larger than that of the substrate surface,

$$\gamma_{\mathrm{sv}} < \gamma_{\mathrm{fs}} + \gamma_{\mathrm{fv}} \tag{38}$$

In this condition, we encounter island (or **Volmer-Weber**) growth [158].

Finally, for the case where we succeed in reducing the film surface energy, and in particular the interfacial energy between film and substrate, to slightly below the substrate surface energy, a combined (or **Stranski-Krastanov**) growth mode occurs,

$$\gamma_{\mathrm{sv}} > \gamma_{\mathrm{fs}} + \gamma_{\mathrm{fv}} \tag{39}$$

This can be achieved by using a buffer layer with a *wetting function* (denoted β, which accounts for the bonding energy between the deposited and underlying materials) that is closer to the (in general, low) surface energy of the substrate [150]. This then allows the higher surface energy metal to be deposited on the buffer layer initially in a layer-by-layer manner, before islands begin to form.

Instead, the Volmer-Weber growth mode is typical for the metallic thin films featured in this thesis. In order to achieve continuous thin films of the type required for spintronic devices, it is thus necessary for the islands to combine. This process occurs in two steps; firstly islands grow individually, and secondly they coalesce into larger clusters [150].

This coalescence can occur by one of three mechanisms [158]:

- Ostwald ripening: a drop in chemical potential energy between smaller and larger islands leads to mass transport between nearby grains.
- Sintering: two islands that come into contact will proceed to rapidly coalesce along a path of minimum energy at their touching point.
- Cluster migration, where islands undergoing random motion over the substrate surface, collide and coalesce.

Differentiation of these different mechanisms can be challenging in practice, however all are driven by the tendency to minimize surface energy by combining smaller islands into larger ones. In general, deposition of a few nanometers of materials is sufficient to ensure coalescence.

However, individual islands must first enlarge to a sufficient size to trigger coalescence. This does not always occur, for example in Section 3.1, where we will find Mn_3Sn films that grow with a discontinuous structure. A chief factor in determining the size to which these nuclei expand in the Volmer-Weber mode is substrate temperature.

Returning to the capillary approximation, we find island size is governed by a balance of film-interface and film surface energy, against the Gibbs free energy associated with the volume of the island [150]. Enlarging an island in size will be energetically unfavorable, up to a certain critical radius, r_c [150]. Above this radius, expanding the island further begins to reduce total energy, thus starting the eventual process of thin film formation. However, at elevated substrate temperatures, it becomes increasingly difficult for islands to initially expand up to the critical radius. Instead, it is energetically favorable to nucleate new clusters. Therefore the number of stable nuclei per unit area of substrate is larger for higher substrate temperatures [158].

Furthermore, the critical radius itself increases with substrate temperature [158]. Therefore, it becomes less likely that any individual island will reach the critical radius required for ongoing growth. These two factors combine to mean that, when deposition is performed at higher substrate temperatures, discontinuous island structure can persist to a higher surface coverage [158]. This is the situation observed in Section 3.1, where the Mn_3Sn films were grown at a high temperature of 500 °C.

Why, then, insist on depositing thin films on substrates held at elevated temperatures? The reason is that higher substrate temperature enables the formation of crystalline thin films via the promotion of adatom mobility[158]. Modeling adatom motion on the substrate surface as diffusive, the mobility of adatoms can be quantified using a diffusion coefficient, D_s,

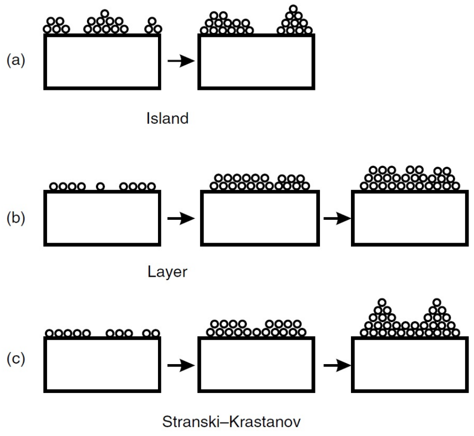

Figure 22: Illustrations of the arrangement of adatoms on a substrate during (a) Volmer-Weber, (b) Frank-Van der Merwe and (c) combined thin film growth modes. The film deposition proceeds from nucleation, left, to layer coalescence, right [150].

$$D_{\mathrm{s}} = D_0 \exp(-\frac{\Delta G_{\mathrm{s}}}{k_{\mathrm{B}} T_{\mathrm{G}}}) \tag{40}$$

where D_0 is a constant representing diffusion coefficient at infinite temperature, ΔG_{s} is the activation energy for surface diffusion, k_{B} is Boltzmann's constant and T_{G} is the growth temperature [150].

Adatoms initially arrive at the substrate and form nuclei in a random arrangement. As islands grow, more mobile adatoms have the ability to move and form new structures. For a particular composition of atoms, it will be energetically favorable to form a particular crystal structure [150]. Thus by depositing films on substrates held at elevated temperatures, where deposited adatoms have sufficient mobility to move into a lower energy formation, we can thus encourage the growth of thin films with desired crystal structure.

Solid-state materials have a crystal structure. This refers to the arrangement of the material's atoms in an organized and regular way. Such an organized and regular arrangement occurs because it is often the lowest energy configuration of atoms within a particular material [162].

A crystal structure consists of a repeating unit of atoms, arranged periodically in three-dimensions on a lattice. The repeating unit of atoms is called the **unit cell**. The translations that map any given point within the unit cell onto an identical point in the next unit cell are called the *lattice vectors* [162]. Combining the lattice vectors and unit cell together, we define our material's crystal structure.

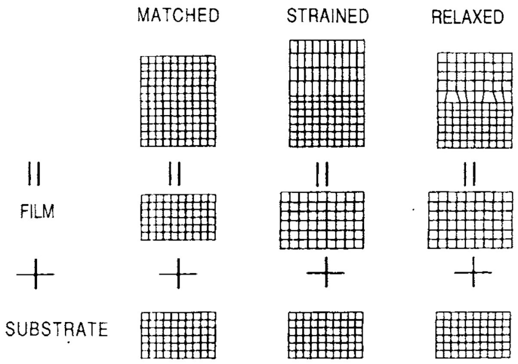

Figure 23: Resulting structure when a (left) perfectly lattice matched, (middle) well lattice matched and (right) poorly lattice matched thin film is deposited on a given substrate. The left panel is typical of homoepitaxy, the middle panel shows high quality strained thin film growth, whilst the right panel shows an epitaxial film containing dislocation defects close to the interface. Adapted from [161].

The lengths of the lattice vectors are equal to the edges of the unit cell; that is, the spacing between repeating units of atoms in crystal structure. We call these the crystal's **lattice parameters** (denoted a, b and c). Similarly, the angles between lattice vectors define shape of the unit cell.

There are seven unique combinations of lattice parameters and vector angles, which cannot be reproduced from one another by a combination of symmetry operations (e.g. reflections or rotations). Fig. 24 shows these. Some of these unique arrangements can, in turn, have either base-, body- or face-centered variations, which, combined, are called the *Bravais lattices.*

Within these lattices, we see there exist several unique directions and planes with respect to the arrangement of atoms. Physical properties often vary between these. We can denote the different planes by defining a set of orthogonal axes with respect to the lattice vectors. From the points at which a plane intercepts these axes, we define three indices, h, k and l. These are called the **Miller indices**, (hkl), and are used to identify different crystal planes. For example, the shaded face in the cubic unit cell in Fig. 24 is the (001) plane. Groups of planes that are symmetrically equivalent are denoted $\{hkl\}$; for example the $\{001\}$ planes in the cubic unit cell are the six faces of the cube.

A direction within the crystal structure is also defined by Miller indices; $[hkl]$ *is the direction perpendicular to the plane* (hkl). Therefore the lattice vectors of the cubic unit cell are parallel to the $\langle 001 \rangle$ group of crystalline directions. This notation for crystallographic planes and directions is used throughout this thesis.

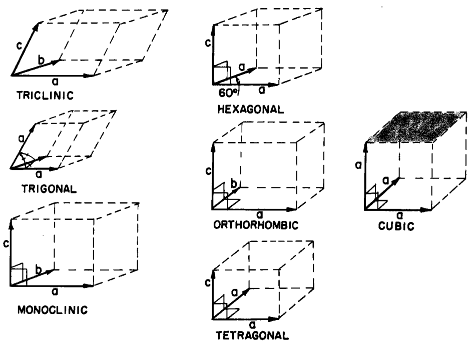

Figure 24: The seven (length and relative angle) combinations of lattice vectors ($\boldsymbol{a}$, $\boldsymbol{b}$ and $\boldsymbol{c}$) that cannot be transformed into one another by symmetry operations. If an atom is positioned at the end of each of lattice vector, we call the resulting repeating unit a primitive unit cell (each cell contains the equivalent of one atom). If an atom is positioned on the top/bottom face, at the center, or on all faces of the primitive unit cell, we call the resulting repeating unit a base-, body- or face-centered unit cell, respectively. Together these form 14 possible combinations, known as the Bravais lattices. Adapted from [162].

In metallic materials, of the type studied in this thesis, the formation of a solid occurs when metal atoms' valence electrons form a sea around ionic cores arranged in a crystal lattice. The delocalized valence electrons (for example the $4s$ electrons of the first period transition metals) lead to electrical conduction (discussed in more detail in Section 1.2.8) whilst the remaining localized electrons in the atoms (such as the $3d$ sub-shell electrons) can cause, for example, magnetism (discussed in more detail in Section 1.2.2).

Meanwhile, the ionic cores form a lowest energy configuration by minimizing the empty space between them. Such maximum packing efficiency is obtained by forming a layer of atoms arranged in a hexagon, as shown in Fig. 25 (a). To construct a three dimensional crystal, a second layer of hexagonally close packed atoms is positioned over three of the six possible interstitial sites of the first layer, as shown in Fig. 25 (b). There are now two possible ways, with equal packing efficiency, of positioning the next layer; either over the interstitial site labeled A, or the interstitial site labeled B.

In the case of A, the third layer is positioned directly over the first layer, forming a **hexagonal unit cell**. In Section 1.2.7, we show that Mn_3Sn adopts a hexagonal crystal lattice.

In the case of B, the third layer is offset from the first two, and the fourth layer will again be positioned directly above the first. This forms the (111) plane of a **face-centered-cubic unit cell**. In Section 1.2.6, we show that Mn_3Ir adopts a face-centered-cubic crystal lattice, and discuss its growth along both [001] and [111] directions.

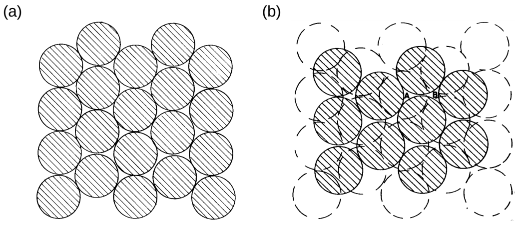

Figure 25: (a) Hexagonally close packed plane of metal atoms, achieving maximum packing efficiency. (b) Positioning of the next layer of atoms over three interstitial sites of the first lattice plane. The next atomic layer can, in turn, be positioned over sites A or B, to construct a hexagonal (with an A-B-A-B. . . stacking sequence) or face-centered-cubic (with an A-B-C-A. . . stacking sequence) crystal structure, respectively. Adapted from [162].

An alternative approach to depositing thin films with a particular crystal structure is instead to use a *postannealing process*. Adatoms are deposited on the substrate at ambient temperatures, which encourages island coalescence such that a continuous thin film is easily formed. However, due to low adatom mobility, the film is likely to have only weak crystal texture [163]. In addition, the film will contain many grains with different crystal orientations and different sizes, determined during the process of island expansion and coalescence.

However, by subsequently heating the continuous, granular, weakly textured thin film to a high temperature, we can encourage it to crystallize. This process is called annealing, and its effects are twofold. The first is to introduce energy to the adatoms, such that they can overcome the energy barrier to reorientation, and thus move their arrangement slightly to achieve a lower energy state (i.e. a crystal lattice).

The second effect is to encourage the motion of grain boundaries [163]. Grain boundaries have an energy barrier to reorientation, after which an expansion of grains and reduction in the number of boundaries becomes energetically favorable. Specifically, larger grains grow at the expense of smaller grains. Annealing provides this activation energy and thus grain size in the film increases and with it regions of the particular desired crystal orientation.

In the sputter system used to prepare the thin films in this thesis, a SiC heater positioned behind the substrate holder in the deposition chamber was used to heat the substrate to a controlled temperature of up to 1000 °C. High temperature deposition or annealing will thus produce high-crystallinity thin films with large grains. However, only the lowest energy configuration of atoms will determine the resulting type of crystal lattice, and grains may be rotated randomly with respect to one another.

How, then, can we selected a specific crystal structure for our material (especially if it has multiple metastable phases, for example Mn_3Sn [164]) or establish a particular coherent alignment of crystal axes between grains (giving our sample the character of a single-crystalline film)? The answer comes from one of the most powerful and unique aspects of thin film growth, which allows preparation of crystal orientation with a high degree of control, and even the stabilization of otherwise metastable crystal configurations [161]. We use substrate crystal structure to seed film crystal structure [159].

This is known as **epitaxial thin film growth**. There is an energy saving associated with adatoms *positioning themselves over the lattice sites of the substrate template* [159]. A balance between the energy minimization achieved by forming its preferred crystal structure, with the energy reduction that results from positioning atoms in concordance with the atomic mesh at the surface of the substrate, governs the crystal orientation of the film.

By providing activation energy either through a moderately heated substrate or postannealing process, adatoms will be mobile enough to find energetically favorable positions above the atoms at the surface of the substrate template, thus seeding the film with a predetermined crystal structure [159]. Where the two crystal lattices are well suited, with the same Bravais structure and similar spacing between atoms, heteroepitaxial growth of a thin film with well-defined structure can be achieved.

We quantify this by defining the lattice mismatch of the system in terms of the IP lattice parameters of the substrate ($a_{\text{substrate}}$) and bulk crystal structure of the film ($a_{\text{film-bulk}}$) [161],

$$\text{Lattice-mismatch}(\%) = \frac{(a_{\text{film-bulk}} - a_{\text{substrate}})}{a_{\text{substrate}}} \times 100 \tag{41}$$

In general, metallic thin films with a lattice mismatch of up to 9 % or even 15 % can still be deposited epitaxially [165].

Where lattice mismatch is small, the film may grow strained on the substrate. This is typical of semiconductor-on-semiconductor heterostructures, and can result in defect-free thin film preparation [161]. Where the lattice mismatch is large, this strain will relax over the course of consecutive crystal planes [161]. This is often found in metallic thin films, and can occur in the form of stacking faults or misfit dislocations [161]. Fig. 23 illustrates strained versus relaxed thin film growth [161].

In Section 2.1, we deposit Mn_3Ir films on a cubic MgO substrate. The lattice mismatch here is $\approx 10\%$. This is large enough that, after 3 nm, the film relaxes and grows with lattice parameters close to the bulk. However, the lattice mismatch is nevertheless sufficiently small that the MgO seeds a cubic structure into the Mn_3Ir film, such that it grows with cube-on-cube epitaxy on the substrate. This is achieved whilst depositing the thin films at much lower temperatures than those in Section 3.1, because the close lattice matching requires only slight adatom movement into the energetically preferable cubic sites over the substrate surface net. This is an example of epitaxial thin film growth.

Here we deposited thin films directly on the oxide substrate surface. However, in Section 2.2, we prepare of ultrathin Mn_3Ir films with (111) orientation on an Al_2O_3 substrate using a buffer layer. This results in highly strained films in the ultrathin regime. Such strain is an example of plastic deformation of the film. The energy associated with this plastic deformation (E_{strain}),

$$E_{\text{strain}} = \frac{Yt\epsilon_{\parallel}^2}{(1-\nu)} \tag{42}$$

where Y is Young's modulus, t is film thickness and ν is Poisson's ratio [166]. Here the IP strain ($\epsilon_{\parallel}$) in the deformed film with measured lattice parameter ($a_{\text{film-measured}}$) is calculated [159],

$$\epsilon_{\parallel} = \frac{(a_{\text{film-measured}} - a_{\text{film-bulk}})}{a_{\text{film-bulk}}} \times 100 \tag{43}$$

This elastic deformation occurs up to a certain critical film thickness (t_c) above which the thin film relaxes [166].

That the first few layers of the film are highly strained suggest that perhaps, in this case, a Stranski-Krastanov growth mode is at work. The first nanometers of the Mn_3Ir (111) films may be deposited in a layer-by-layer manner, with the TaN buffer improving wetting between film and substrate.

Having successfully grown an epitaxial thin film of our desired material, how can we classify its crystal configuration? In the case of thin films grown epitaxially, one particular set of crystal planes will grow parallel to the substrate surface [159]. This crystal lattice will extend laterally throughout the film plane, thus defining its crystal structure. We call this crystal plane the **thin-film orientation.**

Epitaxial film compounds are often denoted together with their orientation, that is, the Miller indices of the crystal plane lying in the film plane [163]. For example, the Mn_3Ir (111) films presented in Section 2.2 have the cubic (111) crystal plane lying in the plane of the thin film.

The resulting top down view of this thin film structure is shown in Fig. 26. For a given orientation, certain crystal axes will lie in different directions within the film plane. In Fig. 26, we see that the $[\bar{1}12]$ and $[1\bar{1}0]$ crystallographic directions are angled orthogonally within the film plane.

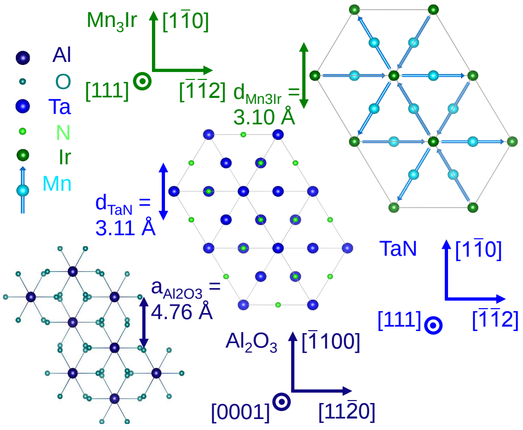

Figure 26: Illustration of the crystal structure of a Mn_3Ir (111) film grown using a TaN (111) buffer layer on an Al_2O_3 (0001) substrate. The relative orientations of the crystal lattices demonstrate the epitaxial relationship between the layers, with IP and OP crystallographic axes labeled. The IP lattice spacing in each layer is also shown.

For epitaxial thin films, the correlation between the OP crystal orientation and IP crystallographic directions in the substrate and film can be expressed through the **epitaxial relationship** [159]. In the example shown in Fig. 26, the epitaxial relationship (analyzed in detail in Section 2.1) is:
Al_2O_3 (0001) $[11\bar{2}0]$ $[\bar{1}100]$ $\parallel$ TaN (111) $[\bar{1}\bar{1}2]$ $[1\bar{1}0]$ $\parallel$ Mn_3Ir (111) $[\bar{1}\bar{1}2]$ $[1\bar{1}0]$.

For such epitaxially grown films, we can compare macroscopic measurement directions (for example, along which magnetic field is applied or electric current flowed) to microscopic crystallographic axes. This allows the observation of anisotropic properties, offering new possibilities for spintronic applications (e.g. the intrinsic AHE in Mn_3Sn discussed in Section 3.2).

Solid-state materials can also consist of many small grains of highly crystallized atoms, which are randomly oriented with respect to one another. These are called polycrystalline [163]. In reality, sputter deposited thin films of the type used for commercial spintronic devices (and therefore, to show the applicability of our results, studied in this thesis) will be somewhere between epitaxial and polycrystalline [163]. They will consist of *large crystallites, within which the material has a well-defined crystal lattice*. These will be coherently oriented with respect to one another, that is, with *high-symmetry crystalline axes pointing along the same directions in the film plane, following the substrate*. However, they will nevertheless exhibit *grain boundary defects between crystallites*.

The epitaxial configuration can have a significant effect on the material properties we wish to utilize for spintronic devices. The long-range ferromagnetic and antiferromagnetic properties (discussed in Sections 1.2.2 and 1.2.3 respectively) depend implicitly on the ordering and spacing of interacting magnetic atoms. In particular, we explained in Section 1.2.4 how the noncollinear AF order that is the topic of this thesis results from a very specific arrangement of atoms. Furthermore, crystal microstructure can have an effect on electrical transport properties, as discussed in Section 1.2.8.

Thus, crystal structure is an integral consideration when engineering materials for spintronic devices [163]. Here, we have introduced crystal structure in solid-state physics and shown how it can be controlled through deposition techniques (see Section 1.3.1). Next, we proceed to introduce how thin film crystal structure can be measured using XRD (Section 1.3.3) and TEM (Section 1.3.6). Later, we progress to we discuss experimental results on the optimization of the crystal structure in epitaxial thin films of Mn_3Ir and Mn_3Sn in the results chapters 2.1 and 3.1, respectively.

1.3.3 X-ray diffraction

Having discussed how to epitaxially deposit thin films, how can we proceed to characterize their crystallinity? XRD is one of the most powerful tools available to a material scientist for analysis of crystal structure, and was the first characterization technique used to study the samples prepared in this thesis. XRD works by shining powerful x-rays at a sample, in an instrument called a diffractometer, and measuring the intensity of the x-rays scattered by the crystal at a variety of different angles.

The x-rays are generated in an x-ray tube, by accelerating a current of electrons (in the present study 40 mA) to a high voltage (here 30 kV) and colliding them with a metallic target. Characteristic electronic transitions emit x-ray photons of certain specific energies. In our case, a Cu target was used, which generates x-ray photons with energies of 8 to 9 keV. A Ni filter window on the x-ray tube attenuates Kβ energy photons, leaving a monochromatic x-ray beam from the Kα_1 excitation (convoluted with some Kα_2 radiation). This has a wavelength of 1.5406 Å [167].

These x-rays are further manipulated by x-ray optics [167]. Before both source and detector, Soller slits (a series of thin metal plates positioned parallel to the scattering plane) are used to reduce the spread of the x-ray beam to between 1 and 5° in a direction perpendicular to the scattering plane. A divergence slit (consisting of two finely spaced blades) is positioned between source and sample, to reduce the divergence of the beam in the scattering plane to a little as 0.1°. These result in a well collimated beam which is focused onto the sample with a line-type shape, across which is a Gaussian intensity profile.

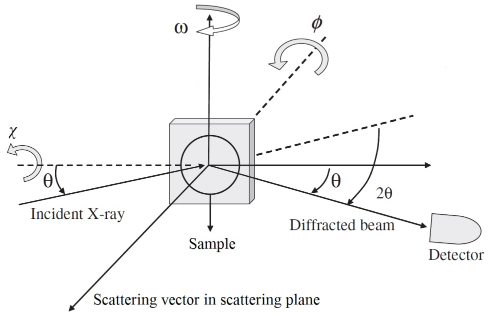

Figure 27: Schematic layout of a single crystal diffractometer, with key measurement axes indicated [168].

In the presently used diffractometer, a modern charge-coupled device detector then measures the intensity of x-rays scattered by the sample. Such a detector contains many pixels (of $50\,\mu m^2$ in size) in a 256 x 256 square array, each consisting of a semiconductor pn-junction. Incident photons on each pixel will excite electron-hole pairs within the depletion region, creating a drain current that is proportional to the intensity of arriving photons [169]. Such an array of charge-coupled devices can produce a two-dimensional map of the diffracted photons, or can be set to operate in a series of pixel channels, with the current detected from each channel allowing an accurate determination of x-ray intensity as a function of angle.

The position of the detector is swept to collect x-rays at different angles (a position we define as θ). In addition, the orientation of the sample can be changed, using a sample holder known as a goiniometer. **Tilt** within the scattering plane (ω), sample plane **rotation** (ϕ) and **azimuthal** motion perpendicular to both sample and scattering planes (χ) angles can all be varied. A schematic of such a diffractometer, including source, detector and goiniometer, is shown in Fig. 27, adapted from Ref. [168].

By controlling the relative angles of source, sample and detector, we can thus explore different possible conditions for x-ray *diffraction*. The wavelength of the x-rays incident on the sample are comparable to the typical spacing of atomic planes within a solid state crystal structure. Therefore, the crystal acts as a diffraction grating, with x-rays scattered from each consecutive crystal plane *interfering* constructively or destructively. Fig. 28, adapted from Ref. [167], illustrates the principle of such diffraction. Depending upon the orientation and spacing of the crystal planes, this produces *peaks* of intensely diffracted radiation at certain angles.

Fig. 28 assumes the position of source and detector in a *specular* diffraction condition [167]. This is where we set the diffractometer to detect at

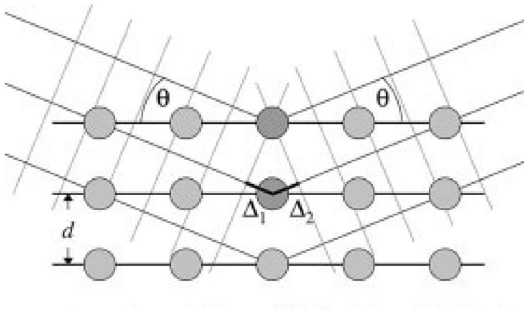

Figure 28: Geometry of x-ray diffraction from a crystal lattice, where the Bragg condition is satisfied [167].

an angle θ, with x-rays incident on the sample also at an angle θ. In most diffractometers the positon of the x-ray source is fixed, and instead the incident angle of x-rays is controlled by setting the sample tilt angle $\omega = \theta$. The detector is therefore set to a position of 2θ. By scanning 2θ and θ simultaneously, we detect x-rays that are diffracted specularly from the sample. In the case of thin films, this yields a scattering vector that is perpendicular to the sample surface, meaning that we are sensitive to diffraction from the crystal planes lying in the film plane.

For polycrystalline bulk, powder XRD of crushed samples involves rotating a pellet at many angles in order to collect diffraction peaks from many different crystal planes (and thus accurately determine lattice parameters, discussed below). However, for the study of epitaxial thin films we perform single crystalline diffractometry. Here we move the relative angles of the goiniometer to search within reciprocal space for high intensity reflections characteristic of well-defined crystal plane orientations. As well as the $2\theta - \theta$ scans discussed above, these can include:

- Partially IP diffraction peaks, scanned in $2\theta - \theta$ mode but with the azimuthal angle of the sample, χ, moved partially IP.
- Pole figure scans, performed by rotating the sample, scanning ϕ, at the position of one of these partially IP peaks, in order to determine planar crystal symmetry.
- Rocking curves, where the sample tilt angle, ω, is varied at a fixed position of 2θ, in order to determine the angular spread of crystal planes within the film (mosaicity).
- Simultaneous measurement of intensity whilst scanning 2θ and ω, in order to measure the positions of off-specular diffraction peaks (such scans are known as reciprocal space maps) [169].

All of the above scan types are made by fixing the incident condition of the x-rays, then measuring diffracted intensity as one of the angles in question is slowly scanned. The resulting plots show peaks of diffraction intensity, occurring at specific angles. These allow us to characterize a sample's crystal structure. Firstly, we *index* the peaks, that is, assign each as belonging to the diffraction condition of a specific set of crystal planes within a certain material. This can be done with reference to the expected diffraction patterns for the material in question found in the literature or simulated using the material's theoretical lattice parameters (see below).

By indexing the peaks and confirming they match those expected, we can not only confirm that we have prepared the correct chemical phase of the desired material, but also the orientation of crystal planes within the material. As discussed in Section 1.3.2, the objective of epitaxial thin film growth is to deposit samples which have a particular set of crystal planes parallel to the substrate. These crystal planes lie in the plane of the film, defining its crystal structure, with a well-defined crystal direction pointing OP. We call this direction the orientation of the film. Using $2\theta-\theta$ scans, the peaks observed allow us to index the orientation of the film, identify whether only a single crystal orientation is present, and (from the peak intensities) estimate how prevalent this orientation is.

Having indexed the peaks, their precise measured positions can be used to calculate the actual lattice parameter of the sample prepared. Both OP, c, and IP, a, lattice parameters can be determined from OP and partially IP peaks respectively. This allows us to quantify, for example, epitaxial strain in the film. A Gaussian type lineshape can be fitted to the diffraction peaks, yielding its detected peak angle, denoted, $2\theta_{\mathrm{hkl}}$.

In order to observe the diffraction peak, we must be in a constructive inference condition for x-rays incident at an angle θ_{hlk} [167]. In the constructive interference condition, the relative phase shift between the incident, δ_{i}, and scattered, δ_{s}, x-rays, must be equal to an integer, n, multiple of the x-ray wavelength, λ,

$$\delta_{\mathrm{i}}+\delta_{\mathrm{s}}=n\lambda \tag{44}$$

The geometric picture illustrated in Fig. 28, shows that this phase difference will be equal to an x-ray path length defined by the interatomic spacing, d_{hkl}, of the particular set of diffracting crystal planes, denoted by the Miller indices (hkl), and the incident angle [167],

$$\delta_{\mathrm{i}}+\delta_{\mathrm{s}}=2d_{\mathrm{hkl}}\sin\theta_{\mathrm{hlk}} \tag{45}$$

This gives the famous Bragg equation,

$$n\lambda = 2d_{\mathrm{hkl}} \sin \theta_{\mathrm{hkl}} \tag{46}$$

using which interatomic spacing can be calculated from the position of a diffraction peak for the crystal planes (hkl). We can use this spacing, in turn, to calculate the crystal's lattice parameter. Taking, for example, a cubic crystal system with lattice parameter a, it can be calculated [37],

$$a = d_{\mathrm{hkl}} \sqrt{h^2 + k^2 + l^2} \tag{47}$$

Finally, the full width at half maximum (β_{hkl}), of the Gaussian profile fitted to the diffraction peak quantifies its broadening. Although broadening will arise from the x-ray optics, the dominant contribution comes from the film. Specifically, the finite dimensions of coherently scattering crystallites will broaden the linewidth [167]. Typical sputtered thin films, even of the highest structural quality, will contain many crystal domains that, whilst coherently oriented to form a quasi-single crystalline layer, will lead to enhanced scattering of diffracted x-rays from grain boundaries. Smaller domains lead to a higher density of grain boundaries and hence broader peaks; narrow peaks in an XRD pattern are thus a sign of high film quality with larger crystallite size.

By making the simplifying assumption that each crystallite has a cubic form, an estimate of grain size, D, can be calculated from (using the Scherrer formula) the peak full width at half maximum, the peak position in radians, the x-ray wavelength and a geometric factor, K [170],

$$D = K\lambda / \beta_{\mathrm{hkl}} \cos \theta_{\mathrm{hkl}} \tag{48}$$

1.3.4 X-ray reflectivity

XRR is a thin film characterization technique that also utilizes x-rays and is performed in a diffractometer as described in Section 1.3.3. However, XRR is measured at small specular angles of 2θ (typically 0 to 5°). In this condition x-rays are *reflected* from the sample.

Specifically, x-rays are reflected from the *interfaces* of each layer within the thin film stack. The different x-rays reflected from each interface will then *interfere* constructively or destructively at consecutive angles of reflection, producing a series of fringes in a plot of intensity against 2θ. These fringes are known as Kiessig fringes, and their angular spacing is determined by the relative distance between each interface in the multilayer (i.e. film thickness) [171, 172]. An example XRR pattern, measured for a $\mathrm{Mn_3Ir}$ (111) [10 nm] sample, is shown in Fig. 29.

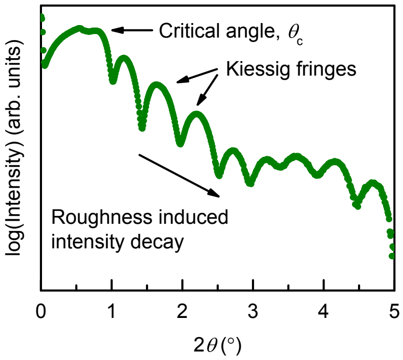

Figure 29: An example XRR pattern measured for a Al_2O_3 (0001) [sub] / TaN (111) [5 nm] / Mn_3Ir (111) [10 nm] / TaN (cap) [2.5 nm] sample, with key features labeled.

As well as the Kiessig fringes, we highlight two important features of the XRR pattern in Fig. 29. The first is the critical angle, θ_c. Below θ_c, all the x-rays incident on the sample are externally reflected from its uppermost surface. Thus, one observes a plateau in reflected intensity [172]. As the reflectivity angle is increased above θ_c, the process moves to one of internal reflection, with x-rays penetrating into the material, and their intensity decaying accordingly. The exact angle at which this internal penetration begins to occur depends on the refractive index of the thin film [172]. This, in turn, depends on its electron density, and so its mass density. Therefore, from the position of the θ_c, one can estimate the mass density of the film.

The second feature is the rate at which the reflected intensity subsequently drops-off. The overall decay of intensity depends on how much radiation remains reflected from the sample, and therefore depends upon the roughness of the thin film's top surface [171]. Increased surface roughness causes a more rapid drop in overall intensity. Simulated reflectivity curves for Si layers with different surface roughnesses are shown in Fig. 30, adapted from Ref. [171] . Meanwhile, the roughness of the interface between film and substrate will act to reduce the intensity of light reflected here, that then forms the interference pattern. Hence, as roughness of the buried interface increases, the amplitude of the Kiessig fringes reduces [171]. By examining the decay of overall reflected intensity and oscillation amplitude, one can estimate film roughness.

The most important parameter that can be determined from XRR is the film thickness. This is found from the periodicity of the Kiessig fringes. Let us consider the most simple case of a single thin film layer deposited on a substrate, as shown in Fig. 31, adapted from [172]. Here, the phase difference

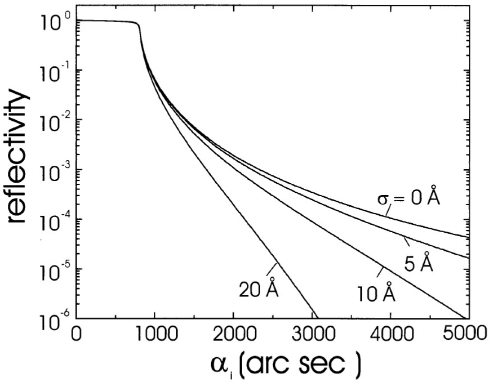

Figure 30: Simulated XRR patterns for Si layers with different values of average surface roughness [171].

between two reflected x-rays, δ, is defined by the x-ray path lengths (AB, BC, AD as in Fig. 31),

$$\delta = (\mathrm{AB} - \mathrm{BC})n - \mathrm{AD} \tag{49}$$

which can in turn be related to the film thickness, t, reflectivity angle, θ, and the x-ray wavelength, λ, by,

$$\delta = 2t \sin\theta \tag{50}$$

For constructive interference (i.e. the peak of the Kiessig fringes) we must satisfy $\delta = m\lambda$, where m is the index number of the fringe. Thus for a fringe m whose peak occurs at an angle θ_{m}, the film thickness can be calculated from,

$$\theta_{\mathrm{m}} = \theta_{\mathrm{c}} + (\lambda/2t)^2 m^2 \tag{51}$$

In modern XRR experiments, where thin film stacks may consist of multiple layers, a computer program can be used to simulate the XRR profile from a model of the multilayer to be measured. Using an iterative approach, mass density, interface roughness and layer thickness in the model can be varied to fit critical angle, amplitude decay and fringe spacing, respectively, to the measured XRR pattern. In this way, XRR allows us to estimate the actual thickness of each film in a grown multilayer structure.

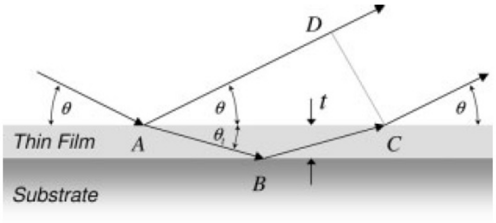

Figure 31: Geometry of x-ray reflection from a single thin film layer on a substrate [172].

1.3.5 Atomic force microscopy

Binning, Quate and Gerber first proposed AFM in 1986 [175]. It has uses across a range of scientific fields, including materials science, nanotechnology and biology. In solid-state physics, we primarily use AFM to measure the sample surface topography and roughness [176]. Together with scanning tunneling microscopy, it comprises the discipline of scanning probe microscopy [176]. This is because AFM uses a sharp probe tip (characteristic radius $< 10\,\text{nm}$), scanned across the specimen surface, to record topographic features with high spatial resolution. An AFM consists of [173]:

- **Vibration damping system**: such as active shock absorption or a passive granite base plate.
- **Optical video microscope**: to identify the broad area of specimen to be investigated further.
- **Course positioning motors and sample stage**: to align this region of interest with the probe tip.
- **Coarse vertical (z-axis) positioning motor**: to bring the tip close to the surface.
- **Piezoelectric positioners**: to scan the sample laterally in the xy-plane over a range of 10 nm to 100 µm, in a raster pattern, to construct a map of surface height.
- **Probe tip and cantilever**: fabricated using a semiconductor lithography process, the tip is atomically sharp to give nanometer resolution, whilst the cantilever undergoes deflection as the probe moves across the surface.
- **Force transducer**: measures cantilever deflection, which is calibrated to be proportional to force applied to the tip, by recording the displacement of a laser beam reflected off the cantilever.
- **Vertical piezoelectric positioner and feedback system**: to dynamically control the z-position of the probe tip in response to force measured.

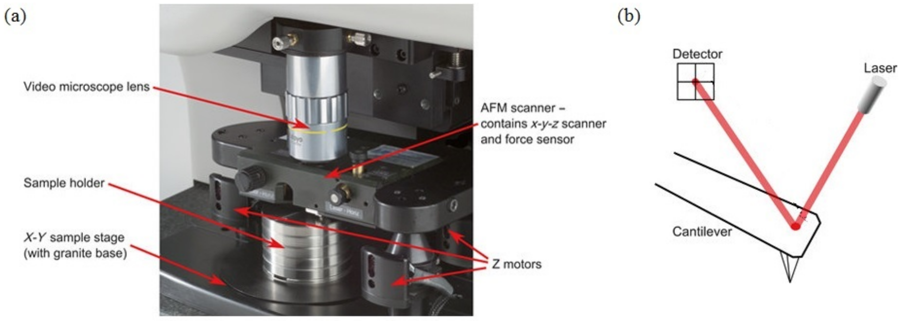

Figure 32: Photograph of an AFM apparatus (a) labeling key components, with the cantilever and probe tip contained in the AFM scanner, shown schematically in (b) diagram showing force transducer, which uses a reflected laser beam to measure the bending of the cantilever and hence force on the probe tip [173].

A photograph of an AFM apparatus is shown in Fig. 32 (a) [173].

An AFM can function in constant-height operation, where the tip is simply scanned across the surface and the deflection of the cantilever recorded (as with a stylus profilometer) [174]. We present a schematic of the force transducer used to measure cantilever bending in Fig. 32 (b). However, should the tip encounter a large feature on the surface, then this risks damage. Instead, we prefer to use the AFM in constant-force operation.

The atoms on the specimen surface exert a van-der-Waals force on the atoms at the tip of the probe [174]. This ‘atomic force’ felt by the tip changes with the sample topography; increasing at protrusions from the surface and decreasing if it dips downwards. A feedback loop uses a piezoelectric manipulator to move the tip in a vertical direction, in order to maintain a constant cantilever deflection. A block diagram outlining this feedback loop is shown in Fig. 33 (a) [173]. As force and hence cantilever bending increases, the tip position will move upwards, and vice versa. This process is illustrated in Fig. 33 (b). In this manner, the z-position traced by the tip mirrors the topographic profile of the specimen [173].

We call this *contact-mode* AFM, and it requires the specimen to exert moderate force on the tip. A plot of such force exerted on the probe as it moves towards the sample is shown in Fig. 34 (a) [174]. As the tip approaches the surface, it initially feels an attractive force and the cantilever will bend towards the sample. As the probe comes into contact with the sample, the cantilever will bend backwards slightly and the tip feels a repulsive force exerted by the sample. We must set the cantilever in this *repulsive regime for contact-mode measurements*. Whilst the forces exerted here are small,

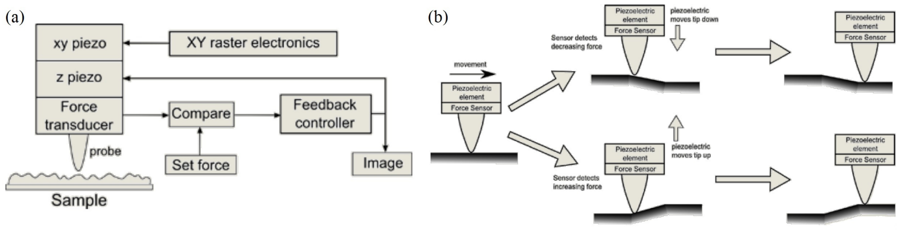

Figure 33: (a) Block diagram showing how AFM image is constructed by rastering probe tip laterally across the sample, whilst maintaining a constant force at the transducer by adjusting (and simultaneously recording) the z-position. (b) Feedback process whereby the vertical piezoelectric actuator adjusts probe tip position to maintain a constant force as specimen topography varies [174].

typical $< 10^{-9}$N, for sensitive specimens this still risks damage. In addition (although it maintains the highest resolution of all AFM modes) large lateral forces are also applied, which can move weakly bonded samples and or harm the tip.

Instead, the AFM can be operated in *noncontact mode*. Here we position the cantilever in the attractive regime, at a distance between points ‘a’ and ‘b’ in Fig. 34 (a) [174]. The tip no longer touches the surface, but now feels only an attractive force. This is tiny and so a more sensitive method of detecting it is needed. We use an oscillatory method. Here a final piezoelectric actuator excites the probe at a frequency close to its resonant frequency (300 to 400 kHz) [174]. Thus, the position of the *laser light reflected from the cantilever oscillates at the same frequency, and can be detected using a lock-in method.* A schematic of this oscillatory method is shown in Fig. 34 (b) [174].

As the tip is scanned across the specimen, changes in the attractive force caused by variations in the sample topography will slightly change the resonant frequency of the probe. This will damp its oscillations and so modify their amplitude at the chosen excitation frequency [174]. The height of the tip is again adjusted to maintain constant oscillation amplitude (in this case of the order 10 nm) and thus constant force, as explained above. We record this vertical position to map the specimen topography and can also record maps of the oscillation amplitude directly. The disadvantage of noncontact-mode AFM, however, is that it is very sensitive to the capillary layer (e.g. adsorbed water or organic molecules) that unavoidably occurs on thin films in ambient conditions [174].

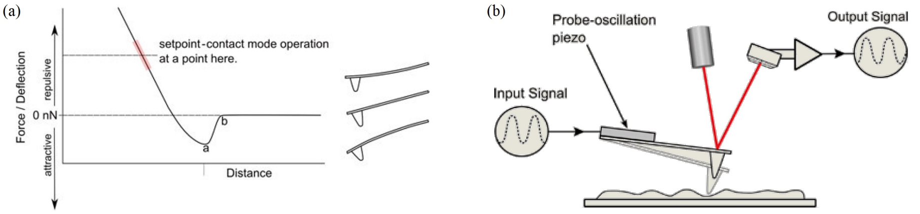

Figure 34: (a) Plot of cantilever deflection (corresponding to force on tip) as a function of distance from the specimen. Between points ‘b’ and ‘a’, the probe is just above the surface, in noncontact mode, and feels an attractive force that bends it towards the sample. At point ‘a’, the tip is just touching the surface. Driving further towards the specimen, into the repulsive regime, sets the cantilever for contact or tapping mode. (b) Schematic showing the oscillating method used for noncontact- or tapping-mode AFM. Atomic force variations caused by the sample topography modify the amplitude and phase of the output signal [174].

By combining contact-mode and oscillatory-method AFM, we can avoid lateral forces that may damage sample or tip, and at the same time penetrate any surface contamination layer our specimens. This is *tapping-mode (or intermittent-contact)* AFM. Here the tip is initially set in the repulsive regime, in contact with the sample, but still allowed to oscillate. *The probe therefore moves up and down onto the surface, from the repulsive to attractive force regimes.* This uses the same experimental set-up as in Fig. 34 (b), but this time with a larger oscillation amplitude of 1 to 100 nm [174].

In other words, the tip taps the sample. As before, variations in topography of the surface change the forces experienced by the tip as it is scanned across the specimen, thus modifying the amplitude of its oscillations and leading to an adjustment in vertical position in order to maintain constant force. We record maps of both this z-position (mirroring the surface height) as well as the oscillation amplitude (which will vary from the set point during the time it takes for the feedback loop to correct, and thus gives an indication of the gradient of features on the surface) [174]. In addition, atomic forces exerted on the probe will also introduce a phase shift to the reflected laser light, which can also be recorded and mapped [174].

In the results chapters of this thesis, we use such tapping-mode AFM to measure the surface roughness of fabricated thin films of noncollinear antiferromagnets with sub-nanometer precision.

1.3.6 Transmission electron microscopy

TEM is a powerful technique for analyzing the crystal structure of thin films on the nanoscale, allowing direct analysis of both local crystal structure, grain boundaries, defects, and interfaces.

The TEM operates by shining a beam of electrons through a thin lamella of sample (<10 µm) [177], then spatially resolving the scattered electrons using a luminescent screen or charge-coupled device camera [178].

The sample lamella can either be oriented in:

- Plane view, where the backside of the substrate is thinned away using ion milling, the electron beam shone along the normal to the specimen, and the film viewed from the top [179].
- Cross-section view, where a focused-ion beam is used to cut a slab through the depth of the film layers and substrate, with the electron beam then imaging the sample from the side [177]. Scanning-electron microscope images showing the fabrication process of such a lamella are presented in Fig. 35.

Once the lamella is aligned in the TEM, electrons are generated (for example, through thermionic emission from a W or LaB_6 filament [180]) and accelerated towards the sample. High accelerating potentials (V) of 100 to 300 kV are typically used. This accelerates electrons to close to $0.5c$ (where c is the speed of light), which, with a typical beam current of between 0.1 and 1 µA, means individual electrons are separated by around 1.6 mm [180])!

Nevertheless, the wave-particle duality of quantum mechanics ensures that, even when single electrons pass through the lamella at one time, they behave like a wave [181]. Their corresponding wavelength (λ) can be calculated (including relativistic effects) using,

$$\lambda = \frac{h}{\sqrt{2m_\mathrm{e}eV(1+\frac{eV}{2m_\mathrm{e}c^2})}} \tag{52}$$

where h is Planck's constant, m_e is electron mass and e is electron charge [182].

These 'electron waves' are directed onto the specimen using a series of magnetic lenses [177]. Two condenser lenses (labeled C1 and C2) focus the electron beam in a plane in front of the lamella. An upper objective lens then produces a parallel beam, of the order 1 to 10 µm across, that uniformly illuminates the specimen. A ray trace showing the electron wave paths through the TEM is show in Fig. 36 (a) [183].

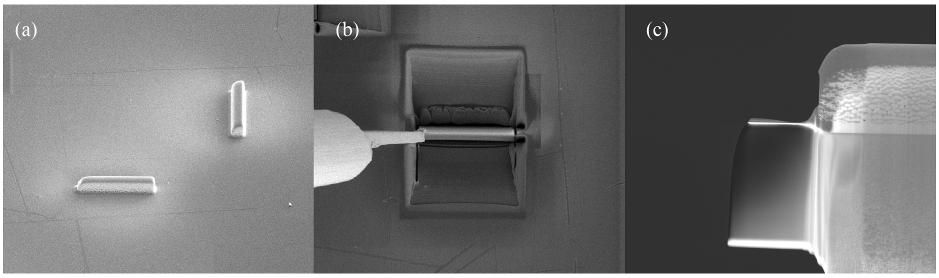

Figure 35: Scanning-electron micrographs showing the process of cross-sectional TEM lamella fabrication using focused ion beam milling: (a) definition of lamella in the thin film, (b) etching a trench into the substrate around the lamella and contacting it with a micromanipulator, (c) removal of the finished lamella and mounting on a TEM grid sample holder.

For a typical accelerating voltage of 300 kV, the incident electron wavelength is ≈2 pm. The effect of this is twofold. Firstly, because the electron wavelength is comparable to the typical lattice spacing in crystal structures, the crystal lattice will behave like a diffraction grating and scatter electrons as discussed in Section 1.3.3. By measuring the resulting diffraction pattern, local information on the specimen's crystal structure can be determined [177].

Furthermore, the resolution of any imaging system can be approximated using the Rayleigh criterion [184]. This defines the radius of the Airy disk (r_{th}, the disk into which a point source blurs as waves are focused through a lens) as the resolution of the microscope, according to the equation,

$$r_{\mathrm{th}} = 0.61\frac{\lambda}{\beta} \tag{53}$$

where β is the semi angle of light collected by the lens (defined by the lens radius or an aperture placed close to the lens) [184].

Therefore, for the electron wavelengths used in TEM, the theoretical resolution limit is extremely small. In practice, however, the resolution of the TEM is limited not by the accelerating voltage of the electrons, but by aberrations caused by technical imperfections in the magnetic lens system. These can include *astigmatism, chromatic aberration and, most importantly, spherical aberration* [184]. Spherical aberration increases with β^3.

Hence when designing a TEM, a balance between decreasing aperture size as much as possible, whilst keeping it large enough not to impinge on the absolute limit set by the Rayleigh criterion, defines the microscope resolution [184]. In a modern aberration-corrected TEM, it is possible to image crystal structure in real space with atomic resolution.

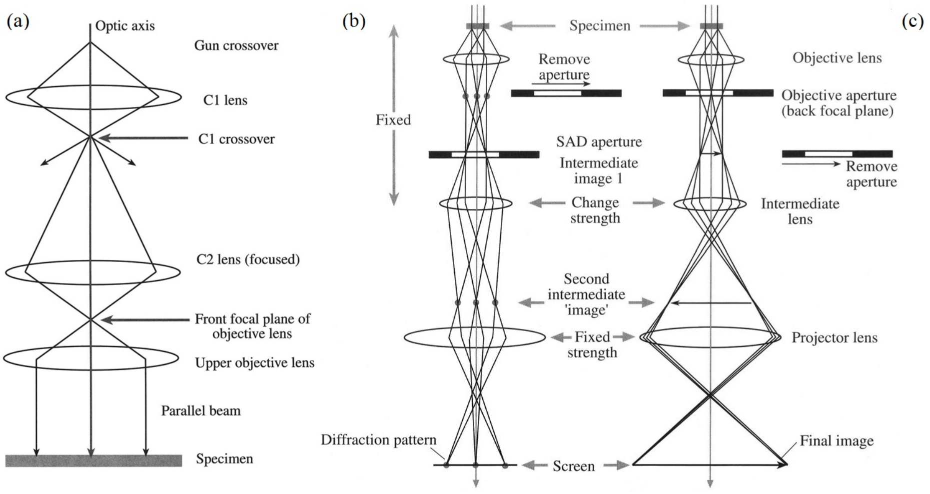

Figure 36: Ray trace diagrams showing electron paths through the magnetic lenses and apertures of a TEM. (a) shows the optics before the specimen, configured to produce an incident parallel beam. (b) and (c) show the optics after the specimen, in a mode to measure either diffraction patterns or real-space images, respectively [183].

Such images are formed using a second set of magnetic lenses, located between the specimen and imaging screen or camera. An **objective lens** collects the electrons scattered by the lamella, focusing them in the back focal plane and producing a first intermediate image shortly thereafter. An **intermediate lens**, whose strength can be tuned to control the magnification of the microscope, then focuses the electrons through a second intermediate image [183]. Finally, a fixed-strength **projector lens** creates a final image on the screen, located at a distance L from the specimen.

By varying the focal length of the intermediate lens, to collect electrons from either the **back focal plane** or **first intermediate image plane** of the objective lens, the TEM can be set to measure either diffraction patterns or real-space images of the specimen. Fig. 36 illustrates the optics used to create both reciprocal- and real-space images [183].

Diffraction patterns. In this mode, the intermediate lens collects electrons from the back focal plane of the objective lens. At this point, ‘electron waves’ diffracted from the lamella will be re-focused into a series of points [177]. These spots occur where the constructive interference condition (in turn depending on the lattice spacing of the crystal) is satisfied. An aperture is placed in the plane of the first intermediate image. By moving the aperture across the intermediate image, we control the region from which diffracted electrons are collected. This produces a SAED pattern [183].

The pattern (allowing local analysis) consists of a series of intensity spots, which, as in an XRD spectrum, can be indexed as arising from electron diffraction from specific crystal planes. Thus, we can distinguish the crystal orientation of the film or, by collecting diffraction patterns across both film and substrate, their epitaxial relationship. For single-crystalline film specimens, electrons are scattered within stacked crystal planes normal to the electron beam [177]. This produces a two-dimensional array of diffraction spots that allows us to identify simultaneously multiple crystal directions within the plane of the lamella.

Furthermore, by measuring the spacing between diffraction spots (r_{hkl}), the lattice spacing (d_{hkl}) of the specimen locally can be calculated,

$$\lambda L = d_{\mathrm{hkl}} r_{\mathrm{hkl}} \tag{54}$$

Here the product λL of electron wavelength at a particular acceleration voltage and effective camera length is often automatically determined by the calibrated TEM [177].

Real-space imaging. Alternatively, we insert an objective aperture in the back focal plane, the size of which will control β and hence the resolution of the microscope [183]. The intermediate lens is then set with its object at the first intermediate image plane. This means it forms on the screen a map of 'electron-wave' amplitude varying in real space after scattering from the lamella [177].

In this mode, contrast in the resulting image gives a direct projection of the specimen microstructure. This makes is possible to identify explicitly the size of crystallites in the film, the nature of grain boundaries between them, defect types and locations (including misfit dislocations and stacking faults), and the roughness of buried interfaces.

The mechanisms giving rise to this contrast are three-fold and can unveil different aspects of the specimen microstructure. *Diffraction contrast* is produced when different regions of the sample diffract electrons with different intensities, producing contrast between differently oriented crystallites [177]. Mass thickness contrast arises directly from the *elastic scattering of incident electrons by atomic nuclei* in the lamella [177]. Morphological changes in the specimen will lead to different rates of such Coulomb interactions, and hence image contrast, between grain boundaries, defects or chemically inhomogeneous regions. Finally, at high magnification, the interaction of electrons with columns of atoms in the crystal lattice causes a *phase shift in the electron wavefunction* [177]. By interfering two such 'electron waves', so that phase shift is converted to amplitude modulation, it is possible to obtain contrast between individual atomic columns within the lamella.

1.3.7 Magnetometry

Having deposited epitaxial thin films (Section 1.3.2) using magnetron sputtering (Section 1.3.1) and characterized their crystal structure (Section 1.3.3), thickness (Section 1.3.4) and roughness (Section 1.3.5), we now wish to measure their magnetism. This is important for the FM and AF films used in spintronic applications, as their magnetic properties are key to device functionality and engineering these is an ongoing research effort (including in this thesis). We will therefore look at magnetism measurements in the next two sections, starting with measurements of bulk magnetic properties.

Let us take a magnetized thin film; how can we measure the magnetic moment, m, of this sample? The magnetic moment will produce a magnetic field, $\mu_0 H_{\text{sample}}$ around the thin film. If the sample is now passed into a tightly wound wire coil, with radius a and N turns, the rate (with respect to time, t) at which magnetic flux (Φ) cuts the coil will induce a voltage (V) according to Faraday's law [185],

$$V = -N\frac{d\Phi}{dt} \tag{55}$$

If the thin film moves into and out of the coil at a frequency f, this induced voltage will oscillate. By performing a lock-in measurement and integrating the voltage measured across the ends of the coil, we find this voltage is proportional to the magnetic field generated by the sample,

$$V = -j2\pi^2 f N a^2 \mu_0 H_{\text{sample}} \tag{56}$$

where j is the imaginary number [186].

Such a measurement is the basis of a **vibrating sample magnetometer**. Here a magnetized thin film is oscillated by a vibrating diaphragm inside a pair of pick-up coils [186]. By accounting for geometric factors, such as the sample fill factor inside the coils and its demagnetizing field, the magnetic moment of the sample is measured [187].

However, what if, as in this thesis, we wish to measure novel spintronic materials such as antiferromagnets or (almost) fully compensated ferrimagnets? Here the magnetic moment, and hence induced voltage, is extremely small. The answer is to use a very sensitive detector of magnetic flux: **a superconducting quantum-interference device**.

Such a combination forms the basis of a SQUID-VSM, an example of which is the Quantum Design MPMS3 magnetometer used in this thesis [187]. A diagram of this instrument's detection scheme is presented in Fig. 37. Because the SQUID is a micrometer scale device, its effective area for flux capture from the vibrating sample would be small.

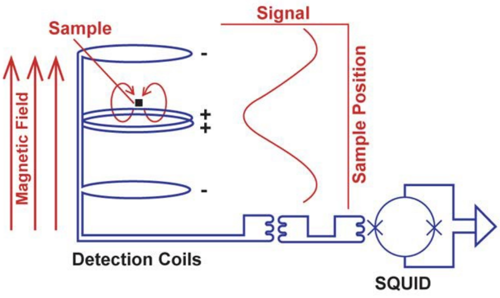

Figure 37: Schematic of the magnetic moment detection system inside a Quantum Design MPMS3 SQUID-VSM. The signal plotted is the voltage measured across the SQUID as the sample oscillates [187].

Instead, a pair of centimeter-sized pick-up coils sit around the specimen, maintaining a large filling factor. The flux of the vibrating sample cuts these coils, inducing a voltage [187]. The resulting oscillating current through the wire in turn generates a magnetic field around a second, smaller coil. This is lithographically fabricated in proximity to the SQUID, meaning they are strongly inductively coupled. A small flux, proportional to the flux induced in the pick-up coils by the magnetized thin film, now cuts the SQUID [188].

As the sample vibrates, the flux cutting the SQUID will change. The SQUID converts this into a low-noise voltage, whose amplitude we can precisely measure and is proportional to the sample magnetic moment. How does the SQUID convert changes in magnetic flux to voltage [188]?

- The SQUID consists of a superconducting ring, interrupted by two Josephson junctions.
- A bias current (I_B) is applied across the device.
- Each Josephson junction has associated with it a critical current (I_C), above which a voltage (V) is induced across the SQUID.
- We bias the SQUID at $I_\mathrm{B} = 2I_\mathrm{C}$, so that a voltage just begins to appear.
- When a magnetic flux begins to cut the SQUID, it modifies the bosonic wavefunction of electron cooper pairs flowing through the superconductor.
- However, their phase can only increase in multiples of 2π.
- Hence, the magnetic flux cutting the SQUID can only increase by a quantized amount.
- We call this the flux quantum, Φ_0.

- The magnetic flux produced by the small coil, Φ_{ext}, will be smaller than this flux quantum.
- Therefore, an addition screening current, I_{circ}, will flow in a circle around the SQUID, to shield out the flux threading the ring.
- Now the current flowing through one Josephson junction will be $I_{\text{C}} - I_{\text{circ}}$, suppressing it below its critical current.
- Meanwhile the current through the second junction will be $I_{\text{C}} + I_{\text{circ}}$, setting up a stable voltage across this junction.
- As flux penetrating the SQUID increases, I_{circ} will increase, and hence the voltage across the SQUID will increase.
- However, once the magnetic flux reaches a value of $\Phi_0/2$, it becomes energetically favorable to allow a full flux quantum to thread the SQUID.
- Therefore, I_{circ} reverses direction, now producing additional flux that adds to Φ_{ext}, to bring the total flux threading the SQUID to Φ_0.
- As external flux through the SQUID is further increased I_{circ}, and hence the voltage across the SQUID, will begin to decrease.
- Once $\Phi_{\text{ext}} = \Phi_0$ then $I_{\text{circ}} = 0$ and $I_{\text{B}} = 2I_{\text{C}}$, and the voltage across the SQUID returns to a minimum.
- As external flux penetrating the SQUID is progressively increased, the voltage changes between a maximum at $n\Phi_0/2$ and a minimum at $n\Phi_0$ (where n is an integer).
- Thus, for small changes in external flux produced by the inductively coupled coil next to the SQUID, we measure a clearly detectable change in voltage across the SQUID.
- Through careful calibration, this voltage can be related back to the magnetic flux cutting the original pick-up coils, and hence the net magnetic moment of the sample.

A diagram of this SQUID circuit, detailing the relevant currents and voltages as external magnetic flux is detected, is shown in Fig. 38 [188].

In this way, we can accurately quantify even very small magnetic moments. By subtracting any background contribution of the substrate (which will typically be weakly diamagnetic for oxide substrates) measured from a reference sample, we are left with just the magnetic moment of the thin film. Using the known film thickness and lateral dimensions of the measured specimen, we can thus calculate the volume magnetization, M, of the material under test [187].

In order to better qualify the nature of this magnetization, and demonstrate its control to help enable spintronic device functionality, we wish to

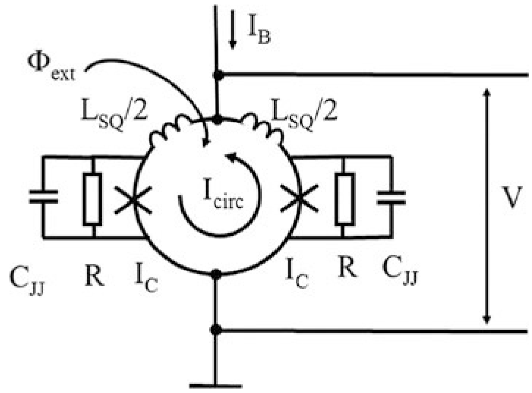

Figure 38: Diagram of the SQUID circuit, whilst detecting external magnetic flux. $L_{\mathrm{SQ}}/2$ is the inductance of each Josephson junction, whilst R and C_{JJ} are a resistance and capacitance designed to damp the SQUID hysteresis [188].

study the behavior of the magnetization in response to an external magnetic field. To do this, we measure thin film magnetization as a function of applied magnetic field. A multitude of physical factors determines its response, such as the exchange interactions in the material or magnetic anisotropies [38]. For example, as external magnetic field is cycled from positive to negative and back again, in the case of a FM material we will record a typical magnetization hysteresis loop as discussed in Section 1.2.2.

However, to study materials with strong anisotropies, such as the AFs discussed in Sections 1.2.3 and 1.2.4, we often need to apply strong magnetic fields of the order 1 to 10 T. To do this in a practical and energy efficient way requires a superconducting magnet, cooled to cryogenic temperatures. In addition, the SQUID device must be cooled to below its superconducting critical temperature [187]. Finally, it is interesting to cool the sample itself, in order to measure its magnetic properties as a function of temperature.

For this reason, we perform SQUID-VSM measurements inside a cryostat. Cryostats, how they can be used to control sample temperature, and superconducting magnets are discussed in more detail in the context of magnetotransport in Section 1.3.10. However, they also enable magnetometry measurements as a function of external magnetic field and temperature. In the next Section 1.3.8, we move onto look at a second technique for measuring thin film magnetic properties that also utilizes a cryogenic-temperature cryostat with a vector magnetic field. This is XMCD.

1.3.8 X-ray magnetic circular dichroism

XMCD is a spectroscopic technique to measure the magnetic properties of a material. X rays are used to excite a sample, for example a thin film composed of a magnetic compound. Their energies are tuned to address specific electronic transitions in the atoms responsible for the magnetism. In this section, we will discuss how this provides a direct probe of magnetic moment in our material.

In XMCD spectroscopy, the interaction between electrons (in shells responsible for generating atomic moments) and x-ray radiation provides information on the magnetic state of a material. Using Gauss' law for electric field together with Maxwell's equations, and neglecting the small magnetic field contribution, the electric field (ϵ) of plane-wave x rays can be expressed,

$$\epsilon(\boldsymbol{r}, t) = \epsilon_0 \hat{\boldsymbol{\epsilon}} \sin\left(k \cdot r - \omega t + \delta_\phi\right) \tag{57}$$

where ϵ_0 is electric field amplitude, $\hat{\boldsymbol{\epsilon}}$ is direction of electric field polarization, $\boldsymbol{k}$ is wavevector, $\boldsymbol{r}$ is displacement in propagation direction, ω is angular frequency and t is time [189]. δ_ϕ represents any phase shift of the wave with respect to a given reference.

We can deconvolute an arbitrary x-ray electric field polarization into orthogonal x and y components. For linearly polarized x-rays, $\hat{\boldsymbol{\epsilon}}$ will point along a fixed axis in the xy plane. For circularly polarized x-rays, the phase difference $\delta_\phi = \phi_\mathrm{x} - \phi_\mathrm{y} = +90°\mathrm{or} - 90°$ for right- (clockwise) and left- (anticlockwise) circularly polarized x rays respectively [190]. A circularly polarized x-ray can, in turn, be deconvoluted into a superposition of linear polarized electric fields, and so defined by a certain $\hat{\boldsymbol{\epsilon}}$.

The time-dependent Schrödinger equation describes the interaction of such an x ray with, for example, a one electron atom. Working in the length gauge, we can write this down as,

$$\mathrm{i}\hbar \frac{\mathrm{d}}{\mathrm{d}t} \Psi(\boldsymbol{r}, t) = \left(H_0 + e\hat{\boldsymbol{\epsilon}} \cdot \boldsymbol{r}\right) \Psi(\boldsymbol{r}, t) \tag{58}$$

where i is the imaginary number, $\hbar$ is reduced Planck's constant, e is electron charge and H_0 is the Hamiltonian of the unperturbed atom [189].

We can use perturbation theory to estimate the likelihood of the radiation exciting the atom's electron from a ground state $\langle \psi_\mathrm{g}|$ to a final state $\langle \psi_\mathrm{f}|$. Using the dipole approximation (size of the atom is much smaller than x-ray wavelength, such that each atom experiences a uniform electric field), the matrix elements for this transition are given by [189],

$$M_\mathrm{fg}^2 = |\langle \psi_f | \hat{\boldsymbol{\epsilon}} \cdot \boldsymbol{D} | \psi_g \rangle|^2 \tag{59}$$

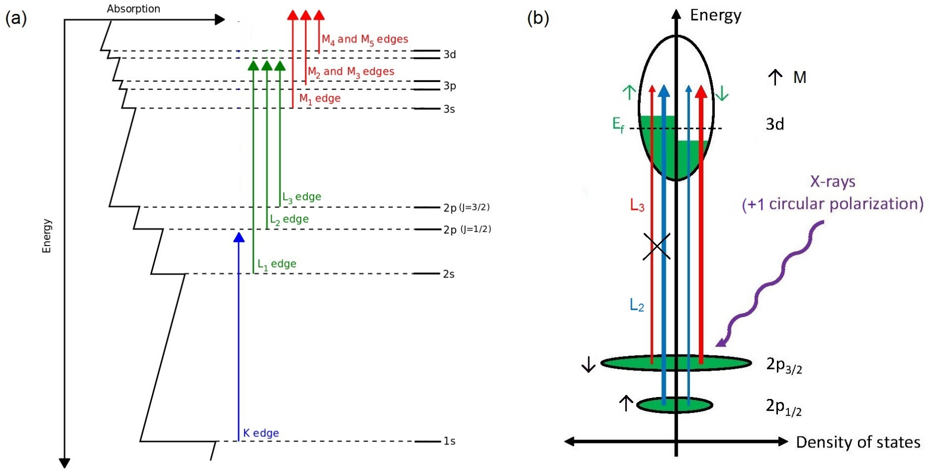

Figure 39: (a) Energy level diagram showing some allowed transitions between different sub-shells for electrons excited from core atomic orbitals. These transitions are typical for magnetic transition-metal and rare-earth elements, and accessible with soft x-rays. The different electron subshells are labeled (using spectroscopic notation), as well as the names of the resulting absorption edges observed in an XAS spectrum [190]. Each transition edge is named with a letter, corresponding to the principle quantum number of the shell, and a subscript, indicating the total angular momentum eigenvalue of the atomic orbital, from which it was excited. Adapted from [191]. (b) Transition pathways for electrons from $2p_{3/2}$ and $2p_{1/2}$ atomic orbitals to unoccupied $3d$ sub-shell states (L_3 and L_2 edges, respectively), excited by right-hand circularly polarized x-rays ($P = +1$). For the L_3 transition (red lines), the majority of transitioning electrons are spin-down ($S = +1/2$, thick line) whilst a minority are spin-up (S = -1/2, thin line). Conversely for the L_2 transition (blue lines), the majority of transitioning electrons are spin-up (S = - 1/2, thick line) whilst a minority are spin-down (S = + 1/2, thin line). Filling of the spin-split density of states around the Fermi level (E_F) in the $3d$ sub-shell is shown, with the spin-polarization of unoccupied states determining transition probability by Equ. 60. Adapted from [192].

Here $\boldsymbol{D} = -e\boldsymbol{r}$ is the atomic dipole operator and $\hat{\boldsymbol{\epsilon}}$ accounts for the effect of the x-ray polarization on the transition.

The probability per unit time (P_fg) of the x rays of energy $\hbar\omega$ triggering this transition from ground energy level E_g to final energy level E_f is then related to M_fg by Fermi's golden rule,

$$P_\mathrm{fg} \propto \sum_\mathrm{fg} M_\mathrm{fg}^2 (1 - D_\mathrm{occu}(E_\mathrm{f}))\delta(\hbar\omega - (E_\mathrm{f} - E_\mathrm{g})) \tag{60}$$

where $D_\mathrm{occu}(E_\mathrm{f})$ is the occupied density of states at the excited level [190]. By analyzing this expression, we can describe three important characteristics of the interaction of radiation with our materials:

- The delta-function shows that the transition occurs when the x-ray photon energy matches the energy difference between the ground and excited electron shells. This is because an electron must absorb a quantum of energy of exactly the right size to allow it to make the transition from one energy level to the next. Therefore, electrons absorb x-ray photons of energy equal to specific atomic excitations in a sample.
- The probability per unit time of an electron transition occurring depends on the occupancy of electron orbits in the target sub-shell. This fact is the origin of the magnetic dichroism, explained below [190].
- The dipole-approximation transition matrix imposes a series of restrictions on the allowed changes in quantum numbers when the electron is excited. Specifically, any change in orbital angular momentum must fulfill,

  $$\Delta m_{\mathrm{L}} = \pm 1 \tag{61}$$

  and there must be no change in electron spin angular momentum,

  $$\Delta m_{\mathrm{S}} = 0 \tag{62}$$

  for a typical transition metal atom [190].

Fig. 39 (a) shows some examples of electron excitations allowed by these selection rules. Electrons are excited from core sub-shell orbitals into unoccupied states in higher energy sub-shells. For every element, each transition has a characteristic energy. Therefore, when x rays with a continuous sweep of energies are incident on a sample, absorption intensity will increase at certain energies determined by the atoms present.

Depending on whether electrons from the core orbitals are excited into continuum states or into higher energy sub-shells, this absorption intensity increase will manifest itself as a step edge at the energy of the core orbital (with respect to vacuum), or as a peak corresponding to the difference between the initial and final sub-shell energies [190]. We call this **x-ray absorption spectroscopy**.

As well as allowing elemental identification of a specimen, the exact energy and shape of the absorption step or peak provides detailed information about the atoms inside a material. This includes valency and ionic bonding state, oxidation state, and specific geometric or chemical environment [190].

Furthermore, this absorption can show dichroism effects. This means a difference in absorption for different x-ray polarizations. Dichroism can arise, for example, along certain crystal structure axes or when a sample shows magnetic order [190].

The later case is particularly pronounced when using circular polarized x-rays. There is a significant difference in absorption of right- and left-circularly polarized x-rays by a magnetized sample. This absorption contrast reverses on switching magnetization direction. This effect is called **x-ray magnetic circular dichroism**.

(Long-range magnetic order can also cause a difference in absorption of x-rays polarized along two perpendicular linear directions; **x-ray magnetic linear dichroism**. This technique is of particular interest for collinear AFs, as introduced in Section 1.2.3. Here orthogonal orientations of the collinear magnetic order absorb x-rays polarized linearity along a certain direction differently, with this contrast reversed on rotation of the polarization linearity [97]. XMLD, when combined with photoemission electron microscopy, has been used to measure the domain structure in collinear AFs [57]. We discuss this X-PEEM technique further in Section 2.2).

How can we use XMCD to measure the magnetization of a transition metal? In such atoms, the $3d$ sub-shells govern magnetic moment. Therefore, we measure XMCD around the $L_{3,2}$ edges. As presented in Fig. 39 (a), these comprise transitions from the $2p_{3/2}$ and $2p_{1/2}$ atomic orbitals into the $3d$ sub-shell, respectively [190].

This results in an XAS absorption spectrum with two peaks, corresponding to the L_3 and L_2 transitions. To measure the spectrum, we scan photon energy whilst recording the absorption coefficient, σ, of our sample. This absorption coefficient is proportional the probability of electron excitation per unit time (the rate of transitions) [190].

How do we measure this absorption coefficient experimentally? Each excited electron leaves behind a hole in the core shell. A second electron from a higher energy shell will relax to fill this hole, and in doing so will release a photon corresponding to its lost energy. For a given incident x-ray energy, the higher the rate of transitions this excites, the higher the intensity of x-ray photon absorption and the higher the intensity of relaxation photon production. Therefore, by detecting the intensity of these relaxation photons, we record the energy dependence of absorption coefficient.

Fig. 40 illustrates two ways to detect these relaxation photons [190]. In the **fluorescence yield** detection mode, relaxation photons emitted from the sample are directly measured. Alternatively, a third electron may absorb the relaxation photon, ejecting it from the atom as an Auger electron. By connecting the specimen to earth, we can draw a small current that is proportional to the number of Auger electrons and, hence, relaxation photon intensity. We call this **total electron yield** detection.

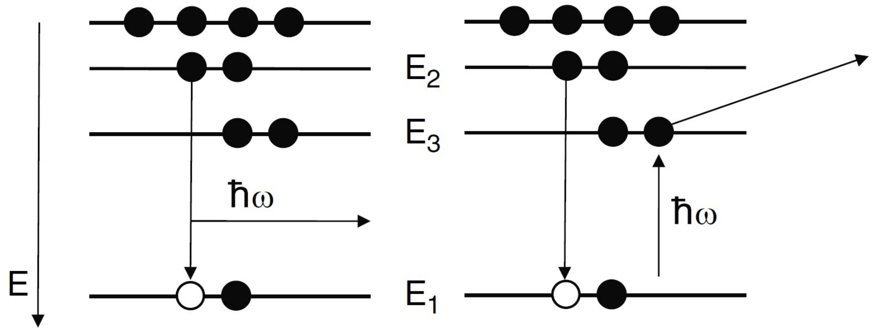

Figure 40: Energy level diagram depicting two possible processes by which an electron can emit energy and relax to fill a core-state hole: Fluorescence (left), where the relaxing electron directly releases a photon of energy $\hbar\omega = E_2 - E_1$ from the atom. The intensity of these ejected photons is proportional to x-ray absorption intensity. Due to the large escape depth of photons, this detection mode is bulk sensitive. Auger electron emission (right), where the relaxation photon is reabsorbed by another electron. This Auger electron is kicked out of the atom with energy $= \hbar\omega - (E_3 - E_1)$. Each Auger electron will, in turn, trigger a cascade of electrons jumping into the conduction band, which contribute to a measurable total electron yield current. Due to the relatively short mean free path of electrons in most solids, this technique is surface sensitive. Adapted from [190].

What, then, is the physical origin of the dichroism detected in the absorption coefficient? To observe XMCD, SOC must split the $2p$ sub-shells of our sample [193]. This couples the direction of each core electron's spin to its orbital angular momentum eigenvalue, resulting in two separate atomic orbitals (with total angular momentum $J = {}^1\!/_2$ and $J = {}^3\!/_2$ respectively).

When core electrons from these atomic orbitals are excited into the $3d$ subshell, the selection rules dictate that $\Delta_{\mathrm{L}} = \pm 1$, whilst $\Delta_{\mathrm{S}} = 0$. When an electron absorbs a circularly polarized x-ray, the helicity of the photon changes its orbital angular momentum: For right-hand circularly polarized photons, $L \Rightarrow L+1$, whilst for left-hand circular polarized photons, $L \Rightarrow L-1$ [193]. Therefore, following the excitation, the electron arrives in a $3d$ subshell orbital corresponding to its new orbital angular momentum.

Thus a series of sub-transitions occur, from $2p$ sub-shell orbitals with certain L eigenvalues to $3d$ sub-shell orbitals with new L eigenvalues (as changed by x-ray photon helicity). *The dipole-approximation transition matrix elements assign a certain probability weight to each of these sub-transitions* [193]. At the same time, an electron's starting L eigenvalue determines its spin angular momentum, which cannot flip during the excitation.

This combination of sub-transitions with different fixed spin directions and different weights results in *the electrons undergoing each net transition having a more likely spin eigenvalue* [193]. Fig. 39 (b) illustrates this mechanism, when excited by right-hand circularly polarized x-rays. For the L_3 transition, the majority of excited electrons are spin-down. For the L_2 transition, the majority of excited electrons are spin-up. The spin-polarization of the transition is reversed if x-ray helicity is switched [193].

Fermi's golden rule shows that the density of unoccupied states in the target sub-shell determines the net transition probability; the more unoccupied states available for an electron to be excited into, the more likely the transition probability per unit time. However, where spin-flip scattering is suppressed ($\Delta m_{\mathrm{S}} = 0$), *an electron may only be excited into an unoccupied state whose spin eigenvalue matches that of the electron* [193].

Since SOC splits the $3d$ sub-band into orbitals available only to spin-up electrons, and orbitals available only to spin-down electrons, the spin-polarization of unoccupied states will be opposite to sample magnetization (this is in similar to the $s - d$ scattering process responsible for anisotropic MR, explained in Section 1.2.8).

As shown in Fig. 39 (b), *magnetization aligned 'upwards' means more electrons are filling spin-up states in the atom. Conversely, there are more available spin-down states.* Thus, there is a higher transition probability for spin-down electrons. Because excitations from the $2p_{3/2}$ atomic orbital are majority spin-down polarized, the rate of L_3 transitions is higher and more x-ray photons are absorbed at this energy [193]. Therefore, in a plot of x-ray energy against absorption coefficient (an XAS spectrum), the peak at the L_3 edge will be enhanced. Conversely, the absorption coefficient around L_2 peak will be lower than usual.

If we now switch x-ray circular polarization, from right-hand to left-hand helicity, the spin polarization of the two transitions switches. Spin-up electrons will now dominate the L_3 transition, suppressing the absorption coefficient around this edge. Conversely, excitation of $2p_{1/2}$ core electrons is *now more likely, into the larger spin-down density of states* [193]. The resulting increased excitation rate around the L_2 edges leads to an increase in x-ray photon absorption at this energy. This, in turn, enhances the absorption coefficient around the L_2 peak.

With fixed left-hand circular x-ray polarization, if we now reverse magnetization direction, then the spin polarization of the density of states will switch. The material now shows a larger density of spin-up unoccupied states. This *enhances the absorption coefficient around the majority spin-up electron L_3 transition*, whilst suppressing the absorption coefficient around the majority spin-down electron L_2 transition [193].

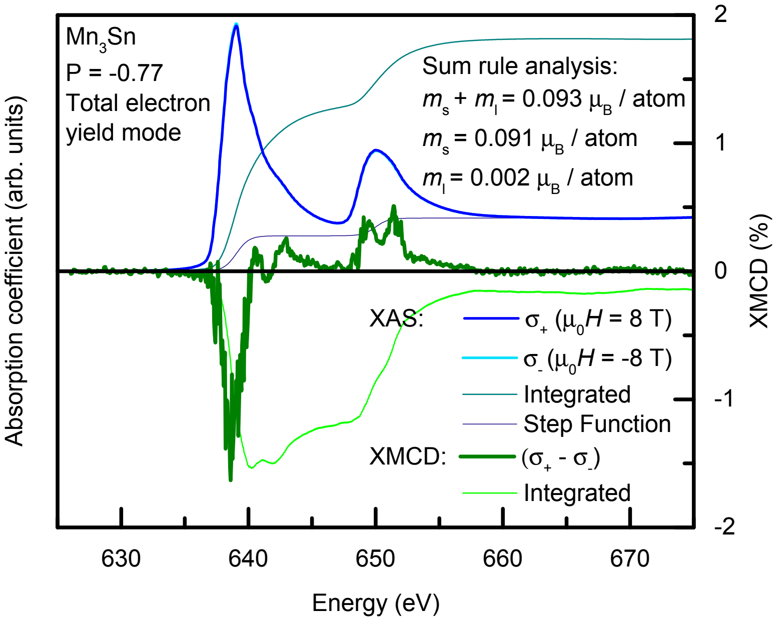

Figure 41: XAS and XMCD spectra around the Mn-$L_{3,2}$ edges in a Mn$_3$Sn film. Spectra were measured with left circularly polarized x-rays (indicated by the, incomplete, degree of beam polarization, $P = -0.77$) in total electron yield mode. XAS spectra were normalized with respect to incident photon intensity on the sample. (We record the total electron yield from an Au grid placed partially in the x-ray beam, which corresponds to incident intensity). Any linear slope present before the rising edge is subtracted. The post-peak region is normalized to unity [193]. The resulting XMCD spectrum, $\sigma_+ - \sigma_-$, is plotted, along with its integral (for sum rule analysis). To account for the contribution to XAS signal of any core electron excitations into continuum states, we fit the spectra with a two-step function (one at L_3 edge and one at L_2 edge). The area under this step function is subtracted, and the remaining area under both XAS curves integrated, as shown. We then calculate spin and orbital magnetic moments for the Mn-3d sub-shell using sum rule analysis.

We show an example of such a measurement in Fig. 41. Two XAS spectra are measured using left circularly polarized x-rays, in a positive and negative magnetic field. In the positive field, the alignment of magnetization enhances the absorption coefficient at the L_2 edge. We label such a spectrum σ_+. In negative magnetic field, the magnetization direction is reversed and the L_2 transition is suppressed. We label this spectrum σ_-. Subtracting one XAS spectrum from the other gives XMCD contrast, $\sigma_+ - \sigma_-$. The resulting XMCD spectrum shows two opposite bumps, typical of transition metals.

The spectra are defined, conventionally, to give a positive bump at the L_2 edge and a negative bump at the L_3 edge under the primary measurement configuration[193] (if right-hand circularly polarized x-rays were used, the sign of the bumps would reverse).

Such XMCD contrast can be observed when either reversing sample magnetization using a fixed x-ray helicity, or reversing circular polarization direction, with a fixed magnetization direction. A nonzero XMCD signal around the $L_{3,2}$ edges is evidence of net magnetization in a material, created by atomic magnetic moments generated in the $3d$ sub-shell of exactly the elements whose transitions are excited by the x-ray photons [190]. A persistent XMCD signal at zero applied magnetic field demonstrates FM ordering.

Furthermore, XMCD allows us to calculate explicitly the orbital (m_l) and spin (m_s) magnetic moments of the atomic sub-shell responsible for a material's magnetization. We do this using the **XMCD sum rules** [194]. This first requires the integration of the area under the XAS and XMCD spectra, as described in Fig. 41. We can then calculate spin and orbital magnetic moments according to [195],

$$m_\mathrm{l} = -\frac{K}{P} N_\mathrm{unoccu} \frac{2(A+B)}{3C} \mu_B \tag{63}$$

$$m_\mathrm{s} = -\frac{K}{P} N_\mathrm{unoccu} \frac{(A-2B)}{C} \mu_B \tag{64}$$

where,

$$A = \int_{L_3} \mathrm{XMCD} = \int_{L_3} (\sigma_+ - \sigma_-)\mathrm{d}E \tag{65}$$

$$B = \int_{L_2} \mathrm{XMCD} = \int_{L_2} (\sigma_+ - \sigma_-)\mathrm{d}E \tag{66}$$

$$C = \frac{1}{2} \int_{L_3 \& L_2} \mathrm{XAS}_{\sigma_+} + \mathrm{XAS}_{\sigma_-} = \frac{1}{2} \int_{L_3 \& L_2} (\sigma_+ + \sigma_-)\mathrm{d}E \tag{67}$$

and,

- K is a proportionality constant, set as 1.4 for Mn, accounting for the overlap of the L_3 and L_2 excitation peaks (caused by mixing of the $J = 1/2$ and $J = 3/2$ orbitals due to weak SOC in the light transition metals) [196].
- P represents the degree of polarization of the x-ray beam
- N_unoccu is the number of unoccupied states in the $3d$ sub-shell of each atom, determined as 4.53 for Mn atoms [195].
- μ_B is the Bohr magneton (see Section 1.2.2).

In Fig. 41, we report the spin and orbital contributions to the uncompensated magnetic moments measured for a Mn_3Sn film, details of which are given in Section 3.2.

Such XMCD spectroscopy can be performed at different temperatures or in different externally applied magnetic fields (using a cryostat as described in Section 1.2.8). Therefore, we can study the temperature dependence of atomic magnetic moment or its magnetic field dependence. In the coming results chapters, we present results of XMCD measurements on noncollinear AF thin films as a function of both magnetic field and temperature.

These measurements were performed in the VEKMAG facility at the BESSY synchrotron [197]. In order to generate the brilliance of x-rays required for XAS measurements with a good signal to noise ratio, and to utilize the complex apparatus needed to tune x-ray photon energy over a broad range, it is necessary to perform XMCD measurements at a synchrotron radiation facility [198].

1.3.9 Lithographic patterning

The technological revolution of the past century has been driven by advances in computational power. This, in turn, was enabled by the production of microelectronics at increasingly tiny scales. Thus, any application of spintronics must be compatible with these **device fabrication** processes.

Basic thin film device fabrication is also necessary for fundamental solid-state research, in order to perform magnetotransport measurements (discussed in Section 1.2.8). Therefore, we explore two key parts of the device fabrication procedure: lithography, *to write patterns onto a sample*, and etching, *to define these structures into the film.*

Lithography is the process of designing a device layout and transferring this pattern onto the surface of a thin film. This occurs in a series of steps:

- Cleaning
- Coating
- Exposure
- Development

Before starting, we *clean the sample* to avoid particulate contamination. Particulates are pieces of material with sizes ranging from 100 µm (width of a human hair) to 100 nm (particulates even one-fifth the size of elements to be fabricated can impair patterning) [199]. For this reason, we perform lithography in a *cleanroom*, with controlled humidity and filtered air to remove the largest particulates [199].

Next, we cover the film with a layer of *resist*, an organic liquid chemical containing long-chain polymers mixed with a photosensitizer. This is *spin coated* onto the sample to ensure homogenous coverage with uniform thickness [200]. Before coating, we heat the sample above 100 °C to evaporate any adsorbed water. In addition, the resist may also need to be *prebaked* after coating, to evaporate excess solvents in the resist [201].

The next step is exposure. We expose the resist-coated sample to *near-UV light by rastering a laser across its surface*, in a path that maps out our desired device layout. Near-UV light is chosen because of its high photon energies, $E \approx 3.3\,\mathrm{eV}$, which corresponds to a wavelength (λ) of,

$$\lambda = \frac{hc}{E} = \frac{6.626 \times 10^{-34} \times 2.997 \times 10^{8}}{3.3 \times 1.602 \times 10^{-19}} \approx 375 \times 10^{-9}\,\mathrm{m} \qquad (68)$$

where h is Planck's constant and c is the speed of light [202].

For this reason, the use of near-UV light offers two advantages. The smallest structure that can be written is considered to be approximately 2.5 times the diffraction limit given by the Rayleigh criterion (Equation 53) [203]. Assuming a (practically achievable) lens semi angle of $\beta = 0.61$ [203], and a UV laser wavelength of 375 nm [204], this gives a resolution of ≈ 1 µm. Current optical lithography apparatus, with optimized resist parameters and instrument optics, can write structures with a resolution of ≈ 500 nm [204].

The second reason is that these photons are energetic enough to trigger photochemical reactions within the resist. Two types of resist are available. In *positive resists*, the long chain polymers are mixed with an inhibitor, which reinforces the polymers against break down by an alkaline developer [200]. UV photos destroy this inhibitor. Therefore, regions of exposed resist become susceptible to dissolution in the developer [205].

In *negative resists*, the photosensitizer encourages the formation of cross-links between polymer strands when it is excited by UV light [207]. Therefore the negative resist gains mechanical stability where it is exposed [207]. Thus, we form a lithographic pattern with one of two polarities: where the exposed resist is weakened (positive resist) or where the exposed resist is strengthened (negative resist).

The *dose* (amount of radiation per unit area) for a given exposure time must be controlled (alternatively, if the dose of the UV source is fixed, *exposure time* must be tuned) [208]. This depends on reflectivity of the sample (as light back-reflection can set up standing waves in the resist) and resist thickness [205].

We must tune dose to match *resist thickness*, which we, in turn, choose for optimized pattern writing. Thinner resists allow for the definition of smaller structures with sharper edges. However, the resist must be thick enough to

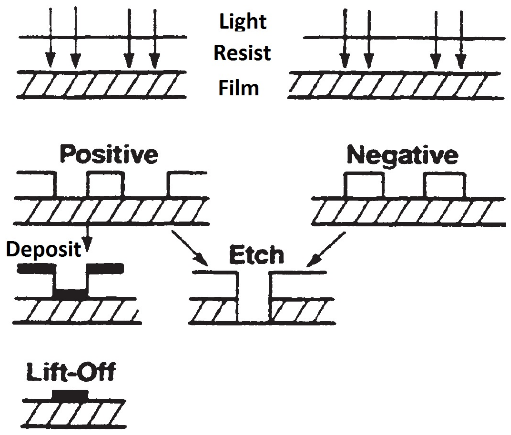

Figure 42: Illustrations showing different steps in the lithography process ranging from exposure (upper), corresponding development of positive and negative resists (middle), and bottom-up versus top-down fabrication procedures (lower). Positive resists typically acquire an 'overcut' sidewall profile during development, whilst negative resists develop with an 'undercut'. This makes negative resists preferable for sensitive lift-off processes, because deposited material does not coat the resist sidewalls. Adapted from [206].

coat the sample uniformly and to protect the film during etching (as a rule of thumb, resist thickness should be several times film thickness) [199].

For a chosen resist thickness, if the dose is too small, the pattern will be *underexposed* (for negative resist) or resist will not be removed after development (for positive resist). If the dose is too high, structures will be *overexposed* with poorly defined edges that are larger (for negative resist) or smaller (for positive resist) than nominal size [208].

During the development step, we aim to strike a balance between this dose used and the development time. The exposed thin film is put into a second chemical for a pre-determined period, during which this *developer* reacts with the resist. For positive resist, the exposed resist will dissolve in the developer faster than the unexposed resist [209]. For negative resist, the exposed area is insoluble in the developer. We calibrate the time of development to ensure that structures are not swollen, whilst maintaining all desired unexposed resist (for positive resist). Negative resist is less sensitive; it can be overdeveloped to remove all unexposed resist whilst retaining sharp cross-linked structures [209].

Sometimes it is necessary to bake the resist a second time, either before or after development. This is known as the *postbake.* Pre-development postbake improves the sharpness of edges in the exposed resist. Post-development postbake further stabilizes the resist before etching [210].

We are now left with our thin film covered in a layer of resist that is hardened in some areas and removed in others. For a *top-down* lithography approach, the resist should be hard over the structures we want to define. Hence, we can use a negative resist and expose only those regions of the film to retain, or use a positive resist and expose the regions to be etched.

For a *bottom-up* lithography approach (where a pattern is first defined, then a film deposited, and the excess material removed by a *lift-off* technique), the reverse procedure is used [211]. For clean lift-off, this resist should be twice as thick as the layer to be deposited [211]. In this case, we expose areas where we want deposited material to remain, which are dissolved during development, with the remaining unexposed positive resist subsequently lifted-off. Fig. 42 summarizes the different lithography approaches with positive and negative resists [206].

Etching is the next stage in a top-down fabrication process [212]. It involves removing pre-existing thin film material from the sample, around the regions where hard resist covers the shape of the device we wish to define. Alternatively, for a bottom-up process, etching may also be used to clean the sample surface or remove a capping layer before material is deposited.

In this thesis, we used etching to define Hall bar structures into Mn_3X films using *ion milling*. The process is very similar to the sputtering explained in Section 1.3.1. Ar ions are used for the milling, because they are inert (will not react with the sample), and heavy but with small atomic radius (therefore transferring significant momentum to the unprotected thin film atoms).

In the case of etching, we bias the sample as the cathode and an Ar-ion plasma forms around the thin film to sputter it away. This is a harsh environment to which to expose our epitaxially-grown film and, even when protected by resist, can lead to sample damage.

An alternative approach is to use ion *beam* milling. Here, we generate the Ar plasma at a separate cathode, then use a potential difference to accelerate the Ar ions in a beam towards the sample. This results in a more controllable etching process, where we can vary both the energy of the plasma and the accelerating voltage. Fig. 43 shows a schematic of an Ar ion beam milling process [212].

Finally, we must clean away the remaining hardened resist [213]. *Solvents* (such as acetone) can remove positive resist, especially if warmed and gently agitated to encourage dissolution of the resist. Negative, cross-linked resist, requires specific *stripping chemicals* (bases or halogenated solvents). Often even these can leave a 1 nm layer of resist [213]. ‘Ashing’ (oxidizing the remaining resist using an oxygen plasma or ozone atmosphere) can remove this. A few seconds of ashing is sufficient to remove the remaining resist, and this process should not damage well-capped films. After a final rinsing step in solvents, the fabricated devices are ready for measurement.

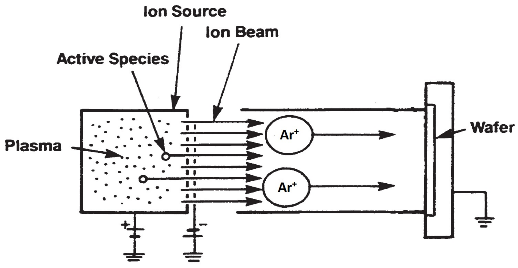

Figure 43: Schematic showing etching using an ion beam milling procedure. A plasma of the active species, in this case Ar, is generated at the ion source (left) and accelerated in an ion beam towards the sample wafer (right). Adapted from [212].

Here we have described a process of optical lithography using a laser writer apparatus [204]. This can define structures down to scale of $\approx 0.5\,\mu$m. It is also possible to perform optical lithography using a *hard mask*, made of chrome with pre-defined structures etched into it. We align this mask over the sample, shine UV light through the mask from behind, and thus expose the resist on the sample [208].

Alternatively, when smaller devices are required, we can use *electron beam lithography*. The process is similar to that of the laser writer, but using accelerated electrons from a modified scanning electron microscope to expose the resist [205]. The small wavelength of such electrons (see Section 1.3.6) makes writing of nanometer-sized structures possible.

Furthermore, a number of other etching processes are available, for example *wet-chemical* or *reactive-gas etching*, for diverse applications [212].

The advantage of using advanced lithography and etching techniques in the fabrication of commercial semiconductor based electronics is clear; the smaller the transistors and other components, the more can be packed into a single integrated circuit and the more powerful the resulting computer. However, why is such effort to prepare devices beneficial to fundamental solid-state physics research? Some reasons include:

- **Formation of novel magnetic structures**. By confining the size and shape of certain magnetic materials, anisotropies can be modified in such a way as to stabilize interesting magnetic structures, such as vortex cores [46].
- **Studying magnetization dynamics**. Similarly, by confining magnetic materials to similar dimensions as the wavelength of spin waves (which can be of the order 100s nm), we can investigate magnetization dynamics microscopically, for example by setting up standing spin waves [214].

- **Fabricating superlattices or heterostructures**. These can form quantum wells or other structures demonstrating new physics (such as topological insulator states) or giving new device functionality (such as resonant tunneling diodes that are useful in GHz-frequency microwave electronics) [203].
- **Manipulating high-frequency radiation**. Higher energy electromagnetic radiation than such microwaves has wavelengths comparable to the device length scales that require lithographic fabrication [203]. In photonic devices that manipulate visible light, submicrometer structures are required. Meanwhile manipulation of THz radiation, which may find a key role in next generation telecommunications technology, requires structures of dimensions matching its 10 to 100 µm wavelength. Devices fabricated by optical lithography are ideal for this task.
- **Entering ballistic transport regime**. When device size is reduced to such an extent that it becomes comparable with the mean free path of electrons (50 to 100 nm in certain semiconductors), electrons begin to flow without elastic scattering [203]. Under these conditions, electron wavefunctions maintain their phase coherence during conduction, leading to the emergence of quantum mechanical wave effects.
- **Exploring quantum transport phenomena**. In this regime where electron wavefunctions maintain their phase coherence, or where their Bloch wavelength is comparable to the size of devices (typically on the nanometer scale), then novel transport phenomena governed by quantum mechanics are observed [203]. Such effects must be measured at extremely low temperatures, to minimize electron perturbations (achieved with a cryostat, see Section 1.3.10).
- **Demonstrating applicability of technological applications**. Some physical effects, such as GMR, can be observed in unpatterned thin films. However, since technological applications will require their miniaturization, it is pertinent to investigate the fundamental behavior of these phenomena at restricted dimensions [215].
- **Ensuring homogeneous material properties**. We find that epitaxially-grown thin films can have grain sizes up to 100s nm (see, for example, Section 3.2). Thus, by fabricating devices on a micro- or even nanometer scale, we minimize the number of individual grains within the measurement region and so ensure a more homogenous spread of crystallographic properties.
- **Defining current paths through a device**. We often wish to control the direction of current flow through a thin film, with respect to an external magnetic field or along a particular crystal axis. Current will

spread diffusively between source and drain, so patterning devices with long, narrow channels between the two electrodes ensures that current flows in the desired direction. Alternatively, for example with MTJs, the TMR effect requires current flow in a direction perpendicular to the thin film plane [216]. This necessitates the definition of pillar-like structures with contact electrodes at the top and bottom, which can only be achieved using lithography.

- **Achieving high current densities**. Often the current a particular source can generate is limited (i.e. it has a certain compliance voltage it can apply across a load device), or there is a maximum voltage drop that can be tolerated by a whole device without damaging it (due to Joule heating caused by excess current flow). Nevertheless, to observe certain physical phenomena of interest to spintronics, for example current-driven domain wall motion [33], or spin-orbit torque switching of magnetization [28], high current densities ($1 \times 10^7\,\mathrm{A\,cm^{-2}}$) are required. Therefore, to achieve this requires the reduction of device dimensions: (a) to reduce the channel width so that current density is larger and (b) to reduce the absolute distance across the device to limit total potential difference across it.
- **Control magnetotransport measurement geometry**. The main motivation for fabricating devices of the Mn_3X films measured in this thesis (see Sections 2.2 and 3.2), is to ensure a controlled geometry for voltage measurements (see Section 1.2.8). For example, if we wish to calculate thin film resistivity, we must accurately know the spacing of the two longitudinal voltage contacts. Alternatively, if we wish to measure Hall effect, the two transverse voltage contacts must be well aligned to avoid mixing components of MR with the Hall signal.

For these reasons, in the results chapters of this thesis, we describe how Hall-bar structures were fabricated from noncollinear AF films using a combination of optical and electron beam lithography, and Ar ion beam milling.

1.3.10 Electrical transport measurements and cryostats

In Section 1.2.8, we explained why the electrical transport in a material was key to determining its usefulness for spintronic applications, and how studies of MR and Hall effect could reveal the fundamental physical processes governing transport properties. Now, we progress to discuss the apparatus that enable us to make such measurements as a function of temperature and magnetic field.

Such magnetotransport can be measured in bulk single crystals, unpatterned thin films or lithographically fabricated devices. We discuss the advantages of measuring structures patterned from thin films in Section 1.3.9. Therefore, we focus on these here.

To investigate the magnetotransport properties of the material, we must simultaneously apply an external magnetic field to our device. Often a strong magnetic field is required, as is the case for AFs with large internal anisotropies. A superconducting magnet can provide this.

The magnetic field, $\mu_0 H$, generated inside a solenoid with N coils of wire over a length M is given by Ampere's law as,

$$\mu_0 H = \frac{NI}{M\epsilon_0 c^2} \tag{69}$$

where ϵ_0 is the permeability of free space, c is the speed of light and I is the current [217]. Thus, if we take a tight coil of superconducting wire, which can carry an extremely large current, then we can generate a very strong magnetic field.

In addition, by varying the current through the coil, we can sweep magnetic field. However, this is only achievable if the superconducting coil is below its critical temperature. To do this we must cool it to cryogenic temperatures. For this reason, **superconducting magnets** are often found in a cryostat [219].

A **cryostat** is an apparatus that can vary temperature and hold a stable temperature, in order to measure a sample's properties as a function of temperature. In our case, it uses liquid He to cool samples down to low temperatures ($300\,\mathrm{K} > T > 2\,\mathrm{K}$).

Fig. 44 shows how a gas-flow cryostat functions [218]. A storage dewar holds liquid He at approx 4 K, supplied by either transferring liquid He from an external source, or by a cryopump compressor [219]. The thin-film-under-test sits inside the sample chamber. The top of the sample chamber is pumped to a low pressure [219]. This creates a pressure gradient with the connected dewar. The *lower pressure decreases the boiling point of liquid He* in the dewar to approx 2 K, causing it to begin evaporating [219]. This 2 K He gas is then drawn along the pressure gradient to the cooling annulus, and flows around the sample chamber, absorbing heat from it [219]. The He gas is then recirculated, either in a closed-cycle inside the cryostat, or through an external helium recovery system [218].

To maintain low temperatures inside the cryostat, a series of vacuum and reflective radiation shields surround the dewar and sample chamber. In addition, lower cost, but higher temperature (boiling point = 77 K), liquid nitrogen may be used as a thermal shield or to precool the cryostat interior [219].

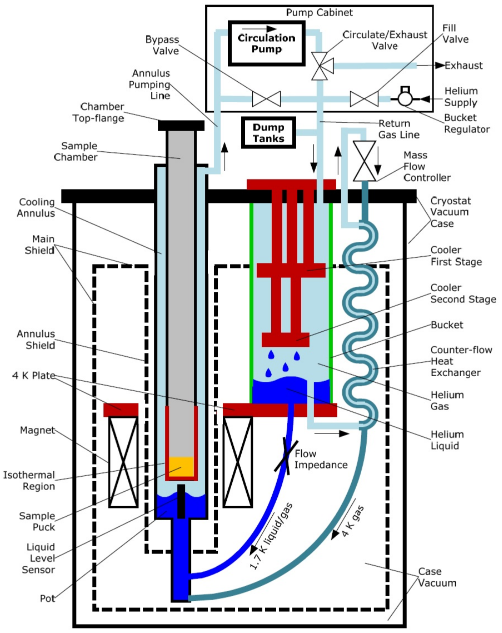

Figure 44: A schematic diagram of the cooling system in a Quantum Design Dynacool PPMS, of the type utilized for this thesis. This is representative of other gas-flow cryostats. The various components of the cooling system are labeled, as explained in the main text. The 'cooler first and second stage' are brought to low temperature (45 and 4 K respectively) using a pulse-tube compressor (not shown). He gas flowing over sample (located in the space colored yellow) is recirculated over the cooler stages and condenses back into the 'bucket'. The superconducting magnet (made of NbTi alloy) is in thermal contact with the '4 K plate' at the bottom of this bucket, cooling it to below its critical temperature ($\approx$ 10 K). The two gas-flow paths, labelled '4 K gas' or '1.7 K liquid/gas' are used to provide cooling power above and below 10 K, respectively [218].

The 2 K He gas may either flow directly over the film-under-test, or through an annulus surrounding it (in turn cooling He transfer gas inside the sample chamber) [218]. In both cases, we must ensure an isothermal region around the film-under-test. We can achieve this using a *sample platform made of Cu*, whose high thermal conductivity and small heat capacity at low temperatures mean the 2 K gas can quickly remove latent heat [220]. Fig. 45 shows a typical design of such a sample platform [220].

A thin film in good thermal contact with the sample platform will thermalize with the Cu and, hence, surrounding 2 K He gas. The actual temperature of the sample holder is monitored by an attached thermometer [221]. The film-under-test's temperature can be varied above the cryostat base temperature by warming the platform using a resistive heater [221]. For efficient

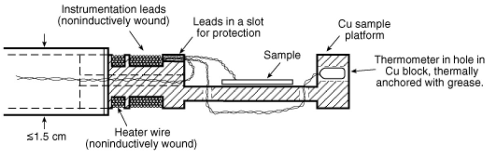

Figure 45: An example design for a typical sample stage, consisting of a Cu sample platform that is inserted into the cryostat. The sample is mounted in the middle of the platform, possibly on a chip carrier package (as explained in Fig. 46). A thermometer is secured in a hole in the Cu platform (using, for example, grease or varnish) for good thermalization. A resistive heater at the top of the platform helps regulate temperature (the leads providing high current to drive the heater are fed-through separately from the instrumentation wires). The twisted pair wires providing current to, and measuring voltage from, the device-under-test are wound around the top of the platform (and secured with varnish or tape). This ensures good thermal contact (but electrical isolation) between the wires and the sample holder (preventing the wires from conducting heat from outside to the sample). A loop is first formed in the wire, and the entire loop wound, to ensure any magnetic fields induced by currents in the wire cancel one another [220].

warming, a needle valve located between the cooling annulus and dewar can close, to limit the flow of cold He gas [221]. A proportional-integral-derivative controller can automatically *vary the combination of needle valve opening and heater power* to cool and warm the film-under test smoothly or to maintain a set-point temperature (in a feedback loop with the thermometer) [221].

The liquid He in the dewar can simultaneously cool a superconducting magnet. This gives us an instrument where we can measure the electrical transport properties of materials as a function of both temperature and magnetic field, allowing us to study both their fundamental physical properties and evaluate their suitability for spintronic applications. Having explained how we create a stable environment inside the cryostat, how do we perform magnetotransport measurements themselves?

The first step is to make electrical contacts to our lithographically-patterned thin-film chip. We can do this efficiently using a *centimeter-sized circuit board package*, onto which we mount our fabricated chip. Fig. 46 shows a diagram of such a chip carrier package [121].

The circuit board contains a number of conducting paths, at one end of which is a bonding pad [121]. In this work, electrical connections were made from the chip carrier bonding pads to the fabricated device using **wire bonding**. This wedge bonding technique is detailed in Fig. 47 [121].

We then secure the chip carrier package to the sample platform for insertion into the cryostat. The opposite ends of the conducting paths on the circuit board plug into terminals, which connect to the instrumentation wires

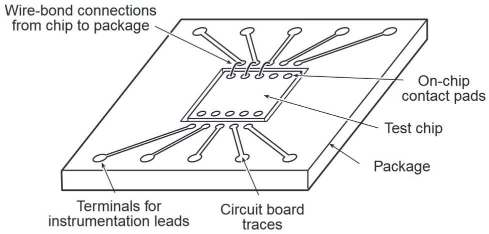

Figure 46: Illustration of a chip carrier (package) to facilitate mounting of a patterned thin film (test chip) in a cryostat. Lithographically-fabricated on-chip contact pads are wire bonded to the bond pads at the end of the circuit board traces (as described in Fig. 47). These are, in turn, connected to terminals that plug into the instrumentation wires that source current and sense voltage across the device-under-test. The chip carrier can be removed from the sample platform for bonding, then reattached with good thermal contact. The chip carrier can also serve to reduce any (potentially damaging) difference in thermal expansion/contraction between the film substrate and the sample platform on heating/cooling. However, the sample and chip carrier must be in good thermal contact (whilst maintaining electrical isolation) to ensure the thin film thermalizes with the sample platform, for example by mounting with a layer of silver paint or varnish [121].

that source current to, and measure voltage across, the chip-under-test.

These wires are made of Cu, typically around 0.127 µm in diameter (American Wire Gauge 36) and electrically insulated with a coating of, for example, polyvinyl formal or (preferably) polyimide [220]. For a good signal to noise ratio, a **twisted pair** configuration is used; two coupled instrumentation wires (for example current-source and current-drain or voltage-high and voltage-low) are wound together over about 1000 turns per meter [220].

Whilst the metal shield of the cryostat is effective in blocking external electric signals, the wires might still be susceptible to spurious induced currents when sweeping the measurement magnetic field [220]. As a solution, the twisted pair of wires allows us to make a differential signal measurement. At the voltmeter, only the difference between the two wires is measured. Any signal present in both wires (a common mode) is rejected.

Because pairs are twisted, on average they are equidistant from the magnetic field. This means that equal current will be induced in both, a common mode that the differential amplifier in the voltmeter will reject [220]. Furthermore, any magnetic fields generated by current flowing within the source and drain wires will cancel-out due to pair twisting, and so not interfere with the signal in other wires in the circuit [220].

There will be a certain resistance associated with these Cu wires. In addition, the contacts to the device will have a characteristic resistivity, ρ_{contact}, limited at the point where the contact interfaces the thin film. In

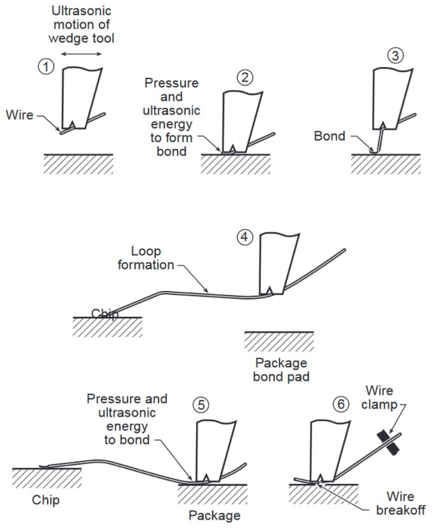

Figure 47: Storyboard showing each step in the wedge bonding process from a patterned sample (chip) to a chip-carrier-type sample holder (package). (1) The wire-threaded wedge tool is positioned above the chip area to be contacted. (2) The wedge tool is lowered onto the surface, with a calibrated force controlled by the instrument, and an ultrasonic pulse applied (providing energy to form a bond between wire and contact pad). (3) The tool is retracted from the new bond, feeding out the wire loop. The loops should be as short as possible and coplanar to any applied magnetic field direction, in order to minimize induced currents. (4) The tool is moved backwards to position it over the bond pad of the chip-carrier package (as illustrated in Fig. 46). (5) The tool is lowered to the pad, as in step (2), to make a second bond. (6) Wire clamp closes on the wire, such that it breaks after the second bond and forms a loop contacting the chip to the bond pad [121].

the devices measured in this study, contact pads were made using bottom-up lithography and lift-off: patterning a resist mask, etching the thin film's capping layer (both detailed in Section 1.3.9) then depositing 5 nm Ru / 60 nm Au contact pads using sputtering (see Section 1.3.1). We then made wire bonds to these pads. Such lithographically fabricated contacts can have $\rho_{\text{contact}} \approx 1 \times 10^{-8}\,\Omega\,\text{cm}^2$ [222]. The resistance associated with such a contact is given by $R_{\text{contact}} = \rho_{\text{contact}}/A_{\text{contact}}$ (where A_{contact} is the area of the contact pad) [222]. For a $150\,\mu\text{m}^2$ contact pad, this yields $R_{\text{contact}} = 1 \times 10^{-8}\,\Omega\,\text{cm}^2/(0.0150\,\text{cm})^2 \approx 0.04\,\text{m}\Omega$.

Although the resistances associated with these contact pads and the instrumentation wires are very small, the voltage drop across them will nevertheless introduce inaccuracies into any measurement of the potential difference across a device we wish to test [121]. This inaccuracy can be avoided using a *four-point resistance measurement geometry*, explained in Section 1.2.8.

1.4 Objectives of thesis

In the preceding introduction, we have discussed the disadvantages of FM spintronics (Section 1.2.2) and the potential advantages offered by AF spintronics (Section 1.2.3), specifically by the topological noncollinear AFs (Section 1.2.4).The main goals of this thesis are, therefore, to explore the preparation of noncollinear AFs, Mn_3X, in thin film form, and their perspectives for incorporation into topological spintronic applications. Use of these Mn_3X AFs in devices requires their growth in thin film form. Furthermore, since their topologically driven phenomena are expected to be sensitive to crystal structure, we require high-quality thin films of these chiral materials.

The first objective of this thesis is, therefore, **to deposit thin films of noncollinear AF materials, and to use various characterization techniques in order to analyze their crystal structure**. Specifically, we aimed for:

- Epitaxial growth with sharp OP orientation and well-defined IP crystallographic axes
- Low defect density layers with large grain size and small mosaicity
- Chemical homogeneity with uniform thickness and a smooth surface suitable for integration into heterostructures

We evaluate progress towards these targets using a combination of XRD, XRR, AFM and TEM, amongst other structural characterization methods, as well as measurements of the Mn_3X films' exchange bias properties in bilayers with a FM material.

In this thesis, we choose to focus on two noncollinear AFs, Mn_3Ir and Mn_3Sn. These were chosen because they show a similar noncollinear AF order and predicted Berry curvature generated magnetotransport properties that result, whilst at the same time possessing contrasting crystal and magnetic structures (as discussed earlier in the introduction in Sections 1.2.6, 1.2.7 and 1.2.9). We present results of the thin film deposition of both materials in Sections 2.1 and 3.1 respectively. Since this is a *cumulative thesis*, these findings take the form of a scientific paper (see structure of thesis in Section 1.5). We assess each scientific paper's contribution towards meeting the objectives of this thesis in a discussion at the beginning of each results chapter.

In a similar way, we report the findings in support of the second major target of this thesis in Section 2.2 and 3.2, for Mn_3Ir and Mn_3Sn respectively. This second objective was **to measure the magnetic and electrical transport properties of each set of thin films, to discuss the physical origins of the observed phenomena, and to evaluate their suitability for application in AF spintronics**.

Having carefully prepared and characterized thin film samples of both Mn_3Ir and Mn_3Sn, we measure their magnetic behavior (using SQUID-VSM and XMCD) and magnetotransport proprieties (as a function of applied magnetic field, temperature and, importantly, film thickness). We then aim to clarify the reasons for the different phenomena observed, in particular:

- Using the careful characterization of the thin films' microstructure to draw conclusions about its effect on both magnetization and electrical transport
- Explain the magnetic properties of the two different types of (inverse) triangular spin texture in the context of chiral domains
- Untangle the interplay between magnetism (such as the presence of uncompensated moments) and magnetotransport (and how it differs between Mn_3Ir and Mn_3Sn)
- Discover, ultimately, Berry curvature driven electrical transport properties (for example, AHE) generated by the topology of the chiral spin textures

In this thesis, we present results elucidating progress towards these goals.

The thesis concludes by discussing the perspectives and outlook for such noncollinear AFs in *chiralitronics.*

1.5 Structure of thesis

We have already presented an introduction (Section 1) to this thesis, beginning with its conceptual foundations (Section 1.2) and a summary of the experimental methods utilized (Section 1.3), before moving on to discuss the objectives of the thesis (Section 1.4). These objectives will now be addressed in the following results chapters. However, we firstly close the introduction with an overview of the thesis structure. Being a *cumulative thesis*, each results chapter takes the form of a **peer-reviewed scientific paper**, published in a leading physics journal.

The results chapters are divided into two halves, labeled Part A and B respectively. Each Part deals with a different noncollinear antiferromagnet: Part A with the cubic Mn_3Ir (possessing triangular spin texture) and Part B with the hexagonal Mn_3Sn (possessing inverse triangular spin texture). Each Part is further divided into two Sections. The first Section in each Part reports the growth and characterization of epitaxial thin films of the two material systems: Mn_3Ir in Section 2.1 and Mn_3Sn in Section 3.1. The second Section in each Part reports the magnetic and electrical transport properties of the two material systems: Mn_3Ir in Section 2.2 and Mn_3Sn in Section 3.2.

Within each Section, the scientific paper comprising the majority of that chapter is proceeded by a brief discussion (including the bibliographic data for the publication in question). This discussion reviews the main results of each paper, connects these findings with the key themes running through the thesis overall and, in turn, fits the outcomes into the wider context of the role of noncollinear antiferromagnets in topological spintronics. These main themes and the broad picture are then drawn together in the conclusion that closes this thesis. Outlooks and perspectives for the field of topological antiferromagnetic spintronics, as well as the specific role of Mn_3X chiral materials within this, are also presented in the conclusion.

We note that the lists of figures and abbreviations at the beginning of this thesis correspond to the introduction. Each scientific paper (forming the results chapters) naturally comprises its own figure numbering and abbreviation system, as well as a self-contained set of citations. Therefore, the set of references cited in the introduction (which do not correspond to those used in each scientific paper) are contained within their own bibliography, presented directly below. Selected key references from this overall bibliography are further cited in the discussion sections proceeding each results chapter.

Let us now proceed to the results chapters of this thesis, along with the discussions as to how these fulfill the objectives of the thesis.

References

[1] C. Chappert, A. Fert, and F. N. V. Dau, “The emergence of spin electronics in data storage”, *Nat. Mater.* **6**, 813 (2007).

[2] S. Fukami, C. Zhang, S. DuttaGupta, A. Kurenkov, and H. Ohno, “Magnetization switching by spin-orbit torque in an antiferromagnet-ferromagnet bilayer system”, *Nat. Mater.* **15**, 535 (2016).

[3] E. Raymenants, A. Vaysset, D. Wan, M. Manfrini, O. Zografos, O. Bultynck, J. Doevenspeck, M. Heyns, I. P. Radu, and T. Devolder, “Chain of magnetic tunnel junctions as a spintronic memristor”, *J. Appl. Phys.* **124**, 152116 (2018).

[4] K. Olejnik et al., “Antiferromagnetic CuMnAs multi-level memory cell with microelectronic compatibility”, *Nat. Commun.* **8**, 15434 (2017).

[5] S. S. P. Parkin, J. Xin, C. Kaiser, A. Panchula, K. Roche, and M. Samant, “Magnetically engineered spintronic sensors and memory”, *Proc. IEEE* **91**, 661 (2003).

[6] S. S. P. Parkin, “Origin of enhanced magnetoresistance of magnetic multilayers: Spin-dependent scattering from magnetic interface states”, *Phys. Rev. Lett.* **71**, 1641 (1993).

[7] M. N. Baibich, J. M. Broto, A. Fert, F. Nguyen Van Dau, F. Petroff, P. Etienne, G. Creuzet, A. Friederich, and J. Chazelas, “Giant magnetoresistance of (001)Fe/(001)Cr magnetic superlattices”, *Phys. Rev. Lett.* **61**, 2472 (1988).

[8] G. Binasch, P. Grunberg, F. Saurenbach, and W. Zinn, “Enhanced magnetoresistance in layered magnetic structures with antiferromagnetic interlayer exchange”, *Phys. Rev. B* **39**, 4828 (1989).

[9] S. S. P. Parkin, N. More, and K. P. Roche, “Oscillations in exchange coupling and magnetoresistance in metallic superlattice structures: Co/Ru, Co/Cr, and Fe/Cr”, *Phys. Rev. Lett.* **64**, 2304 (1990).

[10] R. A. Duine, K. J. Lee, S. S. P. Parkin, and M. D. Stiles, “Synthetic Antiferromagnetic Spintronics”, *Nat. Phys.* **14**, 217 (2018).

[11] S. S. P. Parkin, R. Bhadra, and K. P. Roche, “Oscillatory magnetic exchange coupling through thin copper layers”, *Phys. Rev. Lett.* **66**, 2152 (1991).

[12] B. Dieny, V. S. Speriosu, S. S. P. Parkin, B. A. Gurney, D. R. Wilhoit, and D. Mauri, “Giant magnetoresistance in soft ferromagnetic multilayers”, *Phys. Rev. B* **43**, 1297(R) (1991).

[13] S. S. P. Parkin et al., “Exchange-biased magnetic tunnel junctions and application to nonvolatile magnetic random access memory”, *J. Appl. Phys.* **85**, 5828 (1999).

[14] F. Oyster, “Diagram of the tunnel current for TMR (reused under the term of the Creative Commons Attribution-Share Alike 4.0 International license)”, Wikimedia Commons (2014).

[15] M. Julliere, “Tunneling Between Ferromagnetic Films”, *Phys. Lett. A* **54**, 225 (1975).

[16] T. M. Tezuka and N., “Giant magnetic tunneling effect in Fe/Al_2O_3/Fe junction”, *J. Mag. Mag. Mater.* **139**, L231 (1995).

[17] J. S. Moodera, L. R. Kinder, T. M. Wong, and R. Meservey, “Large magnetoresistance at room temperature in ferromagnetic thin film tunnel junctions”, *Phys. Rev. Lett.* **74**, 3273 (1995).

[18] S. Yuasa, T. Nagahama, A. Fukushima, Y. Suzuki, and K. Ando, “Giant room-temperature magnetoresistance in single-crystal Fe/MgO/Fe magnetic tunnel junctions”, *Nat. Mater.* **3**, 868 (2004).

[19] S. S. P. Parkin, C. Kaiser, A. Panchula, P. M. Rice, B. Hughes, M. Samant, and S. H. Yang, “Giant tunnelling magnetoresistance at room temperature with MgO (100) tunnel barriers”, *Nat. Mater.* **3**, 862 (2004).

[20] J. M. Taylor, “Interface Magnetism in Crystalline Magnetic Tunnel Junctions”, MA thesis (Durham University, Durham, UK, 2013).

[21] W. H. Butler, X. G. Zhang, T. C. Schulthess, and J. M. MacLaren, “Spin-dependent tunneling conductance of Fe/MgO/Fe sandwiches”, *Phys. Rev. B* **63**, 054416 (2001).

[22] J. Mathon and A. Umerski, “Theory of tunneling magnetoresistance of an epitaxial Fe/MgO/Fe(001) junction”, *Phys. Rev. B* **63**, 220403(R) (2001).

[23] L. Liu, C. F. Pai, Y. Li, H. W. Tseng, D. C. Ralph, and R. A. Buhrman, “Spin-torque switching with the giant spin Hall effect of tantalum”, *Science* **336**, 555 (2012).

[24] S. Bhatti, R. Sbiaa, A. Hirohata, H. Ohno, S. Fukami, and S. N. Piramanayagam, “Spintronics based random access memory: a review”, *Mater. Today* **20**, 530 (2017).

[25] J. C. Slonczewski, "Current-driven excitation of magnetic multilayers", *J. Mag. Mag. Mater.* **159**, L1 (1996).

[26] L. Berger, "Emission of spin waves by a magnetic multilayer traversed by a current", *Phys. Rev. B* **54**, 9353 (1996).

[27] D. C. Ralph and M. D. Stiles, "Spin transfer torques", *J. Mag. Mag. Mater.* **320**, 1190 (2008).

[28] I. M. Miron, K. Garello, G. Gaudin, P. J. Zermatten, M. V. Costache, S. Auffret, S. Bandiera, B. Rodmacq, A. Schuhl, and P. Gambardella, "Perpendicular switching of a single ferromagnetic layer induced by in-plane current injection", *Nature* **476**, 189 (2011).

[29] K. Garello, I. M. Miron, C. O. Avci, F. Freimuth, Y. Mokrousov, S. Blugel, S. Auffret, O. Boulle, G. Gaudin, and P. Gambardella, "Symmetry and magnitude of spin-orbit torques in ferromagnetic heterostructures", *Nat. Nanotechnol.* **8**, 587 (2013).

[30] J. Sinova, S. O. Valenzuela, J. Wunderlich, C. H. Back, and T. Jungwirth, "Spin Hall effects", *Rev. Mod. Phys.* **87**, 1213 (2015).

[31] K. U. Demasius, T. Phung, W. Zhang, B. P. Hughes, S. H. Yang, A. Kellock, W. Han, A. Pushp, and S. S. P. Parkin, "Enhanced spin-orbit torques by oxygen incorporation in tungsten films", *Nat. Commun.* **7**, 10644 (2016).

[32] K. S. Ryu, L. Thomas, S. H. Yang, and S. S. P. Parkin, "Chiral spin torque at magnetic domain walls", *Nat. Nanotechnol.* **8**, 527 (2013).

[33] S. H. Yang, K. S. Ryu, and S. S. P. Parkin, "Domain-wall velocities of up to 750 m/s driven by exchange-coupling torque in synthetic antiferromagnets", *Nat. Nanotechnol.* **10**, 221 (2015).

[34] K. Garello et al., "SOT-MRAM 300mm Integration for Low Power and Ultrafast Embedded Memories", in 2018 IEEE Symposium on VLSI Circuits (2018), pp. 81–82.

[35] W. Weber, "Introduction to Magnetism", in *Magnetism and Synchrotron Radiation - New Trends*, edited by E. Beaurepaire, H. Bulou, F. Scheurer, and J.-P. Kappler (Springer, Berlin-Heidelberg, 2010) Chap. 1, pp. 1–40.

[36] R. P. Feynman, "The Magnetism of Matter", in *The Feynman Lectures on Physics*, Vol. 2, edited by R. B. Leighton and M. L. Sands (Addison-Wesley, Reading, MA, 1971) Chap. 34, pp. 34.1–34.11.

[37] C. Kittel, *Introduction to Solid State Physics*, 4th ed. (Wiley, Hoboken, NJ, 1971).

[38] S. Blundell, *Magnetism in Condensed Matter* (Oxford Univeristy Press, Oxford, 2001).

[39] B. H. Bransden and C. J. Joachain, “The interaction of quantum systems with external electric and magnetic fields”, in *Quantum Mechanics*, 2nd ed. (Pearson, London, 2000) Chap. 12, pp. 557–585.

[40] R. P. Feynman, “Ferromagnetism”, in *The Feynman Lectures on Physics*, Vol. 2, edited by R. B. Leighton and M. L. Sands (Addison-Wesley, Reading, MA, 1971) Chap. 36, pp. 36.1–36.11.

[41] B. H. Bransden and C. J. Joachain, “Approximation methods for time-dependent problems”, in *Quantum Mechanics*, 2nd ed. (Pearson, London, 2000) Chap. 9, pp. 431–466.

[42] R. P. Feynman, “Magnetic Materials”, in *The Feynman Lectures on Physics*, Vol. 2, edited by R. B. Leighton and M. L. Sands (Addison-Wesley, Reading, MA, 1971) Chap. 37, pp. 37.1–37.11.

[43] P. Wadley et al., “Electrical switching of an antiferromagnet”, *Science* **351**, 587 (2016).

[44] V. Baltz, A. Manchon, M. Tsoi, T. Moriyama, T. Ono, and Y. Tserkovnyak, “Antiferromagnetic spintronics”, *Rev. Mod. Phys.* **90**, 015005 (2018).

[45] T. Jungwirth, X. Marti, P. Wadley, and J. Wunderlich, “Antiferromagnetic spintronics”, *Nat. Nanotechnol.* **11**, 231 (2016).

[46] H. G. Bauer, M. Sproll, C. H. Back, and G. Woltersdorf, “Vortex core reversal due to spin wave interference”, *Phys. Rev. Lett.* **112**, 077201 (2014).

[47] E. Grimaldi, V. Krizakova, G. Sala, F. Yasin, S. Couet, G. Sankar Kar, K. Garello, and P. Gambardella, “Single-shot dynamics of spin-orbit torque and spin transfer torque switching in three-terminal magnetic tunnel junctions”, *Nat. Nanotechnol.* **15**, 111 (2020).

[48] J. Železný, P. Wadley, K. Olejník, A. Hoffmann, and H. Ohno, “Spin transport and spin torque in antiferromagnetic devices”, *Nat. Phys.* **14**, 220 (2018).

[49] K. Olejník et al., “Terahertz electrical writing speed in an antiferromagnetic memory”, *Sci. Adv.* **4**, eaar3566 (2018).

[50] A. B. Shick, S. Khmelevskyi, O. N. Mryasov, J. Wunderlich, and T. Jungwirth, “Spin-orbit coupling induced anisotropy effects in bimetallic antiferromagnets: A route towards antiferromagnetic spintronics”, *Phys. Rev. Lett.* **81** (2010).

[51] H. Reichlová et al., “Current-induced torques in structures with ultrathin IrMn antiferromagnets”, *Phys. Rev. B* **92**, 165424 (2015).

[52] H. Fujita, “Field-free, spin-current control of magnetization in noncollinear chiral antiferromagnets”, *Phys. Status Solidi RRL* **11**, 1600360 (2017).

[53] D. Kriegner et al., “Multiple-stable anisotropic magnetoresistance memory in antiferromagnetic MnTe”, *Nat. Commun.* **7**, 11623 (2016).

[54] S. Y. Bodnar, L. Šmejkal, I. Turek, T. Jungwirth, O. Gomonay, J. Sinova, A. A. Sapozhnik, H. J. Elmers, M. Kläui, and M. Jourdan, “Writing and reading antiferromagnetic Mn_2Au by Néel spin-orbit torques and large anisotropic magnetoresistance”, *Nat. Commun.* **9**, 348 (2018).

[55] S. D. Ganichev and L. E. Golub, “Interplay of Rashba/Dresselhaus spin splittings probed by photogalvanic spectroscopy - A review”, *Phys. Status Solidi B* **251**, 1801 (2014).

[56] J. Železný, H. Gao, K. Výborný, J. Zemen, J. Mašek, A. Manchon, J. Wunderlich, J. Sinova, and T. Jungwirth, “Relativistic Néel-order fields induced by electrical current in antiferromagnets”, *Phys. Rev. Lett.* **113**, 157201 (2014).

[57] P. Wadley et al., “Current polarity-dependent manipulation of antiferromagnetic domains”, *Nat. Nanotechnol.* **13**, 362 (2018).

[58] L. Šmejkal, Y. Mokrousov, B. Yan, and A. H. MacDonald, “Topological antiferromagnetic spintronics”, *Nat. Phys.* **14**, 242 (2018).

[59] S. Singh et al., “Room-temperature tetragonal non-collinear Heusler antiferromagnet Pt_2MnGa”, *Nat. Commun.* **7**, 12671 (2016).

[60] A. K. Nayak, V. Kumar, T. Ma, P. Werner, E. Pippel, R. Sahoo, F. Damay, U. K. Rossler, C. Felser, and S. S. P. Parkin, “Magnetic antiskyrmions above room temperature in tetragonal Heusler materials”, *Nature* **548**, 561 (2017).

[61] I. Tomeno, H. N. Fuke, H. Iwasaki, M. Sahashi, and Y. Tsunoda, “Magnetic neutron scattering study of ordered Mn_3Ir”, *J . Appl. Phys.* **86**, 3853 (1999).

[62] P. J. Brown, V. Nunez, F. Tasset, J. B. Forsyth, and P. Radhakrishna, “Determination of the magnetic structure of Mn_3Sn using generalized neutron polarization analysis”, *J. Phys.: Condens. Matter* **2**, 9409 (1990).

[63] A. Fert, V. Cros, and J. Sampaio, "Skyrmions on the track", *Nat. Nanotechnol.* **8**, 152 (2013).

[64] L. M. Sandratskii and J. Kübler, "Role of Orbital Polarization in Weak Ferromagnetism", *Phys. Rev. Lett.* **76**, 4963 (1996).

[65] L. Szunyogh, B. Lazarovits, L. Udvardi, J. Jackson, and U. Nowak, "Giant magnetic anisotropy of the bulk antiferromagnets IrMn and $\mathrm{IrMn_3}$ from first principles", *Phys. Rev. B* **79**, 020403 (2009).

[66] P. Park et al., "Magnetic excitations in non-collinear antiferromagnetic Weyl semimetal $\mathrm{Mn_3Sn}$", *npj Quantum Mater.* **3**, 63 (2018).

[67] H. Chen, Q. Niu, and A. H. MacDonald, "Anomalous Hall effect arising from noncollinear antiferromagnetism", *Phys. Rev. Lett.* **112**, 017205 (2014).

[68] J. Kübler and C. Felser, "Non-collinear antiferromagnets and the anomalous Hall effect", *Europhys. Lett.* **108**, 67001 (2014).

[69] H. Yang, Y. Sun, Y. Zhang, W.-J. Shi, S. S. P. Parkin, and B. Yan, "Topological Weyl semimetals in the chiral antiferromagnetic materials $\mathrm{Mn_3Ge}$ and $\mathrm{Mn_3Sn}$", *New J. Phys.* **19**, 015008 (2017).

[70] J. Kübler and C. Felser, "Weyl fermions in antiferromagnetic $\mathrm{Mn_3Sn}$ and $\mathrm{Mn_3Ge}$", *Europhys. Lett.* **120**, 47002 (2017).

[71] C. Shekhar et al., "Extremely large magnetoresistance and ultrahigh mobility in the topological Weyl semimetal candidate NbP", *Nat. Phys.* **11**, 645 (2015).

[72] K. Kuroda et al., "Evidence for magnetic Weyl fermions in a correlated metal", *Nat. Mater.* **16**, 1090 (2017).

[73] Y. Zhang, Y. Sun, H. Yang, J. Železný, S. S. P. Parkin, C. Felser, and B. Yan, "Strong anisotropic anomalous Hall effect and spin Hall effect in the chiral antiferromagnetic compounds $\mathrm{Mn_3}X$ (X = Ge, Sn, Ga, Ir, Rh, and Pt)", *Phys. Rev. B* **95**, 075128 (2017).

[74] M. T. Suzuki, T. Koretsune, M. Ochi, and R. Arita, "Cluster multipole theory for anomalous Hall effect in antiferromagnets", *Phys. Rev. B* **95**, 094406 (2017).

[75] W. Zhang, W. Han, S. H. Yang, Y. Sun, Y. Zhang, B. Yan, and S. S. P. Parkin, "Giant facet-dependent spin-orbit torque and spin Hall conductivity in the triangular antiferromagnet $\mathrm{IrMn_3}$", *Sci. Adv.* **2**, e1600759 (2016).

[76] T. Higo et al., “Large magneto-optical Kerr effect and imaging of magnetic octupole domains in an antiferromagnetic metal”, *Nat. Photon.* **12**, 73 (2018).

[77] A. E. Berkowitz and K. Takano, “Exchange anisotropy - a review”, *J. Magn. Magn. Mater.* **200**, 552 (1999).

[78] H. N. Fuke, K. Saito, Y. Kamiguchi, H. Iwasaki, and M. Sahashi, “Spin-valve giant magnetoresistive films with antiferromagnetic Ir-Mn layers”, *J. Appl. Phys.* **81**, 4004 (1997).

[79] K.-i. Imakita, M. Tsunoda, and M. Takahashi, “Thickness dependence of exchange anisotropy of polycrystalline Mn_3Ir/Co-Fe bilayers”, *J. Appl. Phys.* **97**, 10K106 (2005).

[80] T. P. A. Hase, B. D. Fulthorpe, S. B. Wilkins, B. K. Tanner, C. H. Marrows, and B. J. Hickey, “Weak magnetic moment on IrMn exchange bias pinning layers”, *Appl. Phys. Lett.* **79**, 985 (2001).

[81] H. Takahashi, Y. Kota, M. Tsunoda, T. Nakamura, K. Kodama, A. Sakuma, and M. Takahashi, “Uncompensated antiferromagnetic moments in Mn-Ir/FM (FM = Ni-Co, Co-Fe, Fe-Ni) bilayers: Compositional dependence and its origin”, *J. Appl. Phys.* **110**, 123920 (2011).

[82] H. Ohldag, A. Scholl, F. Nolting, E. Arenholz, S. Maat, A. T. Young, M. Carey, and J. Stöhr, “Correlation between exchange bias and pinned interfacial spins”, *Phys. Rev. Lett.* **91**, 017203 (2003).

[83] U. Nowak, K. D. Usadel, J. Keller, P. Miltényi, B. Beschoten, and G. Güntherodt, “Domain state model for exchange bias. I. Theory”, *Phys. Rev. B* **66**, 014430 (2002).

[84] J. Keller, P. Miltényi, B. Beschoten, G. Güntherodt, U. Nowak, and K. D. Usadel, “Domain state model for exchange bias. II. Experiments”, *Phys. Rev. B* **66**, 014431 (2002).

[85] J. Nogués and I. K. Schuller, “Exchange bias”, *J. Magn. Magn. Mater.* **192**, 203 (1999).

[86] K. O’Grady, L. E. Fernandez-Outon, and G. Vallejo-Fernandez, “A new paradigm for exchange bias in polycrystalline thin films”, *J. Magn. Magn. Mater.* **322**, 883 (2010).

[87] H. Katsumi, N. Ryoichi, H. Hiroyuki, S. Yutaka, and T. Shigeru, “Exchange Coupling between Antiferromagnetic Mn–Ir and Ferromagnetic Ni–Fe Layers”, *Jpn. J. Appl. Phys.* **35**, 607 (1996).

[88] M. Ali, C. H. Marrows, M. Al-Jawad, B. J. Hickey, A. Misra, U. Nowak, and K. D. Usadel, "Antiferromagnetic layer thickness dependence of the IrMn/Co exchange-bias system", *Phys. Rev. B* **68**, 214420 (2003).

[89] M. Tsunoda, K.-i. Imakita, M. Naka, and M. Takahashi, "$L1_2$ phase formation and giant exchange anisotropy in Mn_3Ir/Co–Fe bilayers", *J. Magn. Magn. Mater.* **304**, 55 (2006).

[90] T. Sato, M. Tsunoda, and M. Takahashi, "Orientational dependence of exchange anisotropy of Mn-Ir/Co-Fe epitaxial bilayers", *J. Appl. Phys.* **95**, 7513 (2004).

[91] T. Kume, T. Kato, S. Iwata, and S. Tsunashima, "Exchange anisotropy of (001)-oriented $Mn_{80}Ir_{20}$/NiFe epitaxial bilayers", *J. Magn. Magn. Mater.* **286**, 243 (2005).

[92] S. G. Wang, A. Kohn, C. Wang, A. K. Petford-Long, S. Lee, R. Fan, J. P. Goff, L. J. Singh, Z. H. Barber, and R. C. C. Ward, "Exchange bias in epitaxial Fe/$Ir_{0.2}Mn_{0.8}$ bilayers grown on MgO (001)", *J. Phys. D: Appl. Phys.* **42**, 225001 (2009).

[93] A. Kohn, A. Kovács, R. Fan, G. J. McIntyre, R. C. C. Ward, and J. P. Goff, "The antiferromagnetic structures of $IrMn_3$ and their influence on exchange-bias", *Sci. Rep.* **3**, 2412 (2013).

[94] T. Yamaoka, "Antiferromagnetism in γ-Phase Mn-Ir Alloys", *J. Phys. Soc. Jpn.* **36**, 445 (1974).

[95] M. D. LeBlanc, M. L. Plumer, J. P. Whitehead, and B. W. Southern, "Monte Carlo simulations of the fcc kagome lattice: Competition between triangular frustration and cubic anisotropy", *Phys. Rev. B* **88** (2013).

[96] A. Sakuma, K. Fukamichi, K. Sasao, and R. Y. Umetsu, "First-principles study of the magnetic structures of ordered and disordered Mn-Ir alloys", *Phys. Rev. B* **67**, 024420 (2003).

[97] J. Stöhr, A. Scholl, T. J. Regan, S. Anders, J. Lüning, M. R. Scheinfein, H. A. Padmore, and R. L. White, "Images of the Antiferromagnetic Structure of a NiO(100) Surface by Means of X-Ray Magnetic Linear Dichroism Spectromicroscopy", *Phys. Rev. Lett.* **83**, 1862 (1999).

[98] O. Gomonay, S. Kondovych, and V. Loktev, "Shape-induced anisotropy in antiferromagnetic nanoparticles", *J. Mag. Mag. Mater.* **354**, 125 (2014).

[99] Y. C. Lau, D. Betto, K. Rode, J. M. Coey, and P. Stamenov, "Spin-orbit torque switching without an external field using interlayer exchange coupling", *Nat. Nanotechnol.* **11**, 758 (2016).

[100] Y. W. Oh et al., "Field-free switching of perpendicular magnetization through spin-orbit torque in antiferromagnet/ferromagnet/oxide structures", *Nat. Nanotechnol.* **11**, 878 (2016).

[101] D. Wu et al., "Spin-orbit torques in perpendicularly magnetized $Ir_{22}Mn_{78}$ / $Co_{20}Fe_{60}B_{20}$ / MgO multilayer", *Appl. Phys. Lett.* **109**, 222401 (2016).

[102] L. Qian, W. Chen, K. Wang, X. Wu, and G. Xiao, "Spin Hall effect and current induced magnetic switching in antiferromagnetic IrMn", *AIP Adv.* **8** (2018).

[103] J. B. S. Mendes, R. O. Cunha, O. Alves Santos, P. R. T. Ribeiro, F. L. A. Machado, R. L. Rodríguez-Suárez, A. Azevedo, and S. M. Rezende, "Large inverse spin Hall effect in the antiferromagnetic metal $Ir_{20}Mn_{80}$", *Phys. Rev. B* **89**, 140406(R) (2014).

[104] W. T. Soh, Y. Yeow, X. Zhong, and C. K. Ong, "Inverse spin Hall effect of antiferromagnetic MnIr in exchange biased NiFe/MnIr films", *J. Phys. D: Appl. Phys.* **48**, 345002 (2015).

[105] V. Tshitoyan, C. Ciccarelli, A. P. Mihai, M. Ali, A. C. Irvine, T. A. Moore, T. Jungwirth, and A. J. Ferguson, "Electrical manipulation of ferromagnetic NiFe by antiferromagnetic IrMn", *Phys. Rev. B* **92**, 214406 (2015).

[106] L. Frangou, S. Oyarzún, S. Auffret, L. Vila, S. Gambarelli, and V. Baltz, "Enhanced Spin Pumping Efficiency in Antiferromagnetic IrMn Thin Films around the Magnetic Phase Transition", *Phys. Rev. Lett.* **116**, 077203 (2016).

[107] M. Harder, Y. Gui, and C.-M. Hu, "Electrical detection of magnetization dynamics via spin rectification effects", *Phys. Rep.* **661**, 1 (2016).

[108] H. Iwaki, M. Kimata, T. Ikebuchi, Y. Kobayashi, K. Oda, Y. Shiota, T. Ono, and T. Moriyama, "Large anomalous Hall effect in $L1_2$-ordered antiferromagnetic Mn_3Ir thin films", *Appl. Phys. Lett.* **116** (2020).

[109] Z. Q. Liu et al., "Electrical switching of the topological anomalous Hall effect in a non-collinear antiferromagnet above room temperature", *Nat. Electron.* **1**, 172 (2018).

[110] S. Tomiyoshi and Y. Yamaguchi, "Magnetic Structure and Weak Ferromagnetism of Mn_3Sn Studied by Polarized Neutron Diffraction", *J. Phys. Soc. Jpn.* **51**, 2478 (1982).

[111] T. F. Duan, W. J. Ren, W. L. Liu, S. J. Li, W. Liu, and Z. D. Zhang, “Magnetic anisotropy of single-crystalline Mn_3Sn in triangular and helix-phase states”, *Appl. Phys. Lett.* **107**, 082403 (2015).

[112] S. Tomiyoshi, S. Abe, Y. Yamaguchi, H. Yamauchi, and H. Yamamoto, “Triangular spin structure and weak ferromagnetism of Mn_3Sn at low temperature”, *J. Magn. Magn. Mater.* **54-57**, 1001 (1986).

[113] W. J. Feng, D. Li, W. J. Ren, Y. B. Li, W. F. Li, J. Li, Y. Q. Zhang, and Z. D. Zhang, “Glassy ferromagnetism in Ni_3Sn-type $Mn_{3.1}Sn_{0.9}$”, *Phys. Rev. B* **73**, 205105 (2006).

[114] H. Ohmori, S. Tomiyoshi, H. Yamauchi, and H. Yamamoto, “Spin structure and weak ferromagnetism of Mn_3Sn”, *J. Mag. Mag. Mater.* **70**, 249 (1987).

[115] A. L. Balk, N. H. Sung, S. M. Thomas, P. F. S. Rosa, R. D. McDonald, J. D. Thompson, E. D. Bauer, F. Ronning, and S. A. Crooker, “Comparing the anomalous Hall effect and the magneto-optical Kerr effect through antiferromagnetic phase transitions in Mn_3Sn”, *Appl. Phys. Lett.* **114**, 032401 (2019).

[116] W. Feng, G.-Y. Guo, J. Zhou, Y. Yao, and Q. Niu, “Large magneto-optical Kerr effect in noncollinear antiferromagnets Mn_3X ($X =$ Rh, Ir, Pt)”, *Phys. Rev. B* **92**, 144426 (2015).

[117] Y. Zhang, J. Železný, Y. Sun, J. v. d. Brink, and B. Yan, “Spin Hall effect emerging from a noncollinear magnetic lattice without spin–orbit coupling”, *New J. Phys.* **20**, 073028 (2018).

[118] M. Kimata et al., “Magnetic and magnetic inverse spin Hall effects in a non-collinear antiferromagnet”, *Nature* **565**, 627 (2019).

[119] J. Sticht, K. H. Höck, and J. Kübler, “Non-collinear itinerant magnetism: the case of Mn_3Sn”, *J. Phys.: Condens. Matter* **1**, 8155 (1989).

[120] J. Železný, Y. Zhang, C. Felser, and B. Yan, “Spin-Polarized Current in Noncollinear Antiferromagnets”, *Phys. Rev. Lett.* **119**, 187204 (2017).

[121] J. Ekin, “Sample Holders”, in *Experimental Techniques for Low-Temperature Measurements* (Oxford University Press, New York, 2006) Chap. 7, pp. 271–316.

[122] *Model 6221 AC and DC Current Source - User’s Manual*, 3rd ed. (Keithley Instruments, Cleveland, OH, 2008).

[123] *Model 2182 and 2182A Nanovoltmeter - User’s Manual*, 2nd ed. (Keithley Instruments, Cleveland, OH, 2017).

[124] J. Ekin, "Properties of Solids at Low Temperatures", in *Experimental Techniques for Low-Temperature Measurements* (Oxford University Press, New York, 2006) Chap. 6, pp. 226–269.

[125] R. P. Feynman, "Propagation in a Crystal Lattice", in *The Feynman Lectures on Physics*, Vol. 3, edited by R. B. Leighton and M. L. Sands (Addison-Wesley, Reading, MA, 1971) Chap. 13, pp. 13.1–13.13.

[126] T. R. McGuire and R. I. Potter, "Anisotropic Magnetoresistance in Ferromagnetic 3*d* Alloys", *IEEE Trans. Magn.* **11**, 1018 (1975).

[127] R. P. Feynman, "Semiconductors", in *The Feynman Lectures on Physics*, Vol. 3, edited by R. B. Leighton and M. L. Sands (Addison-Wesley, Reading, MA, 1971) Chap. 14, pp. 14.1–14.11.

[128] S. Byrnes, "Hall Effect Measurement Setup for Electrons", Wikimedia Commons (2012).

[129] N. Nagaosa, J. Sinova, S. Onoda, A. H. MacDonald, and N. P. Ong, "Anomalous Hall effect", *Rev. Mod. Phys.* **82**, 1539 (2010).

[130] E. Liu et al., "Giant anomalous Hall effect in a ferromagnetic Kagome-lattice semimetal", *Nat. Phys.* **14**, 1125 (2018).

[131] S. Nakatsuji, N. Kiyohara, and T. Higo, "Large anomalous Hall effect in a non-collinear antiferromagnet at room temperature", *Nature* **527**, 212 (2015).

[132] N. H. Sung, F. Ronning, J. D. Thompson, and E. D. Bauer, "Magnetic phase dependence of the anomalous Hall effect in Mn_3Sn single crystals", *Appl. Phys. Lett.* **112**, 132406 (2018).

[133] X. Li, L. Xu, H. Zuo, A. Subedi, Z. Zhu, and K. Behnia, "Momentum-space and real-space Berry curvatures in Mn_3Sn", *SciPost Phys.* **5**, 063 (2018).

[134] T. Matsuda, N. Kanda, T. Higo, N. P. Armitage, S. Nakatsuji, and R. Matsunaga, "Room-temperature terahertz anomalous Hall effect in Weyl antiferromagnet Mn_3Sn thin films", *Nat. Commun.* **11**, 909 (2020).

[135] A. K. Nayak et al., "Large anomalous Hall effect driven by a nonvanishing Berry curvature in the noncolinear antiferromagnet Mn_3Ge", *Sci. Adv.* **2**, e1501870 (2016).

[136] N. Kiyohara, T. Tomita, and S. Nakatsuji, "Giant Anomalous Hall Effect in the Chiral Antiferromagnet Mn_3Ge", *Phys. Rev. Appl.* **5**, 064009 (2016).

[137] Z. H. Liu, Y. J. Zhang, G. D. Liu, B. Ding, E. K. Liu, H. M. Jafri, Z. P. Hou, W. H. Wang, X. Q. Ma, and G. H. Wu, "Transition from Anomalous Hall Effect to Topological Hall Effect in Hexagonal Non-Collinear Magnet Mn_3Ga", *Sci. Rep.* **7**, 515 (2017).

[138] T. Higo, D. Qu, Y. Li, C. L. Chien, Y. Otani, and S. Nakatsuji, "Anomalous Hall effect in thin films of the Weyl antiferromagnet Mn_3Sn", *Appl. Phys. Lett.* **113**, 202402 (2018).

[139] T. Ikeda, M. Tsunoda, M. Oogane, S. Oh, T. Morita, and Y. Ando, "Anomalous Hall effect in polycrystalline Mn_3Sn thin films", *Appl. Phys. Lett.* **113**, 222405 (2018).

[140] T. Ikeda, M. Tsunoda, M. Oogane, S. Oh, T. Morita, and Y. Ando, "Improvement of Large Anomalous Hall Effect in Polycrystalline Antiferromagnetic $Mn_{3+x}Sn$ Thin Films", *IEEE Trans. Mag.* **55**, 2501704 (2019).

[141] J. Yoon, Y. Takeuchi, R. Itoh, S. Kanai, S. Fukami, and H. Ohno, "Crystal orientation and anomalous Hall effect of sputter-deposited non-collinear antiferromagnetic Mn_3Sn thin films", *Appl. Phys. Express* **13** (2020).

[142] Y. You, X. Chen, X. Zhou, Y. Gu, R. Zhang, F. Pan, and C. Song, "Anomalous Hall Effect–Like Behavior with In-Plane Magnetic Field in Noncollinear Antiferromagnetic Mn_3Sn Films", *Adv. Electron. Mater.* **5**, 1800818 (2019).

[143] C. Sürgers, G. Fischer, P. Winkel, and H. v. Löhneysen, "Large topological Hall effect in the non-collinear phase of an antiferromagnet", *Nat. Commun.* **5**, 3400 (2014).

[144] A. Neubauer, C. Pfleiderer, B. Binz, A. Rosch, R. Ritz, P. G. Niklowitz, and P. Böni, "Topological Hall effect in the A phase of MnSi", *Phys. Rev. Lett.* **102**, 186602 (2009).

[145] P. Bruno, V. K. Dugaev, and M. Taillefumier, "Topological Hall effect and Berry phase in magnetic nanostructures", *Phys. Rev. Lett.* **93**, 096806 (2004).

[146] K. G. Rana et al., "Observation of topological Hall effect in Mn_2RhSn films", *New J. Phys.* **18** (2016).

[147] J. Yan, X. Luo, H. Y. Lv, Y. Sun, P. Tong, W. J. Lu, X. B. Zhu, W. H. Song, and Y. P. Sun, "Room-temperature angular-dependent topological Hall effect in chiral antiferromagnetic Weyl semimetal Mn_3Sn", *Appl. Phys. Lett.* **115**, 102404 (2019).

[148] X. Li et al., "Chiral domain walls of Mn_3Sn and their memory", *Nat. Commun.* **10**, 3021 (2019).

[149] P. K. Rout, P. V. P. Madduri, S. K. Manna, and A. K. Nayak, "Field-induced topological Hall effect in the noncoplanar triangular antiferromagnetic geometry of Mn_3Sn", *Phys. Rev. B* **99**, 094430 (2019).

[150] K. S. S. Harsha, "Nucleation and Growth of Films", in *Principles of Vapor Deposition of Thin Films* (Elsevier Science, Oxford, 2006) Chap. 9, pp. 686–829.

[151] M. Ohring, "Discharges, Plasmas, and Ion-Surface Interactions", in *Materials Science of Thin Films - Second Edition* (Academic Press, San Diego, 2001) Chap. 4, pp. 145–202.

[152] K. S. S. Harsha, *Principles of Vapor Deposition of Thin Films* (Elsevier Science, Oxford, 2006).

[153] H. Frey, "Relevance of the Vacuum Technology for Thin Film Coatings", in *Basic Principle of Plasma Physics*, edited by H. Frey and H. R. Khan (Springer, Berlin-Heidelberg, 2015) Chap. 4, pp. 73–111.

[154] R. Bosco, J. Van Den Beucken, S. Leeuwenburgh, and J. Jansen, "Surface Engineering for Bone Implants: A Trend from Passive to Active Surfaces", *Coatings* **2**, 95 (2012).

[155] H. Frey, "Relevance of the Vacuum Technology for Thin Film Coatings", in *Handbook of Thin-Film Technology*, edited by H. Frey and H. R. Khan (Springer, Berlin-Heidelberg, 2015) Chap. 2, pp. 5–12.

[156] K. S. S. Harsha, "Gas Flow in Thin Film Processing Systems", in *Principles of Vapor Deposition of Thin Films* (Elsevier Science, Oxford, 2006) Chap. 6, pp. 453–553.

[157] M. Ohring, "Vacuum Science and Technology", in *Materials Science of Thin Films - Second Edition* (Academic Press, San Diego, 2001) Chap. 2, pp. 57–93.

[158] M. Ohring, "Substrate Surfaces and Thin-Film Nucleation", in *Materials Science of Thin Films - Second Edition* (Academic Press, San Diego, 2001) Chap. 7, pp. 357–415.

[159] K. S. S. Harsha, "Epitaxy", in *Principles of Vapor Deposition of Thin Films* (Elsevier Science, Oxford, 2006) Chap. 10, pp. 831–909.

[160] K. S. S. Harsha, "Substrate Preparation", in *Principles of Vapor Deposition of Thin Films* (Elsevier Science, Oxford, 2006) Chap. 11, pp. 912–960.

[161] M. Ohring, “Epitaxy”, in *Materials Science of Thin Films - Second Edition* (Academic Press, San Diego, 2001) Chap. 8, pp. 417–494.

[162] R. P. Feynman, “The Internal Geometry of Crystals”, in *The Feynman Lectures on Physics*, Vol. 2, edited by R. B. Leighton and M. L. Sands (Addison-Wesley, Reading, MA, 1971) Chap. 30, pp. 30.1–30.10.

[163] M. Ohring, “Film Structure”, in *Materials Science of Thin Films - Second Edition* (Academic Press, San Diego, 2001) Chap. 9, pp. 495–558.

[164] D. Zhang, B. Yan, S. C. Wu, J. Kubler, G. Kreiner, S. S. P. Parkin, and C. Felser, “First-principles study of the structural stability of cubic, tetragonal and hexagonal phases in Mn_3Z (Z = Ga, Sn and Ge) Heusler compounds”, *J. Phys.: Condens. Matter* **25**, 206006 (2013).

[165] F. C. Frank and J. H. van der Merwe, “One-dimensional dislocations”, *Proc. Roy. Soc. A* **198**, 205 (1949).

[166] W. D. Nix, “Mechanical Properties Of Thin Films”, *Metall. Trans. A* **20**, 2217 (1989).

[167] M. Birkholz, *Thin Film Analysis by X-Ray Scattering* (Wiley, Weinheim, 2006).

[168] H. W. Wang, C. F. Shieh, H. Y. Chen, W. C. Shiu, B. Russo, and G. Cao, “Standing [111] gold nanotube to nanorod arrays via template growth”, *Nanotechnology* **17**, 2689 (2006).

[169] U. Pietsch, T. Baumbach, and V. Holý, *High-Resolution X-Ray Scattering* (Springer, New York, 2004).

[170] P. Scherrer, *Göttinger Nachrichten Math. Phys.* **2**, 98 (1918).

[171] U. Pietsch, T. Baumbach, and V. Holý, “X-Ray Scattering by Rough Multilayers”, in *High-Resolution X-Ray Scattering* (Springer, New York, 2004) Chap. 11, pp. 235–272.

[172] M. Birkholz, “X-ray Reflectivity (XRR)”, in *Thin Film Analysis by X-Ray Scattering* (Wiley, Weinheim, 2006) Chap. 4.6, pp. 165–175.

[173] P. Eaton and P. West, “AFM instrumentation”, in *Atomic Force Microscopy* (Oxford University Press, New York, 2010) Chap. 2, pp. 10–48.

[174] P. Eaton and P. West, “AFM modes”, in *Atomic Force Microscopy* (Oxford University Press, New York, 2010) Chap. 3, pp. 50–70.

[175] G. Binnig, C. F. Quate, and C. Gerber, “Atomic force microscope”, *Phys. Rev. Lett.* **56**, 930 (1986).

[176] P. Eaton and P. West, “Introduction”, in *Atomic Force Microscopy* (Oxford University Press, New York, 2010) Chap. 1, pp. 1–8.

[177] J. Thomas and T. Gemming, *Analytical Transmission Electron Microscopy - An Introduction for Operators* (Springer, Dordrecht, 2014).

[178] D. B. Williams and C. B. Carter, “How to ”See” Electrons”, in *Transmission Electron Microscopy - A Textbook for Materials Science* (Springer, New York, 1996) Chap. 9, pp. 131–153.

[179] D. B. Williams and C. B. Carter, “Specimen Preparation”, in *Transmission Electron Microscopy - A Textbook for Materials Science* (Springer, New York, 1996) Chap. 10, pp. 155–172.

[180] D. B. Williams and C. B. Carter, “Electron Sources”, in *Transmission Electron Microscopy - A Textbook for Materials Science* (Springer, New York, 1996) Chap. 5, pp. 67–83.

[181] R. P. Feynman, “The Relation of Wave and Particle Viewpoints”, in *The Feynman Lectures on Physics*, Vol. 3, edited by R. B. Leighton and M. L. Sands (Addison-Wesley, Reading, MA, 1971) Chap. 2, pp. 2.1–2.10.

[182] D. B. Williams and C. B. Carter, “The Transmission Electron Microscope”, in *Transmission Electron Microscopy - A Textbook for Materials Science* (Springer, New York, 1996) Chap. 1, pp. 3–16.

[183] D. B. Williams and C. B. Carter, “The Instrument”, in *Transmission Electron Microscopy - A Textbook for Materials Science* (Springer, New York, 1996) Chap. 9, pp. 131–153.

[184] D. B. Williams and C. B. Carter, “Lenses, Apertures, and Resolution”, in *Transmission Electron Microscopy - A Textbook for Materials Science* (Springer, New York, 1996) Chap. 6, pp. 85–104.

[185] R. P. Feynman, “The Laws of Induction”, in *The Feynman Lectures on Physics*, Vol. 2, edited by R. B. Leighton and M. L. Sands (Addison-Wesley, Reading, MA, 1971) Chap. 17, pp. 17.1–17.15.

[186] K. Tashiro, “Induction Coil Magnetometers”, in *High Sensitivity Magnetometers*, edited by A. Grosz, M. J. Haji-Sheikh, and S. C. Mukhopadhyay (Springer, Switzerland, 2017) Chap. 1, pp. 1–39.

[187] *Magnetic Property Measurement System - MPMS 3 User’s Manual*, 15th ed. (Quantum Design, San Diego, 2016).

[188] M. Schmelz and R. Stolz, "Superconducting Quantum Interference Device (SQUID) Magnetometers", in *High Sensitivity Magnetometers*, edited by A. Grosz, M. J. Haji-Sheikh, and S. C. Mukhopadhyay (Springer, Switzerland, 2017) Chap. 10, pp. 279–311.

[189] B. H. Bransden and C. J. Joachain, "The interaction of quantum systems with radiation", in *Quantum Mechanics*, 2nd ed. (Pearson, London, 2000) Chap. 11, pp. 515–555.

[190] Y. Joly, "Interaction of Polarized Light with Matter", in *Magnetism and Synchrotron Radiation - New Trends*, edited by E. Beaurepaire, H. Bulou, F. Scheurer, and J.-P. Kappler (Springer, Berlin-Heidelberg, 2010) Chap. 3, pp. 77–124.

[191] A. Tenderholt, "Diagram showing which transitions contribute to X-ray absorption edges (reused under the term of the Creative Commons Attribution-Share Alike 3.0 International license)", Wikimedia Commons (2009).

[192] T. Sanders, "Diagram of X-ray magnetic circular dichroism (reused under the term of the Creative Commons Attribution-Share Alike 4.0 International license)", Wikimedia Commons (2016).

[193] H. Wende and C. Antoniak, "X-Ray Magnetic Dichroism", in *Magnetism and Synchrotron Radiation - New Trends*, edited by E. Beaurepaire, H. Bulou, F. Scheurer, and J.-P. Kappler (Springer, Berlin-Heidelberg, 2010) Chap. 5, pp. 145–166.

[194] C. T. Chen, Y. U. Idzerda, H. Lin, N. V. Smith, G. Meigs, E. Chaban, G. H. Ho, E. Pellegrin, and F. Sette, "Experimental confirmation of the X-ray magnetic circular dichroism sum rules for iron and cobalt", *Phys. Rev. Lett.* **75**, 152 (1995).

[195] A. A. Sapozhnik, C. Luo, H. Ryll, F. Radu, M. Jourdan, H. Zabel, and H.-J. Elmers, "Experimental determination of exchange constants in antiferromagnetic $\mathrm{Mn_2Au}$", *Phys. Rev. B* **97** (2018).

[196] E. Goering, "X-ray magnetic circular dichroism sum rule correction for the light transition metals", *Philos. Mag.* **85**, 2895 (2005).

[197] T. Noll and F. Radu, "The Mechanics of the VEKMAG Experiment", in *Proc. of MEDSI2016, Barcelona, Spain, September 2016*, edited by V. R. W. Schaa (JACoW, Geneva, 2017), pp. 370–373.

[198] D. Cocco and M. Zangrando, "Synchrotron Radiation Sources and Optical Devices", in *Magnetism and Synchrotron Radiation - New Trends*, edited by E. Beaurepaire, H. Bulou, F. Scheurer, and J.-P. Kappler (Springer, Berlin-Heidelberg, 2010) Chap. 4, pp. 127–143.

[199] W. M. Moreau, “Surface Preparation and Coating”, in *Semiconductor Lithography - Principles, Practices, and Materials* (Plenum Press, New York, 1988) Chap. 6, pp. 259–321.

[200] W. M. Moreau, “Positive Photoresists”, in *Semiconductor Lithography - Principles, Practices, and Materials* (Plenum Press, New York, 1988) Chap. 2, pp. 29–74.

[201] W. M. Moreau, “Prebake (Softbake)”, in *Semiconductor Lithography - Principles, Practices, and Materials* (Plenum Press, New York, 1988) Chap. 7, pp. 329–352.

[202] B. H. Bransden and C. J. Joachain, *Quantum Mechanics*, 2nd ed. (Pearson, London, 2000).

[203] D. K. Ferry and R. O. Grondin, *Physics of Submicron Devices* (Springer, New York, 1991).

[204] *MLA150 Maskless Aligner Fact Sheet* (Heidelberg Instruments, Heidelberg, 2019).

[205] K. A. Valiev, *The Physics of Submicron Lithography* (Springer, New York, 1992).

[206] W. M. Moreau, “Introduction”, in *Semiconductor Lithography - Principles, Practices, and Materials* (Plenum Press, New York, 1988) Chap. 1, pp. 1–22.

[207] W. M. Moreau, “Negative Photoresists”, in *Semiconductor Lithography - Principles, Practices, and Materials* (Plenum Press, New York, 1988) Chap. 4, pp. 157–206.

[208] W. M. Moreau, “Optical Exposure”, in *Semiconductor Lithography - Principles, Practices, and Materials* (Plenum Press, New York, 1988) Chap. 8, pp. 355–403.

[209] W. M. Moreau, “Developing Resist Images”, in *Semiconductor Lithography - Principles, Practices, and Materials* (Plenum Press, New York, 1988) Chap. 10, pp. 459–523.

[210] W. M. Moreau, “Postbake”, in *Semiconductor Lithography - Principles, Practices, and Materials* (Plenum Press, New York, 1988) Chap. 11, pp. 545–564.

[211] W. M. Moreau, “Additive Processes”, in *Semiconductor Lithography - Principles, Practices, and Materials* (Plenum Press, New York, 1988) Chap. 12, pp. 567–620.

[212] W. M. Moreau, “Subtractive Etching”, in *Semiconductor Lithography - Principles, Practices, and Materials* (Plenum Press, New York, 1988) Chap. 13, pp. 631–763.

[213] W. M. Moreau, “Stripping of Resists”, in *Semiconductor Lithography - Principles, Practices, and Materials* (Plenum Press, New York, 1988) Chap. 14, pp. 779–809.

[214] J. Y. Chauleau, H. G. Bauer, H. S. Körner, J. Stigloher, M. Härtinger, G. Woltersdorf, and C. H. Back, “Self-consistent determination of the key spin-transfer torque parameters from spin-wave Doppler experiments”, *Phys. Rev. B* **89**, 020403(R) (2014).

[215] J. R. Childress et al., “All-Metal Current-Perpendicular-to-Plane Giant Magnetoresistance Sensors for Narrow-Track Magnetic Recording”, *IEEE Trans. Magn.* **44**, 90 (2008).

[216] S. Ikeda, K. Miura, H. Yamamoto, K. Mizunuma, H. D. Gan, M. Endo, S. Kanai, J. Hayakawa, F. Matsukura, and H. Ohno, “A perpendicular-anisotropy CoFeB-MgO magnetic tunnel junction”, *Nat. Mater.* **9**, 721 (2010).

[217] R. P. Feynman, “Magnetostatics”, in *The Feynman Lectures on Physics*, Vol. 2, edited by R. B. Leighton and M. L. Sands (Addison-Wesley, Reading, MA, 1971) Chap. 13, pp. 13.1–13.12.

[218] *Physical Property Measurement System - DynaCool User’s Manual*, 4th ed. (Quantum Design, San Diego, 2014).

[219] J. Ekin, “Introduction to Measurement Cryostats and Cooling Methods”, in *Experimental Techniques for Low-Temperature Measurements* (Oxford University Press, New York, 2006) Chap. 1, pp. 3–48.

[220] J. Ekin, “Wiring and Connections”, in *Experimental Techniques for Low-Temperature Measurements* (Oxford University Press, New York, 2006) Chap. 4, pp. 150–184.

[221] J. Ekin, “Temperature Measurement and Control”, in *Experimental Techniques for Low-Temperature Measurements* (Oxford University Press, New York, 2006) Chap. 5, pp. 185–225.

[222] J. Ekin, “Sample Contacts”, in *Experimental Techniques for Low-Temperature Measurements* (Oxford University Press, New York, 2006) Chap. 8, pp. 317–350.

2 Part A - Mn_3Ir

2.1 Epitaxial growth, structural characterization, and exchange bias of noncollinear antiferromagnetic Mn_3Ir thin films

The following chapter of this cumulative thesis consists of the peer-reviewed scientific paper published as:

J. M. Taylor, E. Lesne, A. Markou, F. K. Dejene, B. Ernst, A. Kalache, K. G. Rana, N. Kumar, P. Werner, C. Felser, and S. S. P. Parkin, “Epitaxial growth, structural characterization, and exchange bias of noncollinear antiferromagnetic M_3Ir thin films”, *Phys. Rev. Mater.* **3**, 074409 (2019)

Reprinted with permission from [J. M. Taylor et al., “Epitaxial growth, structural characterization, and exchange bias of noncollinear antiferromagnetic M_3Ir thin films”, *Phys. Rev. Mater.* **3**, 074409 (2019)]. Copyright (2019) by the American Physical Society. DOI: 10.1103/PhysRevMaterials.3.074409

Mn_3Ir, as discussed in Section 1.2.6 is an antiferromagnet with a face-centered cubic crystal structure, where the Mn moments on the face-center sites form a triangular spin texture on a kagome lattice in (111) crystal planes and the Ir atoms on corner sites introduce strong SOC. These properties result in sizable internal magnetic anisotropies, with Mn spins directed parallel to $\langle\bar{1}\bar{1}2\rangle$ crystalline axes, making Mn_3Ir the material of choice for large EB (used, for example, to pin the direction of magnetization in the reference layer of MTJs) [78, 88]. The strong internal anisotropies result in a fixed AF domain state in Mn_3Ir films of moderate thickness at room temperature, which introduces a unidirectional exchange anisotropy to a coupled FM layer. As discussed in Section 1.2.5, the direction of this exchange anisotropy can be set by cooling such bilayers from elevated temperatures in a magnetic field. Typically, maximum exchange bias fields are desired, for which reason polycrystalline films of Mn_3Ir are preferred for applications, where crystallite grain boundaries act to pin AF domain walls and thus increase the stability of the domain state to external perturbations [79, 89].

In the current paper, however, we instead explore the exchange bias of single crystalline Mn_3Ir films coupled to 5 nm thick permalloy ($Ni_{80}Fe_{20}$) FM layers, which have been less frequently studied in previous years. For 10 nm thick films, field annealing of such heterostructures at 250 °C results in large values of exchange bias field, competitive with those achieved for polycrystalline Mn_3Ir. These values of exchange bias field are extracted from the shift along the applied magnetic field axis of the magnetization hysteresis loop measured using SQUID-VSM. Similar measurements with the external magnetic field at different angles with respect to the annealing field direction demonstrate the unidirectional nature of the induced anisotropy.

On the other hand, heterostructures of permalloy coupled to 3 nm Mn_3Ir films do not show EB at room temperature. Instead, because of the weakened internal anisotropy energy in such ultrathin films, the temperature required to stabilize the AF domain state and hence induce EB (referred to as the blocking temperature) is reduced to below 300 K. However, magnetic hysteresis loops measured after cooling to low temperatures show that larger values of exchange bias can be achieved. Blocking temperature is found to be 40 K in the case of 3 nm Mn_3Ir films with (111) orientation. In this case, we find that the shift in the hysteresis loops indicating induced exchange anisotropy decreases during four subsequent cycles of the external magnetic field. This training effect indicates that a significant proportion of the initial exchange bias is caused by interfacial Mn spins that are weakly coupled to the bulk Mn_3Ir AF order. These Mn spins are uncompensated in proximity to the FM layer, with exchange interactions across the interface causing them to couple parallel to the majority Ni moments in the permalloy layer (shown by the resulting negative exchange bias field). As magnetic field is cycled, these weakly pinned interfacial moments are re-oriented, and so no longer contribute to EB. Meanwhile, uncompensated interfacial Mn moments whose direction is pinned by strong coupling to the bulk AF order, in turn stabilized by AF domain walls, mediate the EB after training. This observation provides an indication as to the importance of uncompensated moments in determining the properties of thin films of the Mn_3X noncollinear antiferromagnets, a theme we will expand upon throughout this thesis.

In the case of 3 nm Mn_3Ir films with (001) orientation, measurements of exchange bias after cooling with external magnetic field along different IP directions reveals a dependence of blocking temperature on crystallographic axis. Higher blocking temperature is found with cooling field applied parallel to the [110] crystalline direction, compared with field cooling along the [100] direction. We postulate that this novel result, which could be of interest to technological applications, may be explained by the alignment of Mn moments at 45° to the cubic crystal axes in γ-Mn_3Ir.

Prior to the measurement of exchange bias in these thin films, we perform a comprehensive characterization of the Mn_3Ir films using XRD and TEM, in order to demonstrate the quality of their crystal structure. Films were deposited using magnetron sputtering, with epitaxial engineering used to prepare Mn_3Ir with both [001] and [111] growth direction perpendicular to the film plane. Through XRD measurements, we confirm the preparation of thin films that are chemically disordered, having a γ-Mn_3Ir structure, but that show large crystalline grains with low mosaic spread between them. XRR and AFM measurements indicate that the films are smooth, with an average roughness of $<8\,\text{Å}$. It is important to minimize the surface roughness of the Mn_3Ir films, in order to ensure the cleanest interface possible in subsequently fabricated heterostructure devices. TEM micrographs of the thin films give a visual indication as to their relaxed and low defect density growth. Diffraction patterns extracted from the same cross-sectional TEM images, showing discrete spots, demonstrate that the films contain single-crystalline grains that are coherently oriented throughout.

These diffractograms confirm the epitaxial growth of the respective layers, initially obtained from XRD $\chi-\phi$ maps of IP diffraction peaks. The epitaxial relationships are as follows:
Cube-on-cube growth of Mn_3Ir with (001) orientation on (001) cut single crystal MgO substrates: $\text{MgO}(001)[100]\|\text{Mn}_3\text{Ir}(001)[100]$
Quasi-hexagon-on-hexagon growth of Mn_3Ir with (111) orientation on TaN(111) buffered c-axis oriented Al_2O_3 substrates: $\text{Al}_2\text{O}_3(0001)[11\bar{2}0][\bar{1}100]\|\text{TaN}(111)$ $[\bar{1}12][1\bar{1}0]\|\text{Mn}_3\text{Ir}(111)[\bar{1}12][1\bar{1}0]$

The two orientations of Mn_3Ir, determined from the indexing of characteristic diffraction peaks in $2\theta - \theta$ specular XRD scans, were achieved by selection of appropriate substrates to seed the desired growth direction. In order to achieve (111) oriented Mn_3Ir, Pt and TaN buffer layers were trialed, in order to reduced lattice mismatch and interface free energy with the Al_2O_3 (0001) substrate. We select the TaN buffer to utilize in subsequently measured samples.

The reason for growing Mn_3Ir films of two different orientations was motivated by recent reports of SHE arising from this AF [103, 105, 106]. The efficient conversion of charge current to spin current is an important requirement for future spintronic devices. Furthermore, the use of the resulting spin currents for deterministic SOT switching of FMs, which normally requires the application of a small IP magnetic field, can be achieved field-free in coupled Mn_3Ir/FM heterostructures, due to the EB effect breaking IP symmetry [99, 100]. However, for maximum efficiency, i.e. switching using the smallest possible charge currents, the ratio of charge to spin conversion must be high (quantified by the spin Hall angle of the material in question).

To this end, it was discovered that the spin Hall angle of Mn_3Ir shows a strong facet dependence, with a very large spin Hall angle of 0.2 observed for Mn_3Ir films with (001) orientation (and this value falling by almost half in (111) oriented films) [75]. This variation in spin Hall angle can be attributed to an anisotropic generation of spin currents along different crystallographic directions in Mn_3Ir, for charge current applied in a particular direction [73]. Theoretical calculations of the spin Hall conductivities arising from an intrinsic mechanism in Mn_3Ir have shown a much larger spin Hall conductivity along the [001] direction, supporting the interpretation that in the correct crystal orientation devices can exploit the anisotropic spin currents generated by an intrinsic SHE [75]. This intrinsic SHE arises from the same origin as the intrinsic AHE in Mn_3Ir, namely the Berry curvature driven effective field induced as a result of the symmetry breaking triangular spin texture in this noncollinear AF [73]. This is discussed in more detail in Section 1.2.9.

In order to study these topological magnetotransport effects in more detail, it is thus necessary to deposit Mn_3Ir films of different orientation, in order to access the anisotropic transport components that are the hallmarks of these momentum-space Berry phase generated phenomena. However, it is to be expected that such phenomena may be sensitive to the crystal quality of the Mn_3Ir, with defects and other impurities acting to disrupt the Berry curvature driven electrical transport. Whilst high quality crystal growth is relatively straightforward to achieve in bulk crystals, it is more challenging in thin films, especially whilst controlling orientation, minimizing interface roughness and utilizing industry-compatible deposition techniques such as magnetron sputtering. Nevertheless, preparation of thin films is essential should these topological magnetotransport transport effects be exploited in future spintronic devices.

The magnetron sputtering growth of smooth thin films of Mn_3Ir with high quality crystal structure and controlled crystal orientation is thus an important goal, whose achievement we reported in the upcoming paper J. M. Taylor et al., “Epitaxial growth, structural characterization, and exchange bias of noncollinear antiferromagnetic M_3Ir thin films”, *Phys. Rev. Mater.* **3**, 074409 (2019), which forms the first chapter (Section 2.1) of this cumulative thesis.

PHYSICAL REVIEW MATERIALS **3**, 074409 (2019)

Epitaxial growth, structural characterization, and exchange bias of noncollinear antiferromagnetic Mn_3Ir thin films

James M. Taylor,[1,*] Edouard Lesne,[1] Anastasios Markou,[2] Fasil Kidane Dejene,[1] Benedikt Ernst,[2] Adel Kalache,[2]
Kumari Gaurav Rana,[1] Neeraj Kumar,[1] Peter Werner,[1] Claudia Felser,[2] and Stuart S. P. Parkin[1,†]
[1]*Max Planck Institute of Microstructure Physics, Weinberg 2, 06120 Halle (Saale), Germany*
[2]*Max Planck Institute for Chemical Physics of Solids, Nöthnitzer Str. 40, 01187 Dresden, Germany*

(Received 13 March 2019; published 30 July 2019)

Antiferromagnetic materials are of great interest for spintronics. Here we present a comprehensive study of the growth, structural characterization, and resulting magnetic properties of thin films of the noncollinear antiferromagnet Mn_3Ir. Using epitaxial engineering on MgO (001) and Al_2O_3 (0001) single-crystal substrates, we control the growth of cubic γ-Mn_3Ir in both (001) and (111) crystal orientations, and discuss the optimization of growth conditions to achieve high-quality crystal structures with low surface roughness. Exchange bias is studied in bilayers, with exchange bias fields as large as -29 mT (equivalent to a unidirectional anisotropy constant of $0.115\,\mathrm{erg\,cm^{-2}}$ or $11.5\,\mathrm{nJ\,cm^{-2}}$) measured in Mn_3Ir (111)/Permalloy heterostructures at room temperature. In addition, a distinct dependence of blocking temperature on in-plane crystallographic direction in Mn_3Ir (001)/Permalloy bilayers is observed. These findings are discussed in the context of antiferromagnetic domain structures, and will inform progress towards chiral antiferromagnetic spintronic devices.

DOI: 10.1103/PhysRevMaterials.3.074409

I. INTRODUCTION

Artificial (or synthetic) antiferromagnetic structures (SAFs) [1,2] have played a key role in spintronics since the invention of the spin-valve sensor for detecting tiny magnetic fields in magnetic recording read heads [3] and in magnetic tunnel junction (MTJ) memory bits for magnetic random access memory (MRAM) applications [4]. More recently, highly efficient current-driven motion of domain walls in SAFs was discovered [5], which makes possible racetrack memory devices [6] by utilizing the chirality of the magnetic structure [7]. SAFs and related multilayers are used to eliminate long-range magnetostatic fields that otherwise make nanoscopic spin valves and MTJs inoperable. Furthermore, the resonance frequencies of antiferromagnet (AF) materials can be much higher than of ferromagnet (FM) materials [8], making such materials of interest for ultrafast spin dynamics.

Motivated by these improvements in performance, the field of antiferromagnetic spintronics has rapidly grown [9], investigating a range of different materials. More recent experimental observations include spin-orbit torque switching and electrical readout of the AF state in CuMnAs [10], Mn_2Au [11], and MnTe [12], as well as spin currents and spin Hall magnetoresistance effects in MnPt [13,14]. Understanding of AF domain structure is important for the efficient control of the above effects in these metallic materials, all of which exhibit collinear AF order.

Materials with a noncollinear spin texture, such as Mn_3X ($X =$ Ir, Pt, Sn, Ge), are promising candidates for *topological* AF spintronic applications [15]. This follows the prediction of an intrinsic anomalous Hall effect (AHE) in the $L1_2$ ordered phase of cubic Mn_3Ir [16]. In addition, a facet-dependent spin Hall effect (SHE) has been measured in epitaxial thin films of Mn_3Ir [17], whose origin derives from a Berry curvature-driven effective field generated by a combination of spin-orbit coupling and symmetry breaking arising from the *chiral* AF structure [17,18].

For the related compounds Mn_3Sn and Mn_3Ge, subsequent to theoretical predictions [19], large AHE has been experimentally demonstrated in highly ordered bulk samples [20,21]. This has been enabled by the ability to align a small geometrically frustrated uncompensated in-plane magnetization via an external magnetic field, in turn coherently orienting the triangular spin configuration throughout the material and driving the system into a dominant chiral domain state [22]. Thus, the utilization of uncompensated magnetic moment to manipulate AF domain structure, and hence topological spin texture, is critical to the observation of these phenomena.

While Mn_3Sn has only recently been grown in (0001) c-axis-oriented epitaxial thin films [23], cubic Mn_3Ir has been extensively studied in the context of exchange bias, where textured polycrystalline phases [24,25] were shown to yield the largest effects in pinning the reference magnetic electrode in spin valves and MTJs [4,26]. Later developments have proceeded to use Mn_3Ir as the active element in such AF/FM heterostructures, acting as a source of spin current via SHE [27–29] and in turn generating spin-orbit torques [30] resulting in technologically attractive field-free switching of magnetic layers [31,32] desired in high-density MRAM. With such commercial realizations in mind, the use of magnetron sputtering is vital when demonstrating growth of these material systems, due to its speed, flexibility, and scalability (compared with other deposition techniques). Hence, in all

---

[*] james.taylor@mpi-halle.mpg.de
[†] stuart.parkin@mpi-halle.mpg.de

of the above implementations, samples were prepared via sputtering, resulting in polycrystalline thin films of Mn_3Ir.

On the other hand, the elucidation of novel Berry curvature-driven phenomena arising from the triangular spin texture demands test-bed materials with well-controlled crystallographic properties. To reconcile these two requirements, in this work we report the preparation, using magnetron sputtering, of epitaxial thin films of cubic Mn_3Ir with both (001) and (111) orientations. A detailed study of crystal structure shows that high-quality growth can be achieved with sputtering. By comparing our results to those in the literature, we demonstrate the unique performance of the developed deposition procedures. Measurements of the exchange bias induced in heterostructures are used to investigate the magnetic state of the films. To this end, we examine temperature dependence and training effect of exchange bias in epitaxial Mn_3Ir samples, allowing the identification of a crystalline anisotropy to blocking temperature distribution. These results are discussed in the context of topological domain configuration. By highlighting the subtle relationship between exchange bias and crystal microstructure, we underline the importance of its influence when considering noncollinear antiferromagnetic thin films for future chiral spintronic devices.

II. EXPERIMENTAL METHODS

Mn_3Ir thin films were deposited by magnetron sputtering in a BESTEC UHV system with base pressure $<9 \times 10^{-9}$ mbar, using a process Ar gas pressure of 3×10^{-3} mbar. The substrate-target distance was fixed at $\approx$150 mm, while substrates were rotated to aid homogeneous growth. Thin film samples were grown in both (001) and (111) crystal orientations with various thicknesses, as follows: MgO (001) [substrate]/Mn_3Ir (001) [3 or 10 nm]/TaN [2.5 nm] and Al_2O_3 (0001) [substrate]/TaN (111) [5 nm]/Mn_3Ir (111) [3 or 10 nm]/TaN [2.5 nm]. MgO and Al_2O_3 substrates were ultrasonically cleaned in acetone and ethanol, then clamped mechanically to a holder, and subsequently heated to 250 and 500 °C, respectively, under vacuum for 30 min before deposition.

Mn_3Ir was grown from a $Mn_{80}Ir_{20}$ alloy target, with DC sputtering power of 100 W, resulting in a composition of $Mn_{(0.72\pm0.03)}Ir_{(0.28\pm0.03)}$, that was determined by a combination of Rutherford backscattering spectroscopy (RBS) and energy-dispersive x-ray spectroscopy. As expected from the MnIr phase diagram, and confirmed by later structural measurements, this composition allows the system to form the stoichiometric Mn_3Ir phase with face-centered-cubic (fcc) crystal structure [33]. A TaN capping layer was subsequently grown *in situ* from a Ta target by rf reactive sputtering at 150 W, with 33 vol.% N_2 partial flow introduced to the sputtering gas mixture, resulting in a composition $Ta_{(0.52\pm0.05)}N_{(0.48\pm0.05)}$ as inferred from RBS.

The TaN growth rate was 0.6 Å s^{-1}, while the Mn_3Ir growth rate was 1.2 Å s^{-1}. These were measured using a quartz-crystal microbalance, and deposition times adjusted to obtain desired nominal film thicknesses. Actual thicknesses were subsequently confirmed by measuring x-ray reflectivity (XRR), with fits to the data yielding individual layer thicknesses, as shown in Fig. 1(a). Fringes are observed up to high-reflectivity angles, indicating the growth of smooth films with sharp interfaces. Two thicknesses of Mn_3Ir (3 and 10 nm) were chosen such that their exchange-bias blocking temperatures lie either below or above room temperature, respectively [34].

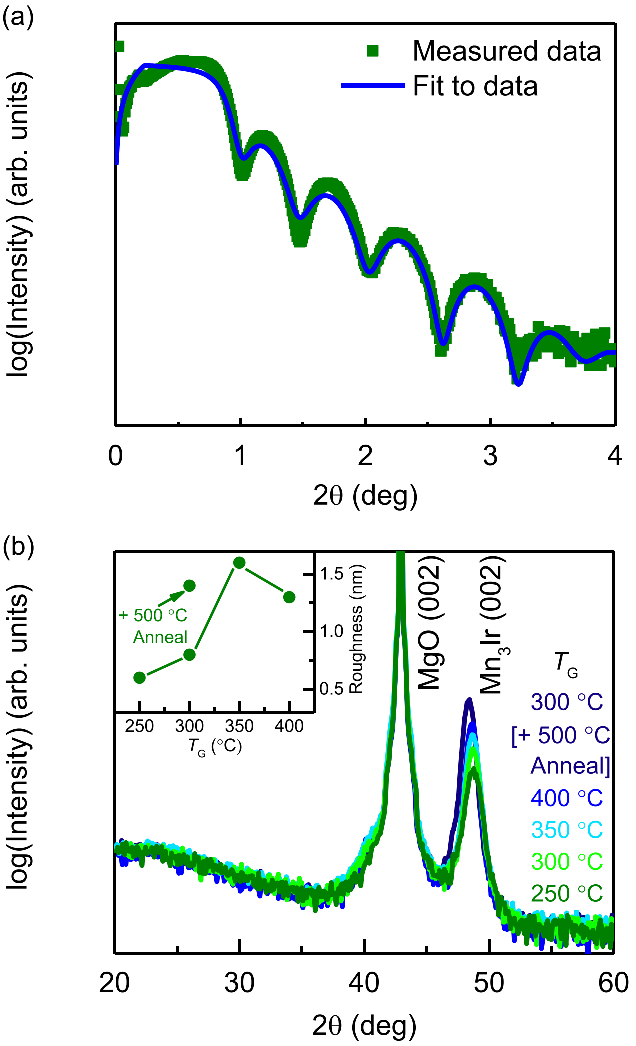

FIG. 1. (a) Measured x-ray reflectivity data from a 10-nm Mn_3Ir (001) film, with fit to determine layer thicknesses. (b) XRD 2θ-θ scans measured for 10-nm Mn_3Ir (001) films grown at different temperatures (inset shows rms roughness measured by AFM for each of these samples).

The films' crystal structure was investigated using a combination of x-ray diffraction (XRD) and transmission electron microscopy (TEM). XRD was performed using a PANalytical X'Pert^3 diffractometer with Cu $K_{\alpha1}$ radiation ($\lambda = 1.5406$ Å). Plane-view high-resolution TEM and cross-sectional high-angle annular dark-field scanning TEM (HAADF-STEM) were measured using an FEI Titan 80–300 microscope, after fabricating thin lamella via focused ion-beam milling.

III. FILM GROWTH AND STRUCTURAL CHARACTERIZATION

Mn_3Ir films with a (001) orientation were achieved by growing on (001) cut single-crystal MgO substrates [35].

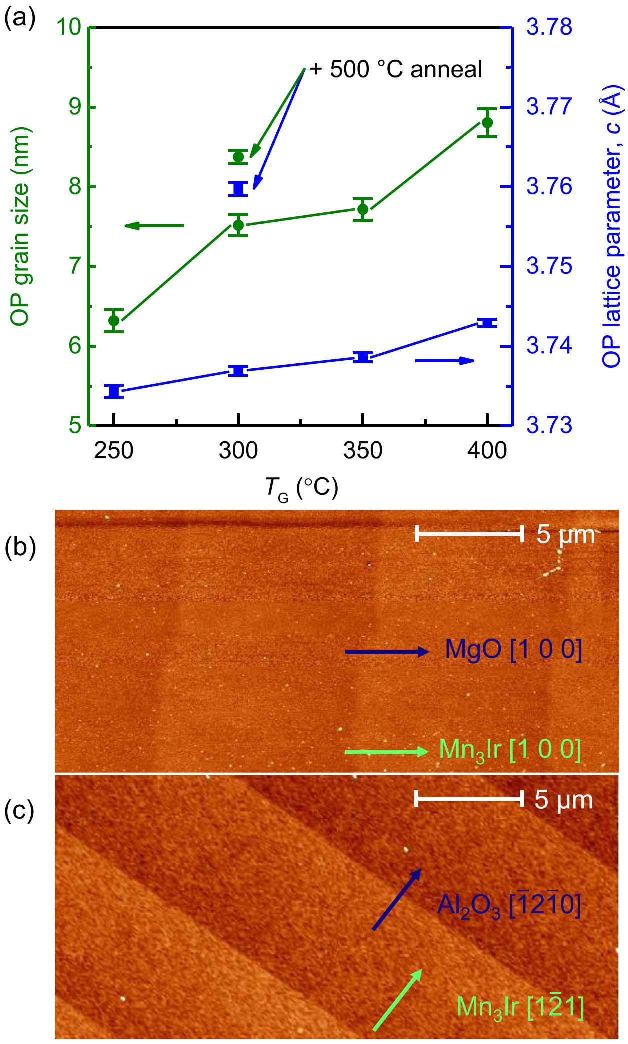

FIG. 2. (a) Dependence of grain size and OP lattice parameter on growth temperature. AFM topography maps of 3-nm Mn$_3$Ir films with (b) (001) and (c) (111) orientation.

Mn$_3$Ir was deposited as described above, at different elevated substrate temperatures (growth temperature, T_G). Figure 1(b) shows specular out-of-plane (OP) 2θ-θ XRD patterns for the resulting 10-nm-thick films. In all cases a Mn$_3$Ir (002) diffraction peak is observed, indicating growth of Mn$_3$Ir with a (001) crystal orientation. From the full width at half maximum (FWHM) of this peak, the size of crystalline grains in the OP direction can be estimated using the Scherrer formula, as plotted in Fig. 2(a). The intensity of the (002) peak increases with T_G, while its FWHM decreases. This indicates the (001) texture of the film strengthens with increasing T_G, due to the growth of larger grains of consistent crystal orientation. Such a process is further enhanced by *in situ* annealing for 60 min at 500 °C.

The variation of OP lattice parameter, c, is also plotted in Fig. 2(a). As T_G is increased, c relaxes towards the bulk value, presumably because of a combination of the elevated temperature improving adatom mobility and the lower thermal expansion coefficient of the insulating substrate with respect to the metallic film. This process is accentuated by postannealing, after which c approaches the bulk value of 3.780 Å.

The average roughness of the Mn$_3$Ir layers as a function of growth temperature is plotted in the inset of Fig. 1(b), as measured from atomic force microscopy (AFM) studies. The roughness increases markedly for T_G above 300 °C and after postannealing. As such, subsequent samples were grown at 300 °C without postannealing, to achieve a compromise between high-quality crystal structure and a smooth surface. Under these conditions, $c = (3.737 \pm 0.001)$ Å, remaining slightly below the bulk value. Figure 2(b) shows an AFM topographical map from a 3-nm-thick film grown under such conditions, where terraces of the MgO substrate can be seen stacked along the [100] crystal axis, with the Mn$_3$Ir following these and showing a low root-mean-square (rms) roughness of ≈ 8 Å (measured over an area of 25 μm^2). This is in agreement with the roughness parameter of ≈ 6 Å extracted from fitting XRR measurements.

In this growth mode, Mn$_3$Ir has a fcc crystal lattice, and can grow in either an $L1_2$ ordered phase ($Pm\bar{3}m$, space group = 221), the crystal and magnetic structure of which is displayed in Fig. 3(a), or a γ disordered phase ($Fm\bar{3}m$, space group = 225) showing site disorder on the respective sublattices [36]. Contrary to previous reports, no (001) superstructure peak from Mn$_3$Ir is observed in the XRD patterns in Fig. 1(b) [37,38]. Instead, our thin films grow in the γ-Mn$_3$Ir phase, possessing the noncollinear AF order determined by Kohn *et al.* [36], where the Mn moments have been shown to cant slightly out of the (111) plane.

To evaluate the in-plane (IP) orientation of the Mn$_3$Ir (001) thin films grown at 300 °C, pole figure XRD measurements were performed in which the azimuthal angle Φ is scanned as a function of tilt angle χ, with 2θ-θ fixed at the (111) reflection of a 10-nm Mn$_3$Ir (001) film. The [100] and [010] edges of the MgO substrate were aligned along $\phi = 0^\circ$ and $\phi = 90^\circ$, respectively. The resulting map is shown in Fig. 3(b), with the four sharp peaks demonstrating well-defined IP crystal axes arising from a highly oriented thin film with cubic symmetry [37,39]. Furthermore, the peak positions indicate cube-on-cube growth with respect to the MgO substrate, with the epitaxial relationship: MgO (001) [100] ∥ Mn$_3$Ir (001) [100]. A schematic illustration of this relationship is displayed in Fig. 3(a).

Having determined their IP orientation, 2θ-θ XRD scans (longitudinal direction) at different ω offset angles (transverse direction) were recorded such that the (111) reflections from both the 10-nm Mn$_3$Ir (001) film and the MgO (001) substrate were observed. Figure 4(a) shows a map of such off-specular ($\theta \neq \omega$) measurements, in which the FWHM of the Mn$_3$Ir peak in the transverse scans along the ω axis demonstrates a mosaicity $\approx 2^\circ$, comparable with that reported for molecular-beam epitaxy (MBE)-grown films [36]. Table I summarizes the structural parameters obtained for both the (001) and (111) oriented films deposited here, and compares them with results previously reported in the literature. Meanwhile, the FWHM in longitudinal scans along the 2θ axis can be converted to an average crystallite size of (10.6 ± 0.7) nm, comparable with other reports [37]. This contains both IP and OP contributions to grain size suggesting that, since vertical grain size was already determined to be slightly below film

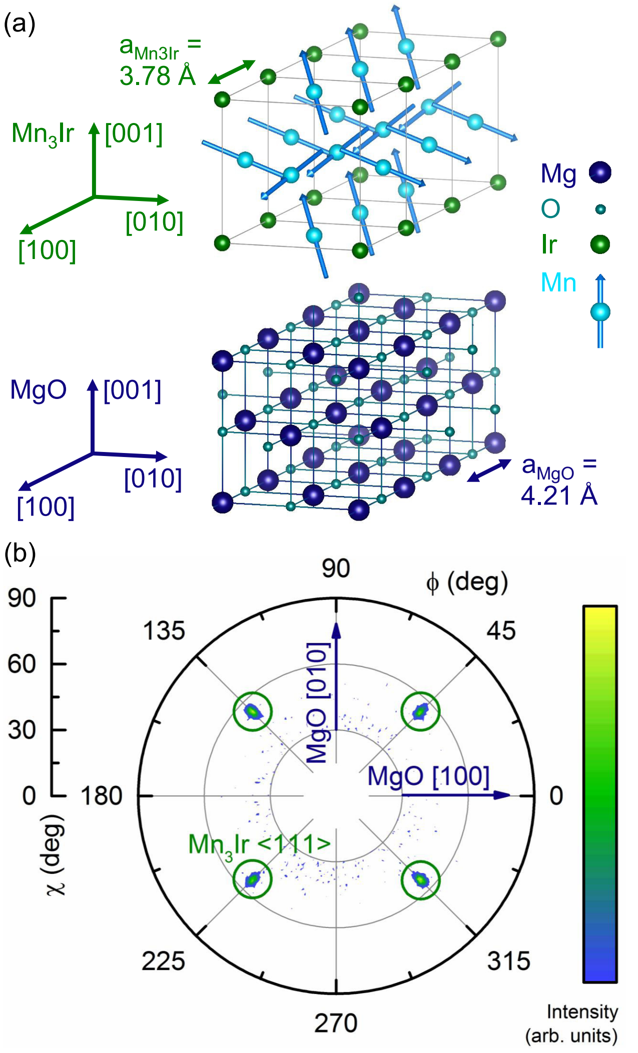

FIG. 3. (a) Crystal and magnetic structure of $L1_2$ ordered Mn_3Ir with [001] axis directed out-of-plane, demonstrating cube-on-cube epitaxy with a (001)-oriented MgO substrate. (b) XRD χ-ϕ pole figure measuring ⟨111⟩ peaks in a 10-nm Mn_3Ir film with (001) orientation, aligned such that the [100] and [010] axes of the MgO substrate are directed along $\phi = 0^\circ$ and $\phi = 90^\circ$, respectively.

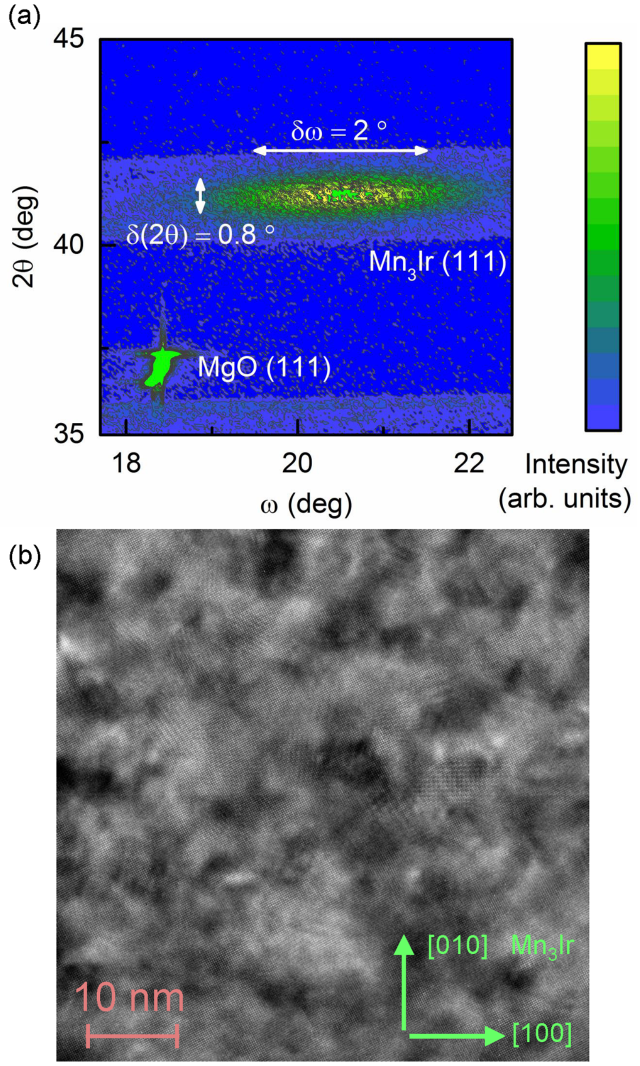

FIG. 4. (a) XRD off-specular scan map measuring (111) reflections from a 10-nm Mn_3Ir film with (001) orientation and the MgO (001) substrate upon which it is grown. (b) Plane-view TEM image of a 3-nm Mn_3Ir (001) thin film, prepared using ion-beam backside thinning.

thickness, crystallites grow larger laterally. This is confirmed by plane-view TEM measurements, displayed in Fig. 4(b). The in-plane microstructure of the sample is visible, with high contrast produced between crystallites with small mosaic spread, showing lateral grain sizes between 10 and 15 nm.

Finally, the IP lattice parameter, a, for a 10-nm Mn_3Ir (001) film grown at 300 °C was calculated to be $a = (3.808 \pm 0.009)$ Å, using the relationship $a = \frac{1}{\sqrt{2}}\sqrt{[(3d_{111})^2 - c^2]}$ [where d_{111} is the interplanar lattice spacing determined from the (111) peak position]. Thus, the film grows with an IP lattice expansion $\varepsilon_{\parallel} = 0.74\%$, and a corresponding OP lattice contraction $\varepsilon_{\perp} = -1.14\%$, in agreement with the literature [36]. Due to a large lattice mismatch (≈10%) with MgO (001) ($a = 4.212$ Å), the Mn_3Ir (001) film couples only weakly to the substrate which, while sufficient to seed cube-on-cube growth, will not introduce epitaxial strain. Instead, $\varepsilon_{\parallel}$ and $\varepsilon_{\perp}$ can be understood in terms of the film undergoing a small elastic distortion, where unit-cell volume remains almost unchanged with respect to the bulk. We note that mosaicity is increased and lateral grain size suppressed with respect to (111)-orientated films described subsequently. This can be explained by the simultaneous weak substrate-film interaction, combined with the inherent energetic instability of the (001) surface in fcc crystal structures, leading to frequent relaxation of the slight tetragonal distortion in Mn_3Ir, creating a higher areal density of grain boundaries and an enhanced rotation between neighboring grains.

Moving on to the characterization of Mn_3Ir thin films with a (111) orientation deposited on Al_2O_3 (0001) substrates ($a =$ 4.759 Å), in this case γ-Mn_3Ir grows with the same fcc structure, but with the (111) crystal planes lying in the film plane in registry with the hexagonal substrate. Figure 5(a) shows

TABLE I. Summary of crystal-structure parameters indicative of high-quality thin films, comparing the superior quality growth achieved in this work with previously published results discussed in the main text. Magnitude of exchange-bias fields reported for different heterostructure configurations, as well as the resulting interfacial exchange anisotropy energy densities, are also quoted alongside the thickness of the Mn$_3$Ir film utilized and the temperature of the measurement.

Growth technique	Material system	Lattice parameter (Å)	Mosaic spread (°)	Grain size (nm)	Exchange bias field, $\mu_0 H_{\rm EB}$ (mT)	Exchange anisotropy energy density, $J_{\rm K}$ (erg cm^{-2})
Magnetron sputtering [this work]	γ-Mn$_3$Ir (001) [/NiFe]	c, 3.737 ± 0.001 a, 3.808 ± 0.009	2	OP: 7.5 IP: 10–15	28 (10 nm@RT) 121 (3 nm@5 K with $\mu_0 H_{\rm FC}$ ∥ [110]) 104 (3 nm@5 K with $\mu_0 H_{\rm FC}$ ∥ [100]) 77 (3 nm@5 K with $\mu_0 H_{\rm FC}$ ∥ [100] after training)	0.107 (10 nm@RT) 0.462 (3 nm@5 K with $\mu_0 H_{\rm FC}$ ∥ [110]) 0.397 (3 nm@5 K with $\mu_0 H_{\rm FC}$ ∥ [100]) 0.294 (3 nm@5 K with $\mu_0 H_{\rm FC}$ ∥ [100] after training)
	γ-Mn$_3$Ir (111) [/NiFe]	c, 3.797 ± 0.001 a, 3.84 ± 0.08	0.5	OP: 10.1 IP: 20	29 (10 nm@RT) 95 (3 nm@5 K) 27 (3 nm@5 K after training)	0.115 (10 nm@RT) 0.361 (3 nm@5 K) 0.103 (3 nm@5 K after training)
MBE [37]	[Fe (001)/] γ-Mn$_3$Ir (001)	a, 3.79 ± 0.05	6	10	4 (10 nm@RT)	
MBE [36]	[Fe (001)/] γ-Mn$_3$Ir (001)	c, 3.736 ± 0.008 a, 3.80	2		6 (15 nm@RT)	0.07 (15 nm@RT)
	$L1_2$-Mn$_3$Ir (001) [/Fe (001)]	c, 3.725 ± 0.005 a, 3.81			31 (15 nm@RT)	0.37 (15 nm@RT)
Magnetron sputtering [38]	$L1_2$-Mn$_3$Ir (111)	c, 3.78 a, 3.80	2.8	15		
Magnetron sputtering [59,60]	$L1_2$-Mn$_3$Ir (111) [/CoFe]			8.5	≈200 mT (10 nm@RT)	1.3 (10 nm@RT)
Magnetron sputtering [39]	γ-Mn$_3$Ir (001) [/CoFe]			OP :≈ 10 IP: >20		≈0.2 (10 nm@RT)
	γ-Mn$_3$Ir (111) [/CoFe]					≈0.35 (10 nm@RT)
	γ-Mn$_3$Ir (poly) [/CoFe]					≈0.45 (10 nm@RT)
Magnetron sputtering [25]	γ-Mn$_3$Ir (poly) [/CoFe]			6	≈42 mT (9 nm@RT)	
				12	≈35 mT (9 nm@RT)	
				≈6	≈40 mT (3 nm@ ≈ 5 K)	
Magnetron sputtering [46]	γ-Mn$_3$Ir (poly) [/CoFe]				≈8 mT	

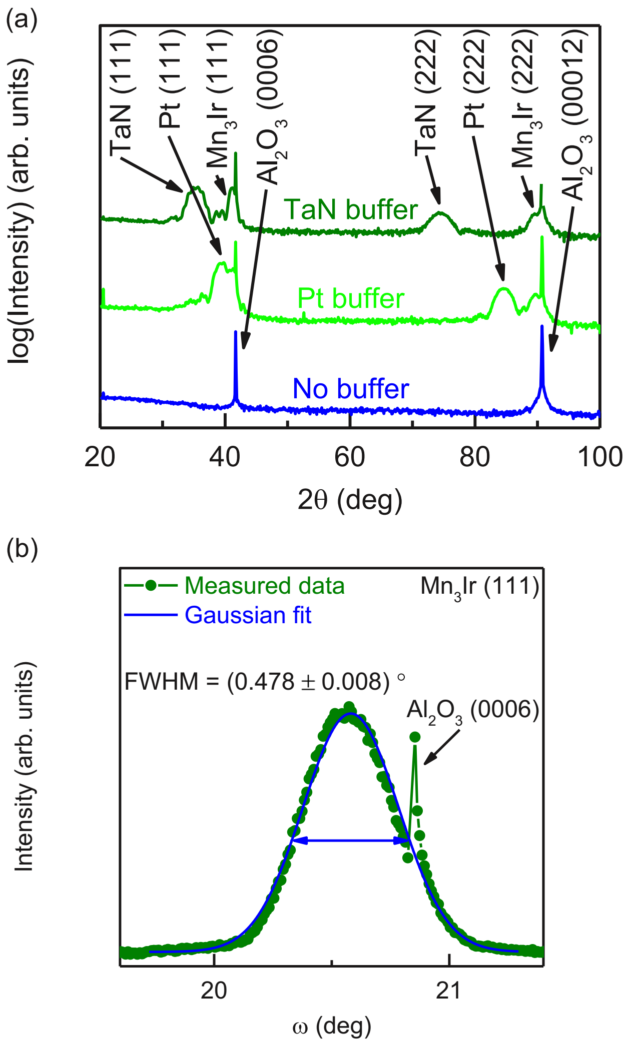

FIG. 5. (a) XRD 2θ-θ patterns measured for 10-nm Mn_3Ir (111) films grown using different buffer layers (scans are offset for clarity). (b) XRD ω rocking curve for a 10-nm Mn_3Ir (111) film grown on a TaN buffer layer, with fit to determine FWHM.

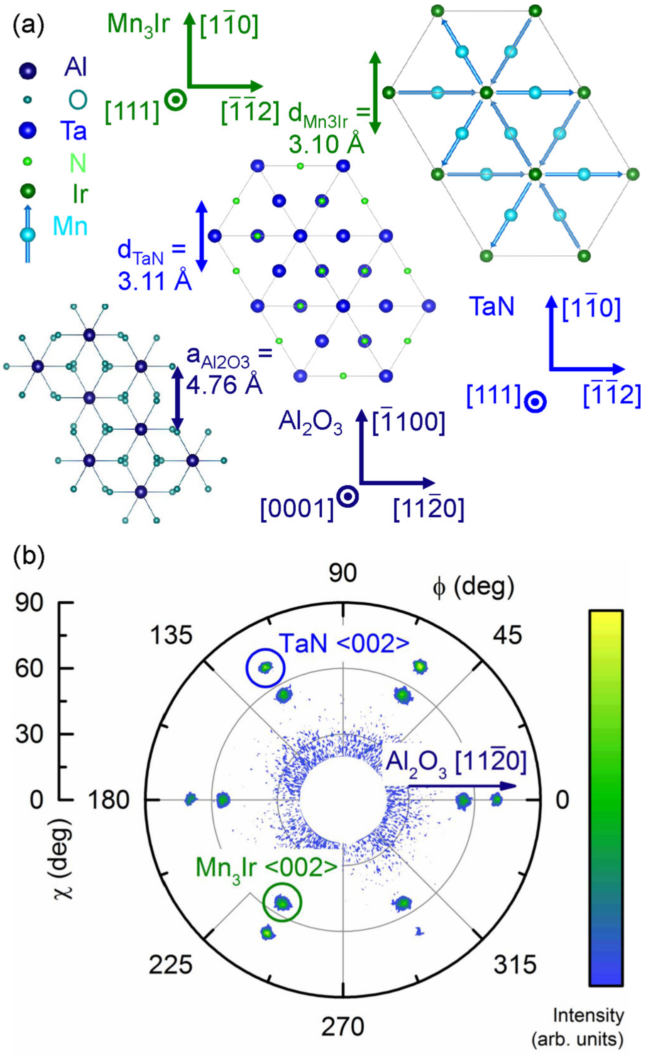

FIG. 6. (a) Crystal and magnetic structure of (111) planes in $L1_2$ ordered Mn_3Ir, of (111) planes in TaN and of (0001) planes in Al_2O_3, showing the epitaxial relation between them as viewed along the OP axis. (b) XRD χ-ϕ pole figure measuring ⟨002⟩ peaks in a 10-nm Mn_3Ir film with (111) orientation and a 5-nm TaN (111) buffer layer, aligned such that the [$11\bar{2}0$] axis of the Al_2O_3 substrate is directed along $\phi = 0°$.

specular OP 2θ-θ XRD patterns for 10-nm Mn_3Ir films grown according to the previously discussed conditions, but now utilizing various buffer layers. In the case where Mn_3Ir is grown directly on Al_2O_3 (0001), no crystalline structure is observed. This can be explained by a significant variation in interface free energies between the Al_2O_3 (0001) and Mn_3Ir (111) surfaces making this growth mode unfavorable [40], a difference that may be reduced by the introduction of a buffer layer.

Therefore, two different buffer layers were employed; either 5-nm Pt or 5-nm TaN was deposited on Al_2O_3 substrates held at 500 °C. TaN was prepared according to the conditions described above, while Pt was deposited using a DC sputtering power of 50 W at a rate of 1.0 Å s^{-1}. Intense (111) and (222) peaks arising from both Pt and TaN are observed in Fig. 5(a), indicating that both films grow epitaxially on the hexagonal substrate with a sharp (111) texture [41]. Furthermore, both buffer layers seed a (111) orientation into the subsequently deposited 10-nm Mn_3Ir. A TaN buffer was chosen for further samples, giving the advantages of chemical stability, a smooth surface (with rms roughness of <3 Å confirmed by AFM), and a high resistance (measured as >2 mΩ cm via a four-probe method, in agreement with literature values [42]). From the OP 2θ-θ XRD pattern in Fig. 5(a), a lattice parameter for TaN of (4.397 ± 0.004) Å is measured, which is close to the value for relaxed TaN thin films of 4.383 Å [42].

A lattice parameter value of (3.797 ± 0.001) Å is deduced for Mn_3Ir (111). This is very close to the bulk value, indicating that the film grows fully relaxed, in agreement with sputtered films prepared by Jara *et al.* [38]. OP grain size is calculated via the Scherrer formula to be (10.1 ± 0.3) nm, again demonstrating the correlation of grain size vertically with film thickness. A low mosaic spread in the film is measured as (0.478 ± 0.008)° by recording a ω rocking curve XRD scan about the Mn_3Ir (111) peak, displayed in Fig. 5(b). This low mosaicity, alongside the high-quality (111) crystal structure, can be attributed to the small lattice mismatch when using a TaN buffer layer, allowing relaxed film growth with minimal introduction of misfit dislocations or other defects. Indeed, between two periods of the Al_2O_3 substrate lattice and three of the TaN buffer, the lattice mismatch amounts to 2.0%, which in turn reduces to just 0.3% between the (111)-oriented TaN and the kagome planes of Mn atoms, based on measured lattice parameters. The rms roughness of the films is <4 Å, as extracted from Fig. 2(c), where the step and terrace topography of the Al_2O_3 substrate is observed via AFM through a 3-nm Mn_3Ir (111) film.

Based on this analysis of lattice mismatch, Fig. 6(a) displays the expected IP orientation of the stack, alongside experimentally determined lattice parameters. This mode of epitaxial growth was confirmed by XRD pole figures, presented in Fig. 6(b), measuring the (002) reflections of (111)-oriented TaN and Mn_3Ir when the $[11\bar{2}0]$ axis of the substrate was aligned along $\phi = 0^\circ$. The sharp peaks observed provide evidence of coherent IP crystallographic directions, while their sixfold symmetry suggests rotational twinning between (111) crystal planes [38,39]. The relative positions of the reflections confirm pseudo-hexagon-on-hexagon epitaxial growth throughout the stack, and allow the determination of the following epitaxial relationship, illustrated in Fig. 6(a): $Al_2O_3\,(0001)\,[11\bar{2}0]\,[\bar{1}100] \parallel \mathrm{TaN}(111)\,[\bar{1}\bar{1}2]\,[1\bar{1}0] \parallel Mn_3Ir(111)\,[\bar{1}\bar{1}2]\,[1\bar{1}0]$.

Additional TEM measurements on the (111)-oriented samples investigated the film structure at the nanoscale. A cross-section HAADF-STEM image of a 10-nm Mn_3Ir film is displayed in Fig. 7(a), viewed along the $[1\bar{1}0]$ zone axis. The epitaxial growth of the TaN (111) buffer and Mn_3Ir (111) film is clearly seen, demonstrating high-quality crystal structure with sharp interfaces and few defects. An absence of grain boundaries observed within the field of view suggests growth of large grains in the lateral direction, with a size of >20 nm.

Figure 7(b) shows a fast Fourier transform diffractogram of the lattice plane image in Fig. 7(a), with (*hkl*) diffraction peaks indexed. The positions of the diffraction spots confirm the epitaxial relationship between the layers. They further allow the determination of the predominantly IP lattice parameter along the [001] direction: (4.35 ± 0.09) Å for TaN and (3.84 ± 0.08) Å for Mn_3Ir. These agree, within uncertainty, with the OP lattice parameters measured from XRD, confirming the relaxed growth of Mn_3Ir (111). Table I collates the different crystal-structure figures of merit measured for our thin films, demonstrating the competitive performance of the magnetron sputtering growth protocols developed here with those previously published.

IV. EXCHANGE BIAS

Exchange bias (EB) was studied in bilayer samples of Mn_3Ir/FM. To achieve this, replicas of the above samples were prepared incorporating a layer of 5 nm $Ni_{80}Fe_{20}$ (=Py, Permalloy), grown from a $Ni_{80}Fe_{20}$ alloy target at a rate of $1.2\,\text{Å}\,\text{s}^{-1}$ via 75-W DC magnetron sputtering after samples had cooled to room temperature (RT), resulting in the growth of polycrystalline Py with composition $Ni_{(0.80\pm0.01)}Fe_{(0.20\pm0.01)}$ (measured by RBS). The magnetic properties of the resulting heterostructures were measured using superconducting quantum interference device vibrating sample magnetometry (Quantum Design MPMS3).

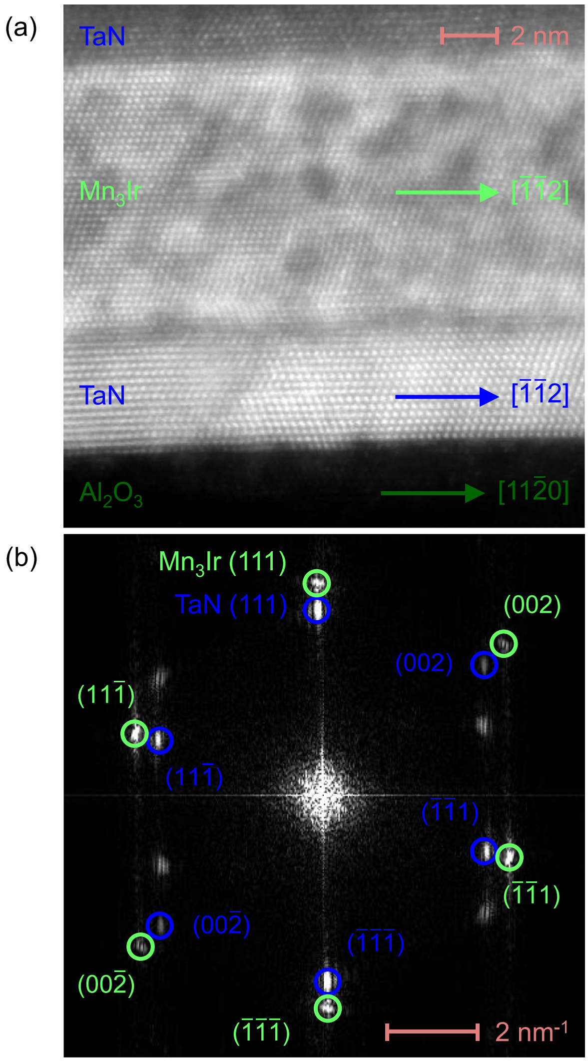

FIG. 7. (a) Cross-sectional HAADF-STEM image of a 10-nm Mn_3Ir (111) film, grown on an Al_2O_3 substrate with (0001) orientation using a 5-nm (111) textured TaN buffer layer, viewed along the $[1\bar{1}0]$ zone axis. (b) Diffractogram (fast Fourier transform) of the above experimental image. The epitaxial correlation between the Mn_3Ir and TaN lattices is demonstrated by the corresponding indexed reflections.

EB occurs in coupled AF/FM systems, introducing a unidirectional anisotropy to the bilayer. This manifests itself as a shift in the FM magnetization hysteresis loop along the applied field axis, the exchange-bias field ($\mu_0 H_{\mathrm{EB}}$), as well as an enhancement of coercive field ($\mu_0 H_{\mathrm{C}}$) [43,44]. EB is generally regarded as resulting from uncompensated spins at the interface of the AF [45,46], which exchange couple to moments in the FM layer [47,48]. These uncompensated AF spins are, in turn, strongly pinned in the direction of unidirectional anisotropy by AF domains that extend into the bulk of the film [49,50]. EB is set in a given direction at sufficient temperatures to overcome an energy barrier to AF domain reorientation, namely the blocking temperature, T_{B}. Here the application of an external magnetic field that saturates the FM

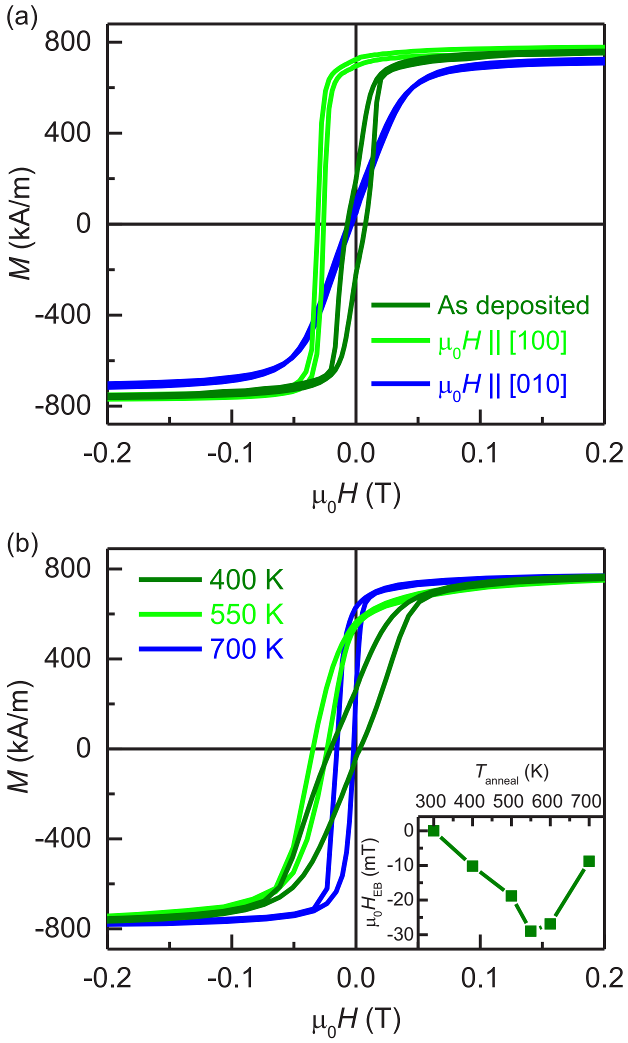

FIG. 8. (a) Magnetization hysteresis loops at 300 K for an as-deposited 10-nm Mn_3Ir (001)/Py bilayer, and for the same sample after 1-T IP field annealing at 550 K (with $\mu_0 H_{FA} \parallel [100]$), with IP measurement field directed parallel and perpendicular to $\mu_0 H_{FA}$. (b) Magnetization hysteresis loops at 300 K for a 10-nm Mn_3Ir (111)/Py bilayer after 1-T IP field annealing at different temperatures (with $\mu_0 H_{FA} \parallel [\bar{1}\bar{1}2]$) (inset shows variation of $\mu_0 H_{EB}$ with annealing temperature).

will also align the coupled uncompensated moments, in turn leading to coherent orientation of bulk AF domains [51,52]. As the heterostructure is cooled, the preferential AF domain alignment becomes fixed below T_B and exchange anisotropy is set in the direction of the external field [49,50]. The various characteristics of EB are determined by the thermal stability of the resulting AF domain walls, and hence depend intimately on film microstructure [53,54].

For the case of 10-nm Mn_3Ir/Py bilayers, T_B lies above 300 K, meaning an EB can be stabilized at RT [24]. Figure 8(a) shows magnetization (M) measured as a function of IP field ($\mu_0 H$) for a 10-nm Mn_3Ir (001)/Py bilayer; both as-deposited and after 30-min magnetic-field annealing (FA) at 550 K and subsequent cooling in a 1-T magnetic field ($\mu_0 H_{FA}$) applied along the [100] crystal direction (performed *ex situ* in a furnace at a pressure $<9 \times 10^{-6}$ mbar). The field annealing procedure did not result in modification of the crystal structure of the bilayer, as confirmed by XRD measurements. In the as-deposited state, no shift in the magnetization hysteresis (*MH*) loop can be seen. Following the IP field-annealing procedure, a shift in the *MH* loop of $\mu_0 H_{EB} = -28$ mT, measured with applied field along the [100] axis in Mn_3Ir, demonstrates the onset of EB. This value of $\mu_0 H_{EB}$ is equivalent to a unidirectional anisotropy energy density (defined as $J_K = M_S d_F \mu_0 H_{EB}$, where M_S is the saturation magnetization and d_F is the thickness of the FM layer [55]) of $J_K = 0.107\,\mathrm{erg\,cm^{-2}}$ (in turn equivalent to $10.7\,\mathrm{nJ\,cm^{-2}}$). Magnetization measured with external field along the perpendicular [010] crystallographic direction shows a hard axis response, confirming the unidirectional nature of the induced anisotropy. The negative shift of the hysteresis loops indicates the exchange anisotropy is set in the same direction as the field applied during annealing. This is because of the parallel coupling between interfacial Mn spins and Ni magnetic moments, which is shown to dominate over antiparallel coupling with Fe when smoothly varying Py to a Ni-rich composition [56]. These uncompensated AF moments become, in turn, strongly pinned in their preferred direction by the dominant AF domain state in the bulk of the Mn_3Ir film as the sample is cooled through T_B [55].

Figure 8(b) shows *MH* loops measured for a 10-nm Mn_3Ir (111)/Py heterostructure with field applied along the $[\bar{1}\bar{1}2]$ crystalline direction after 30-min *ex situ* 1-T IP field annealing at different temperatures, T_{anneal}. In all cases, a negative shift of the hysteresis loop indicates the introduction of a unidirectional exchange anisotropy. The inset of Fig. 8(b) shows the variation in $\mu_0 H_{EB}$ with T_{anneal}. A maximum $\mu_0 H_{EB} = -29$ mT is achieved after IP FA at 550 K, corresponding to a unidirectional anisotropy energy density of $J_K = 0.115\,\mathrm{erg\,cm^{-2}}$ ($J_K = 11.5\,\mathrm{nJ\,cm^{-2}}$). Higher annealing temperatures lead to a degradation of $\mu_0 H_{EB}$, indicating that T_B of these bilayers is close to 550 K, comparable to other values for epitaxially grown Mn_3Ir films in the literature [35]. Contrary to Ref. [39], where larger $\mu_0 H_{EB}$ is measured for (111) textured films of similar thickness, we find similar $\mu_0 H_{EB}$ for both Mn_3Ir orientations. In our case, larger than expected $\mu_0 H_{EB}$ for (001)-orientated films may be explained by these samples containing a higher density of grain boundaries and larger mosaicity compared with the (111) films, as discussed above, which may act to enhance EB by introducing pinning sites to stabilize AF domain formation [57].

Table I compares EB values achieved in these bilayers with optimized $\mu_0 H_{EB}$ and J_K previously reported. The $\mu_0 H_{EB}$ and J_K values achieved here compare favorably with other epitaxially grown films, also reinforcing the assertion that our Mn_3Ir thin films possess a noncollinear AF order (since EB is shown to degrade significantly when transitioning towards the collinear AF phase of $Mn_{50}Ir_{50}$ [58]). Nevertheless, for both orientations we measure lower $\mu_0 H_{EB}$ and J_K compared to maximized values in the literature. This is because larger values of $\mu_0 H_{EB}$ and J_K are obtained in textured polycrystalline films containing much smaller grains (thus more pinning sites) [25] and a fraction of $L1_2$ ordered Mn_3Ir phase [59,60].

On the other hand, the T_B of 3 nm Mn_3Ir/Py bilayers will lie below RT. It has been shown that T_B decreases rapidly when

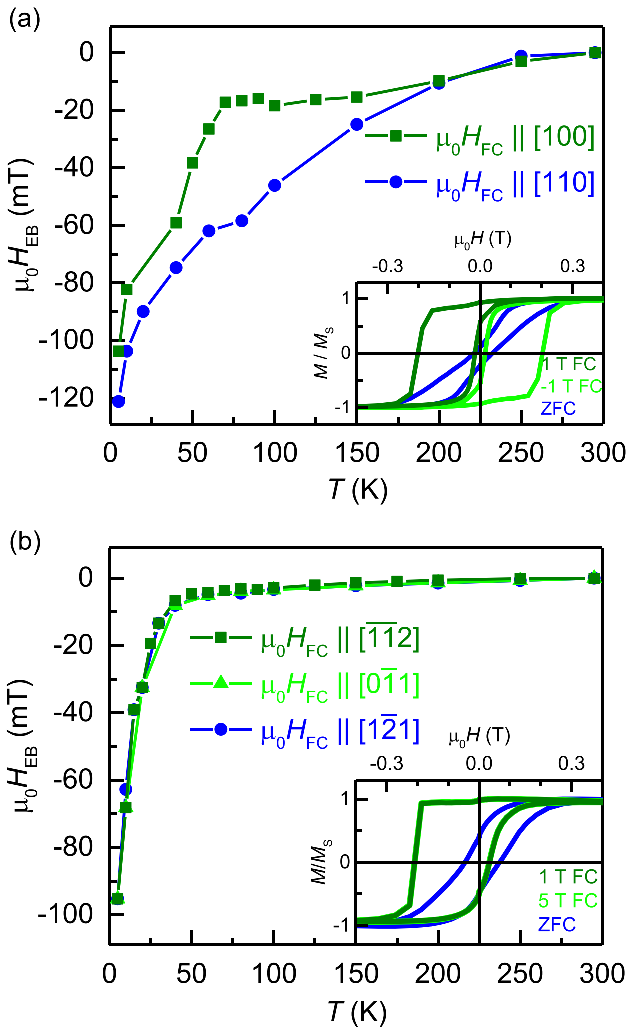

FIG. 9. (a) $\mu_0 H_{\rm EB}$ measured at different temperatures after 1-T IP field cooling from 400 K for a 3-nm $\rm Mn_3Ir$ (001)/Py bilayer, with $\mu_0 H_{\rm FC} \parallel [100]$ and [110] crystal axes (inset shows normalized magnetization hysteresis loops recorded at 5 K after different field-cooling protocols with $\mu_0 H_{\rm FC} \parallel [100]$). (b) $\mu_0 H_{\rm EB}$ measured at different temperatures after 1-T IP field cooling from 400 K for a 3-nm $\rm Mn_3Ir$ (111)/Py bilayer, with $\mu_0 H_{\rm FC} \parallel [\bar{1}\bar{1}2]$, $[0\bar{1}1]$, and $[1\bar{2}1]$ crystal axes (inset shows normalized magnetization hysteresis loops recorded at 5 K after different field-cooling protocols with $\mu_0 H_{\rm FC} \parallel [\bar{1}\bar{1}2]$).

$\rm Mn_3Ir$ thickness is reduced below 5 nm [24,57] due to the reduced thermal stability of the AF domain state [61]. However, no studies of EB in ultrathin epitaxial $\rm Mn_3Ir$ films have previously been reported. Figure 9(a) shows the value of $\mu_0 H_{\rm EB}$ measured for such a bilayer with (001) orientation after 1 T IP field cooling (FC) from 400 K to different temperatures, T. The inset to Fig. 9(a) shows an example of the individual *MH* loops measured at 5 K after zero-field cooling (ZFC), +1-T IP field cooling and −1-T IP field cooling. Shifting of the *MH* loop along the applied field axis after field cooling, as opposed to ZFC, indicates the onset of EB at low temperatures and demonstrates the essential role of the external field ($\mu_0 H_{\rm FC}$) in selecting a preferred direction for interfacial AF spins. The reversal of the unidirectional anisotropy after −1-T field cooling confirms the parallel coupling of the uncompensated Mn and FM Ni moments, while also showing the ability to manipulate interfacial magnetic structure and AF domain orientation as a function of field cooling.

Figure 9(a) also shows the change in $\mu_0 H_{\rm EB}$ when exchange anisotropy is induced by cooling the sample (and subsequently measuring) with magnetic field applied along different crystallographic directions. An onset of $\mu_0 H_{\rm EB}$ increase indicates $T_{\rm B}$ of the heterostructures. With EB along the [110] crystal axis, a higher $T_{\rm B} \approx 150\,{\rm K}$ is observed compared with the [100] axis ($T_{\rm B} \approx 60\,{\rm K}$), as well as larger values of $\mu_0 H_{\rm EB}$ at equivalent temperatures, in agreement with Ref. [35]. There is no obvious relation between microstructure (e.g., film terrace orientation measured by AFM) and this preferential axis for unidirectional anisotropy. However, an epitaxial AF layer can imprint its magnetocrystalline anisotropy onto a polycrystalline FM layer in exchange-coupled heterostructures [62]. EB phenomena are then governed by a combination of unidirectional exchange anisotropy set through field cooling, and an anisotropy determined by the AF crystal symmetry. In our case, the enhanced $T_{\rm B}$ along the [110] direction may be caused by a different magnetocrystalline anisotropy compared with the [100] axis, in turn connected to the alignment of Mn moments in the γ-$\rm Mn_3Ir$ structure at 45° to the cubic crystallographic edges. The triangular spin texture of epitaxial $\rm Mn_3Ir$ films has been shown to have a significant influence on the magnetization reversal mechanism in AF/FM bilayers [36], and, while the relationship between $\mu_0 H_{\rm EB}$ and magnetocrystalline easy axes of epitaxial FM layers has been studied [63], the effect of crystalline anisotropy in noncollinear AF films on EB is open to further exploration.

The measurement of $\mu_0 H_{\rm EB}$ in a 3-nm $\rm Mn_3Ir$ (111)/Py bilayer at different temperatures after 1-T IP field cooling from 400 K is shown in Fig. 9(b). In this case, no difference is seen in $\mu_0 H_{\rm EB}$ with cooling field applied along different crystal directions. This may be due to sixfold IP crystalline symmetry in these samples, such that no direction provides a preferential axis for EB setting. Observed $T_{\rm B} \approx 40\,{\rm K}$ is found to be lower than (001)-oriented $\rm Mn_3Ir$, as is $\mu_0 H_{\rm EB}$ at equivalent temperatures, with maximum $\mu_0 H_{\rm EB} = -95$ mT at 5 K. Again, this may be attributable to higher-quality epitaxial growth of (111) films, introducing less defects and grain boundaries to stabilize AF domains at a given temperature [57].

The inset of Fig. 9(b) shows individual *MH* loops recorded at 5 K following IP field cooling with different external field strengths. The asymmetric shape of the hysteresis loops indicates that the magnetization of the Py layer reverses via the same two distinct mechanisms, domain-wall nucleation/propagation on the downward sweep of magnetic field and coherent magnetization rotation on the recoil branch, as previously discovered for $\rm Mn_3Ir$ [64]. In addition, $\mu_0 H_{\rm EB}$ is invariant with field strength as expected, again indicating the potential uses of EB in manipulating AF order using low applied fields. Indeed, EB may play a valuable role when utilizing chiral AFs for spintronic applications, by setting a dominant domain state in a material [51] with otherwise large internal anisotropy fields, when the uncompensated moment induced at the interface [48] acts to coherently orient triangular spin configuration. Extending this concept to materi-

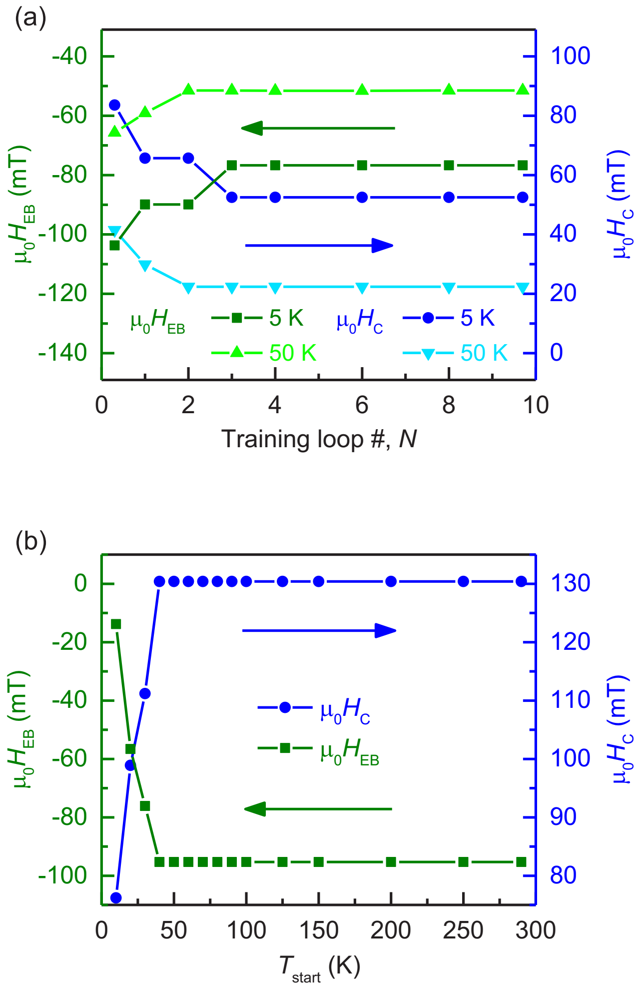

FIG. 10. (a) Exchange-bias training effect showing variation of μ_0H_{EB} and μ_0H_C with successive measurement field cycles at different temperatures after 1-T IP field cooling from 300 K for a 3-nm Mn_3Ir (001)/Py bilayer (with $\mu_0H_{FC} \parallel [100]$). (b) Blocking temperature distribution showing μ_0H_{EB} and μ_0H_C measured at 5 K after 1-T IP FC from different starting temperatures for a 3-nm Mn_3Ir (111)/Py bilayer (with $\mu_0H_{FC} \parallel [\bar{1}\bar{1}2]$).

als such as Mn_3Sn [20], where weak magnetization can be used to directly manipulate chiral domain orientation [22], exchange interactions across heterostructures of epitaxially grown noncollinear AF films could be used to control topological spin textures. AF domains in Mn_3Ir, and their relation to uncompensated moment, are considered in our subsequent work [65].

For such realizations, an important consideration is the EB training effect. Here the measured μ_0H_{EB} and μ_0H_C decrease over the course of successive external applied magnetic-field cycles. This arises because a portion of the uncompensated AF moments at the interface, that contribute to exchange coupling after the initial field-cooling procedure, are only weakly pinned to the bulk AF structure. They are thus free to follow the reversing magnetization of the FM layer, and so are reorientated by the external field [45]. In Fig. 10(a) the change in μ_0H_{EB} and μ_0H_C measured over the course of consecutive training-field cycles is shown for a (001)-oriented 3-nm Mn_3Ir/Py bilayer, following 1-T IP field cooling from 300 K to different temperatures. In all cases, it is observed that, after at most four applied field cycles, both μ_0H_{EB} and μ_0H_C reach equilibrium values and do not change further. At this point all weakly pinned uncompensated Mn spins are relaxed. The remaining exchange bias is modulated by interfacial AF spins that are strongly coupled to the bulk Mn_3Ir domain state [48]. Similar results are seen for 3-nm Mn_3Ir (111)/Py heterostructures (not shown).

These resulting values of exchange bias therefore depend on the stability of the AF order, and hence on the temperature to which the bilayer was field cooled. While before training both Mn_3Ir orientations show large $\mu_0H_{EB} \geqslant -95\,\mathrm{mT}$ at 5 K, the maximum post-training $\mu_0H_{EB} = -77$ mT for a 3-nm Mn_3Ir (001)/Py bilayer and $\mu_0H_{EB} = -27$ mT for the (111) orientation. The dramatic decrease in μ_0H_{EB} for the 3-nm Mn_3Ir (111)/Py bilayer may indicate the significant contribution to the initial exchange-bias setting of weakly coupled uncompensated Mn moments in ultrathin films of this orientation, as discussed further in our subsequent work [65].

Finally, in order to confirm the T_B of bilayers with ultrathin Mn_3Ir, further temperature-dependent measurements of exchange bias were performed. In Fig. 10(b) the variation in μ_0H_{EB} and μ_0H_C, extracted from magnetization hysteresis loops measured at 5 K after 1-T IP field cooling from different starting temperatures, T_{start}, is shown for a 3-nm Mn_3Ir/Py bilayer with (111) orientation. A sharp decrease in both μ_0H_{EB} and μ_0H_C is observed when cooling from temperatures below 40 K, indicating that T_{start} is no longer completely above the maximum of the bilayer's T_B distribution, and thus insufficiently energetic to fully reorient AF domains in order to obtain maximum exchange bias. Variation in grain size within the Mn_3Ir film results in a distribution of these activation energies and hence of T_B, accounting for the steady decrease in μ_0H_{EB} towards zero as T_{start} is further decreased [25].

V. CONCLUSION

In summary, recipes for the sputter deposition of γ-Mn_3Ir with (001) orientation on MgO substrates, and with (111) orientation on TaN buffered Al_2O_3 substrates, are reported. A combination of XRD and TEM analysis demonstrates the epitaxial growth of the films and the resulting high-quality crystal structure, with Mn_3Ir (111) films in particular showing low mosaicity and large grain size. The ability to manipulate crystal texture through epitaxial engineering, while achieving single-crystalline thin-film structure using magnetron sputtering, represents an important springboard for exploiting epitaxial thin films of Mn_3Ir and other chiral antiferromagnets in topological spintronic applications.

Exchange bias was studied in bilayer samples, with values up to $\mu_0H_{EB} = -29\,\mathrm{mT}$ ($J_K = 0.115\,\mathrm{erg\,cm^{-2}}$ or $11.5\,\mathrm{nJ\,cm^{-2}}$) achieved after 1-T in-plane field annealing at 550 K. For heterostructures with ultrathin epitaxial antiferromagnetic layers, the temperature dependence of exchange bias is studied. Exchange bias is observed below room temperature, with $T_B \approx 40\,\mathrm{K}$ in 3-nm Mn_3Ir (111)/Py samples and a notable dependence of exchange coupling on in-plane crystalline direction in 3-nm Mn_3Ir (001)/Py bilayers. Here a higher $T_B \approx 150\,K$ and larger values of $\mu_0 H_{EB}$ are measured when unidirectional anisotropy is set along the [110] crystallographic axis. These findings may inform future studies of spin-orbit torques in such heterostructures.

Finally, we explore how these macroscopic exchange-bias properties provide a clue as to the underlying antiferromagnetic domain structure, based on the domain-state model. By discussing exchange anisotropy in the context of our detailed analysis of crystal microstructure, this paper provides groundwork as to how exchange coupling might be used to control triangular spin textures in heterostructures of noncollinear antiferromagnets utilized in *chiralitronic* devices.

ACKNOWLEDGMENTS

We acknowledge Dr. Andrew Kellock for RBS measurements, and Dr. Holger L. Meyerheim for assistance with XRD analysis. We thank Prof. Gernot Güntherodt for helpful discussion. This work was partially funded by ASPIN (EU H2020 FET Open Grant No. 766566).

---

[1] S. S. P. Parkin, N. More, and K. P. Roche, Phys. Rev. Lett. **64**, 2304 (1990).
[2] S. S. P. Parkin and D. Mauri, Phys. Rev. B **44**, 7131 (1991).
[3] S. S. P. Parkin, J. Xin, C. Kaiser, A. Panchula, K. Roche, and M. Samant, Proc. IEEE **91**, 661 (2003).
[4] S. S. P. Parkin, K. P. Roche, M. G. Samant, P. M. Rice, R. B. Beyers, R. E. Scheuerlein, E. J. O'Sullivan, S. L. Brown, J. Bucchigano, D. W. Abraham, Y. Lu, M. Rooks, P. L. Trouilloud, R. A. Wanner, and W. J. Gallagher, J. Appl. Phys. **85**, 5828 (1999).
[5] S. H. Yang, K. S. Ryu, and S. S. P. Parkin, Nat. Nanotechnol. **10**, 221 (2015).
[6] S. S. P. Parkin, M. Hayashi, and L. Thomas, Science **320**, 190 (2008).
[7] K. S. Ryu, L. Thomas, S. H. Yang, and S. S. P. Parkin, Nat. Nanotechnol. **8**, 527 (2013).
[8] A. J. Sievers and M. Tinkham, Phys. Rev. **129**, 1566 (1963).
[9] V. Baltz, A. Manchon, M. Tsoi, T. Moriyama, T. Ono, and Y. Tserkovnyak, Rev. Mod. Phys. **90**, 015005 (2018).
[10] P. Wadley, B. Howells, J. Železný, C. Andrews, V. Hills, R. P. Campion, V. Novák, K. Olejník, F. Maccherozzi, S. S. Dhesi, S. Y. Martin, T. Wagner, J. Wunderlich, F. Freimuth, Y. Mokrousov, J. Kuneš, J. S. Chauhan, M. J. Grzybowski, A. W. Rushforth, K. W. Edmonds, B. L. Gallagher, and T. Jungwirth, Science **351**, 587 (2016).
[11] S. Y. Bodnar, L. Šmejkal, I. Turek, T. Jungwirth, O. Gomonay, J. Sinova, A. A. Sapozhnik, H. J. Elmers, M. Kläui, and M. Jourdan, Nat. Commun. **9**, 348 (2018).
[12] D. Kriegner, K. Výborný, K. Olejník, H. Reichlová, V. Novák, X. Marti, J. Gazquez, V. Saidl, P. Němec, V. V. Volobuev, G. Springholz, V. Holý, and T. Jungwirth, Nat. Commun. **7**, 11623 (2016).
[13] S. DuttaGupta, R. Itoh, S. Fukami, and H. Ohno, Appl. Phys. Lett. **113**, 202404 (2018).
[14] S. Fukami, C. Zhang, S. DuttaGupta, A. Kurenkov, and H. Ohno, Nat. Mater. **15**, 535 (2016).
[15] L. Šmejkal, Y. Mokrousov, B. Yan, and A. H. MacDonald, Nat. Phys. **14**, 242 (2018).
[16] H. Chen, Q. Niu, and A. H. MacDonald, Phys. Rev. Lett. **112**, 017205 (2014).
[17] W. Zhang, W. Han, S. H. Yang, Y. Sun, Y. Zhang, B. Yan, and S. S. P. Parkin, Sci. Adv. **2**, e1600759 (2016).
[18] Y. Zhang, Y. Sun, H. Yang, J. Železný, S. S. P. Parkin, C. Felser, and B. Yan, Phys. Rev. B **95**, 075128 (2017).
[19] J. Kübler and C. Felser, Europhys. Lett. **108**, 67001 (2014).
[20] S. Nakatsuji, N. Kiyohara, and T. Higo, Nature (London) **527**, 212 (2015).
[21] A. K. Nayak, J. E. Fischer, Y. Sun, B. Yan, J. Karel, A. C. Komarek, C. Shekhar, N. Kumar, W. Schnelle, J. Kübler, C. Felser, and S. S. P. Parkin, Sci. Adv. **2**, e1501870 (2016).
[22] T. Higo, H. Man, D. B. Gopman, L. Wu, T. Koretsune, O. M. J. van 't Erve, Y. P. Kabanov, D. Rees, Y. Li, M. T. Suzuki, S. Patankar, M. Ikhlas, C. L. Chien, R. Arita, R. D. Shull, J. Orenstein, and S. Nakatsuji, Nat. Photonics **12**, 73 (2018).
[23] A. Markou, J. M. Taylor, A. Kalache, P. Werner, S. S. P. Parkin, and C. Felser, Phys. Rev. Mater. **2**, 051001(R) (2018).
[24] K.-i. Imakita, M. Tsunoda, and M. Takahashi, J. Appl. Phys. **97**, 10K106 (2005).
[25] K. O'Grady, L. E. Fernandez-Outon, and G. Vallejo-Fernandez, J. Magn. Magn. Mater. **322**, 883 (2010).
[26] H. N. Fuke, K. Saito, Y. Kamiguchi, H. Iwasaki, and M. Sahashi, J. Appl. Phys. **81**, 4004 (1997).
[27] J. B. S. Mendes, R. O. Cunha, O. Alves Santos, P. R. T. Ribeiro, F. L. A. Machado, R. L. Rodríguez-Suárez, A. Azevedo, and S. M. Rezende, Phys. Rev. B **89**, 140406(R) (2014).
[28] V. Tshitoyan, C. Ciccarelli, A. P. Mihai, M. Ali, A. C. Irvine, T. A. Moore, T. Jungwirth, and A. J. Ferguson, Phys. Rev. B **92**, 214406 (2015).
[29] L. Frangou, S. Oyarzún, S. Auffret, L. Vila, S. Gambarelli, and V. Baltz, Phys. Rev. Lett. **116**, 077203 (2016).
[30] H. Reichlová, D. Kriegner, V. Holý, K. Olejník, V. Novák, M. Yamada, K. Miura, S. Ogawa, H. Takahashi, T. Jungwirth, and J. Wunderlich, Phys. Rev. B **92**, 165424 (2015).
[31] Y. C. Lau, D. Betto, K. Rode, J. M. Coey, and P. Stamenov, Nat. Nanotechnol. **11**, 758 (2016).
[32] Y. W. Oh, S. H. Chris Baek, Y. M. Kim, H. Y. Lee, K. D. Lee, C. G. Yang, E. S. Park, K. S. Lee, K. W. Kim, G. Go, J. R. Jeong, B. C. Min, H. W. Lee, K. J. Lee, and B. G. Park, Nat. Nanotechnol. **11**, 878 (2016).
[33] A. Sakuma, K. Fukamichi, K. Sasao, and R. Y. Umetsu, Phys. Rev. B **67**, 024420 (2003).
[34] H. Reichlová, V. Novák, Y. Kurosaki, M. Yamada, H. Yamamoto, A. Nishide, J. Hayakawa, H. Takahashi, M. Maryško, J. Wunderlich, X. Marti, and T. Jungwirth, Mater. Res. Express **3**, 076406 (2016).
[35] T. Kume, T. Kato, S. Iwata, and S. Tsunashima, J. Magn. Magn. Mater. **286**, 243 (2005).
[36] A. Kohn, A. Kovács, R. Fan, G. J. McIntyre, R. C. C. Ward, and J. P. Goff, Sci. Rep. **3**, 2412 (2013).

[37] S. G. Wang, A. Kohn, C. Wang, A. K. Petford-Long, S. Lee, R. Fan, J. P. Goff, L. J. Singh, Z. H. Barber, and R. C. C. Ward, J. Phys. D: Appl. Phys. **42**, 225001 (2009).

[38] A. A. Jara, I. Barsukov, B. Youngblood, Y.-J. Chen, J. Read, H. Chen, P. Braganca, and I. N. Krivorotov, IEEE Magn. Lett. **7**, 3104805 (2016).

[39] T. Sato, M. Tsunoda, and M. Takahashi, J. Appl. Phys. **95**, 7513 (2004).

[40] C. Tusche, H. L. Meyerheim, N. Jedrecy, G. Renaud, A. Ernst, J. Henk, P. Bruno, and J. Kirschner, Phys. Rev. Lett. **95**, 176101 (2005).

[41] G. R. Harp and S. S. P. Parkin, Thin Solid Films **288**, 315 (1996).

[42] H. B. Nie, S. Y. Xu, S. J. Wang, L. P. You, Z. Yang, C. K. Ong, J. Li, and T. Y. F. Liew, Appl. Phys. A **73**, 229 (2001).

[43] J. Nogués and I. K. Schuller, J. Magn. Magn. Mater. **192**, 203 (1999).

[44] A. E. Berkowitz and K. Takano, J. Magn. Magn. Mater. **200**, 552 (1999).

[45] C. Binek, Phys. Rev. B **70**, 014421 (2004).

[46] F. Radu, A. Westphalen, K. Theis-Bröhl, and H. Zabel, J. Phys.: Condens. Matter **18**, L29 (2006).

[47] T. P. A. Hase, B. D. Fulthorpe, S. B. Wilkins, B. K. Tanner, C. H. Marrows, and B. J. Hickey, Appl. Phys. Lett. **79**, 985 (2001).

[48] H. Ohldag, A. Scholl, F. Nolting, E. Arenholz, S. Maat, A. T. Young, M. Carey, and J. Stöhr, Phys. Rev. Lett. **91**, 017203 (2003).

[49] U. Nowak, K. D. Usadel, J. Keller, P. Miltényi, B. Beschoten, and G. Güntherodt, Phys. Rev. B **66**, 014430 (2002).

[50] J. Keller, P. Miltényi, B. Beschoten, G. Güntherodt, U. Nowak, and K. D. Usadel, Phys. Rev. B **66**, 014431 (2002).

[51] F. Nolting, A. Scholl, J. Stöhr, J. W. Seo, J. Fompeyrine, H. Siegwart, J. P. Locquet, S. Anders, J. Lüning, E. E. Fullerton, M. F. Toney, M. R. Scheinfein, and H. A. Padmore, Nature (London) **405**, 767 (2000).

[52] H. Ohldag, T. J. Regan, J. Stöhr, A. Scholl, F. Nolting, J. Lüning, C. Stamm, S. Anders, and R. L. White, Phys. Rev. Lett. **87**, 247201 (2001).

[53] J. van Driel, F. R. de Boer, K. M. H. Lenssen, and R. Coehoorn, J. Appl. Phys. **88**, 975 (2000).

[54] A. Migliorini, B. Kuerbanjiang, T. Huminiuc, D. Kepaptsoglou, M. Muñoz, J. L. F. Cuñado, J. Camarero, C. Aroca, G. Vallejo-Fernández, V. K. Lazarov, and J. L. Prieto, Nat. Mater. **17**, 28 (2018).

[55] M. Tsunoda, T. Sato, T. Hashimoto, and M. Takahashi, Appl. Phys. Lett. **84**, 5222 (2004).

[56] H. Takahashi, Y. Kota, M. Tsunoda, T. Nakamura, K. Kodama, A. Sakuma, and M. Takahashi, J. Appl. Phys. **110**, 123920 (2011).

[57] M. Ali, C. H. Marrows, M. Al-Jawad, B. J. Hickey, A. Misra, U. Nowak, and K. D. Usadel, Phys. Rev. B **68**, 214420 (2003).

[58] H. Katsumi, N. Ryoichi, H. Hiroyuki, S. Yutaka, and T. Shigeru, Jpn. J. Appl. Phys. **35**, 607 (1996).

[59] M. Tsunoda, K.-i. Imakita, M. Naka, and M. Takahashi, J. Magn. Magn. Mater. **304**, 55 (2006).

[60] K.-i. Imakita, M. Tsunoda, and M. Takahashi, Appl. Phys. Lett. **85**, 3812 (2004).

[61] S. S. P. Parkin and V. S. Speriosu, in *Magnetic Properties of Low Dimensional Systems II*, Springer Proceedings in Physics, edited by L. M. Falicov, F. Mejia-Lira, and J. L. Moran-Lopez (Springer, Berlin, 1990), p. 110.

[62] E. Arenholz and K. Liu, Appl. Phys. Lett. **87**, 132501 (2005).

[63] W. Zhang and K. M. Krishnan, J. Appl. Phys. **111**, 07D712 (2012).

[64] J. McCord, R. Schäfer, R. Mattheis, and K. U. Barholz, J. Appl. Phys. **93**, 5491 (2003).

[65] J. M. Taylor, E. Lesne, A. Markou, F. K. Dejene, P. K. Sivakumar, S. Pöllath, K. G. Rana, N. Kumar, C. Luo, H. Ryll, F. Radu, F. Kronast, P. Werner, C. H. Back, C. Felser, and S. S. P. Parkin, arXiv:1904.04797 [Appl. Phys. Lett. (to be published)].

2.2 Magnetic and electrical transport signatures of uncompensated moments in epitaxial thin films of the noncollinear antiferromagnet Mn_3Ir

The following chapter of this cumulative thesis consists of the peer-reviewed scientific paper (and its supplementary material) published as:

J. M. Taylor, E. Lesne, A. Markou, F. K. Dejene, P. K. Sivakumar, S. Pöllath, K. G. Rana, N. Kumar, C. Luo, H. Ryll, F. Radu, F. Kronast, P. Werner, C. H. Back, C. Felser, and S. S. P. Parkin, "Magnetic and electrical transport signatures of uncompensated moments in epitaxial thin films of the noncollinear antiferromagnet Mn_3Ir", *Appl. Phys. Lett.* **115**, 062403 (2019)

Reprinted from [J. M. Taylor et al., "Magnetic and electrical transport signatures of uncompensated moments in epitaxial thin films of the noncollinear antiferromagnet Mn_3Ir", *Appl. Phys. Lett.* **115**, 062403 (2019)], with the permission of AIP Publishing. DOI: 10.1063/1.5099428

The previous Section 2.1 detailed the growth and structural characterization of epitaxial thin films of Mn_3Ir. We demonstrated that smooth films of thicknesses down to 3 nm could be grown with a highly oriented crystal structure, large grain size and low mosaicity. The reason for optimizing the crystal structure of the films was to attempt to measure the topological electrical transport properties of Mn_3Ir, as discussed in Section 1.2.9. This includes the theoretically predicted AHE driven by a Berry curvature induced effective field arising from the time-reversal symmetry breaking of the noncollinear AF order in Mn_3Ir [67]. The origin of this effect was discussed in Section 1.2.9 and is, importantly, found to be odd with respect to triangular spin texture chirality [73]. In its equilibrium state, the noncollinear magnetic structure of Mn_3Ir will break into multiple AF domains, each of which will posses an opposite handedness of triangular spin texture. For this reason, the anomalous Hall conductivity from oppositely oriented domains will cancel over a macroscopic sample, and no net AHE will be observed. This is unless the system can be driven into a dominant chiral domain state. However, the strong internal anisotropy fields of Mn_3Ir mean that manipulation of its noncollinear magnetic structure using an external magnetic field is challenging [65]. Extremely large magnetic fields are expected to be necessary in order to drive the material into a single AF domain state that would show a saturating, finite AHE. For this reason, observation of the AHE in Mn_3Ir has remained elusive.

However, Berry phase generated AHE has been successfully measured in the closely related compound Mn_3Pt [109]. This was achieved by growing Mn_3Pt thin films on a piezoelectric substrate, $BaTiO_3$, which resulted in the growth of films with IP tensile strain. In these strained films, a large AHE was observed, attributed to the Berry curvature mechanism. Magnitude of anomalous Hall conductivity increased with decreasing film thickness (and thus increasing strain). Simultaneously, a small uncompensated magnetization (1 to 5 $\mathrm{m}\mu_\mathrm{B}$/f.u.) was measured, whose size also increases with increasing tensile strain. This suggests that the weak magnetization may play a role in allowing the observation of a large AHE, by allowing manipulation of the domain structure in a similar way to Mn_3Sn (discussed in the second half, Part B, of this thesis), with the tensile strain acting either to induce this moment or additionally modify the domain structure directly.

We were therefore motivated to explore a similar relationship in our epitaxial thin films of Mn_3Ir. By comparing films of different thicknesses, and studying their microstructural, magnetic and electrical transport properties, we hoped to help clarify the connection between epitaxial strain, induced uncompensated magnetic moment, and the resulting magnetotransport properties in cubic noncollinear AFs. This forms the objective of the second chapter of this thesis, Section 2.2, consisting of the paper: J. M. Taylor et al., “Magnetic and electrical transport signatures of uncompensated moments in epitaxial thin films of the noncollinear antiferromagnet Mn_3Ir”, *Appl. Phys. Lett.* **115**, 062403 (2019).

Here the (111) oriented films, shown in the previous paper to grow on TaN (111) buffered Al_2O_3, are the primary candidate material. This is because, in this case, the kagome lattice of Mn atoms, which forms the noncollinear AF order, lies in the film plane. Thus, as current is passed through the (111) crystal planes, electrons encounter the triangular spin texture and should therefore acquire the momentum-space Berry phase that drives AHE.

To this end, the (111) oriented Mn_3Ir films, which were grown as part of the study in Section 2.1, with two example thicknesses of 10 nm and 3 nm, were lithographically patterned into Hall bar devices, as explained in Section 1.3.9. We then measured their electrical transport properties as a function of external magnetic field at different temperatures, using a cryostat system as described in Section 1.2.8, with the objective of measuring the topologically generated AHE.

Such measurements of Hall effect as a function of OP applied magnetic field in 10 nm and 3 nm Mn_3Ir (111) films reveal an absence of large, Berry curvature driven AHE. Indeed, at room temperature both thicknesses show an ordinary Hall effect. However, when measured at low temperature, an important difference between the two thickness regimes becomes apparent. Whilst for the 10 nm thick film, the ordinary Hall response hardly changes between high and low temperature regimes, in the 3 nm ultrathin film an anomalous Hall-like response is measured at low temperature. This switches polarity as external magnetic field is reversed and is saturated in a field of around 2 T. However, the magnitude of this AHE is much smaller than the predicted Berry phase generated anomalous Hall conductivity [67]. What is more, this AHE is accompanied by a negative MR. Negative MR arises because of a decrease in sample resistivity to flowing electrons, when magnetic moments in the material are driven into an ordered configuration by an external magnetic field. This suggests that, in fact, the low temperature behavior in 3 nm Mn_3Ir (111) films may be a conventional AHE driven by the presence of a net magnetization, rather than a topological mechanism.

We confirm this interpretation using XMCD spectroscopy measurements performed in the same samples. XMCD, whose origin and interpretation is discussed in Section 1.3.8, was measured as a function of magnetic field applied OP. In the 10 nm Mn_3Ir (111) film, a linear response of XMCD to magnetic field parallel to the [111] crystal direction can be explained by tilting of the Mn moments out of the kagome planes in the presence of a strong external magnetic field. Meanwhile the ultrathin 3 nm films show a small hysteresis in their response of XMCD to OP applied magnetic field, with a coercivity of around 0.3 T, and a small remnant signal at zero field. Using sum rule analysis, we calculate that this corresponds to an uncompensated Mn moment of $0.02\mu_B$ per atom

We therefore conclude that there is a tiny uncompensated Mn moment, which reverses hysterically in magnetic field and generates a small anomalous Hall-like response, present in ultrathin Mn_3Ir (111) films. By performing detailed analysis of the thin film microstructure, we are able to suggest an origin for this weak magnetization. TEM measurements were made of each films' crystal structure. By extracting diffractograms for each of the two thicknesses, we observe sharp spots indicative of single crystalline structure. These can be indexed and, from their relative positions, the IP and OP lattice parameters of each thin film calculated.

In the 10 nm thick films, we found the lattice parameters to be very close to the bulk, as discussed in Section 2.1. However, for the 3 nm Mn_3Ir (111) films, an inelastic expansion of the IP lattice parameter was discovered, corresponding to significant IP tensile strain. This increased IP lattice parameter may act to modify the exchange interactions between neighboring Mn atoms, the sign of whose coupling is known to be very sensitive to interatomic spacing. Thus the IP tensile strain in ultrathin Mn_3Ir (111) films may induce the small uncompensated Mn moment observed in both magnetic and electrical transport measurements.

This finding could prove useful when designing potential AF spintronic devices based on such materials, where epitaxial engineering can be used to control thin film strain, and thus the resulting magnetotransport properties. These results are similar to the case of Mn_3Pt[109], but with an important difference. Whereas in Mn_3Pt the weak magnetization in the strained films appears to help induce the Berry phase driven AHE, in our case only a conventional AHE is observed. This suggests that the uncompensated Mn moments in Mn_3Ir (111) remain decoupled from the bulk AF order, and therefore that their reorientation in an applied magnetic field is unable to modify the configuration of the overall triangular spin texture (the importance of which was discussed in relation to Mn_3Sn in Section 1.2.7). Thus an external magnetic field is unable to move domain walls in the Mn_3Ir (111) thin films, and no net Berry curvature generated AHE is observed, as the sample remains in a multi-domain state.

Finally, therefore, in an attempt to measure this chiral domain structure of Mn_3Ir, we performed X-PEEM measurements, as described in Section 1.3.8. We measured XMCD andXMLD, detected using X-PEEM. Measurements were made in 10 nm thick Mn_3Ir samples at zero magnetic field and low temperature. Here we do not expect to observe any weak magnetization, but instead to image the equilibrium AF domain state of Mn_3Ir. Using both linear (which would be sensitive to the triangular spin texture) and circular (whose absorption should depend on the chirality of the noncollinear AF order) polarized x-rays, no contrast is discerned above the sample surface topography background and no AF domains are resolved. Not only does this confirm that Mn_3Ir is not in a dominant chiral domain state at equilibrium, but also that the domains in the resulting multi-domain state are very small (that is, below the 20 nm resolution of the electron microscope). Therefore, we conclude that our Mn_3Ir thin films contain many tiny AF domains of opposite chirality, yielding no net Berry curvature driven AHE and that, even in ultrathin Mn_3Ir (111) samples with an IP tensile strain induced uncompensated moment, this is decoupled from the bulk AF order and thus unable to drive the Mn_3Ir into a dominant chiral domain state.

These results speak to the important interplay of epitaxial strain, uncompensated magnetic moment, chiral domain structure and electrical transport behavior in AF materials, a relationship that forms a common theme throughout this thesis and which, as we will explore in Part B, is key to the potential utilization of noncollinear AFs in topological spintronic applications.

Finally, recent electronic structure simulations [67] predict that Mn moments will cant out of the (111) planes in Mn_3Ir by $\approx 0.1^{\circ}$. This is calculated to result in an net magnetic moment of $0.0067\mu_{\mathrm{B}}$ per atom, and to generate a corresponding anomalous Hall conductivity of $1\,\Omega^{-1}\,\mathrm{cm}^{-1}$.

The origin of this canting is attributed to the anisotropy introduced by local cubic symmetry breaking (explained in Section 1.2.6) around each Mn moment in the kagome plane of Mn_3Ir [65]. LeBlanc *et al.* predict that this anisotropy cants Mn moments towards the cubic crystal axes, resulting in an uncompensated magnetic moment along the [111] direction [95].

We highlight the fact, as an extension to the discussion given in paper J. M. Taylor et al., “Magnetic and electrical transport signatures of uncompensated moments in epitaxial thin films of the noncollinear antiferromagnet Mn_3Ir”, *Appl. Phys. Lett.* **115**, 062403 (2019), that this theoretically predicted net magnetic moment somewhat matches with the uncompensated Mn moment measured along the [111] direction in our 3 nm Mn_3Ir films using XMCD. Furthermore, our measured anomalous Hall conductivity is calculated as $\sigma_{\mathrm{xy}} = \rho_{\mathrm{xy}}/(\rho_{\mathrm{xx}})^2 = 3 \times 10^{-3}\,\mu\Omega\,\mathrm{cm}/(81\,\mu\Omega\,\mathrm{cm})^2 = 0.46\,\Omega^{-1}\,\mathrm{cm}^{-1}$. Whilst this is half of the simulated value, the difference can be accounted for by the measured longitudinal resistivity in an experimental device.

The uncompensated Mn moment observed in our ultrathin Mn_3Ir (111) films may, therefore, be attributed to this same anisotropy. We also note that the presence of lattice site disorder in Mn_3Ir leads to the tilting of Mn moments towards the cubic crystal axes [93]. Thus, the presence of γ-Mn_3Ir in our epitaxial thin films may encourage such an anisotropic canting of Mn moments out of the kagome planes.

However, that the net Mn moment measured experimentally remains larger than the predicted value suggests other sources of noncollinear AF order variation or uncompensated magnetic moment may play a role (for example strain, as discussed in the paper). Furthermore, that reversal of the net Mn moment does not seem to modify the chiral domain structure of Mn_3Ir, so as to induce larger changes in topological magnetotransport properties, suggests the source of uncompensated magnetic moment may be de-coupled from the bulk triangular spin texture.

Applied Physics Letters ARTICLE scitation.org/journal/apl

Magnetic and electrical transport signatures of uncompensated moments in epitaxial thin films of the noncollinear antiferromagnet Mn_3Ir

Cite as: Appl. Phys. Lett. **115**, 062403 (2019); doi: 10.1063/1.5099428
Submitted: 10 April 2019 · Accepted: 5 July 2019 ·
Published Online: 6 August 2019

James M. Taylor,[1,a)] Edouard Lesne,[1] Anastasios Markou,[2] Fasil Kidane Dejene,[1] Pranava Keerthi Sivakumar,[1] Simon Pöllath,[3] Kumari Gaurav Rana,[1] Neeraj Kumar,[1] Chen Luo,[4,5] Hanjo Ryll,[4] Florin Radu,[4] Florian Kronast,[4] Peter Werner,[1] Christian H. Back,[3,5] Claudia Felser,[2] and Stuart S. P. Parkin[1,b)]

AFFILIATIONS

[1]Max Planck Institute of Microstructure Physics, Weinberg 2, 06120 Halle (Saale), Germany
[2]Max Planck Institute for Chemical Physics of Solids, Nöthnitzer Str. 40, 01187 Dresden, Germany
[3]Institute of Experimental Physics, University of Regensburg, 93040 Regensburg, Germany
[4]Helmholtz-Zentrum Berlin for Materials and Energy, Albert-Einstein-Str. 15, Berlin 12489, Germany
[5]Institute of Experimental Physics of Functional Spin Systems, Technical University Munich, James-Franck-Str. 1, 85748 Garching b. München, Germany

[a)]james.taylor@mpi-halle.mpg.de
[b)]stuart.parkin@mpi-halle.mpg.de

ABSTRACT

Noncollinear antiferromagnets, with either an $L1_2$ cubic crystal lattice (e.g., Mn_3Ir and Mn_3Pt) or a $D0_{19}$ hexagonal structure (e.g., Mn_3Sn and Mn_3Ge), exhibit a number of phenomena of interest to topological spintronics. Among the cubic systems, for example, tetragonally distorted Mn_3Pt exhibits an intrinsic anomalous Hall effect (AHE). However, Mn_3Pt only enters a noncollinear magnetic phase close to the stoichiometric composition and at suitably large thicknesses. Therefore, we turn our attention to Mn_3Ir, the material of choice for use in exchange bias heterostructures. In this letter, we investigate the magnetic and electrical transport properties of epitaxially grown, face-centered-cubic γ-Mn_3Ir thin films with (111) crystal orientation. Relaxed films of 10 nm thickness exhibit an ordinary Hall effect, with a hole-type carrier concentration of $(1.500 \pm 0.002) \times 10^{23}\,\mathrm{cm}^{-3}$. On the other hand, TEM characterization demonstrates that ultrathin 3 nm films grow with significant in-plane tensile strain. This may explain a small net magnetic moment, observed at low temperatures, shown by X-ray magnetic circular dichroism spectroscopy to arise from uncompensated Mn spins. Being of the order of 0.02 μ_B/atom, this dominates electrical transport behavior, leading to a small AHE and negative magnetoresistance. These results are discussed in terms of crystal microstructure and chiral domain behavior, with spatially resolved XML(C)D-PEEM supporting the conclusion that small antiferromagnetic domains, <20 nm in size, with differing chirality account for the absence of observed Berry curvature driven magnetotransport effects.

Antiferromagnetic (AF) spintronics is a growing research field,[1] motivated by a number of potential advantages for applications, including ultrafast magnetization dynamics[2] and improved stability against external perturbations at reduced dimensions. For example, synthetic antiferromagnetic structures (SAFs)[3] are already employed to eliminate magnetostatic fields in spin-valve sensors[4] and magnetic tunnel junction (MTJ) memory bits.[5] Furthermore, an efficient current-driven domain-wall motion has been demonstrated in such SAFs[6] by utilizing the chirality of the magnetic structure.[7]

Indeed, chiral spin textures play a key role in the emerging field of topological AF spintronics.[8] Of particular interest are the noncollinear AFs Mn_3X (X = Ir, Pt, Sn, Ge), which can stabilize with either a face-centered-cubic (fcc) or a hexagonal crystal structure. The symmetry breaking noncollinear spin texture of these materials, combined with spin–orbit coupling, gives rise to a Berry curvature driven effective field that is predicted to generate an intrinsic anomalous Hall effect (AHE).[9,10] In the case of cubic Mn_3Ir, a facet-dependent spin Hall effect (SHE) emerging from the same origin has been discovered.[11] While this intrinsic SHE is even with respect to the handedness of topological AF order, contributions to the AHE will cancel out over domains with opposite chirality of spin texture.[12]

Experimental measurements of the intrinsic AHE have been realized in bulk single crystals of hexagonal noncollinear AFs, namely Mn_3Sn,[13] and Mn_3Ge.[14] This has been enabled by the small in-plane magnetic moment exhibited by these materials, also demonstrated in epitaxial thin films of Mn_3Sn,[15] which arises from geometric frustration of the inverse triangular spin texture. Alignment of this weak magnetization via an external magnetic field in turn coherently orients the AF order throughout the material, driving it into a dominant chiral domain state.[16]

Such control of AF domains is challenging in the fcc noncollinear systems, which are normally fully compensated with strong internal anisotropy fields.[17] However, Liu *et al.*[18] have recently discovered a large AHE in Mn_3Pt films epitaxially grown with in-plane tensile strain on $BaTiO_3$ substrates. Mn_3Pt undergoes a first-order magnetic phase transition from the noncollinear to a collinear AF state above ≈360 K. AHE is only observed below this transition temperature, where a small uncompensated magnetization is also measured. The size of this net moment correlates with the magnitude of the Berry curvature driven AHE and shows a dependence on the degree of tetragonal distortion of the films, although the exact relationship between them (including the role of chiral domain manipulation) remains open for further study.

While the magnetic phase transition of Mn_3Pt has allowed the important demonstration of electric field control of this topological AHE, by applying additional piezoelectric strain to move between the collinear and noncollinear states,[18] it also presents an upper limit to the operating temperature in the resulting spintronic structures. On the other hand, the closely related cubic noncollinear AF Mn_3Ir can be stabilized with a triangular spin texture below its high Néel temperature, $T_N \approx 700$ K,[19] over a broad composition range in the phase diagram.[20]

While Mn_3Ir has previously been utilized as an exchange bias pinning layer in heterostructures with ferromagnets (FMs),[21,22] and subsequently spin–orbit torques studied in such bilayers,[23,24] further understanding of the magnetotransport properties of Mn_3Ir alone is required before its potential implementation in future chiral spintronic applications.[25–27] Therefore, in this letter, we explore further the subtle interplay between the crystal microstructure, uncompensated moments, and electrical transport properties of this noncollinear AF. In order to elucidate the behavior of Berry curvature driven phenomena in these materials, thin film samples with high-quality crystal structure are required, while the commercial realization of AF spintronic devices requires deposition using fast and flexible techniques.[28]

To this end, the epitaxial films utilized here were grown by magnetron sputtering according to our recipe published in Ref. 29. Mn_3Ir films with (111) planes parallel to the substrate surface were selected for further study, grown with the sample structure: Al_2O_3 (0001) [Substrate]/TaN (111) [5 nm]/$Mn_{(0.72 \pm 0.03)}Ir_{(0.28 \pm 0.03)}$ (111) [3 or 10 nm]/TaN [2.5 nm]. The two different sample thicknesses were chosen to display different structural properties, while both having a T_N above room temperature (RT).[24] Comprehensive characterization is detailed in Ref. 29, demonstrating that these films grow in an fcc γ-Mn_3Ir phase and suggesting a noncollinear magnetic structure.[19]

As detailed in the supplementary material, 10 nm Mn_3Ir (111) films grow fully relaxed, with a large grain size in the lateral direction of ≥20 nm. In the case of 3 nm ultrathin films, high-resolution TEM operated at 300 kV (FEI Titan 80–300) was used to further analyze the crystal structure. Figure 1(a) shows a typical micrograph of the epitaxial growth of <111> oriented Mn_3Ir, with sharp interfaces and uniform thickness. Examples of grain boundary defects are highlighted, indicating slightly smaller laterally oriented grains in these ultrathin films. Indeed, examination of different regions of the TEM lamella allows an estimation of lateral grain size of 15–20 nm.

The inset of Fig. 1(a) displays a fast Fourier transform diffractogram for the 3 nm Mn_3Ir (111) film, taken from the marked area. Indexing of Mn_3Ir (111) and (002) diffraction peaks allows the calculation of out-of-plane, OP (d_{111}), and in-plane, IP ($d_{\bar{1}\bar{1}2} = \sqrt{2/3}\, d_{002}$), lattice spacing, respectively. In the OP direction, the lattice plane separation, $d_{111} = (2.19 \pm 0.09)$ Å, agrees within uncertainty with the bulk value (2.182 Å). Meanwhile, the estimated IP crystal lattice spacing is $d_{\bar{1}\bar{1}2} = (1.9 \pm 0.1)$ Å. In spite of the high uncertainty in this

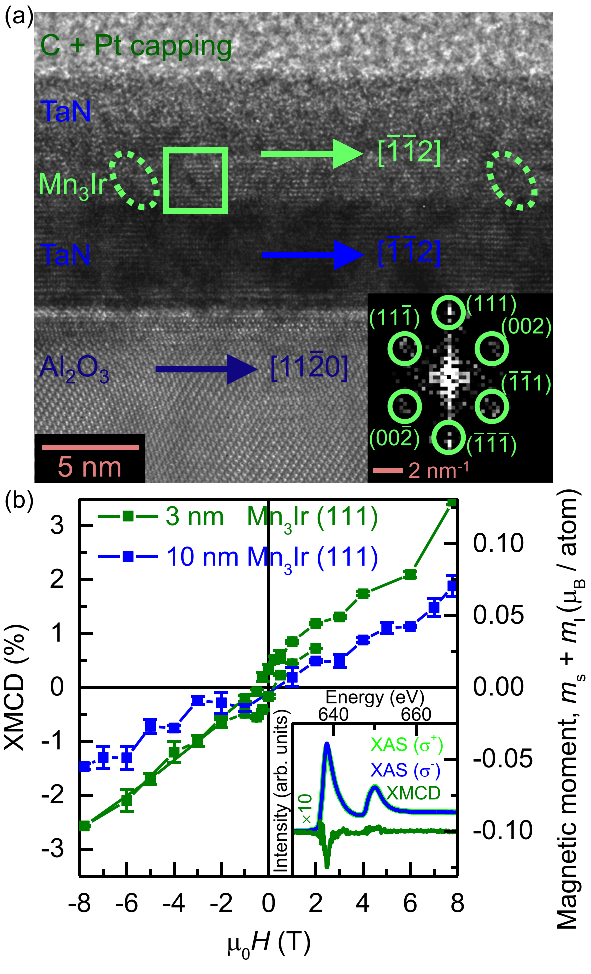

FIG. 1. (a) TEM image of a 3 nm Mn_3Ir (111) film, viewed along the [$1\bar{1}0$] zone axis, with in-plane crystallographic directions indicated and grain boundaries highlighted by dashed lines (inset shows a diffractogram from the region marked by green box). (b) XMCD measured for 10 nm and 3 nm Mn_3Ir (111) films at 10 K (inset shows XAS spectra recorded at the Mn-L_3 edge using right- and left-circularly polarized X-rays after sweeping the magnetic field to −8 T, and the resulting XMCD spectrum, for a 3 nm thin film).

measurement, which arises from the low intensity of the diffractogram extracted from such an ultrathin layer, it is significantly larger than the bulk value (1.543 Å). This indicates that the 3 nm Mn_3Ir (111) film grows with appreciable IP strain. The resulting volume expansion of the unit cell was also previously found in < 5 nm thick films of Mn-based Heusler compounds.[30,31] This is expected to lead to a modification of magnetic properties (as observed, for example, in the noncollinear AF Mn_3Ge under hydrostatic pressure[32]) due to changing interatomic distances between Mn atoms.[33]

Characterization of these samples' magnetism using SQUID vibrating sample magnetometry proved challenging, as previously reported for ultrathin ferrimagnetic films[30] and discussed further in the supplementary material. Instead, direct measurements of the films' magnetic moment (m) were performed using X-ray magnetic circular dichroism (XMCD) spectroscopy at the VEKMAG endstation of the PM2 beamline at BESSY.[34] X-ray absorption spectra (XAS) were recorded around the Mn-L_3 edge in the total electron yield mode [shown in the inset of Fig. 1(b)], using alternating right- and left-circularly polarized X-rays (σ^+ and σ^-, respectively), at temperature $T = 10$ K. Figure 1(b) displays the resulting XMCD signal, $(\sigma^+ - \sigma^-)/(\sigma^+ + \sigma^-)$, as a function of the OP applied magnetic field along the [111] direction, $\mu_0 H$. In the case of a 10 nm Mn_3Ir (111) film, a small linear response of the Mn magnetic moment (calculated using the XMCD sum rules[35]) is observed, explained by their slight canting out of the (111) plane under the influence of an external magnetic field. Due to the high magnetic anisotropy of Mn_3Ir,[17] we estimate that the fields used during these experiments remain well below any spin-flip transition.

For a 3 nm Mn_3Ir (111) film, an XMCD signal which is hysteretic for $\mu_0 H < 2$ T is measured, with a coercivity of approximately 0.3 T. A subtle plateau in the XMCD signal (where low-field hysteretic behavior reverts to a linear response) is seen at around 0.5%, corresponding to a net Mn moment of 0.02 μ_B/atom. This demonstrates a small saturating component of magnetization in ultrathin Mn_3Ir (111) films, which can be manipulated by an external magnetic field and arises from uncompensated Mn spins. Since both chemical composition and defect density are similar in 10 nm and 3 nm thick samples, this effect could be interface driven, for example, by reorientation of the noncollinear AF structure.[36] However, no similar effect has been observed in ultrathin polycrystalline $Mn_{0.8}Ir_{0.2}$ films.[23] Therefore, the origin of this uncompensated moment may instead be strain in our epitaxial 3 nm Mn_3Ir (111) films. This is consistent with the results of Liu *et al.*,[18] and can be explained by the slightly increased interatomic distance beginning to favor the parallel coupling of Mn spins.[37] Modification of remanent magnetization by IP strain has also been reported in epitaxially distorted thin films of the noncollinear AF Mn_3Ga.[31]

The thin films were then patterned into Hall bars, using electron beam lithography and Ar ion etching, with dimensions ranging from $150 \times 50\,\mu m^2$ down to $3 \times 1\,\mu m^2$. Current ($I_c = 200\ \mu A$) flow was directed along Hall bars fabricated in different IP crystalline directions. The inset of Fig. 2(b) displays the electrical measurement geometry, for an exemplar $15 \times 5\,\mu m^2$ device. Previous magnetotransport measurements in polycrystalline $Mn_{0.8}Ir_{0.2}$ utilized anisotropic magnetoresistance (AMR)[25] or tunneling-AMR[26] to detect AF order. In our case, longitudinal (ρ_{xx}) and transverse (ρ_{xy}) resistivity were measured at different temperatures, as a function of external magnetic field applied OP.

Figure 2(a) records the measurements of transverse resistivity in a $150 \times 50\,\mu m^2$ Hall bar of a 3 nm Mn_3Ir (111) film. We observe an anomalous-type behavior of ρ_{xy} at 2 K, saturating at comparable fields to the hysteretic part of the XMCD signal. The inset of Fig. 2(a) shows that this is accompanied by a negative longitudinal magnetoresistance (MR), $([\rho_{xx}(\mu_0 H) - \rho_{xx}(0)]/\rho_{xx}(0)) \times 100\%$, which points to a magnetic origin, namely the presence of uncompensated Mn moments, for the exhibited AHE in strained ultrathin Mn_3Ir (111) films. We find a comparable AHE across devices of different sizes, down to the smallest $3 \times 1\,\mu m^2$ Hall bars, as shown in the supplementary material, Fig. S2(a). Similar electrical measurements of uncompensated Mn spins have been made at RT by Kosub *et al.*[27]

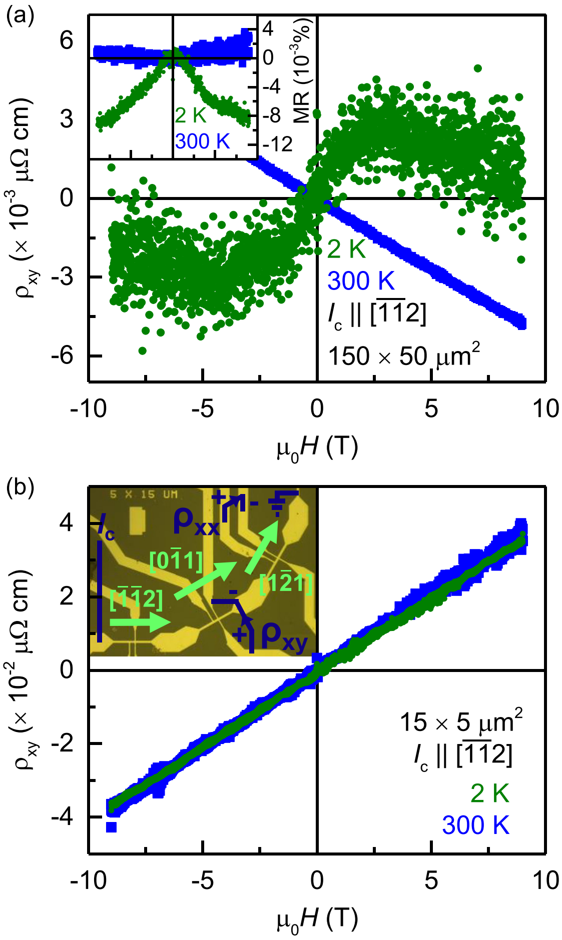

FIG. 2. (a) Hall effect for a 3 nm Mn_3Ir (111) film in a $150 \times 50\,\mu m^2$ Hall bar directed along $[\bar{1}\bar{1}2]$ at 300 K and at 2 K (inset shows variation in longitudinal magnetoresistance over the same magnetic field range). (b) Hall effect for a 10 nm Mn_3Ir (111) film in a $15 \times 5\,\mu m^2$ Hall bar directed along $[\bar{1}\bar{1}2]$ at 300 K and at 2 K (inset shows an optical image of an example patterned device with measurement geometry indicated).

In our case, as the temperature is increased above 50 K, both the AHE and negative MR are replaced by an ordinary Hall effect and positive MR, respectively, demonstrated for a measurement at 300 K in Fig. 2(a). We attribute this change in behavior to a vanishing of the strain-induced uncompensated moment at higher temperatures. In spite of this, supplementary Fig S2(a) shows that low temperature transport properties are not modified after cooling from 400 K in a 9 T magnetic field along the [111] axis. This implies that samples remain antiferromagnetic up to and above RT (i.e., have respective $T_N > 400$ K), because it is known that field cooling analogous polycrystalline $Mn_{0.8}Ir_{0.2}$ films through T_N can modify their electrically detected AF order.[38]

These different temperature dependencies imply that strain-mediated uncompensated Mn moments are decoupled from the bulk triangular AF order. They are therefore unable to coherently orient spin texture under external magnetic field and thus induce Berry curvature driven AHE, which would be expected to produce a larger ρ_{xy} signal, as is the case for Mn_3Pt.[18] In addition, the magnitude of ρ_{xy} measured in 3 nm Mn_3Ir (111) films is smaller than that for 10 nm thick samples, reported below. We can attribute this to a short mean free path of electrons (as calculated in the supplementary material), meaning interface scattering will contribute significantly to resistivity in the 3 nm films, in turn acting to reduce transverse voltage. Furthermore, a sign change of ρ_{xy} (with respect to 10 nm films) indicates the presence of electronlike carriers in the 3 nm ultrathin regime. Such a change in charge carrier type indicates a modification of band structure between the two different film thicknesses. This can be explained by considering the variation of longitudinal resistivity with temperature, displayed in the inset of supplementary Fig. S2(a). While scattering is defect dominated in 10 nm Mn_3Ir (111), the actual band structure at the Fermi level may be sensitive to, for example, the observed structural changes in 3 nm Mn_3Ir (111).

Figure 2(b) shows the transverse resistivity of a 10 nm Mn_3Ir (111) film measured at 300 and 2 K in a $15 \times 5\,\mu m^2$ Hall bar fabricated along the $[\bar{1}\bar{1}2]$ crystallographic axis. A positive linear response of ρ_{xy} is measured across the temperature range, indicating hole-type charge carriers. Fitting the gradient ($\rho_{xy}/\mu_0 H$) of this ordinary Hall effect at RT allows determination of the carrier concentration, $h = (1.500 \pm 0.002) \times 10^{23}\,cm^{-3}$. As well as demonstrating a lack of uncompensated Mn moments, such an ordinary Hall effect is consistent with an absence of Berry curvature driven AHE. This is because the moderate magnetic fields applied in this experiment are insufficient to drive Mn_3Ir into a single chiral domain state. Instead, AHE cancels over multiple degenerate AF domains with opposing orientation of a triangular spin texture.[11]

To investigate this further, ρ_{xy} was measured in Hall bar devices fabricated along different crystalline directions, because the intrinsic AHE is predicted to be highly anisotropic.[12] However, a linear Hall effect is observed along all crystallographic axes, demonstrated in supplementary Fig. S2(b) for a $15 \times 5\,\mu m^2$ Hall bar fabricated along the $[1\bar{2}1]$ crystalline direction. This isotropic behavior suggests that any intrinsic AHE may cancel over multiple differently oriented AF domains, which follow the six-fold symmetry of the epitaxial crystal structure. To isolate individual chiral domains, we performed measurements of ρ_{xy} in devices of differing size. Again, the ordinary Hall effect found in all devices points to the AF domain size in epitaxial 10 nm Mn_3Ir (111) thin films being significantly smaller than the lowest Hall bar dimension tested (1 μm).

Therefore, in an attempt to elucidate the chiral domain structure of 10 nm Mn_3Ir (111) thin films, we performed X-ray magnetic linear (circular) dichroism photoemission electron microscopy, XML(C)D-PEEM (or X-PEEM), at the beamline UE49_PGM at BESSY. Experimental details are described in the supplementary material. Figure 3(a) shows an XMCD-PEEM image, taken at the Mn-L_3 edge, at 45 K with no applied external magnetic field. For this film without remanent Mn moment, no net XMCD signal is observed. Instead, only small intensity fluctuations at the resolution limit of the electron microscope create contrast in the image.

XMLD-PEEM imaging has been shown to exhibit contrast between domains with orthogonal Néel vector orientations in collinear AFs.[39,40] We postulate that, in the same way, differences in the orientation between the linearly polarized X-rays and the Néel vector defining the chirality of the triangular spin texture would lead to a difference in absorption between opposite chirality AF domains. Figure 3(b) shows such an XMLD-PEEM image measured at the Mn-L_3 edge for the same 10 nm Mn_3Ir (111) sample; no XMLD contrast is discerned above the sample surface topography background. Possible reasons are discussed in the supplementary material, one of which may be that AF domains are smaller than the resolution limit of the PEEM ($\approx$ 20 nm), which will indeed be the case if they are correlated with the grain size in the film measured using TEM.

Finally, in an attempt to enlarge chiral domains in Mn_3Ir to an observable size, exchange bias was utilized to introduce a preferential AF domain orientation through coupling with a ferromagnetic (FM) layer.[22] X-PEEM was therefore imaged at both the Ni-L_3 and Mn-L_3 edges in a 3 nm Mn_3Ir (111)/5 nm $Ni_{80}Fe_{20}$ bilayer. We have demonstrated that such heterostructures show large exchange anisotropy after cooling below their blocking temperature of 40 K.[29] Figure 3(c) exhibits an approximately equal distribution of oppositely oriented FM domains in an XMCD-PEEM image recorded at the Ni-L_3 edge at RT. After cooling the bilayer to 70 K under a 20 mT IP magnetic field, Fig. 3(d) displays a repeat XMCD-PEEM image of the same area, in which the FM domains have grown but no preferential domain direction has been set. This is likely due to the bilayer not having passed through its blocking temperature. Finally, XMCD- and XMLD-PEEM images were recorded at the Mn-L_3 edge after this IP field cooling routine, shown in Figs. 3(e) and 3(f), respectively. No uncompensated Mn spins are observed at the interface, as expected if the temperature is not low enough to induce large exchange bias.[21] Finally, no AF domains of differing chirality are resolved, which may be due to the concomitant difficulty in observing the buried interface through a 5 nm $Ni_{80}Fe_{20}$ layer[41] combined with the intrinsic spatial resolution limit of X-PEEM discussed above.

In conclusion, we studied the magnetic and electrical properties of fully relaxed 10 nm Mn_3Ir (111) samples and of ultrathin films

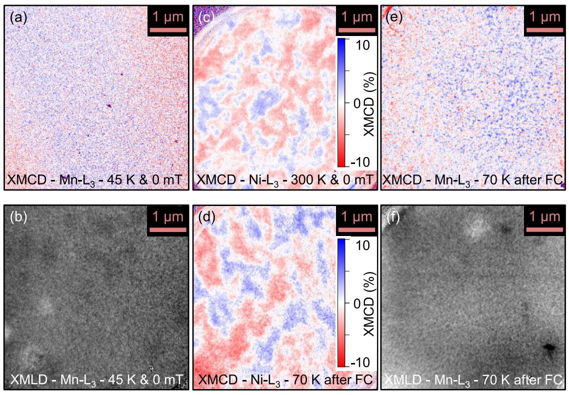

FIG. 3. XPEEM images ($5 \times 5\,\mu m^2$) of a 10 nm Mn_3Ir (111) film acquired using (a) XMCD and (b) XMLD at the Mn-L_3 edge; of a 3 nm Mn_3Ir (111)/5 nm $Ni_{80}Fe_{20}$ bilayer using XMCD at the Ni-L_3 edge both at (c) 300 K and (d) 70 K after 20 mT IP field cooling, and using (e) XMCD and (f) XMLD at the Mn-L_3 edge after 20 mT IP field cooling.

exhibiting significant IP lattice distortion. This tensile strain may be the origin of an uncompensated Mn magnetic moment observed by XMCD spectroscopy. Because of this net Mn magnetization, the 3 nm Mn_3Ir (111) films demonstrate a small negative MR and an AHE at low temperatures. On the other hand, 10 nm Mn_3Ir (111) films exhibit an ordinary Hall effect, which is isotropic with respect to the IP crystallographic direction. The lack of Berry curvature driven electrical transport effects can be explained by the presence of multiple AF domains of differing triangular spin texture chirality, suggested by XML(C)D-PEEM imaging to be correlated with film grain size, and thus < 20 nm. Our results illuminate the intimate connection between crystal structure, uncompensated spins, and magnetotransport properties, therefore informing further implementation of noncollinear Mn_3X thin films in *chiralitronic* devices.

See the supplementary material for characterization of 10 nm Mn_3Ir (111) thin films, supporting magnetic and electrical transport measurements, and details of X-PEEM experimental procedures.

We acknowledge Helmholtz-Zentrum Berlin (HZB) for the synchrotron beamtime at UE49_PGM SPEEM (Proposal No. 181-06569) and at PM2 VEKMAG (Proposal No. 171-04784). Financial support for the VEKMAG project and for the PM2 VEKMAG beamline is provided by the German Federal Ministry for Education and Research (Nos. BMBF 05K10PC2, 05K10WR1, and 05K10KE1) and by HZB, and Steffen Rudorff is thanked for technical support. This work was partially funded by ASPIN (EU H2020 FET Open Grant No. 766566).

REFERENCES

[1] V. Baltz, A. Manchon, M. Tsoi, T. Moriyama, T. Ono, and Y. Tserkovnyak, Rev. Mod. Phys. **90**(1), 015005 (2018).

[2] A. J. Sievers and M. Tinkham, Phys. Rev. **129**(4), 1566–1571 (1963).

[3] S. S. P. Parkin, N. More, and K. P. Roche, Phys. Rev. Lett. **64**(19), 2304–2307 (1990).

[4] S. S. P. Parkin, J. Xin, C. Kaiser, A. Panchula, K. Roche, and M. Samant, Proc. IEEE **91**(5), 661–680 (2003).

[5] S. S. P. Parkin, K. P. Roche, M. G. Samant, P. M. Rice, R. B. Beyers, R. E. Scheuerlein, E. J. O'Sullivan, S. L. Brown, J. Bucchigano, D. W. Abraham, Y. Lu, M. Rooks, P. L. Trouilloud, R. A. Wanner, and W. J. Gallagher, J. Appl. Phys. **85**(8), 5828–5833 (1999).

[6] S. H. Yang, K. S. Ryu, and S. S. P. Parkin, Nat. Nanotechnol. **10**(3), 221–226 (2015).

[7] K. S. Ryu, L. Thomas, S. H. Yang, and S. S. P. Parkin, Nat. Nanotechnol. **8**(7), 527–533 (2013).

[8] L. Šmejkal, Y. Mokrousov, B. Yan, and A. H. MacDonald, Nat. Phys. **14**(3), 242–251 (2018).

[9] H. Chen, Q. Niu, and A. H. MacDonald, Phys. Rev. Lett. **112**(1), 017205 (2014).

[10] J. Kübler and C. Felser, Europhys. Lett. **108**(6), 67001 (2014).

[11] W. Zhang, W. Han, S. H. Yang, Y. Sun, Y. Zhang, B. Yan, and S. S. P. Parkin, Sci. Adv. **2**(9), e1600759 (2016).

[12] Y. Zhang, Y. Sun, H. Yang, J. Železný, S. S. P. Parkin, C. Felser, and B. Yan, Phys. Rev. B **95**(7), 075128 (2017).

[13] S. Nakatsuji, N. Kiyohara, and T. Higo, Nature **527**(7577), 212–215 (2015).

[14] A. K. Nayak, J. E. Fischer, Y. Sun, B. Yan, J. Karel, A. C. Komarek, C. Shekhar, N. Kumar, W. Schnelle, J. Kübler, C. Felser, and S. S. P. Parkin, Sci. Adv. **2**(4), e1501870 (2016).

[15] A. Markou, J. M. Taylor, A. Kalache, P. Werner, S. S. P. Parkin, and C. Felser, Phys. Rev. Mater. **2**(5), 051001(R) (2018).

[16] T. Higo, H. Man, D. B. Gopman, L. Wu, T. Koretsune, O. M. J. van 't Erve, Y. P. Kabanov, D. Rees, Y. Li, M. T. Suzuki, S. Patankar, M. Ikhlas, C. L. Chien, R. Arita, R. D. Shull, J. Orenstein, and S. Nakatsuji, Nat. Photonics **12**(2), 73–78 (2018).

[17] L. Szunyogh, B. Lazarovits, L. Udvardi, J. Jackson, and U. Nowak, Phys. Rev. B **79**(2), 020403 (2009).

[18] Z. Q. Liu, H. Chen, J. M. Wang, J. H. Liu, K. Wang, Z. X. Feng, H. Yan, X. R. Wang, C. B. Jiang, J. M. D. Coey, and A. H. MacDonald, Nat. Electron. **1**(3), 172–177 (2018).

[19] A. Kohn, A. Kovács, R. Fan, G. J. McIntyre, R. C. C. Ward, and J. P. Goff, Sci. Rep. **3**, 2412 (2013).

[20] K. Sasao, R. Y. Umetsu, K. Fukamichi, and A. Sakuma, J. Alloys Compd. **352**(1), 21–25 (2003).

[21] H. Ohldag, A. Scholl, F. Nolting, E. Arenholz, S. Maat, A. T. Young, M. Carey, and J. Stöhr, Phys. Rev. Lett. **91**(1), 017203 (2003).

[22] T. Eimüller, T. Kato, T. Mizuno, S. Tsunashima, C. Quitmann, T. Ramsvik, S. Iwata, and G. Schütz, Appl. Phys. Lett. **85**(12), 2310–2312 (2004).

[23] H. Reichlová, D. Kriegner, V. Holý, K. Olejník, V. Novák, M. Yamada, K. Miura, S. Ogawa, H. Takahashi, T. Jungwirth, and J. Wunderlich, Phys. Rev. B **92**(16), 165424 (2015).

[24] L. Frangou, S. Oyarzún, S. Auffret, L. Vila, S. Gambarelli, and V. Baltz, Phys. Rev. Lett. **116**(7), 077203 (2016).

[25] R. Galceran, I. Fina, J. Cisneros-Fernández, B. Bozzo, C. Frontera, L. López-Mir, H. Deniz, K. W. Park, B. G. Park, L. Balcells, X. Martí, T. Jungwirth, and B. Martínez, Sci. Rep. **6**, 35471 (2016).

[26] B. G. Park, J. Wunderlich, X. Martí, V. Holý, Y. Kurosaki, M. Yamada, H. Yamamoto, A. Nishide, J. Hayakawa, H. Takahashi, A. B. Shick, and T. Jungwirth, Nat. Mater. **10**(5), 347–351 (2011).

[27] T. Kosub, M. Kopte, F. Radu, O. G. Schmidt, and D. Makarov, Phys. Rev. Lett. **115**(9), 097201 (2015).

[28] A. A. Jara, I. Barsukov, B. Youngblood, Y. Chen, J. Read, H. Chen, P. Braganca, and I. N. Krivorotov, IEEE Magn. Lett. **7**, 1–5 (2016).

[29] J. M. Taylor, E. Lesne, A. Markou, F. K. Dejene, B. Ernst, A. Kalache, K. G. Rana, N. Kumar, P. Werner, C. Felser, and S. S. P. Parkin, Phys. Rev. Mater. **3**(7), 074409 (2019).

[30] A. Köhler, I. Knez, D. Ebke, C. Felser, and S. S. P. Parkin, Appl. Phys. Lett. **103**(16), 162406 (2013).

[31] J. T. Holguín-Momaca, C. J. Muñoz-Carnero, H. Sharma, C. R. Santillán-Rodríguez, J. A. Matutes-Aquino, C. V. Tomy, and S. F. Olive-Méndez, J. Magn. Magn. Mater. **471**, 329–333 (2019).

[32] A. S. Sukhanov, S. Singh, L. Caron, T. Hansen, A. Hoser, V. Kumar, H. Borrmann, A. Fitch, P. Devi, K. Manna, C. Felser, and D. S. Inosov, Phys. Rev. B **97**(21), 214402 (2018).

[33] R. M. Gutiérrez-Pérez, J. T. Holguín-Momaca, J. T. Elizalde-Galindo, F. Espinosa-Magaña, and S. F. Olive-Méndez, J. Appl. Phys. **117**(12), 123902 (2015).

[34] T. Noll and F. Radu, in *Proceedings of MEDSI2016, Barcelona, Spain, September 2016*, edited by V. R. W. Schaa (JACoW, Geneva, Switzerland, 2017), pp. 370–373.

[35] C. T. Chen, Y. U. Idzerda, H. Lin, N. V. Smith, G. Meigs, E. Chaban, G. H. Ho, E. Pellegrin, and F. Sette, Phys. Rev. Lett. **75**(1), 152–155 (1995).

[36] F. Hellman, A. Hoffmann, Y. Tserkovnyak, G. S. D. Beach, E. E. Fullerton, C. Leighton, A. H. MacDonald, D. C. Ralph, D. A. Arena, H. A. Dürr, P. Fischer, J. Grollier, J. P. Heremans, T. Jungwirth, A. V. Kimel, B. Koopmans, I. N. Krivorotov, S. J. May, A. K. Petford-Long, J. M. Rondinelli, N. Samarth, I. K. Schuller, A. N. Slavin, M. D. Stiles, O. Tchernyshyov, A. Thiaville, and B. L. Zink, Rev. Mod. Phys. **89**(2), 025006 (2017).

[37] N. Yamada, J. Phys. Soc. Jpn. **59**, 273 (1990).

[38] D. Petti, E. Albisetti, H. Reichlová, J. Gazquez, M. Varela, M. Molina-Ruiz, A. F. Lopeandía, K. Olejník, V. Novák, I. Fina, B. Dkhil, J. Hayakawa, X. Martí, J. Wunderlich, T. Jungwirth, and R. Bertacco, Appl. Phys. Lett. **102**(19), 192404 (2013).

[39] P. Wadley, S. Reimers, M. J. Grzybowski, C. Andrews, M. Wang, J. S. Chauhan, B. L. Gallagher, R. P. Campion, K. W. Edmonds, S. S. Dhesi, F. Maccherozzi, V. Novak, J. Wunderlich, and T. Jungwirth, Nat. Nanotechnol. **13**(5), 362–365 (2018).

[40] A. A. Sapozhnik, M. Filianina, S. Y. Bodnar, A. Lamirand, M. A. Mawass, Y. Skourski, H. J. Elmers, H. Zabel, M. Kläui, and M. Jourdan, Phys. Rev. B **97**(13), 134429 (2018).

[41] Y. Wang, C. Song, G. Wang, J. Miao, F. Zeng, and F. Pan, Adv. Funct. Mater. **24**(43), 6806–6810 (2014).

Magnetic and electrical transport signatures of uncompensated moments in epitaxial thin films of the non-collinear antiferromagnet Mn$_3$Ir

James M. Taylor * [1], Edouard Lesne [1], Anastasios Markou [2], Fasil Kidane Dejene [1], Pranava Keerthi Sivakumar [1], Simon Pöllath [3], Kumari Gaurav Rana [1], Neeraj Kumar [1], Chen Luo [4,5], Hanjo Ryll [4], Florin Radu [4], Florian Kronast [4], Peter Werner [1], Christian H. Back [3,5], Claudia Felser [2], Stuart S. P. Parkin † [1]

[1] Max Planck Institute of Microstructure Physics, Weinberg 2, 06120 Halle (Saale), Germany
[2] Max Planck Institute for Chemical Physics of Solids, Nöthnitzer Str. 40, 01187 Dresden, Germany
[3] Institute of Experimental Physics, University of Regensburg, 93040 Regensburg, Germany
[4] Helmholtz-Zentrum Berlin for Materials and Energy, Albert Einstein Str. 15, Berlin 12489, Germany
[5] Institute of Experimental Physics of Functional Spin Systems, Technical University Munich, James-Franck-Str. 1, 85748 Garching b. München, Germany

Supplementary Material

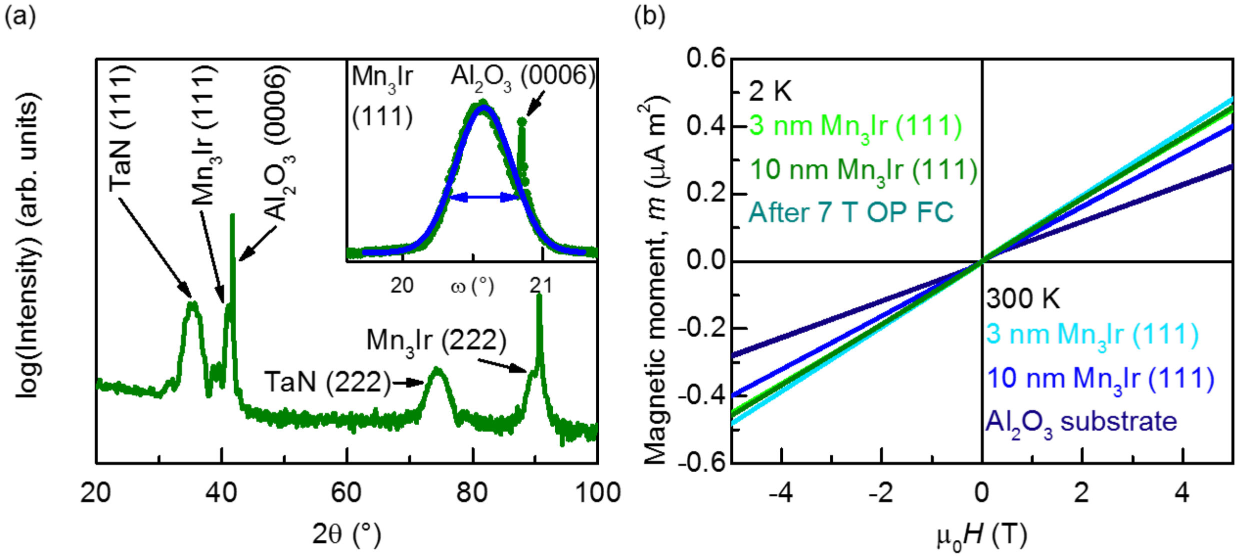

Supplementary FIG. S1. (a) XRD 2θ-θ pattern for a 10 nm Mn$_3$Ir (111) film, with diffraction peaks indexed (inset shows XRD ω rocking curve about Mn$_3$Ir (111) peak). (b) Magnetic moment measured using SQUID-VSM for 10 nm and 3 nm Mn$_3$Ir (111) films at 300 K and 2K, for a 3 nm ultrathin film at 2 K after 7 T OP field cooling, and for a substrate reference sample at 300 K.

---

* james.taylor@mpi-halle.mpg.de
† stuart.parkin@mpi-halle.mpg.de

I – Growth and structural characterization

Comprehensive details of the thin film growth procedure and subsequent structural characterization are given in our previous paper [1]. These demonstrate that the <111> oriented films grow in an fcc γ-Mn_3Ir phase ($Fm\bar{3}m$, space group = 225), shown by Kohn *et al.* to possess a non-collinear antiferromagnetic (AF) structure as detailed in Ref. [2]. Atomic force microscopy measurements indicate the films' smooth growth, with RMS roughness < 4 Å. Meanwhile X-ray diffraction (XRD) ϕ scan pole figures confirm the pseudo hexagon-on-hexagon growth of the TaN (111) buffer, and in turn the Mn_3Ir (111) thin film, on the Al_2O_3 (0001) substrate with the epitaxial relationship: Al_2O_3 (0001) $[11\bar{2}0]$ $[\bar{1}100]$ || TaN (111) $[\bar{1}\bar{1}2]$ $[1\bar{1}0]$ || Mn_3Ir (111) $[\bar{1}\bar{1}2]$ $[1\bar{1}0]$.

In the main text, we determine the crystal lattice spacing for an ultrathin Mn_3Ir film, and relate the observed in-plane (IP) tensile strain to the resulting magnetic properties. For the case of a thicker 10 nm Mn_3Ir (111) film, Supplementary Fig. S1(a) displays a specular 2θ-θ XRD scan, from which an out-of-plane (OP) lattice parameter of $c = (3.797 \pm 0.001)$ Å is measured. Combined with transmission electron microscopy (TEM) studies reported in Ref. [1], such 10 nm thick films were found to grow fully relaxed, with both IP and OP lattice parameters close to the bulk value (a = 3.780 Å). IP grain size > 20 nm is observed, indicating the growth of large crystallites in the lateral direction (slightly larger than in the ultrathin films). Further rocking curve measurements, ω XRD scans, an example of which is inset in Supplementary Fig. S1(a), show the films' low mosaicity of 0.5°. The combination of low roughness and mosaicity, with large lateral grain size and sharp crystal texture, demonstrate the high-quality epitaxial growth of these thin films.

II – Magnetic properties

Initially, the magnetic moments of the 10 nm and 3 nm Mn_3Ir (111) thin films were measured as a function of external magnetic field applied OP along the [111] direction ($\mu_0 H$) using the vibrating sample mode of a SQUID magnetometer (Quantum Design MPMS3). Supplementary Fig. S1(b) records such magnetic hysteresis loops for both 10 nm and 3 nm Mn_3Ir (111) samples at room temperature (RT) and 2 K. In addition, measurements of a reference Al_2O_3 substrate prepared under the same conditions, and of an ultrathin film after field cooling from 400 K to 2 K in a 9 T external magnetic field || [111], are shown. All samples exhibit a large paramagnetic signal, dominated by the substrate background, combined with a small non-linear low-field contribution (also present in the substrate control sample). These results demonstrate the futility of such measurements using conventional magnetometry applied to AF thin films, because of the challenge disentangling tiny film signals from magnetic contamination of the substrate during sample preparation and other background signals. Instead, element specific measurements of the magnetic moment arising from the metallic film alone were made using X-ray magnetic circular dichroism (XMCD) in total electron yield mode, as described in the main text.

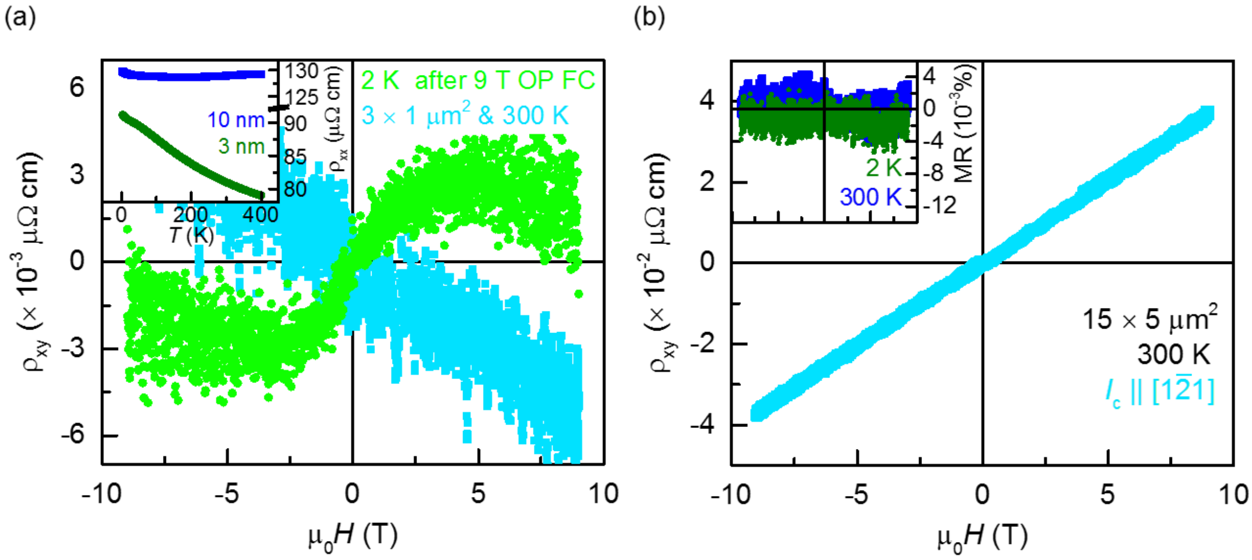

Supplementary FIG. S2. (a) Hall effect for a 3 nm Mn_3Ir (111) film in 3 × 1 μm^2 Hall bar at 300 K (data smoothed using adjacent averaging), and in 150 × 50 μm^2 Hall bar at 2 K after 9 T OP field cooling (inset shows variation in longitudinal resistivity with temperature for 10 nm and 3 nm thin films). (b) Hall effect for a 10 nm Mn_3Ir (111) film in 15 × 5 μm^2 Hall bar directed along $[1\bar{2}1]$ (inset shows longitudinal magnetoresistance over same magnetic field range at 300 K and 2 K).

III – Electrical transport properties

As discussed in the main text, measurements of transverse resistivity, ρ_{xy}, as a function of $\mu_0 H$ were made in Mn_3Ir (111) Hall bar devices of various dimensions. No changes in magnetotransport properties were observed across devices of different sizes. A representative example is shown in Supplementary Fig. S2(a), for a 3 × 1 μm^2 Hall bar fabricated in a 3 nm ultrathin film. Here, the voltage drop data collected across such a small device have been smoothed using a 10 point adjacent averaging filter. The Hall effect at RT is comparable with that reported in Fig. 2(a) of the main text. In addition, measurements were made after field cooling samples from 400 K to 2 K under a 9 T external magnetic field || [111]. Again, no change in anomalous Hall effect (AHE) behavior was measured, demonstrated in Supplementary Fig. S2(a) for a 150 × 50 μm^2 Hall bar in a 3 nm Mn_3Ir (111) film.

Longitudinal resistivity (ρ_{xx}) on cooling from 400 K to 2 K is plotted in the inset of Supplementary Fig. S2(a) for both 10 nm and 3 nm thin films fabricated into 15 × 5 μm^2 and 150 × 50 μm^2 Hall bars respectively. For 10 nm Mn_3Ir (111), ρ_{xx} shows little change as a function of temperature (T), indicating that defect scattering dominates resistivity. In particular, the large residual resistivity at low temperature can be attributed to disorder occurring in the γ-Mn_3Ir phase [3]. Conversely, 3 nm Mn_3Ir (111) shows an increase in ρ_{xx} with decreasing temperature. This semiconductor-like behavior suggests a partially gapped band structure, in agreement with simulations of open Dirac points arising close to the Fermi level due to a combination of non-collinear spin texture and strong spin-orbit coupling [4]. Modification of this complex band structure via subtle changes to crystal structure, or a shift in Fermi energy because of small variations in composition, could therefore lead to changes in the electrical transport properties of ultrathin films. This may explain the change in charge carrier type seen between 10 nm and 3 nm Mn_3Ir (111) samples.

In addition, calculation of the electron mean free path, λ, at RT (assuming electron rest mass) yields $\lambda \approx 3.4$ Å for 10 nm Mn_3Ir (111) and $\lambda \approx 1.5$ Å for 3 nm Mn_3Ir (111). It can be seen that for 3 nm ultrathin films, electron mean free path begins to comprise a notable portion of the film's thickness. Therefore interface scattering effects will begin to play an increasingly significant role in the magnetotransport characteristics of 3 nm Mn_3Ir (111) films, as discussed in the main text.

For 10 nm Mn_3Ir (111) thin films, no AHE driven by either uncompensated magnetization or Berry curvature was observed. Instead an ordinary Hall effect is seen at both 300 K and 2 K, with only a small change in carrier concentration between temperatures ($h = (1.545 \pm 0.001) \times 10^{23}$ cm^{-3} at 2 K). This ordinary Hall effect is isotropic with current flow directed along different IP crystallographic directions, as explained in the main text. This is shown in Supplementary Fig. 2(b), for the example of a 15 × 5 μm^2 Hall bar directed along the $[1\bar{2}1]$ crystal axis at RT. Finally, the inset of Supplementary Fig. 2(b) plots longitudinal magnetoresistance (MR) as a function of $\mu_0 H$ for the same 15 × 5 μm^2 Hall bars directed along $[\bar{1}\bar{1}2]$ as measured in Fig. 2(b) of the main text. The absence of negative MR at both 300 K and 2 K underlines the conclusion that unstrained 10 nm Mn_3Ir (111) films exhibit no uncompensated Mn moment. The small positive MR seen is attributed to Lorentz force scattering of electrons in large applied magnetic fields.

IV – X-ray magnetic linear (circular) dichroism photo-emission electron microscopy, XML(C)D-PEEM (or X-PEEM)

In an attempt to elucidate AF domain structure, X-PEEM measurements were made in 10 nm Mn_3Ir (111) thin films, and 3 nm Mn_3Ir (111) / 5 nm $Ni_{80}Fe_{20}$ heterostructures. Further details of the bilayer samples are given in Ref. [1]. Experiments were performed at beamline UE49_PGM at BESSY, using a combination of linearly and circularly polarized X-ray radiation to excite photo-emitted electrons from the thin film surface, which are then spatially imaged using an electron microscope. For XMCD, X-PEEM images were formed by taking the difference of images recorded using right- and left-handed circularly polarized X-rays. Here the presence of ferromagnetic (FM) domains or uncompensated AF moments would be expected to produce non-zero XMCD signal, with spatial variation in orientation yielding contrast in the image. This is represented in the color scale of the XMCD-PEEM images in Fig. 3 of the main text, with blue (red) contrast showing areas of positive (negative) XMCD signal respectively. In images (c) and (d), XMCD at the Ni-L_3 edge is set on a scale of ± 10%, whilst in images (a) and (e) the scale bar is normalized to the maximum/minimum signal at the Mn-L_3 edge.

For XMLD measurements, linearly polarized X-rays were incident at an angle of 16° to the sample surface, with polarization lying in the film plane. Previous seminal studies have utilized the contrast produced by differing absorption between AF domains with Néel vectors aligned either parallel or perpendicular to the linearly polarized X-rays, in order to image orthogonally oriented domains in collinear AFs [5,6]. Two images were taken with X-ray energies (E) tuned to both the absorption peak at the Mn-L_3 edge (E_B) and to a lower energy just below the rising edge of the peak (E_A), with the asymmetry between the images' signal intensities (I) giving XMLD contrast according to $[I_{Max}(E_B)-I_{Min}(E_A)]/[I_{Max}(E_B)+I_{Min}(E_A)]$ [7]. The greyscale in the XMLD-PEEM images in Fig. 3 of the main text corresponds to the magnitude of this asymmetry, with the maximum/minimum of the scale bar in images (b) and (f) set to give optimum contrast. In this measurement mode, the spatial resolution of the PEEM is ≈ 20 nm. We hypothesized that differences in orientation between the linearly polarized X-rays and the Néel vector defining the chirality of AF domains would lead to a difference in absorption across domains of opposite chirality, and hence a contrast in the photo-emitted electron image. However, as shown in Fig. 3(b) of the main text, no discernable XMLD contrast is observed for a 10 nm Mn_3Ir (111) thin film. Instead, the speckled image corresponds to intensity fluctuations at the resolution limit of the electron microscope, with no structure between extended topological domains of different chirality visible. We therefore postulate this may be due to either AF domains in this high-anisotropy material being smaller than the resolution limit of the PEEM (< 20 nm, which maybe be the case if domain size is correlated with grain size in the film), the limited escape depth of photo-electrons from these films (that are capped with a 2.5 nm layer of TaN), or the possible insensitivity of the triangular AF structure to in-plane polarized X-rays [8].

In an attempt to enlarge chiral domains in Mn_3Ir to an observable size, exchange bias was utilized to introduce a preferential AF domain orientation through coupling to an FM layer in a 3 nm Mn_3Ir (111) / 5 nm $Ni_{80}Fe_{20}$ heterostructure. By cooling such AF / FM bilayers through their blocking temperature (in this case 40 K [1]) in an applied magnetic field, a unidirectional exchange anisotropy, and hence a dominant pinned AF domain state, can be set. Using a combination of XMLD- and XMCD-PEEM, a direct correlation between externally manipulatable FM domains and exchange coupled AF domains has previously been observed [8-10]. We therefore took X-PEEM images at both the Ni-L_3 and Mn-L_3 edges, with the results reported in the main text.

Supplementary References

[1] J. M. Taylor *et al.*, arXiv:1903.05539 (2019).

[2] A. Kohn, A. Kovács, R. Fan, G. J. McIntyre, R. C. C. Ward, and J. P. Goff, Sci. Rep. **3**, 2412 (2013).

[3] Y. Jin, R. Skomski, P. Kharel, S. R. Valloppilly, and D. J. Sellmyer, AIP Adv. **7** (2017).

[4] H. Chen, Q. Niu, and A. H. MacDonald, Phys. Rev. Lett. **112**, 017205 (2014).

[5] J. Stöhr, A. Scholl, T. J. Regan, S. Anders, J. Lüning, M. R. Scheinfein, H. A. Padmore, and R. L. White, Phys. Rev. Lett. **83**, 1862 (1999).

[6] A. Scholl *et al.*, Science **287**, 1014 (2000).

[7] M. J. Grzybowski *et al.*, Phys. Rev. Lett. **118**, 057701 (2017).

[8] T. Eimüller, T. Kato, T. Mizuno, S. Tsunashima, C. Quitmann, T. Ramsvik, S. Iwata, and G. Schütz, Appl. Phys. Lett. **85**, 2310 (2004).

[9] F. Nolting *et al.*, Nature **405**, 767 (2000).

[10] H. Ohldag, T. J. Regan, J. Stöhr, A. Scholl, F. Nolting, J. Lüning, C. Stamm, S. Anders, and R. L. White, Phys. Rev. Lett. **87**, 247201 (2001).

3 Part B - Mn_3Sn

3.1 Noncollinear antiferromagnetic Mn_3Sn films

The following chapter of this cumulative thesis consists of the peer-reviewed scientific paper (and its supplementary material) published as:

A. Markou, J. M. Taylor, A. Kalache, P. Werner, S. S. P. Parkin, and C. Felser, "Noncollinear antiferromagnetic Mn_3Sn films", *Phys. Rev. Mater.* **2**, 051001(R) (2018)

Reprinted with permission from [A. Markou et al., "Noncollinear antiferromagnetic Mn_3Sn films", *Phys. Rev. Mater.* **2**, 051001(R) (2018)]. Published (2018) by the American Physical Society under the terms of the Creative Commons Attribution 4.0 license. DOI: 10.1103/PhysRevMaterials.2.051001

In the second half of this thesis, Part B, we move onto an investigation of the material Mn_3Sn. As discussed in Section 1.2.7, Mn_3Sn is a noncollinear AF similar to Mn_3Ir, but with a hexagonal crystal structure and an *inverse* triangular spin texture. In Section 2.2, we explored how the theoretically predicted intrinsic AHE could not be observed for Mn_3Ir, even in strained ultrathin films showing an uncompensated magnetic moment, because the material remains fixed in a multi-domain state. This is due to the strong internal anisotropies of Mn_3Ir, meaning that its magnetic order cannot be manipulated by even comparatively strong magnetic fields. This stable multi-domain state makes Mn_3Ir attractive for EB applications, but prohibits its evolution to become the active component of AF spintronic devices.

Mn_3Sn, on the other hand, exhibits a number of different properties that make it more attractive than Mn_3Ir for applications in topological spintronics. Mn_3Sn has a hexagonal crystal structure, consisting of atomic planes stacked along the c-axis. Within each of these basal planes, Mn moments are arranged on a kagome-type lattice, with Sn atoms located at the center of each hexagon. This results in a complex interplay of AF exchange coupling between Mn atoms and DMI, which stabilizes the magnetic order of Mn_3Sn in the inverse triangular structure, as discussed in Section 1.2.7 [64]. Added to this, the crystal directions joining nearest neighbor Sn atoms, that is, $\langle 2\bar{1}\bar{1}0\rangle$, act as magnetic easy axes [111]. This magnetocrystalline anisotropy results in an equilibrium spin configuration where one Mn moment points along such a $\langle 2\bar{1}\bar{1}0\rangle$ direction, with the other two moments in the inverse triangular spin texture canting slightly away from their default 120° alignment towards these easy axes [110]. The spins no longer fully compensate, resulting in a tiny net magnetic moment pointing locally along $\langle 2\bar{1}\bar{1}0\rangle$ crystallographic directions.

A relatively small magnetic field can be used to couple to this resulting weak magnetization and manipulate it; that is, align the net uncompensated moment with the applied magnetic field. The uncompensated moment can freely to rotate within the *ab*-plane of Mn_3Sn, and will follow the direction of the external magnetic field. The magnetic field can saturate the weak magnetization and its direction will reverse hysterically when looping applied magnetic field. However, unlike the strained Mn_3Ir films studied in Section 2.2, in the case of Mn_3Sn, the fact that the uncompensated moment arises fundamentally from a canting of the inverse triangular spin texture means that modifying the direction of this uncompensated moment will, in turn, act to rotate the entire noncollinear AF order. In other words, saturating the weak magnetization in one direction corresponds to aligning the entire inverse triangular spin texture into a single chirality. In practice, this means than an external magnetic field can be used to drive a Mn_3Sn sample into a single chiral domain state, and then to reverse this chirality throughout the material.

Contrary to the case of Mn_3Ir, one would therefore expect a Berry curvature driven AHE to be measurable in Mn_3Sn, whose polarity follows the magnetization reversal of the uncompensated moment (i.e. whose sign can be reversed when the chirality of the AF order is inverted) and which saturates at high magnetic field. Indeed, such an observation was first made in 2015 [131], followed shortly afterwards by a comparable finding in the closely related compound Mn_3Ge [135]. This measurement was made in single crystals of Mn_3Sn, in a conventional Hall effect geometry where magnetic field is applied within the *ab*-plane, with current applied either along an orthogonal direction within the basal plane or along the *c*-axis [131]. The magnetization of the sample was extremely small, as expected, and the large anomalous Hall conductivity measured was therefore attributed to the momentum-space Berry phase mechanism discussed in Section 1.2.9. A number of related observations followed, including an experimental demonstration of the presence of theoretically predicted Weyl points in Mn_3Sn [72], which act as the sources and sinks of the Berry flux generating these topological transport properties.

These landmark experiments highlight Mn_3Sn as a test-bed for studying the electrical and magnetic properties of noncollinear antiferromagnets, and have elucidated a number of fundamental physical phenomena emerging from the field of topological magnetism. Furthermore, the exciting magnetotransport properties offer much promise for the potential applications of Mn_3Sn in antiferromagnetic spintronics. To achieve this, however, it is necessary to fabricate devices using *thin films* of Mn_3Sn. At the time of the first theoretical predictions [68] and experimental observations [131] of AHE in Mn_3Sn, preparation of this compound had not yet been demonstrated in thin film form. Realization of this goal was achieved in the paper forming Section 3.1 of this thesis.

We succeeded in growing thin films of $D0_{19}$ hexagonally structured Mn_3Sn on $Y{:}ZrO_2$ substrates using a 5 nm Ru buffer layer. (111) cut $Y{:}ZrO_2$ substrates seed the growth of smooth, single crystalline Ru with (0001) orientation. Co-sputtering of Mn and Sn onto this surface in turn stabilized Mn_3Sn, with the c-axis directed OP. The crystal structure and lattice parameters of the multilayers were determined from XRD $2\theta - \theta$ measurements. We deposited Mn_3Sn (0001) films with thicknesses as low as 5 nm, and found a slight reduction in the a lattice parameter (and increase in the c lattice parameter) as film thickness was reduced. The layers grew heteroexpitaxially on the substrate, and using azimuthal XRD scans we determined their epitaxial relationship to be: $Y{:}ZrO_2(111)[1\bar{1}0][\bar{1}12]\|(0001)[11\bar{2}0][01\bar{1}0]\|(0001)][11\bar{2}0][01\bar{1}0]$.

We characterized the magnetic properties of the thin films using SQUID-VSM. Firstly, we measured the magnetization response of a Mn_3Sn sample directly, as a function of magnetic field applied both IP and OP. As expected, we observe a mostly paramagnetic response, with only small hysteresis, when magnetic field is applied OP along the (0001) hard axis. However, with external magnetic field in the basal plane, the expected small uncompensated moment arising from the canting of Mn spins is observed. This weak magnetization is found to be reversible in magnetic field, with a magnitude of $34\,\mathrm{kA\,m^{-1}}$ for a 40 nm Mn_3Sn (0001) film. This is significantly larger than that found for bulk crystals, which can be explained by the presence of inherent structural defects in thin films, as well as chemical disorder caused by the films stabilizing in a slightly off-stoichiometric composition and by antisite disordering. These may act to disrupt the subtle balance of exchange coupling, DMI and MCA that combine to determine the canting of Mn moments within the basal plane, which may increase this canting slightly and thus enhance the IP uncompensated Mn moment in thin films.

In addition, we prepared replica Mn_3Sn (0001) samples, this time capped with a layer of FM permalloy ($Ni_{80}Fe_{20}$). In order to prove the AF character of the Mn_3Sn thin films, we measured EB across these bilayer samples (see Section 1.2.5). The Néel temperature of Mn_3Sn, 420 K, results in a blocking temperature for these heterostructures below room temperature. Therefore, it was necessary to cool the samples in order to measure EB, using the same method described in Section 2.1. We observe sizeable EB below 50 K, with exchange bias fields as large as 8 mT obtained at low temperatures after training. This introduction of a unidirectional anisotropy to the FM layer, as a result of exchange interactions across the interface, confirms that the Mn_3Sn films are indeed AF.

Finally, we performed TEM analysis to evaluate thin film structure at the nanoscale. This confirmed the heteroepitaxial growth of the films (through SAED patterns), their chemical homogeneity (using EDXS mapping) and the high quality crystal structure of the Mn_3Sn layer. Specifically, sharps spots in the SAED patterns indicate quasi-single-crystalline growth, whilst scanning-TEM images with atomic resolution indicate a series of stacking faults within the first few crystal planes (occurring as initial epitaxial strain in the film relaxes) after which the Mn_3Sn grows almost defect free.

TEM micrographs also revealed that the films prepared in this study were discontinuous. Island growth morphology typically arises when adatoms deposited using physical vapor deposition methods arrive with excessive energy, allowing them to migrate across the substrate surface and coalesce. This suggests that the growth temperature of the films was too high. Such a high growth temperature may have been necessary to seed hexagonal crystal structure to the multilayers due to their sizable lattice mismatch with the $Y{:}ZrO_2$ substrate. Unfortunately, the island-like morphology prevented measurement of electrical transport properties in these samples. Instead, progress towards this ultimate goal will be discussed later in this thesis. Nevertheless, the present results represent the first demonstration of the growth of Mn_3Sn in thin film form, and are reported in the following paper: A. Markou et al., “Noncollinear antiferromagnetic Mn_3Sn films”, *Phys. Rev. Mater.* **2**, 051001(R) (2018).

PHYSICAL REVIEW MATERIALS **2**, 051001(R) (2018)

Rapid Communications

Noncollinear antiferromagnetic Mn_3Sn films

A. Markou,[1,*] J. M. Taylor,[2] A. Kalache,[1] P. Werner,[2] S. S. P. Parkin,[2] and C. Felser[1,†]
[1] *Max Planck Institute for Chemical Physics of Solids, Nöthnitzer Str. 40, 01187 Dresden, Germany*
[2] *Max Planck Institute of Microstructure Physics, Weinberg 2, 06120 Halle, Germany*

(Received 12 February 2018; published 2 May 2018)

Noncollinear hexagonal antiferromagnets with almost zero net magnetization were recently shown to demonstrate giant anomalous Hall effect. Here, we present the structural and magnetic properties of noncollinear antiferromagnetic Mn_3Sn thin films heteroepitaxially grown on $Y:ZrO_2$ (111) substrates with a Ru underlayer. The Mn_3Sn films were crystallized in the hexagonal $D0_{19}$ structure with c-axis preferred (0001) crystal orientation. The Mn_3Sn films are discontinuous, forming large islands of approximately 400 nm in width, but are chemical homogeneous and characterized by near perfect heteroepitaxy. Furthermore, the thin films show weak ferromagnetism with an in-plane uncompensated magnetization of $M = 34$ kA/m and coercivity of $\mu_0 H_c = 4.0$ mT at room temperature. Additionally, the exchange bias effect was studied in Mn_3Sn/Py bilayers. Exchange bias fields up to $\mu_0 H_{EB} = 12.6$ mT can be achieved at 5 K. These results show Mn_3Sn films to be an attractive material for applications in antiferromagnetic spintronics.

DOI: 10.1103/PhysRevMaterials.2.051001

I. INTRODUCTION

Antiferromagnetic spintronics is a rapidly developing field that has received much attention in recent years and could represent the next advance in spintronic applications, as antiferromagnets show several advantages compared to the ferromagnets currently utilized. Antiferromagnets do not produce stray fields, are robust to external perturbations from magnetic fields, and show ultrafast spin dynamics and current-induced phenomena [1–6]. Among many different antiferromagnetic [7–9] or artificial antiferromagnetic materials [10,11], the noncollinear chiral antiferromagnets have attracted much interest, due to their remarkable structural, magnetic, and electrotransport properties. The trianglular spin structure of these compounds gives rise to a large anomalous Hall effect (AHE) [12,13], thermoelectric effect [14–16], magneto-optical Kerr effect [17,18], and spin Hall effect (SHE) [19]. Inspired by experimental work in Mn_3Ir [19], *ab initio* calculations confirmed large anisotropic anomalous Hall current and spin Hall current in these materials [20], while predicting that charge current is also spin polarized [21].

Hexagonal Mn_3Z (Z = Ga, Ge, and Sn) compounds are noncollinear antiferromagnets that crystallize in the $D0_{19}$ structure. Mn_3Sn and Mn_3Ge were theoretically predicted to show large AHE driven by nonvanishing Berry curvature [13], while band-structure calculations reveal that both compounds demonstrate a Weyl semimetal state with several Weyl points around the Fermi level [22,23]. In accordance with these theoretical calculations, single crystals of Mn_3Sn and Mn_3Ge were found to exhibit large AHE [24–26] and large anomalous Nernst effect [14,15], reaching the same order of magnitude as in ferromagnetic materials. These studies concern bulk single crystal, but to extend to spintronic devices thin films of these materials are required.

Up to now, the only report on hexagonal noncollinear antiferromagnetic thin films is from Mn_3Ga, as a bottom pinning antiferromagnet layer for magnetic tunnel junctions [27]. The Mn_3Ga film was (0001) oriented, showing low magnetization and large coercivity. The magnetic properties measured parallel and perpendicular to the film plane indicate that the net magnetization of the Mn_3Ga film was almost isotropic.

Mn_3Sn crystallizes in the hexagonal Mg_3Cd-type structure ($D0_{19}$), with space group $P6_3/mmc$ (No. 194) as shown in Fig. 1(a) and lattice constants of $a = b = 5.670$ Å, $c = 4.530$ Å. The Mn atoms form a kagome-type lattice in basal planes stacked along the c axis, where Sn atoms are located at the center of hexagons formed by Mn atoms. Mn_3Sn has a Néel temperature of $T_N = 420$ K. Neutron diffraction studies have demonstrated that a noncollinear triangular spin configuration of the Mn moments is obtained below T_N, where the neighboring moments are aligned at an angle of 120° [28,29], as shown in Fig. 1(b). Furthermore, Mn_3Sn shows weak ferromagnetism [30], owing to geometrical frustration of the Dzyaloskinskii-Moriya interaction (DMI) stabilized antiferromagnetic structure, which slightly cants spins toward in-plane easy axes.

In this work, we present the structural and magnetic properties of antiferromagnetic Mn_3Sn films with hexagonal structure and the results of exchange bias using these thin films. For this purpose, we performed systematic x-ray diffraction (XRD), transmission electron microscopy (TEM), and magnetic characterization of films heteroepitaxially grown on ZrO_2 substrates.

---

[*] anastasios.markou@cpfs.mpg.de
[†] claudia.felser@cpfs.mpg.de

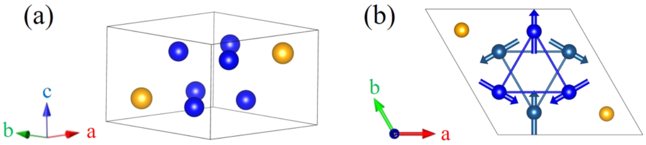

FIG. 1. (a) Crystal and (b) magnetic structure of Mn_3Sn, where the blue and orange spheres correspond to the Mn and Sn atoms, respectively.

II. EXPERIMENTAL DETAILS

Mn_3Sn films with thicknesses of 5–40 nm have been grown heteroepitaxially on single-crystal yttrium stabilized ZrO_2 (111) substrates with a 5 nm Ru underlayer. A BESTEC UHV magnetron sputtering system was used for the deposition of the films, with Mn (2″), Sn (2″), and Ru (2″) sources in confocal geometry. The target to substrate distance was 8″. Prior to deposition, the chamber was evacuated to a base pressure less than 2×10^{-8} mbar, while the process gas (Ar 5 N) pressure was 3×10^{-3} mbar. The total stack was Y:ZrO_2/Ru(5 nm)/Mn_3Sn(5–40 nm)/Al(2 nm). The Ru underlayer was deposited at a rate of 0.27 Å/s by applying 40 W dc power. The Mn_3Sn films were grown by cosputtering. The Mn was deposited at a rate of 0.48 Å/s by applying 55 W dc power and the Sn at a rate of 0.29 Å/s by applying 10 W dc power. The growth rates and the film thicknesses were determined by a quartz crystal microbalance and confirmed by using x-ray reflectivity measurements. The substrates were rotated during deposition, to ensure homogeneous growth. The Ru underlayer and the Mn_3Sn films were grown at 500 °C and then post-annealed *in situ* for an additional 10 min. In order to study the exchange bias effect, an additional stack was prepared of Y:ZrO_2/Ru(10 nm)/Mn_3Sn(40 or 20 nm)/Py(5 nm)/Al(2 nm), under the same conditions, with the Permalloy (Py = $Ni_{80}Fe_{20}$) film grown at room temperature (RT). All samples were capped at RT with a 2-nm-thick Al film to prevent oxidation.

Stoichiometry was estimated as $Mn_{74}Sn_{26}$ by energy-dispersive x-ray spectroscopy (EDXS) and verified by inductively coupled plasma optical emission spectrometry. XRD was measured with a PANalytical X'Pert^3 MRD diffractometer, using Cu Kα1 radiation (λ = 1.5406 Å). Conventional TEM, high-resolution TEM, and scanning transmission electron microscopy (STEM) were performed using a FEI Titan 80-300 microscope. For high-resolution STEM imaging, the high-angle annular dark-field technique (HAADF-STEM) was applied. Additionally, the Titan was equipped with EDXS for element mapping with high spatial resolution. Cross-section samples were prepared by focused ion beam milling. A protective C-Pt layer was deposited on the stack before starting the cross-section preparation. Magnetic measurements were carried out using a Quantum Design (MPMS 3 SQUID-VSM) magnetometer.

III. RESULTS AND DISCUSSION

A. Structural properties

Different XRD measurements, 2θ-ω scan, rocking curve (ω scan), and phi-scan, were performed to study the structure, the crystallinity, and the heteroepitaxial relationship between the films and the substrate, respectively. The lattice mismatch between the substrate and the Ru underlayer is 4.44%, and between the Ru underlayer and the Mn_3Sn film is 5.26%, which allow the heteroepitaxial growth of *c*-axis oriented films. Figure 2(a) shows the XRD pattern of the 40 nm Mn_3Sn film. The (111) and (222) reflections from the Y:ZrO_2 substrate, and the (0002) and (0004) reflections from the hcp Ru were observed, suggesting that the Ru underlayer is (0001) oriented. The Ru main diffraction peaks are surrounded by Pendellösung fringes ($n_{\pm1}$, $n_{\pm2}$), which indicate a sharp interface between film and substrate and a high-crystalline quality along the *c* axis. Only the (0002) and (0004) reflections from the Mn_3Sn film were observed in XRD patterns, which demonstrates that the sample is crystallized in the hexagonal $D0_{19}$ structure with (0001) preferred orientation and the *c* axis normal to the film plane.

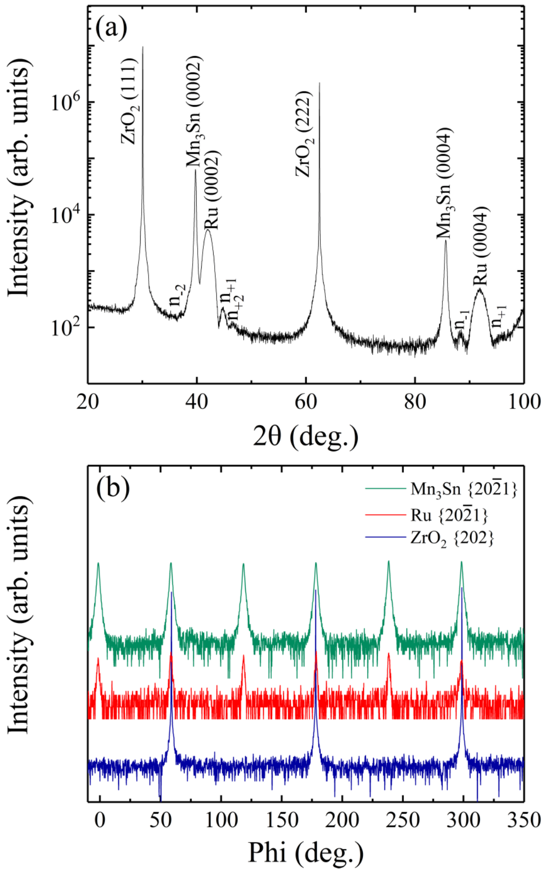

FIG. 2. (a) XRD pattern of the 40 nm Mn_3Sn film on 5 nm Ru underlayer. (b) Phi-scan patterns of the hexagonal $\{20\bar{2}1\}$ planes from the Mn_3Sn film and Ru underlayer, and the cubic {202} planes from the ZrO_2 substrate.

Phi-scan patterns of the hexagonal $\{20\bar{2}1\}$ planes from the Mn_3Sn film and Ru underlayer, and the cubic {202} planes from the Y:ZrO_2 substrate, are depicted in Fig. 2(b). The six reflections of the Mn_3Sn film and Ru underlayer show sixfold symmetry with 60° intervals, suggesting hexagonal single-crystalline epilayers with well-defined in-plane orientation. The three different sets of lattice planes occur at the same azimuthal angle ϕ, which indicates that the

TABLE I. Lattice constants a and c, and the FWHM of the (0002) rocking curve profile, for Mn$_3$Sn thin films with different thicknesses.

Thickness (nm)	a (Å) ± 0.002 Å	c (Å) ± 0.002 Å	FWHM (deg.)
5	5.689	4.537	0.780
10	5.691	4.534	0.759
20	5.694	4.532	0.748
40	5.695	4.532	0.566

unit cells of the Mn$_3$Sn film and Ru underlayer are well aligned in the basal planes of the Y:ZrO$_2$ substrate. The crystallographic orientation relationship is thus determined as $\mathrm{Y{:}ZrO_2(111)[1\bar{1}0]\|Ru(0001)[11\bar{2}0]\|Mn_3Sn(0001)[11\bar{2}0]}$.

The measured lattice parameters a and c, and the full width at half maximum (FWHM) of the (0002) out-of-plane rocking curve are summarized in Table I. The lattice parameter c is deduced from the (0002) and (0004) reflections of the out-of-plane XRD patterns, while the lattice parameter a is estimated from the in-plane $(20\bar{2}1)$ reflection. For the measurement of the in-plane reflection, the detector was used in 0D scanning mode to create a 2D $2\theta/\omega$-χ scan map, in which the $(20\bar{2}1)$ reflection appears as a peak with Gaussian shape. The $(20\bar{2}1)$ reflection was chosen because its intensity is the strongest, thus making investigation of the reflection possible even for 5-nm-thick films. The c and a lattice parameters are very close to the bulk values. As the film thickness is decreased, a decreases, while c increases. This dependence of the lattice constants with decreasing film thickness can be explained in terms of inner strain, due to lattice mismatch and different thermal expansion coefficients between the epilayers and the substrate. The crystal quality of the Mn$_3$Sn films was evaluated from the FWHM values of rocking curves measured around (0002) reflections. The high intensity of the curve combined with small FWHM $\approx 0.566^\circ$ suggests that the 40-nm-thick sample shows high-crystalline quality with low mosaicity (see Supplemental Material [31]). At lower thicknesses the FWHM is slightly higher, owing to the limited film thickness and/or presence of defects.

B. TEM analysis

TEM was performed to evaluate the film quality on the nanoscale. A cross-section high-resolution HAADF-STEM image of the 40-nm-thick Mn$_3$Sn film is represented in Fig. 3(a). The crystal lattice of the Mn$_3$Sn film is characterized by nearly perfect heteroepitaxy. Close to the interface between the Mn$_3$Sn film and the Ru underlayer, a small amount of planar defects are observed. They have the character of stacking faults within the stacking sequence of the (0001) planes along the [0001] growth direction. An example is shown in Fig. 3(a), where stacking faults are indicated by dashed lines. We attribute these planar faults to strain relaxation in the Mn$_3$Sn lattice, as similarly observed in other heteroepitaxial systems [32,33]. Moving away from the interface, further epitaxial growth of the Mn$_3$Sn layer proceeds along the [0001] direction without defects. The inset of Fig. 3(a) illustrates the scheme of the Mn$_3$Sn crystal lattice according to the chosen $\langle 01\bar{1}0\rangle$ orientation for the TEM observation. The large orange spheres and the smaller blue spheres correspond to the Sn and Mn atoms, respectively. In the HAADF-STEM image the lattice of the Ru underlayer is locally blurred. This can be attributed to local strains and a misalignment of the crystal lattice due to strained-induced mosaicity. Furthermore, the TEM analysis reveals that the Mn$_3$Sn film is discontinuous, forming large islands of approximately 400 nm in width (see Supplemental Material). The growth of islands can be attributed to the large lattice mismatch between the Ru underlayer and Mn$_3$Sn film, which is 5.26%. Furthermore, the kinetic conditions (i.e., growth rate, temperature, and atomic mobility) during thin-film deposition may affect the morphology of the films, similar to the case of Mn$_3$Ga [34].

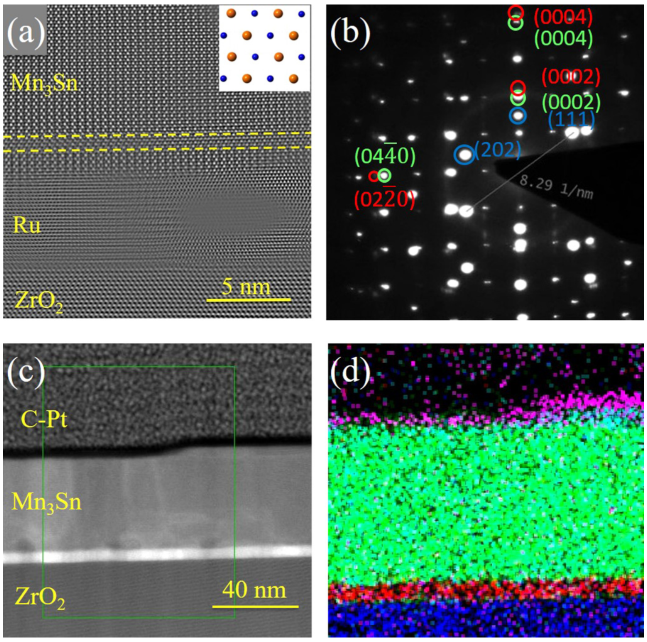

FIG. 3. (a) Cross-section HRSTEM image of the 40 nm Mn$_3$Sn film grown on Y:ZrO$_2$ substrate with a 5 nm Ru underlayer. The inset illustrates the scheme of the Mn$_3$Sn crystal lattice in the $\langle 01\bar{1}0\rangle$ direction, where the large orange spheres and the small blue spheres correspond to the Sn and Mn atoms, respectively. (b) SAED pattern showing the diffraction spots from Mn$_3$Sn (green open circles), Ru (red open circles), and Y:ZrO$_2$ (blue open circles). (c) Cross-section HAADF-STEM image, where the green box denotes the area where chemical mapping was performed. (d) Elemental mapping of Zr (blue), Ru (red), Mn (green), Sn (light blue), and Al (purple).

The selected area electron diffraction (SAED) pattern of the same sample is depicted in Fig. 3(b), where the electron beam is parallel to the $\langle 11\bar{2}0\rangle$ zone axis of the epilayers. The blue, red, and green open circles correspond to the diffraction spots from the substrate, the Ru underlayer, and the Mn$_3$Sn film, respectively. The three different sets of diffraction spots are aligned, confirming the coherent heteroepitaxial growth of the epilayers on the substrate. The indexed SAED pattern reveals that the Mn$_3$Sn film is crystallized in the hexagonal $D0_{19}$ structure. The lattice constants were determined to be $a = 5.676$ Å and $c = 4.495$ Å, which are in a good agreement with the XRD measurements. The small difference can be attributed to the larger measurement error result-

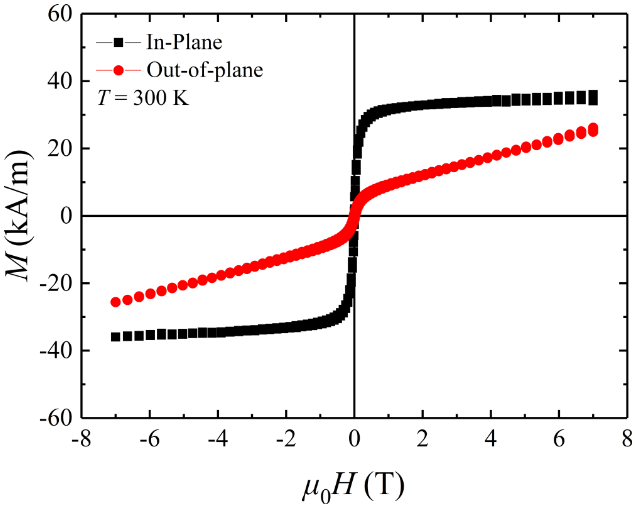

FIG. 4. In-plane and out-of-plane magnetization hysteresis loops of the 40 nm Mn_3Sn film.

ing from the analysis of local restricted electron diffraction patterns.

The element distribution within the Mn_3Sn films was analyzed by EDXS element mapping in the HAADF mode. An example is shown in Figs. 3(c) and 3(d). The green box in the HAADF image [Fig. 3(c)] indicates the area where the elemental analysis was performed. The spatial distribution of the count rate intensity for Mn, Sn, Ru, and Zr elements are represented with different colors in Fig. 3(d). Mn and Sn were detected at exactly the same sample regions, therefore confirming the homogeneity of the Mn_3Sn film. Due to the sharp interface between the Ru and Mn EDXS signals, we conclude that intermixing between the Mn_3Sn film and Ru underlayer does not occur.

C. Magnetic properties and exchange bias

Typical in-plane and out-of-plane magnetization hysteresis loops for the 40 nm Mn_3Sn film measured at 300 K are shown in Fig. 4. The Mn_3Sn film shows small spontaneous magnetization in plane. This uncompensated moment in otherwise noncollinear antiferromagnetic Mn_3Sn has been explained experimentally [28,30] and theoretically [35], due to geometric frustration of the Mn moments leading to canting in the *a*-*b* plane. Even though the Mn moments are expected to lie only in the *a*-*b* plane, a smaller additional moment is observed out of plane, indicating that Mn moments are tilted slightly toward the *c* axis, similar to bulk Mn_3Ge [25]. The weak ferromagnetism in this class of materials is useful, as it allows control of their transport properties, since a small external field can switch the moment orientation of the chiral spin structure.

In contrast with previously reported Mn_3Ga films, which show isotropic uncompensated magnetization in plane and out of plane accompanied by large coercivity ($\mu_0 H_c > 3$ T) [27], these Mn_3Sn films are anisotropic. The 40 nm film has an in-plane uncompensated moment of $M = 34$ kA/m and coercivity of $\mu_0 H_c = 4.0$ mT, while for a 20 nm film the magnetic properties are similar with an uncompensated moment of $M = 37$ kA/m and coercivity of $\mu_0 H_c = 3.8$ mT (see Supplemental Material). The in-plane uncompensated moment of the 40 nm film corresponds to $0.21\mu_B$/f.u. which is one order of magnitude larger than similar bulk single crystals [24–26]. The structure of bulk Mn_3Sn is stable in excess of Mn, which randomly occupies the Sn site, but in thin films it is stable even with less Mn (Mn:Sn ∼74:26 at.%). We therefore propose that the larger magnetization observed in films compared to bulk can be attributed to additional uncompensated moments arising from disorder effects. The disorder is caused due to the excess of Sn randomly occupying Mn sites or due to Mn vacancies, as well as a possible slight antisite disorder with Sn/Mn exchanging their positions. Furthermore, the DMI, which is responsible for the triangular spin configuration, can produce only an in-plane moment, since the D_{ij} vector has to lie along the *c* axis. Thus the smaller out-of-plane moment observed in Fig. 4 indicates a small disruption to the expected anisotropy that tilts the Mn moments slightly toward the *c* axis. This shows that the excess of Sn on Mn sites or vacancies can cause a disorder in the triangular spin configuration, which in turn affects the magnetization through an increase of uncompensated moment. In addition, surface or bulk defects, lattice strain, and grain boundaries may introduce further uncompensated moment contributions.

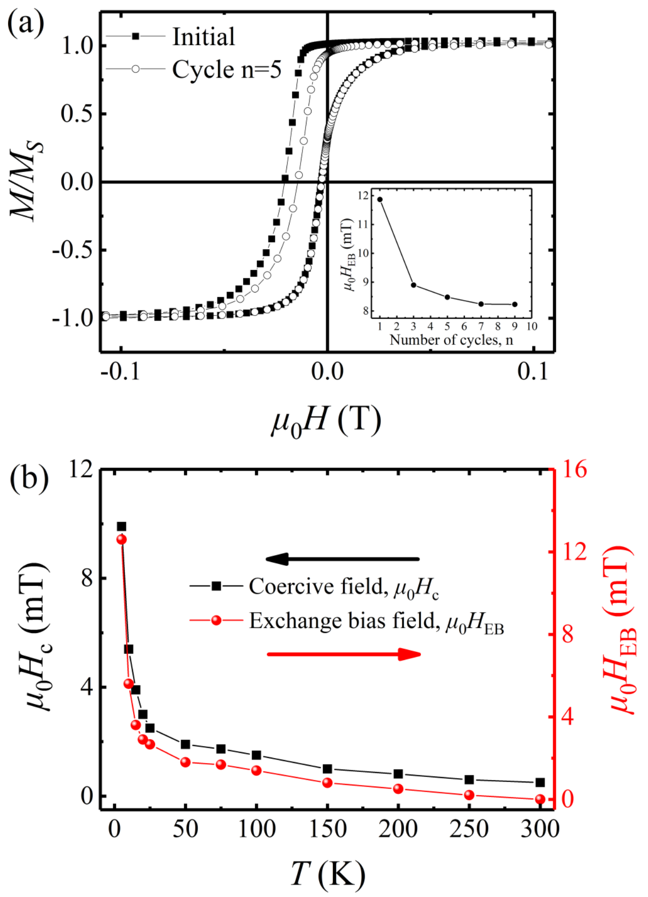

FIG. 5. (a) Initial (solid symbols) and trained (open symbols) in-plane magnetization hysteresis loops of the Mn_3Sn (40 nm)/Py (5 nm) bilayer at 5 K after 1 T FC. (b) Temperature dependence of exchange bias and coercive fields during field cooling.

Exchange bias (EB) results from interfacial exchange interactions between coupled antiferromagnetic and ferromagnetic (AFM/FM) systems [36]. EB is characterized by a shift in the magnetization hysteresis loop of the FM along the applied field axis, called the exchange bias field ($\mu_0 H_{\mathrm{EB}}$), accompanied by a coercivity ($\mu_0 H_{\mathrm{c}}$) enhancement. This phenomenon arises below a certain characteristic temperature of the AFM/FM system, known as the blocking temperature (T_{B}). EB is utilized to pin the magnetization of a FM layer in a desired direction in spintronic devices such as spin valves [37] and magnetic random-access memories [38].

The initial in-plane normalized magnetization hysteresis curve (solid symbols) of the $\mathrm{Mn_3Sn}$ (40 nm)/Py (5 nm) bilayer measured at 5 K after field cooling (FC) from 400 K under a 1 T in-plane magnetic field is depicted in Fig. 5(a). After FC the measured hysteresis loop is shifted along the negative direction of the applied field axis, and also vertically by $+15$ kA/m. The vertical loop shift indicates the presence of uncompensated pinned interfacial spins [39,40]. After correcting for the vertical shift, values of $\mu_0 H_{\mathrm{c}} = 10.0$ mT and $\mu_0 H_{\mathrm{EB}} = 12.6$ mT are determined. These results suggest the observed EB is mediated by a layer of uncompensated spins induced in $\mathrm{Mn_3Sn}$ at the interface with Py, a fraction of which are pinned (demonstrated by the vertical hysteresis loop shift) due to strong exchange coupling to the bulk $\mathrm{Mn_3Sn}$ antiferromagnetic order and thus inducing unidirectional anisotropy in the Py film. Following a number of hysteresis loop measurements, as shown in Fig. 5(a) (open symbols), a training effect of this exchange bias is observed. After five repeat cycles, we obtain consistent values of $\mu_0 H_{\mathrm{EB}} = 8.0$ mT [inset of Fig. 5(a)]. This training effect can be attributed to a relaxation of uncompensated interfacial moments during field cycling, in turn lessening exchange bias. In addition, the exchange bias field is reversible when field cooled under a negative applied field, but otherwise found to be independent of cooling field strength (see Supplemental Material).

The temperature dependence of $\mu_0 H_{\mathrm{c}}$ and $\mu_0 H_{\mathrm{EB}}$ for the $\mathrm{Mn_3Sn}$ (40 nm)/Py (5 nm) bilayer is shown in Fig. 5(b). Each data point represents the displacement in the $M(H)$ loop measured after the bilayer was cooled from 400 K to different temperatures under a 1 T in-plane magnetic field. As the bilayer passes through its characteristic T_{B}, increasing exchange interactions act to pin the magnetization of Py. A rapid increase in both $\mu_0 H_{\mathrm{c}}$ and $\mu_0 H_{\mathrm{EB}}$ below 50 K indicates the onset of exchange coupling, allowing us to place the blocking temperature of a 40-nm-thick $\mathrm{Mn_3Sn}$ film in this range (see Supplemental Material).

IV. CONCLUSIONS

In summary, we have studied the structural and magnetic properties of $\mathrm{Mn_3Sn}$ films heteroepitaxially grown on Y:$\mathrm{ZrO_2}$ (111) substrates with a 5 nm Ru underlayer. The films were crystallized in the hexagonal $D0_{19}$ structure with (0001) preferred orientation. TEM analysis reveals that the $\mathrm{Mn_3Sn}$ films, although discontinuous, are chemically homogeneous and characterized by near perfect heteroepitaxy. Magnetic measurements show weak anisotropic ferromagnetism in the films. The weak ferromagnetism in this class of materials allows control of their electrical transport properties, since a small external field can switch the moment orientation of the chiral spin structure. Furthermore, we have studied the exchange bias of $\mathrm{Mn_3Sn}$/Py bilayers. Exchange bias fields up to $\mu_0 H_{\mathrm{EB}} = 12.6$ mT are achieved at 5 K. Such exchange biased heterostructures open up the possibility of further interesting study investigating the spin-orbit torque produced by $\mathrm{Mn_3Sn}$, similar to $\mathrm{Mn_3Ir}$/Py [19], following predictions of a large SHE [20] and spin-polarized current [21]. Our results show that $\mathrm{Mn_3Sn}$ is an attractive material to study novel phenomena which may have a major impact in antiferromagnetic spintronic applications.

ACKNOWLEDGMENT

This work has been funded by EU FET Open RIA Grant No. 766566.

[1] E. V. Gomonay and V. M. Loktev, Low Temp. Phys. **40**, 17 (2014).

[2] T. Jungwirth, X. Marti, P. Wadley, and J. Wunderlich, Nat. Nanotechnol. **11**, 231 (2016).

[3] A. H. MacDonald and M. Tsoi, Philos. Trans. R. Soc. A **369**, 3098 (2011).

[4] J. Železný, H. Gao, K. Výborný, J. Zemen, J. Mašek, A. Manchon, J. Wunderlich, J. Sinova, and T. Jungwirth, Phys. Rev. Lett. **113**, 157201 (2014).

[5] A. S. Núñez, R. A. Duine, P. Haney, and A. H. MacDonald, Phys. Rev. B **73**, 214426 (2006).

[6] H. V. Gomonay and V. M. Loktev, Phys. Rev. B **81**, 144427 (2010).

[7] P. Borisov, A. Hochstrat, X. Chen, W. Kleemann, and C. Binek, Phys. Rev. Lett. **94**, 117203 (2005).

[8] A. B. Shick, S. Khmelevskyi, O. N. Mryasov, J. Wunderlich, and T. Jungwirth, Phys. Rev. B **81**, 212409 (2010).

[9] P. Wadley, V. Novák, R. P. Campion, C. Rinaldi, X. Martí, H. Reichlová, J. Zelezný, J. Gazquez, M. A. Roldan, M. Varela, D. Khalyavin, S. Langridge, D. Kriegner, F. Máca, J. Masek, R. Bertacco, V. Holý, A. W. Rushforth, K. W. Edmonds, B. L. Gallagher, C. T. Foxon, J. Wunderlich, and T. Jungwirth, Nat. Commun. **4**, 2322 (2013).

[10] S. S. P. Parkin, N. More, and K. P. Roche, Phys. Rev. Lett. **64**, 2304 (1990).

[11] P. J. H. Bloemen, H. W. van Kesteren, H. J. M. Swagten, and W. J. M. de Jonge, Phys. Rev. B **50**, 13505 (1994).

[12] H. Chen, Q. Niu, and A. H. MacDonald, Phys. Rev. Lett. **112**, 017205 (2014).

[13] J. Kübler and C. Felser, Europhys. Lett. **108**, 67001 (2014).

[14] M. Ikhlas, T. Tomita, T. Koretsune, M.-T. Suzuki, D. Nishio-Hamane, R. Arita, Y. Otani, and S. Nakatsuji, Nat. Phys. **13**, 1085 (2017).

[15] X. Li, L. Xu, L. Ding, J. Wang, M. Shen, X. Lu, Z. Zhu, and K. Behnia, Phys. Rev. Lett. **119**, 056601 (2017).

[16] H. Narita, M. Ikhlas, M. Kimata, A. A. Nugroho, S. Nakatsuji, and Y. Otani, Appl. Phys. Lett. **111**, 202404 (2017).

[17] W. Feng, G.-Y. Guo, J. Zhou, Y. Yao, and Q. Niu, Phys. Rev. B **92**, 144426 (2015).

[18] T. Higo, H. Man, D. B. Gopman, L. Wu, T. Koretsune, O. M. J. van 't Erve, Y. P. Kabanov, D. Rees, Y. Li, M.-T. Suzuki, S. Patankar, M. Ikhlas, C. L. Chien, R. Arita, R. D. Shull, J. Orenstein, and S. Nakatsuji, Nat. Photon. **12**, 73 (2018).
[19] W. Zhang, W. Han, S.-H. Yang, Y. Sun, Y. Zhang, B. Yan, and S. S. P. Parkin, Sci. Adv. **2**, e1600759 (2016).
[20] Y. Zhang, Y. Sun, H. Yang, J. Železný, S. P. P. Parkin, C. Felser, and B. Yan, Phys. Rev. B **95**, 075128 (2017).
[21] J. Železný, Y. Zhang, C. Felser, and B. Yan, Phys. Rev. Lett. **119**, 187204 (2017).
[22] H. Yang, Y. Sun, Y. Zhang, W.-J. Shi, S. S. P. Parkin, and B. Yan, New J. Phys. **19**, 015008 (2017).
[23] J. Kübler and C. Felser, Europhys. Lett. **120**, 47002 (2018).
[24] S. Nakatsuji, N. Kiyohara, and T. Higo, Nature (London) **527**, 212 (2015).
[25] A. K. Nayak, J. E. Fischer, Y. Sun, B. Yan, J. Karel, A. C. Komarek, C. Shekhar, N. Kumar, W. Schnelle, J. Kübler, C. Felser, and S. S. P. Parkin, Sci. Adv. **2**, e1501870 (2016).
[26] N. Kiyohara, T. Tomita, and S. Nakatsuji, Phys. Rev. Appl. **5**, 064009 (2016).
[27] H. Kurt, K. Rode, H. Tokuc, P. Stamenov, M. Venkatesan, and J. M. D. Coey, Appl. Phys. Lett. **101**, 232402 (2012).
[28] T. Nagamiya, S. Tomiyoshi, and Y. Yamaguchi, Solid State Commun. **42**, 385 (1982).
[29] S. Tomiyoshi, J. Phys. Soc. Jpn. **51**, 803 (1982).
[30] S. Tomiyoshi and Y. Yamaguchi, J. Phys. Soc. Jpn. **51**, 2478 (1982).
[31] See Supplemental Material at http://link.aps.org/supplemental/10.1103/PhysRevMaterials.2.051001 for further details on experimental measurements of the Mn_3Sn films.
[32] K. Aoyagi, Y. Kodama, T. Kiguchi, Y. Ehara, H. Funakubo, and T. J. Konno, Mater. Sci. Eng. B **177**, 528 (2012).
[33] C. H. Hsiao, Y. D. Yao, S. C. Lo, H. W. Chang, and C. H. Ouyang, Appl. Phys. Lett. **107**, 142407 (2015).
[34] C. L. Zha, R. K. Dumas, J. W. Lau, S. M. Mohseni, S. R. Sani, I. V. Golosovsky, Å. F. Monsen, J. Nogués, and J. Åkerman, J. Appl. Phys. **110**, 093902 (2011).
[35] L. M. Sandratskii and J. Kübler, Phys. Rev. Lett. **76**, 4963 (1996).
[36] J. Nogués and I. K. Schuller, J. Magn. Magn. Mater. **192**, 203 (1999).
[37] B. Dieny, V. S. Speriosu, S. S. P. Parkin, B. A. Gurney, D. R. Wilhoit, and D. Mauri, Phys. Rev. B **43**, 1297 (1991).
[38] S. S. P. Parkin, K. P. Roche, M. G. Samant, P. M. Rice, R. B. Beyers, R. E. Scheuerlein, E. J. O'Sullivan, S. L. Brown, J. Bucchigano, D. W. Abraham, Y. Lu, M. Rooks, P. L. Trouilloud, R. A. Wanner, and W. J. Gallagher, J. Appl. Phys. **85**, 5828 (1999).
[39] H. Ohldag, A. Scholl, F. Nolting, E. Arenholz, S. Maat, A. T. Young, M. Carey, and J. Stöhr, Phys. Rev. Lett. **91**, 017203 (2003).
[40] P. Kappenberger, S. Martin, Y. Pellmont, H. J. Hug, J. B. Kortright, O. Hellwig, and E. E. Fullerton, Phys. Rev. Lett. **91**, 267202 (2003).

Supplemental Material

1 Structural, morphological and magnetic characterization of Mn_3Sn films

Fig. 1(a) shows the XRD patterns of the Mn_3Sn films with different thicknesses. All films grow heteroepitaxially with (0001) preferred orientation. Fig. 1(b) shows the full width at half maximum (FWHM) of the 40 nm Mn_3Sn film. The combination of a high intensity peak with a small value of FWHM $\approx 0.566°$ reveals that the film has high crystal quality with low mosaicity.

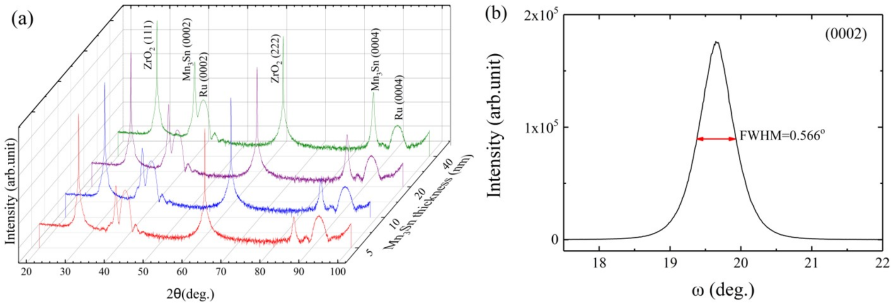

Figure 1: (a) XRD patterns of the Mn_3Sn films with different thicknesses. (b) FWHM of the (0002) out-of-plane rocking curve for the 40 nm Mn_3Sn film.

Fig. 2(a) shows the cross-section scanning transmission electron microscopy (STEM) image of the 40 nm Mn_3Sn film. The film is discontinuous, forming large islands of approximately 400 nm in width. The growth of islands during thin film deposition can be attributed to the large lattice mismatch between the Ru underlayer and Mn_3Sn film, which is 5.26 %. Furthermore, the kinetic conditions (i.e. growth rate, atomic mobility, temperature) during thin film deposition may affect the morphology of the films. A transition from island-growth to continuous films has been observed in different systems as the film thickness is increased [1]. The films, although discontinuous, are characterized by nearly perfect heteroepitaxial growth. Fig. 2(b) depicts the cross-section high resolution transmission electron microscopy (HRTEM) image of the same sample, where the substrate, the Ru underlayer, the Mn_3Sn film and the Al capping layer can be observed.

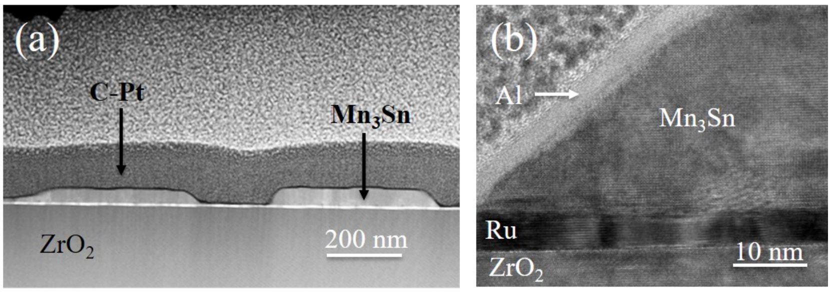

Figure 2: (a) Cross-section STEM image of the 40 nm film. The Mn_3Sn islands are covered by C-Pt protection layer. (b) Cross-section HRTEM image of the same sample.

The in-plane hysteresis curve of a 20 nm thick Mn_3Sn film measured at 300 K, is illustrated in Fig. 3. The sample shows an in-plane uncompensated magnetization of $M = 37\,\mathrm{kA/m}$ and coercivity of $\mu_0 H_\mathrm{c} = 3.8\,\mathrm{mT}$.

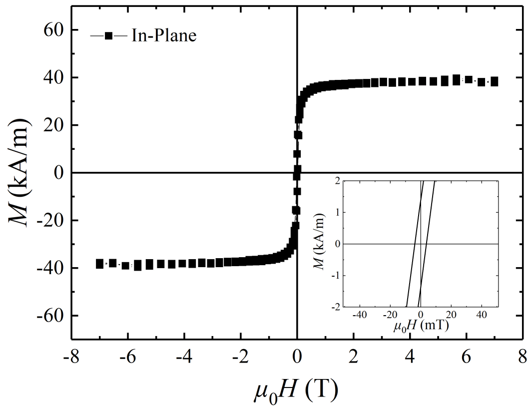

Figure 3: In-plane magnetization hysteresis loop of the 20 nm Mn_3Sn film. The inset shows the ± 50 mT region.

2 Exchange bias in Mn_3Sn/Py bilayers

The XRD pattern of the Mn_3Sn(40 nm)/Py(5 nm) bilayer grown on $Y{:}ZrO_2$ substrate with a 10 nm Ru underlayer is depicted in Fig 4. The hexagonal Mn_3Sn and Ru are (0001) oriented, while the Py ($Ni_{80}Fe_{20}$) film is heteroepitaxially grown on top of the Mn_3Sn film with (111) preferred orientation (only the (111) and (222) reflections are observed).

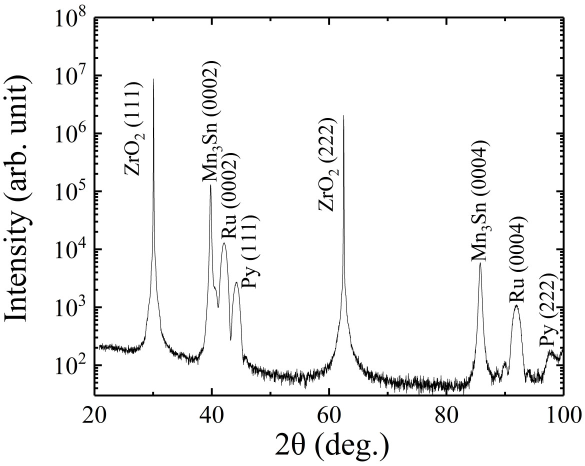

Figure 4: XRD pattern of the Mn_3Sn/Py bilayer.

In order to clarify the blocking temperature of the Mn_3Sn(40 nm)/Py(5 nm) bilayer, a second set of measurements was performed. Here, we measured the samples at 5 K after field cooling (FC) under 1 T in-plane applied magnetic field from a series of different starting temperatures. As the starting temperature is decreased below the blocking temperature, a reduction in the exchange bias field and coercive field is expected. Fig 5(a) shows $\mu_0 H_\mathrm{c}$ and $\mu_0 H_\mathrm{EB}$ as a function of the starting temperature before FC. Below 150 K exchange bias field begins to decrease, whilst for a starting temperature of 20 K no exchange bias is achieved. This demonstrates a blocking temperature distribution, which may be due to varying grain size or other defects in the Mn_3Sn film. Nevertheless a rapid decrease in $\mu_0 H_\mathrm{EB}$ is observed when FC begins below 50 K, showing that in this temperature range less pinning of the Py magnetization is being thermally activated, thus supporting the conclusion that $T_\mathrm{B} \approx 50$ K.

The in-plane magnetization hysteresis loops of the Mn_3Sn(40 nm)/Py(5 nm) bilayer measured after field-cooling (FC) from 300 K to 5 K under different in-plane magnetic fields are illustrated in Fig. 5(b). The exchange bias field is found, as expected, to be independent of field cooling strength (1-5 T). Furthermore it is reversible when field-cooled under a negative applied field of -1 T (hysteresis loop is shifted along the positive direction of the applied field axis).

The temperature dependence of $\mu_0 H_\mathrm{c}$ and $\mu_0 H_\mathrm{EB}$ for a thinner Mn_3Sn(20 nm)/Py(5 nm) bilayer is shown in Fig. 6. The results are broadly similar to the Mn_3Sn(40 nm)/Py bilayer. Here a coercive field of $\mu_0 H_\mathrm{c} = 15$ mT and an exchange bias field of $\mu_0 H_\mathrm{EB} = 9$mT are observed after FC in an 1 T in-plane applied magnetic field from 400 K to 2 K. The variation of $\mu_0 H_\mathrm{c}$ and $\mu_0 H_\mathrm{EB}$ after 1 T FC from 400 K to sequential temperatures shows smaller exchange bias fields and a lower blocking

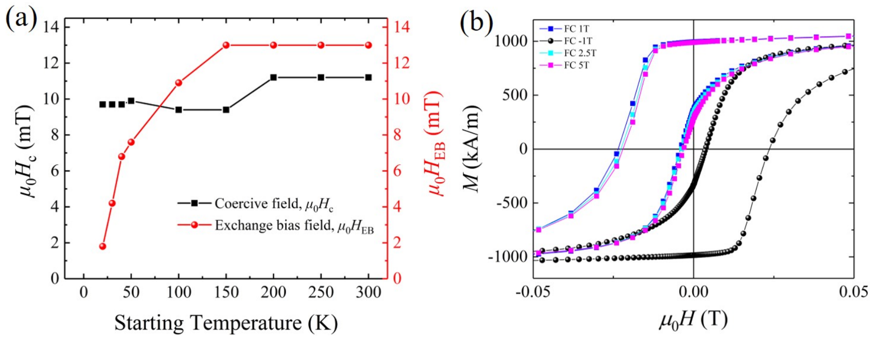

Figure 5: (a) Exchange bias and coercive fields measured at 5 K as a function of the starting temperature before 1 T FC. (b) In-plane magnetization hysteresis loops of the Mn_3Sn(40 nm)/Py(5 nm) bilayer, after FC to 5 K under different in-plane magnetic fields.

temperature ($T_B \approx 30$ K) compared with the Mn_3Sn(40 nm)/Py bilayer. This is as exected for a thinner anitferromagnetic film in an exchange bias system, where grain size may be smaller (leading to reduced blocking temperature) and the anisotropy of the antiferromagnetic order weaker (lessening the pinning of the ferromagnetic layer).

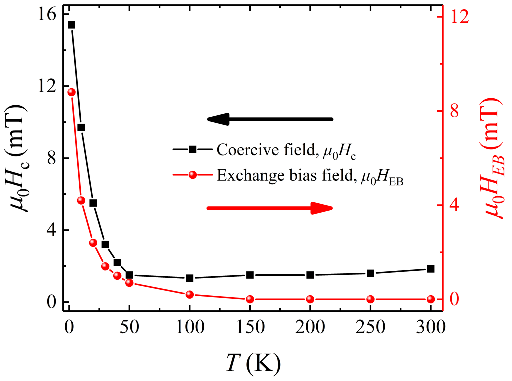

Figure 6: Temperature dependence of exchange bias and coercive fields during 1 T FC from 400 K .

References

[1] M. Berti, A.V. Drigo, M. Mazzer, F. Romanato, L. Lazzarini, P. Franzosi, G.C. Salviati and D. Bertone, Mater. Sci. Eng. B, **28**, 214 (1994).

3.2 Anomalous and topological Hall effects in epitaxial thin films of the noncollinear antiferromagnet Mn_3Sn

The following chapter of this cumulative thesis consists of the peer-reviewed scientific paper (and its supplementary material) published as:

J. M. Taylor, A. Markou, E. Lesne, P. K. Sivakumar, C. Luo, F. Radu, P. Werner, C. Felser, and S. S. P. Parkin, "Anomalous and topological Hall effects in epitaxial thin films of the noncollinear antiferromagnet Mn_3Sn", *Phys. Rev. B* **101**, 094404 (2020)

In Section 3.1, we demonstrated the ability to grow hexagonal Mn_3Sn in thin film form. However, we were unable to measure the magnetotransport properties of the resulting samples, because the films were discontinuous. This was attributed to the large lattice mismatch between the $Y{:}ZrO_2$ substrate and the Ru buffer layer (5.7%) and the subsequent Mn_3Sn film (10.7%). By switching to substrates with lower lattice mismatch, we were able to deposit Mn_3Sn onto the Ru buffer at RT and seed hexagonal crystal structure by post annealing at 300 °C alone. This is a lower energy process than the high temperature growth used in Section 3.1, thus limiting the mobility of adatoms and ensuring continuous growth. The fabrication, structural analysis, magnetic properties and magnetotransport behavior of such continuous Mn_3Sn films is reported in the paper J. M. Taylor et al., "Anomalous and topological Hall effects in epitaxial thin films of the noncollinear antiferromagnet Mn_3Sn", *Phys. Rev. B* **101**, 094404 (2020), which forms the final chapter of this thesis.

In order to achieve this continuous growth, we deposited Mn_3Sn thin films on Ru buffered $SrTiO_3$ (111) single crystal substrates. Here, the lattice mismatch between $SrTiO_3$ (111) and Ru (-2.0%) and Mn_3Sn (2.6%) is reduced compared with the $Y{:}ZrO_2$ substrates. The Ru buffer layer grew with its c-axis OP on top of the $SrTiO_3$ (111) surface, which in turn seeded the growth of (0001) oriented Mn_3Sn. XRD and TEM analysis of the resulting crystal structure reveals relaxed film growth with lattice parameters close to bulk values, comparable crystal quality to that reported in Section 3.1, and the same epitaxial relationship as the thin films grown on Y:ZrO_2 substrates. However, the important difference is that the Mn_3Sn (0001) films grown in this case are, as confirmed by wide-view TEM images and AFM topography maps, continuous.

This allowed us to fabricate Hall bar devices from the samples, and therefore attempt to measure their Berry phase driven magnetotransport properties. Specifically, transverse resistivity (partially-parallel to the $[2\bar{1}\bar{1}0]$ direction) was measured with current flow along the $[01\bar{1}0]$ crystallographic direction, as a function of OP external magnetic field along the c-axis. At room temperature, we observed a linear response of transverse resistivity to applied field, that is, an ordinary Hall effect. This is as expected, however, for the case where magnetic field is applied along the (0001) crystalline direction. This is a magnetic hard axis, and thus external field is unable to manipulate the weak magnetization that is confined to the sample ab-plane. Since it cannot align the uncompensated moment, the magnetic field cannot reorient the inverse triangular spin texture into a single chirality. Thus anomalous Hall conductivities from neighboring domains of opposite chirality cancel out.

As the sample temperature was lowered, a significant change in the behavior of the Hall effect was observed. Below 50 K, we see a small anomalous-like Hall response begin to occur. This can be explained by the well-known transition of Mn_3Sn into a glassy FM state below 50 K [113]. Upon this transition, Mn moments are frustrated to tilt out of the basal planes [112]. This results in a net magnetization arising along the (0001) direction, which in turn produces a conventional AHE.

For Hall bars patterned in the film plane, it would be impossible to measure the topologically generated AHE at room temperature using a conventional Hall effect measurement geometry in these Mn_3Sn (0001) samples. We therefore proceeded to prepare thin films where the c-axis lies partially IP, thus allowing a component of the OP applied magnetic field to manipulate uncompensated moment in the basal plane. To achieve this, we changed substrates again, this time depositing Mn_3Sn on Ru buffered MgO (001) cubic substrates. Here, XRD $2\theta - \theta$ scans revealed the Mn_3Sn films to have the $[40\bar{4}3]$ crystal axis directed OP. This is an unusual thin film growth orientation, and we therefore performed further XRD $\chi - \phi$ pole figure maps and TEM analysis, in order to fully characterize the obtained crystal structure.

We again find the films to be continuous, with grain boundary defects separating crystallites whose crystallographic axes are well correlated to follow one of the ⟨110⟩ cubic diagonals in the MgO substrate. Sharp spots in both XRD pole figures and TEM diffractograms reveal the single crystalline nature of individual grains and their low mosaicity, whilst TEM micrographs demonstrate the high quality crystal structure of the thin films in general, with small roughness, uniform thickness and low defect density. We find that the (0001) crystal planes grow tilted out of the film plane, with the *c*-axis lying at an angle of approximately 55° to the film normal, the $[2\bar{1}\bar{1}0]$ magnetic easy axis lying at an angle of approximately 35° to the film normal, and the $[01\bar{1}0]$ crystallographic direction lying completely IP.

Therefore, by patterning Hall bars into these $(40\bar{4}3)$ oriented Mn_3Sn films, current was passed along the $[01\bar{1}0]$ crystallographic direction, and transverse resistivity measured in a direction partially along the [0001] axis. Hall effect was then recorded at different temperatures, as a function of magnetic field applied OP; that is, along the $[40\bar{4}3]$ direction but with a significant component of external field parallel to the $[2\bar{1}\bar{1}0]$ magnetic easy axis. The magnetic field was thus able to align the uncompensated moment arising within the basal planes, and therefore to reorient the entire sample into a single chirality of the inverse triangular spin texture. As a result, we succeeded in measuring Berry curvature driven AHE in these Mn_3Sn $(40\bar{4}3)$ samples at room temperature.

By taking into account the current shunted through the Ru buffer, modeling the multilayer as a set of parallel resistors, and subtracting the ordinary Hall effect background arising from both layers, we calculate the remnant zero-field anomalous Hall conductivity at 300 K to be $\sigma_{\mathrm{xy}}(\mu_0 H = 0\,\mathrm{T}) = 21\,\Omega^{-1}\,\mathrm{cm}^{-1}$. This is found to be nearly independent of film thickness, meaning that we observe momentum-space Berry curvature driven AHE down to thicknesses as low as 30 nm. Coercive field also shows no dependence on film thickness, with a value of $\mu_0 H_{\mathrm{c}} = 1.3\,\mathrm{T}$. This value of coercivity is much larger than that observed in single crystals of Mn_3Sn, and reflects the important relationship between uncompensated magnetic moment, chiral domain configuration, and film microstructure in noncollinear AFs that we introduced in Section 2.2.

We have already discussed how the weak magnetization in Mn_3Sn can be used to reorient the inverse triangular spin texture. Recently, Higo *et al.* [76], by exploiting the large MOKE contrast arising between different chiralities of this inverse triangular spin texture (which is also related to the Berry phase generated magnetotransport properties, as discussed in Section 1.2.7), showed that this reorientation occurs through a process of domain nucleation and propagation. In other words, they imaged the multi-domain state of Mn_3Sn, and showed that application of an external magnetic field to align the weak magnetization drives the motion of domain walls, expanding domains of a certain preferred chirality, until the sample reaches a single domain state (and AHE is saturated) [76]. The opposite process occurs on the reverse field sweep. Such AF domain dynamics are currently an area of great interest, in order to understand the magnetotransport behavior of AF materials for spintronic applications. In our present results, the enhanced coercivity is a reflection of this domain wall motion mechanism. Defects and impurities, that are inherent in sputter deposited thin film samples, as well as the grain boundaries occurring between the four-fold symmetric crystallites discussed above, act to pin domain wall motion. Therefore, a stronger magnetic field is required to drive the sample into a single chiral domain state, resulting in a larger coercive field.

Finally, the nature of the domain walls between these chiral domains is of interest to the fundamental physics of noncollinear AFs, but also yields some potentially exciting applications, as we demonstrate in the last part of this work. Very recently, Xi *et al.* [148] measured symmetric features in the planar Hall effect of Mn_3Sn single crystals, which they concluded arise from *chiral domain walls*. Not only do these chiral domain walls have measurable magnetotransport signatures, but Xi *et al.* showed that their internal moment configuration depends on the magnetic history of the sample and thus shows a memory effect [148].

In the case of our Mn_3Sn $(40\bar{4}3)$ films, as we measure Hall effect at lower temperatures, the magnitude of the Berry curvature driven AHE decreases. This is because the sample begins to loose the inverse triangular AF order that yields Berry curvature induced AHE. Towards 50 K, the sample undergoes a magnetic phase transition to the spin glass state discussed above. In Mn_3Sn films with this $(40\bar{4}3)$ orientation, we do not observe the conventional AHE generated by this glassy FM state (because we are not sensitive to magnetization induced along the c-axis in this measurement configuration). Instead, the Hall effect hysteresis loops begin to show clear asymmetry. This is a signature of the THE, which, as discussed in Section 1.2.10, occurs when electrons propagating through a noncoplanar, noncollinear spin texture acquire real-space Berry phase and thus a transverse component of momentum.

Specifically, two 'bumps' in Hall resistivity are measured, close to the coercive field of the Mn_3Sn $(40\bar{4}3)$ films. Therefore, electrons encounter a spin texture with nonzero scalar spin chirality at the point where reversed AF domains are beginning to nucleate and propagate. In other words, the formation of domain walls is the source of the observed THE, and we therefore conclude that chiral domain walls are also present in our Mn_3Sn thin films. The polarity of these THE bumps are symmetric in magnetic field. According to the model put forth by Xi *et al.* (where the domain wall structure consists of an IP rotation of moments between one domain and the next) this means that the internal configuration of Mn moments within the domain walls remains the same on forward and reverse field sweeps, whilst the sense of rotation of the spins within the domain wall is inverted [148]. In our Mn_3Sn ($40\bar{4}3$) films, a domain wall consisting of Mn moments rotating within the basal plane will appear as a noncollinear, noncoplanar spin texture to electrons propagating within the plane of the film, thus subtending a finite scalar spin chirality that, in turn, induces THE.

Furthermore, the sign of the bumps in Hall resistivity is reversed depending on the field cooling condition applied as the sample passes through the magnetic phase transition at 50 K. In the first example, Mn_3Sn was driven to saturation of a negative AHE by applying a magnetic field up to $+9\,\mathrm{T}$, setting the sample into a particular single domain state, which then remains stable as external field is brought back to zero. When the sample is then zero field cooled, the THE bumps observed are negative. In the opposite case, following zero field cooling after saturation of a positive AHE in a $-9\,\mathrm{T}$ magnetic field, the THE bumps measured are positive. Both of these effects are enhanced by field cooling directly in a $\pm 9\,\mathrm{T}$ magnetic field.

The polarity of the THE bump indicates the sign of the real-space Berry phase, which arises from the value of the finite scalar spin chirality of the noncollinear, noncoplanar spin texture generating it. Because this, in turn, depends on the internal moment configuration within the domain walls, we conclude that the handedness of the inverse triangular spin texture set at room temperature directly evolves to favor a particular chirality of domain walls in the low temperature magnetic state. From the current results, it is not clear whether the chiral domain walls appear only following the transition to the glassy FM state, or whether they persist up to room temperature as measured by Xi *et al.* [148]. This is because, in the present measurement, we only observe THE after the momentum-space Berry curvature driven AHE has been suppressed below 50 K. Xi *et al.* attribute the magnetic field history effect to the presence of minority domains, that remain after external field has been removed and act to seed a preferentially domain wall chirality during subsequent measurements [148]. This mechanism fits with our observation of an enhanced THE following direct field cooling, since the applied field may act to stabilize the domains that select the preferred chirality through the magnetic phase transition. However, further work is needed to explore the details of this mechanism, and indeed the role of chiral domains in noncollinear AFs more generally.

Nevertheless, the present observation of a THE generated by chiral domain walls open up new possibilities for Mn_3Sn films in spintronic devices based on topological AFs.

PHYSICAL REVIEW B **101**, 094404 (2020)

Anomalous and topological Hall effects in epitaxial thin films of the noncollinear antiferromagnet Mn_3Sn

James M. Taylor,[1,*] Anastasios Markou,[2] Edouard Lesne,[1] Pranava Keerthi Sivakumar,[1] Chen Luo,[3]
Florin Radu,[3] Peter Werner,[1] Claudia Felser,[2] and Stuart S. P. Parkin[1,†]
[1]*Max Planck Institute of Microstructure Physics, Weinberg 2, 06120 Halle (Saale), Germany*
[2]*Max Planck Institute for Chemical Physics of Solids, Nöthnitzer Str. 40, 01187 Dresden, Germany*
[3]*Helmholtz-Zentrum Berlin for Materials and Energy, Albert Einstein Str. 15, 12489 Berlin, Germany*

(Received 9 October 2019; accepted 13 January 2020; published 2 March 2020)

Noncollinear antiferromagnets with a $D0_{19}$ (space group = 194, $P6_3/mmc$) hexagonal structure have garnered much attention for their potential applications in topological spintronics. Here, we report the deposition of continuous epitaxial thin films of such a material, Mn_3Sn, and characterize their crystal structure using a combination of x-ray diffraction and transmission electron microscopy. Growth of Mn_3Sn films with both (0001) c-axis orientation and $(40\bar{4}3)$ texture is achieved. In the latter case, the thin films exhibit a small uncompensated Mn moment in the basal plane, quantified via magnetometry and x-ray magnetic circular dichroism experiments. This cannot account for the large anomalous Hall effect simultaneously observed in these films, even at room temperature, with magnitude $\sigma_{xy}(\mu_0 H = 0\ \mathrm{T}) = 21\ \Omega^{-1}\ \mathrm{cm}^{-1}$ and coercive field $\mu_0 H_c = 1.3$ T. We attribute the origin of this anomalous Hall effect to momentum-space Berry curvature arising from the symmetry-breaking inverse triangular spin structure of Mn_3Sn. Upon cooling through the transition to a glassy ferromagnetic state at around 50 K, a peak in the Hall resistivity close to the coercive field emerges. This indicates the onset of a topological Hall effect contribution, arising from a nonzero scalar spin chirality that generates a real-space Berry phase. We demonstrate that the polarity of this topological Hall effect, and hence the chiral nature of the noncoplanar magnetic structure driving it, can be controlled using different field-cooling conditions.

DOI: 10.1103/PhysRevB.101.094404

I. INTRODUCTION

Antiferromagnets (AF) are of interest for spintronic applications [1]; however, they struggle to produce readout signals of the size required for devices. Large magnetotransport signatures, such as the intrinsic anomalous Hall effect (AHE) [2], generated by topological materials may offer the solution [3]. In particular, topological noncollinear AFs of the form Mn_3X are of interest.

Mn_3Sn is a noncollinear AF with Mn moments arranged in hexagonal crystal planes [4], which exhibits an inverse triangular spin structure resulting from a combination of exchange and Dzyaloshinskii-Moriya (DM) interactions [5]. The inverse triangular AF order breaks time-reversal symmetry, thus introducing momentum-space Berry curvature. In turn, this induces a fictitious magnetic field, which has been theoretically predicted [6] to drive a highly anisotropic AHE [7]. This was subsequently experimentally measured in single crystals of hexagonal Mn_3Sn [8] and Mn_3Ge [9].

The emergence of Berry curvature is connected with Weyl points arising in Mn_3Sn [10–12]. The presence of such Weyl quasiparticles close to the Fermi level also induces an anomalous Nernst effect [13–15]. Further enhancement of the attractiveness of Mn_3Sn for spintronics stems from its hosting of a Berry curvature-driven intrinsic spin Hall effect [16–18], which was originally discovered in the cubic noncollinear AF Mn_3Ir [19].

The symmetry-breaking inverse triangular spin texture also gives rise to a magneto-optical Kerr effect [20–22]. Kerr microscopy imaging of this effect reveals that Mn_3Sn contains AF domains possessing opposite chiralities of the noncollinear spin structure. These reversed chiralities correspond to opposite signs of a cluster octupole order parameter [23] and, hence, reversed polarities of magnetotransport properties across different AF domains [24].

An external magnetic field can be used to propagate AF domains of a particular chirality [22], in order to generate a net magnetotransport output. The applied magnetic field couples to the small uncompensated magnetic moment [25] that is created in the hexagonal crystal planes of Mn_3Sn by spins spontaneously canting slightly towards magnetocrystalline easy axes [26]. This weak magnetization can freely rotate within the basal plane [5], in turn acting to orient the entire inverse triangular spin texture, and, when saturated, achieving a single chiral domain state.

As Mn_3Sn is cooled, its magnetic order changes depending on microstructure [27]. At 275 K, Mn-deficient samples

---

[*] james.taylor@mpi-halle.mpg.de
[†] stuart.parkin@mpi-halle.mpg.de

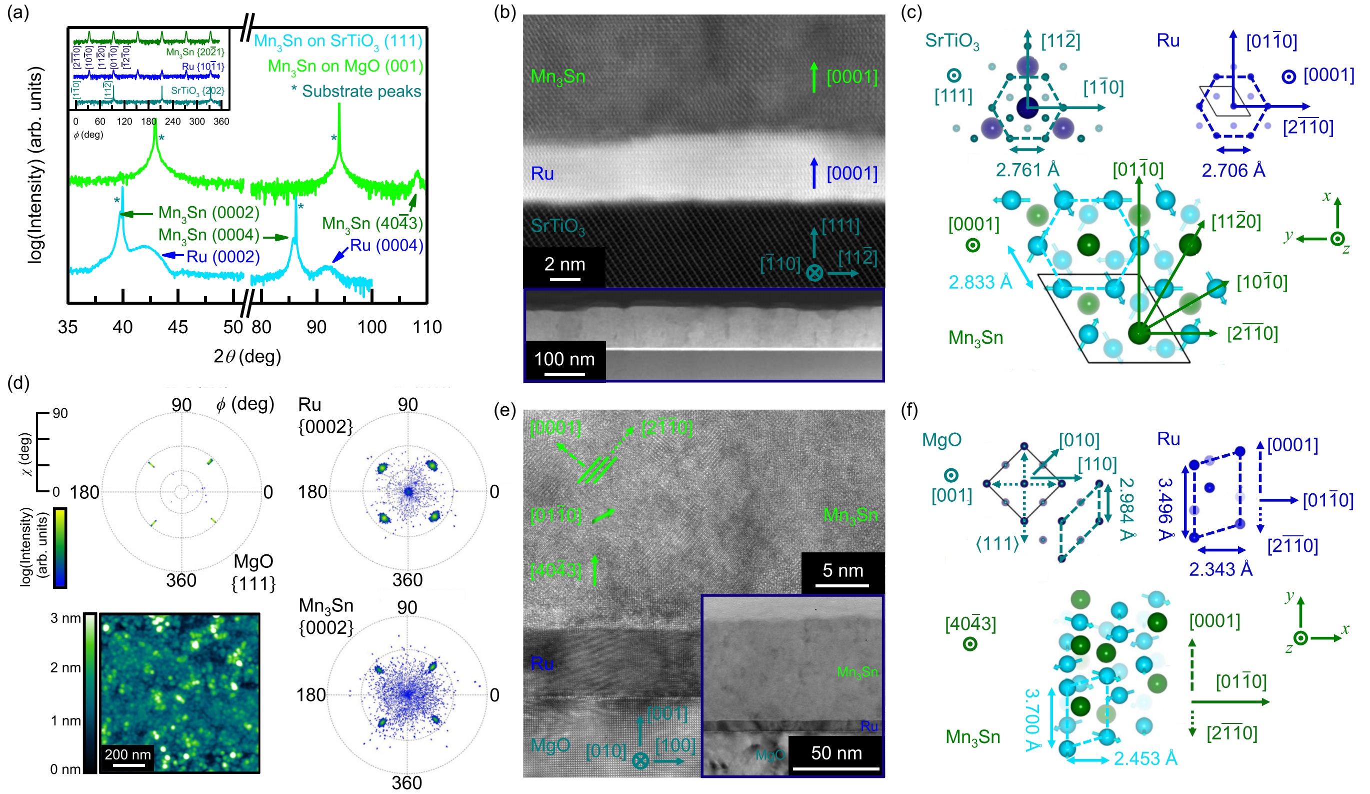

FIG. 1. (a) 2θ-θ x-ray diffraction scans measured for a 70-nm Mn$_3$Sn (0001) film grown on a SrTiO$_3$ (111) substrate, and for a 60-nm Mn$_3$Sn (40$\bar{4}$3) film grown on a MgO (001) substrate. Inset shows azimuthal ϕ scans of the SrTiO$_3$ {202}, Ru {10$\bar{1}$1}, and Mn$_3$Sn {20$\bar{2}$1} reflections for a 70-nm Mn$_3$Sn (0001) sample. The corresponding positions of in-plane crystallographic directions are indicated. (b) Cross-section scanning-TEM micrograph of a 70-nm Mn$_3$Sn (0001) film, viewed along the [$\bar{1}$10] zone axis of the SrTiO$_3$ (111) substrate. Inset shows a wide-view image over an extended region of the same lamella. (c) Representative crystal structure of Mn$_3$Sn (0001) films grown on SrTiO$_3$ (111) substrates using a Ru buffer layer. (d) χ-ϕ x-ray pole figures measured for a 60-nm Mn$_3$Sn (40$\bar{4}$3) sample. The MgO [100] crystalline axis was aligned with $\phi = 0^\circ$. Inset shows an atomic force microscopy topographic map for a similar 50-nm Mn$_3$Sn (40$\bar{4}$3) film, capped with 2-nm Ru. (e) Cross-section high-resolution TEM micrograph of a 60-nm Mn$_3$Sn (40$\bar{4}$3) film, viewed along the [010] zone axis of the MgO (001) substrate. Inset shows an overview TEM image measured for the same sample. (f) Representative crystal structure of Mn$_3$Sn (40$\bar{4}$3) films grown on MgO (001) substrates using a Ru buffer layer.

transition to a helical magnetic phase [28]. Around 50 K, the magnetic structure changes to a "glassy" ferromagnetic (FM) (or spin-glass) state [29], regardless of composition, in which Mn moments are frustrated to cant out of the basal planes [30]. Studies in bulk samples [31] show this is accompanied by the onset of a topological Hall effect (THE) [32], attributed to a possible magnetic skyrmion phase [33], or to chiral domain walls [34].

Recently, AHE has been measured in polycrystalline Mn$_3$Sn films [35–37]. In addition, a planar Hall effect has been observed in epitaxial films [38]. In this paper, we extend these previous results by studying the structural and magnetic properties of epitaxial Mn$_3$Sn thin films, and demonstrating the presence of both AHE and THE.

II. RESULTS AND DISCUSSION

A. Film growth and structural characterization

We previously grew Mn$_3$Sn films that were epitaxial but discontinuous [39]. By changing substrate and optimizing postannealing temperature, we succeeded in fabricating continuous Mn$_3$Sn films (details in the Supplemental Material [40]). Figure 1(a) shows 2θ-θ x-ray diffraction (XRD) patterns measured for films deposited on SrTiO$_3$ (111) and MgO (001) substrates. In both cases, a 5-nm Ru buffer layer was used [39]. The presence of {0002} diffraction peaks indicates the growth of *c*-axis oriented films on SrTiO$_3$ (111) substrates. Lattice parameters calculated from these XRD measurements establish that these hexagonal Mn$_3$Sn (0001) films grow fully relaxed (analysis in the Supplemental Material [40]). Azimuthal XRD ϕ scans of partially in-plane (IP) peaks, shown in the inset of Fig. 1(a), demonstrate the same epitaxial relationship as in Ref. [39]: SrTiO$_3$(111)[11$\bar{2}$][1$\bar{1}$0]||Ru(0001)[01$\bar{1}$0][2$\bar{1}\bar{1}$0]||Mn$_3$Sn(0001)[01$\bar{1}$0][2$\bar{1}\bar{1}$0], depicted schematically in Fig. 1(c).

We studied film structure at the nanoscale using transmission electron microscopy (TEM). Figure 1(b) shows a cross-section scanning-TEM micrograph from a 70-nm film deposited on SrTiO$_3$ (111), which demonstrates explicitly the epitaxial growth of (0001)-oriented Mn$_3$Sn on a Ru (0001) buffer. The inset of Fig. 1(b) displays a wide-view scanning-TEM image of the same lamella, confirming the preparation of continuous films.

Figure 1(a) also shows a single peak in the 2θ-θ XRD scan for a 60-nm film deposited on MgO (001); this corresponds to the growth of single-phase hexagonal Mn_3Sn with $(40\bar{4}3)$ orientation. We analyzed this crystal texture by recording χ-ϕ XRD pole-figure maps around the expected positions of the {111} reflections of MgO, {0002} reflections of Ru, and {0002} reflections of Mn_3Sn, as presented in Fig. 1(d). The {0002} reflections of Ru follow the cubic {111} MgO peaks, indicating that the hexagonal planes of Ru are tilted to lie at the same angle as the (111) planes of the substrate. The {0002} reflections of Mn_3Sn in turn follow the Ru diffraction peaks, confirming that the basal planes of Mn_3Sn are seeded to grow at the same angle as those in the buffer layer. This results in a structure for Mn_3Sn $(40\bar{4}3)$ with the [0001] crystalline direction at almost 55° to the film normal, the $[2\bar{1}\bar{1}0]$ magnetic easy axis [26] at approximately 35° to the film normal, and the $[01\bar{1}0]$ crystallographic axis lying completely IP. This epitaxial relationship is illustrated in Fig. 1(f).

The Mn_3Sn {0002} reflections are fourfold symmetric. This indicates four distinct crystallite orientations in which the c axis, and in turn the orthogonal $[01\bar{1}0]$ direction, follows one of the possible IP ⟨110⟩ MgO axes. Therefore, for a chosen macroscopic measurement direction, there will be equivalent numbers of Mn_3Sn crystal grains with either the [0001] or $[01\bar{1}0]$ axes parallel to this.

Nevertheless, high-resolution TEM of an individual Mn_3Sn $(40\bar{4}3)$ crystallite, as depicted in Fig. 1(e), confirms single-crystalline growth. The $[01\bar{1}0]$ crystallographic axis is directed at 45° into the plane of the image. The basal planes of Mn_3Sn are clearly visible, while the $[2\bar{1}\bar{1}0]$ magnetic easy axis is aligned almost out of plane (OP). That these crystal grains coherently coalesce to form a continuous thin film is ascertained from wide-view TEM images, an example of which is shown in the inset of Fig. 1(e).

Finally, we used atomic force microscopy to quantify the roughness of Mn_3Sn. An example topographic map is shown in the inset of Fig. 1(d), which yields an average roughness of $\approx$0.5 nm over a 1-μm^2 region of a 50-nm Mn_3Sn $(40\bar{4}3)$ film capped with 2-nm Ru.

B. Magnetic properties

Figure 2(a) shows the magnetization (M) of a 60-nm Mn_3Sn $(40\bar{4}3)$ film measured using superconducting quantum interference device vibrating sample magnetometry (SQUID-VSM, Quantum Design MPMS3), after subtracting the background contribution from a MgO substrate/5-nm Ru reference sample. When magnetic field ($\mu_0 H$) is applied OP, with a component along the $[2\bar{1}\bar{1}0]$ easy axis, an opening of the loop in the region ±1.5 T is attributed to the reversal of the small uncompensated moment expected in the basal plane of Mn_3Sn.

With magnetic field applied along one of two orthogonal IP directions, a similar hysteretic behavior is observed, but with a smaller magnitude and an isotropic response. This is because magnetization is averaged over many crystallites, which can be fourfold symmetrically oriented with either $[01\bar{1}0]$ (in the plane where uncompensated moment freely rotates) or partially IP [0001] (hard axis) directions parallel to the magnetic field.

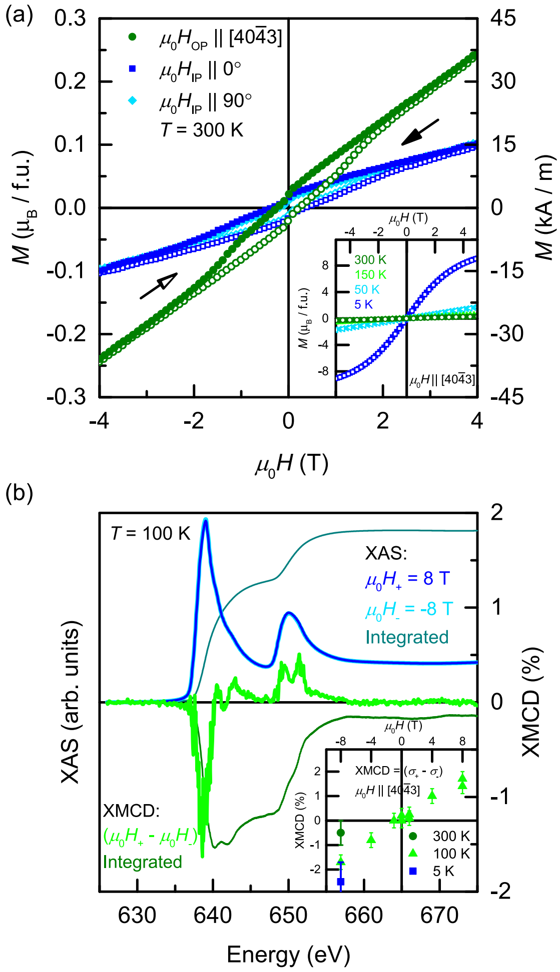

FIG. 2. (a) Magnetization measured as a function of magnetic field for a 60-nm Mn_3Sn $(40\bar{4}3)$ film at 300 K. Magnetic field was applied either out of plane or along one of two orthogonal in-plane directions (closed and open symbols represent down and up field sweeps, respectively). Inset shows magnetization as a function of out-of-plane magnetic field, measured at different temperatures. (b) X-ray absorption spectroscopy and XMCD spectra for a 70-nm Mn_3Sn $(40\bar{4}3)$ film, recorded using σ_- polarized x-rays in $\mu_0 H_\pm = \pm 8$ T magnetic fields applied out of plane, at 100 K. Inset shows XMCD, calculated as the difference between spectra recorded with $\sigma_\pm$ polarized x-rays, measured in different out-of-plane magnetic fields at 100 K, as well as that measured in -8 T at 300 and 5 K.

The inset of Fig. 2(a) plots magnetization response to magnetic field at different temperatures (T). At 5 K, a significant enhancement of magnetization demonstrates the appearance of the glassy FM phase [29].

X-ray magnetic circular dichroism (XMCD) was measured at the BESSY synchrotron facility [41], using negative, σ_-, polarized x rays in an OP magnetic field of $\mu_0 H_\pm = \pm 8$ T. Nonzero XMCD around the Mn $L_{2,3}$ edges at 100 K, displayed in Fig. 2(b), confirms the presence of a net Mn moment that is reversible by external magnetic field. Using XMCD sum-rule analysis [42], an uncompensated magnetic moment of $m_{s+l} = 0.279$ μ_B/f.u. was calculated, comprising spin, $m_s = 0.273$ μ_B/f.u., and orbital, $m_l = 0.006$ μ_B/f.u. moments respectively. Measured m_l is of the same order of magnitude as that simulated [25], while m_s is found to be substantially larger than the theoretically predicted value for zero-field weak magnetization.

We explain this by considering the inset of Fig. 2(b), showing the magnetic-field dependence of XMCD, measured as in Ref. [43]. XMCD increases approximately linearly, because of Mn spins tilting out of the film plane in response to strong applied magnetic fields [43]. This therefore enhances m_s, whose magnitude is in agreement with that determined from SQUID-VSM, which indicates similar paramagnetic behavior after the closing of the hysteresis loop.

Nevertheless, both measurements reveal that the uncompensated moment overall is enhanced compared with bulk crystals, including the remnant weak magnetization within the basal plane measured at zero-applied magnetic field using SQUID-VSM. This uncompensated moment is exacerbated because of structural defects and chemical disorder present in the thin films, which may act to modify the balance of AF exchange, DM interactions, and magnetocrystalline anisotropy, thus increasing the spontaneous canting of Mn spins [39].

The inset of Fig. 2(b) also presents XMCD measured in a −8-T magnetic field at different temperatures. XMCD is reduced at 300 K, while its enhancement at 5 K evidences an increased net moment after transition to the spin-glass state.

C. Magnetotransport measurements

We now report magnetotransport measurements in Mn_3Sn thin films lithographically patterned into 75×25-μm^2 Hall bar devices. Figure 3(a) shows the variation in longitudinal resistivity (ρ_{xx}) for a 70-nm-thick Mn_3Sn (0001) film as a function of temperature, during either zero-field cooling (ZFC) or cooling in a 7-T OP magnetic field (FC), followed in both cases by zero-field warming (ZFW). A background contribution from the 5-nm Ru buffer layer has been subtracted (see Supplemental Fig. S2 [40]). On cooling, a deviation from metallic behavior below 100 K, down to a bump in resistivity close to 50 K, provides evidence for the transition to the glassy FM phase. No change is observed between ZFC and FC protocols, as expected with cooling field parallel to the [0001] hard axis.

During subsequent ZFW, a thermal hysteresis is seen. Resistivity first drops between 50 and 100 K. The resulting difference in resistivity is maintained, as above 100 K resistivity rises at the same rate compared to ZFC but with a smaller absolute value, until the film is warmed above room temperature. This may indicate that the transition from the inverse triangular to glassy FM state that occurs on cooling is not fully reversible until the thin film reaches close to the Néel temperature of Mn_3Sn ($T_N = 420$ K [4]). This can be explained if regions of the spin-glass structure become pinned at defects via their chiral domain walls (discussed below).

Figure 3(b) plots the variation in transverse resistivity (ρ_{xy}) as a function of OP magnetic field for the same 70-nm Mn_3Sn (0001) film. At room temperature, we observe a linear Hall effect. This is because external field is applied along the c axis, which is a magnetic hard axis. Therefore, applied field is unable to manipulate the weak magnetization, which occurs within the basal plane, and is thus unable to drive the thin film into a dominant chiral domain state (which would yield a net contribution to Berry curvature-induced AHE). Between 100 and 50 K, this ordinary Hall effect changes to an AHE as Mn_3Sn transitions into the glassy FM phase. Here, moments are frustrated to cant along the [0001] axis [30], with the resulting FM-like component of magnetization producing a conventional AHE in response to an OP magnetic field.

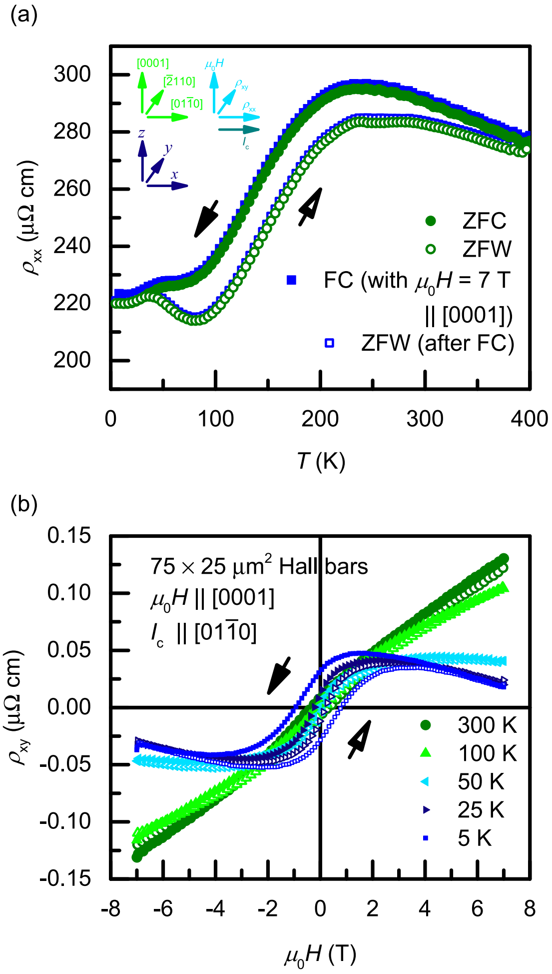

FIG. 3. Magnetotransport for a 70-nm Mn_3Sn (0001) film patterned into 75×25-μm^2 Hall bars, with 500-μA current parallel to the [01$\bar{1}$0] in-plane crystallographic direction. (a) Longitudinal resistivity measured as a function of temperature during either zero-field cooling, or cooling in a 7-T magnetic field applied out of plane (closed symbols), and subsequent zero-field warming (open symbols). Diagram illustrates measurement geometry in relation to different crystallographic directions in the Mn_3Sn (0001) film. (b) Hall resistivity measured as a function of magnetic field applied out of plane at different temperatures. Transverse resistivity was measured along the [$\bar{2}$110] crystalline axis (closed and open symbols represent down and up field sweeps, respectively).

Moving onto the Mn_3Sn (40$\bar{4}$3) films, we sourced current (I_c) along the [01$\bar{1}$0] direction and measured a component of Hall resistivity partially orthogonal to the (0001) crystal planes. Magnetic field was applied parallel to the [40$\bar{4}$3] direction, thus with a significant component along the [2$\bar{1}\bar{1}$0] easy axis. A schematic of this measurement configuration is inset in Fig. 4(b). These crystalline directions are as defined in

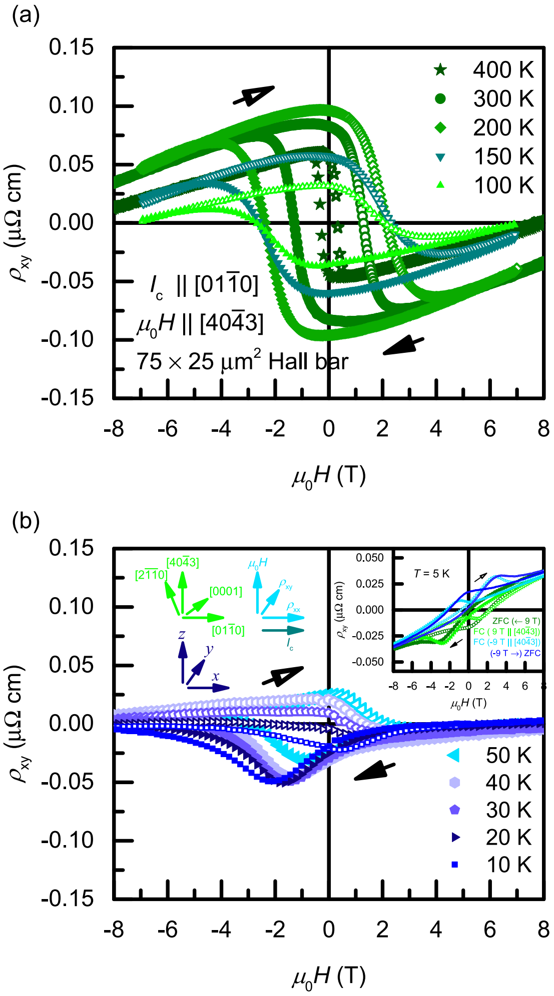

FIG. 4. Magnetotransport for a 60-nm Mn_3Sn (40$\bar{4}$3) film patterned into 75 × 25-μm^2 Hall bars. Transverse resistivity was measured normal to the (0001) crystal plane, with 500-μA current parallel to the [01$\bar{1}$0] in-plane crystallographic direction (closed and open symbols represent down and up field sweeps, respectively). Isothermal Hall resistivity measured as a function of magnetic field applied out of plane in the (a) higher-temperature regime and (b) lower-temperature regime. Diagram illustrates measurement geometry in relation to different crystallographic directions in the Mn_3Sn (40$\bar{4}$3) film. Inset shows the Hall effect measured for a 30-nm Mn_3Sn (40$\bar{4}$3) film at 5 K, after cooling under different field conditions.

one of the four equivalent structural grains (see Supplemental Fig. S5 [40]).

Figures 4(a) and 4(b) show isothermal measurements of Hall effect for a 60-nm Mn_3Sn (40$\bar{4}$3) film, in two temperature regimes. At room temperature, we measure a large AHE driven by momentum-space Berry curvature [8]. A tiny longitudinal magnetoresistance (<0.02% at 8 T) is simultaneously observed (see Supplemental Material [40]), ruling out FM contributions to magnetotransport.

Consistent AHE is measured across a series of Mn_3Sn (40$\bar{4}$3) samples of different thicknesses, as discussed in the Supplemental Material [40]. We extract a remnant anomalous Hall conductivity, $\sigma_{xy}(\mu_0 H = 0\ \text{T}) = 21\ \Omega^{-1}\ \text{cm}^{-1}$, comparable to previous reports [35].

Figure 4(a) shows that as temperature is increased towards T_N, coercive field decreases because of a softening of the magnetic structure. However, as temperature is decreased below 100 K, the magnitude of the Berry curvature-generated AHE drops concomitantly, as Mn_3Sn begins to leave the inverse triangular AF phase.

Below 50 K, Mn_3Sn transitions into the glassy FM state, where momentum-space Berry curvature-driven and (in this measurement configuration) conventional AHE are no longer detected. Instead, as shown in Fig. 4(b), the hysteresis loop becomes prominently asymmetric; a signature of the THE, caused when electrons acquire a real-space Berry phase upon encountering a magnetic structure with nonzero scalar spin chirality [32].

The inset of Fig. 4(b) explores this THE in a 30-nm Mn_3Sn (40$\bar{4}$3) film undergoing different field-cooling protocols. In the first case, the sample is saturated in a 9-T OP magnetic field, setting a particular chirality of the inverse triangular spin texture, which is maintained as the field is decreased to zero. The film is then cooled (ZFC). Here a downward bump arising close to the point of magnetization reversal (when external field is swept from positive to negative) indicates a negative THE. A bump with the same negative polarity is seen at coercivity on the reverse (negative to positive) field sweep. This demonstrates the formation of a noncollinear, noncoplanar spin texture close to the coercive field, at which point magnetic order is reversing through a mechanism of domain nucleation and propagation.

Therefore, we attribute the THE to the nucleation of chiral domain walls. Mn moments forming the domain walls will rotate within the basal plane, in order to invert magnetic structure between one domain and the next [31]. A domain wall with such arrangement will appear as a noncollinear, noncoplanar spin texture possessing finite scalar spin chirality to electrons propagating within the plane of these Mn_3Sn (40$\bar{4}$3) films. The even sign of THE suggests that the sense of rotation of spins in the domain walls is opposite during forward and reverse magnetization processes, while the internal moment configuration within the domain walls remains the same.

These results are in agreement with Li *et al.* [34], who measure a symmetric planar Hall effect in Mn_3Sn single crystals. This is attributed to chiral domain walls with a fixed internal moment configuration, which is maintained during both positive to negative, and negative to positive, field sweeps. The sense of rotation of spins within the domain walls must therefore be inverted between forward and reverse field sweeps. They also observe a dependence of the planar Hall effect polarity on applied field history.

We measure a similar magnetic state history in Mn_3Sn (40$\bar{4}$3) films. The inset of Fig. 4(b) shows that in the second case, when the thin film is ZFC after saturation in a −9-T OP magnetic field, the polarities of both symmetric THE peaks invert. This represents a sign change of real-space Berry phase, corresponding to an opposite sign of the finite scalar spin chirality generating it. We propose, therefore, that the handedness of the inverse triangular spin texture set at room temperature favors a certain chirality of domain wall formed during low-temperature magnetization reversal.

Furthermore, the THE bumps with either negative or positive polarity are enhanced after cooling in a +9-T or −9-T OP magnetic field, respectively. This may be explained by the external field further stabilizing the preferred domain-wall moment configuration during cooling. We thus demonstrate a memory effect in noncollinear AF thin films, that can be controlled by setting the orientation of the inverse triangular spin texture from which the chirality of domain walls evolves, which may find applications in neuromorphic computing.

III. CONCLUSION

In conclusion, we have grown epitaxial thin films of Mn_3Sn with both (0001) *c*-axis orientation and $(40\bar{4}3)$ crystallographic structure. In the latter case, Berry curvature-driven AHE is observed at room temperature. Upon cooling through the magnetic phase transition at 50 K, a peak in the Hall resistivity indicates the appearance of a THE. The sign of this THE signal, and hence the chirality of the noncoplanar spin texture generating it, can be manipulated through field-cooling conditions, thus furthering the potential of Mn_3Sn in *chiralitronic* devices.

ACKNOWLEDGMENTS

We acknowledge Dr. Dominik Kriegner for preparation of the Mn_3Sn $(40\bar{4}3)$ χ-ϕ XRD pole-figure maps. We thank Prof. Christian Back for provision of synchrotron beamtime at Helmholtz-Zentrum Berlin on beamline PM2 VEKMAG (under Proposal No. 191–07803), and acknowledge Wolfgang Simeth and Denis Mettus for assistance with measurements. Financial support for the VEKMAG project and for the PM2 VEKMAG beamline is provided by the German Federal Ministry for Education and Research (BMBF Contracts No. 05K10PC2, No. 05K10WR1, and No. 05K10KE1) and by Helmholtz-Zentrum Berlin, with Steffen Rudorff thanked for technical support. This work was partially funded by ASPIN (EU H2020 FET Open Grant No. 766566).

[1] V. Baltz, A. Manchon, M. Tsoi, T. Moriyama, T. Ono, and Y. Tserkovnyak, Antiferromagnetic spintronics, Rev. Mod. Phys. **90**, 015005 (2018).
[2] N. Nagaosa, J. Sinova, S. Onoda, A. H. MacDonald, and N. P. Ong, Anomalous Hall effect, Rev. Mod. Phys. **82**, 1539 (2010).
[3] L. Šmejkal, Y. Mokrousov, B. Yan, and A. H. MacDonald, Topological antiferromagnetic spintronics, Nat. Phys. **14**, 242 (2018).
[4] P. J. Brown, V. Nunez, F. Tasset, J. B. Forsyth, and P. Radhakrishna, Determination of the magnetic structure of Mn_3Sn using generalized neutron polarization analysis, J. Phys.: Condens. Matter **2**, 9409 (1990).
[5] S. Tomiyoshi and Y. Yamaguchi, Magnetic structure and weak ferromagnetism of Mn_3Sn studied by polarized neutron diffraction, J. Phys. Soc. Jpn. **51**, 2478 (1982).
[6] J. Kübler and C. Felser, Non-collinear antiferromagnets and the anomalous Hall effect, Europhys. Lett. **108**, 67001 (2014).
[7] Y. Zhang, Y. Sun, H. Yang, J. Železný, S. S. P. Parkin, C. Felser, and B. Yan, Strong anisotropic anomalous Hall effect and spin Hall effect in the chiral antiferromagnetic compounds Mn_3X (X = Ge, Sn, Ga, Ir, Rh, and Pt), Phys. Rev. B **95**, 075128 (2017).
[8] S. Nakatsuji, N. Kiyohara, and T. Higo, Large anomalous Hall effect in a non-collinear antiferromagnet at room temperature, Nature (London) **527**, 212 (2015).
[9] A. K. Nayak, J. E. Fischer, Y. Sun, B. Yan, J. Karel, A. C. Komarek, C. Shekhar, N. Kumar, W. Schnelle, J. Kübler, C. Felser, and S. S. P. Parkin, Large anomalous Hall effect driven by a nonvanishing Berry curvature in the noncolinear antiferromagnet Mn_3Ge, Sci. Adv. **2**, e1501870 (2016).
[10] H. Yang, Y. Sun, Y. Zhang, W.-J. Shi, S. S. P. Parkin, and B. Yan, Topological Weyl semimetals in the chiral antiferromagnetic materials Mn_3Ge and Mn_3Sn, New J. Phys. **19**, 015008 (2017).
[11] J. Kübler and C. Felser, Weyl fermions in antiferromagnetic Mn_3Sn and Mn_3Ge, Europhys. Lett. **120**, 47002 (2017).
[12] K. Kuroda, T. Tomita, M. T. Suzuki, C. Bareille, A. A. Nugroho, P. Goswami, M. Ochi, M. Ikhlas, M. Nakayama, S. Akebi, R. Noguchi, R. Ishii, N. Inami, K. Ono, H. Kumigashira, A. Varykhalov, T. Muro, T. Koretsune, R. Arita, S. Shin, T. Kondo, and S. Nakatsuji, Evidence for magnetic Weyl fermions in a correlated metal, Nat. Mater. **16**, 1090 (2017).
[13] M. Ikhlas, T. Tomita, T. Koretsune, M.-T. Suzuki, D. Nishio-Hamane, R. Arita, Y. Otani, and S. Nakatsuji, Large anomalous Nernst effect at room temperature in a chiral antiferromagnet, Nat. Phys. **13**, 1085 (2017).
[14] X. Li, L. Xu, L. Ding, J. Wang, M. Shen, X. Lu, Z. Zhu, and K. Behnia, Anomalous Nernst and Righi-Leduc Effects in Mn_3Sn: Berry Curvature and Entropy Flow, Phys. Rev. Lett. **119**, 056601 (2017).
[15] C. Wuttke, F. Caglieris, S. Sykora, F. Scaravaggi, A. U. B. Wolter, K. Manna, V. Süss, C. Shekhar, C. Felser, B. Büchner, and C. Hess, Berry curvature unravelled by the anomalous Nernst effect in Mn_3Ge, Phys. Rev. B **100**, 085111 (2019).
[16] Y. Zhang, J. Železný, Y. Sun, J. v. d. Brink, and B. Yan, Spin Hall effect emerging from a noncollinear magnetic lattice without spin–orbit coupling, New J. Phys. **20**, 073028 (2018).
[17] M. Kimata, H. Chen, K. Kondou, S. Sugimoto, P. K. Muduli, M. Ikhlas, Y. Omori, T. Tomita, A. H. MacDonald, S. Nakatsuji, and Y. Otani, Magnetic and magnetic inverse spin Hall effects in a non-collinear antiferromagnet, Nature (London) **565**, 627 (2019).
[18] P. K. Muduli, T. Higo, T. Nishikawa, D. Qu, H. Isshiki, K. Kondou, D. Nishio-Hamane, S. Nakatsuji, and Y. Otani, Evaluation of spin diffusion length and spin Hall angle of the antiferromagnetic Weyl semimetal Mn_3Sn, Phys. Rev. B **99**, 184425 (2019).
[19] W. Zhang, W. Han, S. H. Yang, Y. Sun, Y. Zhang, B. Yan, and S. S. P. Parkin, Giant facet-dependent spin-orbit torque and spin Hall conductivity in the triangular antiferromagnet $IrMn_3$, Sci. Adv. **2**, e1600759 (2016).

[20] W. Feng, G.-Y. Guo, J. Zhou, Y. Yao, and Q. Niu, Large magneto-optical Kerr effect in noncollinear antiferromagnets Mn_3X (X = Rh, Ir, Pt), Phys. Rev. B **92**, 144426 (2015).

[21] A. L. Balk, N. H. Sung, S. M. Thomas, P. F. S. Rosa, R. D. McDonald, J. D. Thompson, E. D. Bauer, F. Ronning, and S. A. Crooker, Comparing the anomalous Hall effect and the magneto-optical Kerr effect through antiferromagnetic phase transitions in Mn_3Sn, Appl. Phys. Lett. **114**, 032401 (2019).

[22] T. Higo, H. Man, D. B. Gopman, L. Wu, T. Koretsune, O. M. J. van't Erve, Y. P. Kabanov, D. Rees, Y. Li, M. T. Suzuki, S. Patankar, M. Ikhlas, C. L. Chien, R. Arita, R. D. Shull, J. Orenstein, and S. Nakatsuji, Large magneto-optical Kerr effect and imaging of magnetic octupole domains in an antiferromagnetic metal, Nat. Photon. **12**, 73 (2018).

[23] M. T. Suzuki, T. Koretsune, M. Ochi, and R. Arita, Cluster multipole theory for anomalous Hall effect in antiferromagnets, Phys. Rev. B **95**, 094406 (2017).

[24] H. Reichlová, T. Janda, J. Godinho, A. Markou, D. Kriegner, R. Schlitz, J. Železný, Z. Soban, M. Bejarano, H. Schultheiss, P. Němec, T. Jungwirth, C. Felser, J. Wunderlich, and S. T. B. Goennenwein, Imaging and writing magnetic domains in the non-collinear antiferromagnet Mn_3Sn, Nat. Commun. **10**, 5459 (2019).

[25] L. M. Sandratskii and J. Kübler, Role of Orbital Polarization in Weak Ferromagnetism, Phys. Rev. Lett. **76**, 4963 (1996).

[26] T. F. Duan, W. J. Ren, W. L. Liu, S. J. Li, W. Liu, and Z. D. Zhang, Magnetic anisotropy of single-crystalline Mn_3Sn in triangular and helix-phase states, Appl. Phys. Lett. **107**, 082403 (2015).

[27] E. Krén, J. Paitz, G. Zimmer, and É. Zsoldos, Study of the magnetic phase transformation in the Mn_3Sn phase, Physica B **80**, 226 (1975).

[28] N. H. Sung, F. Ronning, J. D. Thompson, and E. D. Bauer, Magnetic phase dependence of the anomalous Hall effect in Mn_3Sn single crystals, Appl. Phys. Lett. **112**, 132406 (2018).

[29] W. J. Feng, D. Li, W. J. Ren, Y. B. Li, W. F. Li, J. Li, Y. Q. Zhang, and Z. D. Zhang, Glassy ferromagnetism in Ni_3Sn-type $Mn_{3.1}Sn_{0.9}$, Phys. Rev. B **73**, 205105 (2006).

[30] S. Tomiyoshi, S. Abe, Y. Yamaguchi, H. Yamauchi, and H. Yamamoto, Triangular spin structure and weak ferromagnetism of Mn_3Sn at low temperature, J. Magn. Magn. Mater. **54–57**, 1001 (1986).

[31] X. Li, L. Xu, H. Zuo, A. Subedi, Z. Zhu, and K. Behnia, Momentum-space and real-space Berry curvatures in Mn_3Sn, SciPost Phys. **5**, 063 (2018).

[32] C. Sürgers, G. Fischer, P. Winkel, and H. v. Löhneysen, Large topological Hall effect in the non-collinear phase of an antiferromagnet, Nat. Commun. **5**, 3400 (2014).

[33] P. K. Rout, P. V. P. Madduri, S. K. Manna, and A. K. Nayak, Field-induced topological Hall effect in the noncoplanar triangular antiferromagnetic geometry of Mn_3Sn, Phys. Rev. B **99**, 094430 (2019).

[34] X. Li, C. Collignon, L. Xu, H. Zuo, A. Cavanna, U. Gennser, D. Mailly, B. Fauqué, L. Balents, Z. Zhu, and K. Behnia, Chiral domain walls of Mn_3Sn and their memory, Nat. Commun. **10**, 3021 (2019).

[35] T. Ikeda, M. Tsunoda, M. Oogane, S. Oh, T. Morita, and Y. Ando, Anomalous Hall effect in polycrystalline Mn_3Sn thin films, Appl. Phys. Lett. **113**, 222405 (2018).

[36] T. Higo, D. Qu, Y. Li, C. L. Chien, Y. Otani, and S. Nakatsuji, Anomalous Hall effect in thin films of the Weyl antiferromagnet Mn_3Sn, Appl. Phys. Lett. **113**, 202402 (2018).

[37] T. Ikeda, M. Tsunoda, M. Oogane, S. Oh, T. Morita, and Y. Ando, Improvement of large anomalous Hall effect in polycrystalline antiferromagnetic $Mn_{3+x}Sn$ thin films, IEEE Trans. Magn. **55**, 2501704 (2019).

[38] Y. You, X. Chen, X. Zhou, Y. Gu, R. Zhang, F. Pan, and C. Song, Anomalous Hall effect–like behavior with in-plane magnetic field in noncollinear antiferromagnetic Mn_3Sn films, Adv. Electron. Mater. **5**, 1800818 (2019).

[39] A. Markou, J. M. Taylor, A. Kalache, P. Werner, S. S. P. Parkin, and C. Felser, Noncollinear antiferromagnetic Mn_3Sn films, Phys. Rev. Mater. **2**, 051001(R) (2018).

[40] See Supplemental Material at http://link.aps.org/supplemental/10.1103/PhysRevB.101.094404 for additional details of the thin-film growth procedure, as well as supporting magnetotransport results.

[41] T. Noll and F. Radu, in *Proceedings of MEDSI2016, Barcelona, Spain, September* 2016, edited by V. R. W. Schaa (JACoW, Geneva, Switzerland, 2017), p. 370.

[42] P. Carra, B. T. Thole, M. Altarelli, and X. Wang, X-ray Circular Dichroism and Local Magnetic Fields, Phys. Rev. Lett. **70**, 694 (1993).

[43] J. M. Taylor, E. Lesne, A. Markou, F. K. Dejene, P. K. Sivakumar, S. Pöllath, K. G. Rana, N. Kumar, C. Luo, H. Ryll, F. Radu, F. Kronast, P. Werner, C. H. Back, C. Felser, and S. S. P. Parkin, Magnetic and electrical transport signatures of uncompensated moments in epitaxial thin films of the noncollinear antiferromagnet Mn_3Ir, Appl. Phys. Lett. **115**, 062403 (2019).

Anomalous and topological Hall effects in epitaxial thin films of the noncollinear antiferromagnet Mn_3Sn
-
Supplemental Material

James M. Taylor,[1] Anastasios Markou,[2] Edouard Lesne,[1] Pranava Keerthi Sivakumar,[1]
Chen Luo,[3] Florin Radu,[3] Peter Werner,[1] Claudia Felser,[2] and Stuart S. P. Parkin[1]
[1]*Max Planck Institute of Microstructure Physics, Weinberg 2, 06120 Halle (Saale), Germany*
[2]*Max Planck Institute for Chemical Physics of Solids, Nöthnitzer Str. 40, 01187 Dresden, Germany*
[3]*Helmholtz-Zentrum Berlin for Materials and Energy,*
Albert Einstein Str. 15, 12489 Berlin, Germany

(Dated: 10 January 2020)

Noncollinear antiferromagnets with a $D0_{19}$ (space group = 194, P$6_3/mmc$) hexagonal structure have garnered much attention for their potential applications in topological spintronics. Here, we report the deposition of continuous epitaxial thin films of such a material, Mn_3Sn, and characterize their crystal structure using a combination of x-ray diffraction and transmission electron microscopy. Growth of Mn_3Sn films with both (0001) c-axis orientation and $(40\bar{4}3)$ texture is achieved. In the latter case, the thin films exhibit a small uncompensated Mn moment in the basal plane, quantified via magnetometry and x-ray magnetic circular dichroism experiments. This cannot account for the large anomalous Hall effect simultaneously observed in these films, even at room temperature, with magnitude σ_{xy} $(\mu_0 H = 0\ \mathrm{T}) = 21\ \Omega^{-1}\mathrm{cm}^{-1}$ and coercive field $\mu_0 H_{\mathrm{c}} = 1.3$ T. We attribute the origin of this anomalous Hall effect to momentum-space Berry curvature arising from the symmetry-breaking inverse triangular spin structure of Mn_3Sn. Upon cooling through the transition to a glassy ferromagnetic state at around 50 K, a peak in the Hall resistivity close to the coercive field emerges. This indicates the onset of a topological Hall effect contribution, arising from a nonzero scalar spin chirality that generates a real-space Berry phase. We demonstrate that the polarity of this topological Hall effect, and hence the chiral-nature of the noncoplanar magnetic structure driving it, can be controlled using different field cooling conditions.

I. THIN FILM GROWTH AND STRUCTURAL CHARACTERIZATION

The epitaxial thin film samples of Mn_3Sn utilized in this study were deposited using magnetron sputtering following the procedure described in Ref. [39] of the Main Text. However, in this case single crystal substrates of either (111) cut $SrTiO_3$ or (001) cut MgO were used to seed either (0001) c-axis texture or $(40\bar{4}3)$ orientation respectively. In order to achieve continuous films, we made modifications to the temperatures during growth and post-annealing of the different layers. The Ru buffer layer was grown at 400 °C, and allowed to cool to room temperature. Mn and Sn were then co-sputtered at room temperature, and the films post-annealed by heating to 300 °C at a rate of 10 °C / minute, holding for 10 minutes, then allowing to cool back to room temperature over a period of approximately 60 minutes.

Stacks were subsequently capped with 2.5 nm Al, which partially oxidizes, thus protecting the Mn_3Sn without shorting too much current during transport measurements. Since the surface of the resulting Al(Oxide) is rough, samples used for atomic force microscopy measurements were instead capped with 2 nm Ru, which closely follows the topography of the underlying Mn_3Sn, thus allowing an accurate quantification of its roughness.

Additional reference samples, consisting of either 30 nm or 5 nm Ru buffer layers alone, grown on MgO (001) and MgO (111) substrates respectively, were also prepared. Due to the proximity of the sets of peaks in 2θ-θ position, the pole figure scans of the Ru {0002} reflections shown in Fig. 1(d) of the Main Text were measured from the 30 nm Ru buffer reference film. Meanwhile, the 5 nm reference sample was used to measure the contribution of the Ru to electrical transport, discussed below, and to record the background magnetization contribution from the substrate and buffer layer (subtracted from the total signal measured by SQUID-VSM, as explained in the discussion around Fig. 2(a) of the Main Text).

The composition of the thin film stacks was quantified, using energy dispersive X-ray spectroscopy measured in a scanning electron microscope, as $Mn_{0.76}Sn_{0.24}$. We denote this as Mn_3Sn, although we point out that the films grow with a slightly Mn-rich composition (and are thus not expected to show a first-order phase transition to a helical magnetic state below 275 K).

Mn_3Sn has a hexagonal crystal structure, with Mn moments arranged in a kagome lattice in the basal plane. Its bulk lattice parameters are: in-plane (IP), $a_{\mathrm{Mn_3Sn}} = 5.665$ Å and out-of-plane (OP) $c_{\mathrm{Mn_3Sn}} = 4.531$ Å. The bulk IP and OP lattice parameters of hexagonal Ru are $a_{\mathrm{Ru}} = 2.706$ Å and $c_{\mathrm{Ru}} = 4.282$ Å respectively. The lattice mismatches between the different orientations of the Mn_3Sn film and Ru buffer layer, and the various substrates (as well as the Y:ZrO_2 used in our earlier study, see Ref. [39] of the Main Text)

Supplemental Table S1 – Lattice mismatch calculated between different orientations of Mn_3Sn thin films and Ru buffer layers, and the various substrates utilized to achieve each epitaxial relationship. We calculate lattice mismatch from bulk lattice parameters, using the same layer stacking sequences as in our deposited multilayers.

	$Y{:}ZrO_2$ (111)	$SrTiO_3$ (111)	Ru (0001)	Mn_3Sn (0001)	MgO (001)	Ru $(40\bar{4}3)$	Mn_3Sn $(40\bar{4}3)$
$Y{:}ZrO_2$ (111)	-		5.7%	10.7%			
$SrTiO_3$ (111)		-	-2.0%	2.6%			
Ru (0001)	5.7%	-2.0%	-	4.7%			
Mn_3Sn (0001)	10.7%	2.6%	4.7%	-			
MgO (001)					-	17.2%	24.0%
Ru $(40\bar{4}3)$					17.2%	-	5.8%
Mn_3Sn $(40\bar{4}3)$					24.0%	5.8%	-

are shown in Supplemental Table S1. The lattice mismatch between the $SrTiO_3$ (111) substrates and the Ru buffer layer (and, in turn, the subsequent *c*-axis oriented Mn_3Sn film) is less than that with the previously utilized $Y{:}ZrO_2$ substrates. This motivated our choice to switch to depositing on $SrTiO_3$ (111) substrates. A smaller lattice mismatch likely results in a higher quality Ru buffer layer, which may subsequently contribute to the seeding of continuous Mn_3Sn films in the present case. The choice of cubic MgO (001) substrates, whilst poorly lattice matched with both Ru and Mn_3Sn, nevertheless succeeded in seeding the growth of a Ru buffer layer with sharp crystal structure, which is, in turn, relatively well lattice matched to the $(40\bar{4}3)$ textured Mn_3Sn.

In both cases, x-ray diffraction (XRD) measurements were performed using a PANalytical X'Pert^3 diffractometer with Cu K_{α_1} radiation ($\lambda = 1.5406$ Å). For the *c*-axis oriented films, by fitting the positions of the Mn_3Sn and Ru (0002) and (0004) peaks from the 2θ-θ scan with a Gaussian profile, we can extract values for their OP hexagonal lattice parameters, *c*. These are found to be $c_{\mathrm{Mn_3Sn}} = 4.524$ Å and $c_{\mathrm{Ru}} = 4.312$ Å respectively. Separate measurements of the Mn_3Sn $(20\bar{2}1)$ and Ru $(10\bar{1}1)$ partially IP diffraction peaks (not shown) allow us to calculate the IP hexagonal lattice parameters, *a*. These are found to be $a_{\mathrm{Mn_3Sn}} = 5.684$ Å and $a_{\mathrm{Ru}} = 2.695$ Å respectively. In all cases, the measured lattice parameters are close to the bulk values, with no systematic epitaxial strain observed.

By setting the diffractometer to the 2θ-θ position of each of these partially IP peaks and scanning the rotational angle, ϕ, the azimuthal scans in the inset of Fig. 1(a) of the Main Text were recorded. The substrate was aligned with its $[1\bar{1}0]$ edge along $\phi = 0°$. From these, we determined the epitaxial relationship of the $SrTiO_3$ (111) / Ru (0001) / Mn_3Sn (0001) multilayers. In a similar way, the pole figures shown in Fig. 1(d) of the Main Text were mapped by performing individual ϕ azimuthal scans at consecutive values of the OP to IP rotation angle χ.

We confirm the interpretation of the epitaxial relationship for the $(40\bar{4}3)$ textured films through plane-view transmission electron microscopy (TEM) measurements. Supplemental Fig. S1 displays such a plane-view TEM image taken for a 60 nm Mn_3Sn $(40\bar{4}3)$ film and viewed along the MgO $[00\bar{1}]$ zone axis. The sample was prepared for measurement by conventional backside thinning and subsequent ion beam milling. The plane-view micrograph confirms the continuity of the films, whilst simultaneously demonstrating their granular structure. We observe large crystallites of around 200 nm in size, with grain boundary defects between them (which may contribute to enhancing the coercive field of these thin films through domain wall pinning, see below). TEM contrast is produced between neighboring crystallites exhibiting one of four possible orientations, with their *c*-axis aligned along one of the symmetric $\langle 111 \rangle$ directions in the cubic substrate, as discussed in the Main Text.

The selected area electron diffraction (SAED) pattern, shown in the right hand panel of Supplemental Fig. S1, supports this interpretation of the epitaxial growth mode. $\langle 01\bar{1}0 \rangle$ reflections of the Mn_3Sn film are coordinated with the cubic diagonal directions of the MgO, showing that the principle IP crystalline axis of Mn_3Sn aligns with one of the four $\langle 110 \rangle$ directions in the substrate. Nevertheless, this SAED pattern confirms that individual grains possess a single-crystalline structure. The discrete, sharp diffraction spots demonstrate that the Mn_3Sn film exhibits well defined IP crystallographic axes that are coherently oriented across multiple domains, with small relative mosaic spread between successive crystallites.

II. CONTRIBUTION OF Ru BUFFER LAYER TO ELECTRICAL TRANSPORT PROPERTIES

The metallic Ru buffer layer will act to short some electric current during transport measurements. To quantify this contribution, the magnetotransport properties of a 5 nm Ru (0001) reference sample grown on MgO (111) were measured in the Van der Pauw geometry, with current applied parallel to the $[2\bar{1}\bar{1}0]$ crystal direction. Electrical transport was measured in a Quantum Design Physical Property Measurement System (Dynacool PPMS), using a Keithley 6221 current source and 2182A nanovoltmeter. Supplemental Fig. S2 shows the variation in the longitudinal resistivity (ρ_{xx}) of the Ru layer as a function of temperature (T) during zero field cool-

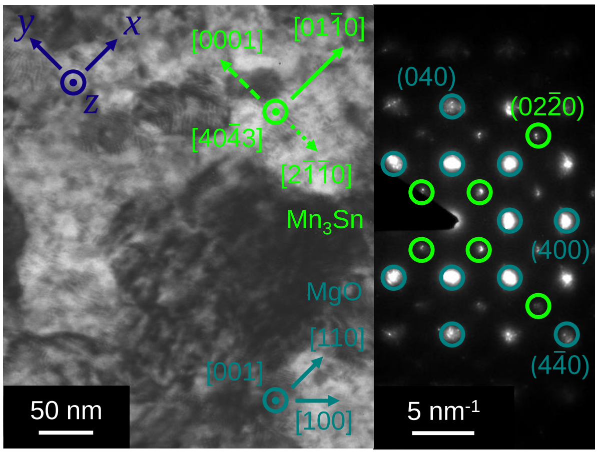

Supplemental FIG. S1 - Plane-view TEM image of a 60 nm Mn$_3$Sn (40$\bar{4}$3) film, viewed along the [00$\bar{1}$] zone axis of the MgO (001) substrate. The primary [01$\bar{1}$0] crystallographic direction of the Mn$_3$Sn layer lies in-plane, with the [0001] and [2$\bar{1}\bar{1}$0] crystalline axes partially out-of-plane. The coordinate system defined for subsequent magnetotransport measurements is indicated. Right panel shows a selected-area electron diffraction pattern measured for the same planar sample, with reflections from the substrate and Mn$_3$Sn thin film indexed.

ing (ZFC) and zero field warming (ZFW). The resistivity decreases metallically, before saturating at low temperatures. This is because of defects and impurities modifying electrical transport in the low temperature regime.

Both longitudinal magnetoresistance (MR) and transverse resistivity (ρ_{xy}) were then measured as a function of magnetic field ($\mu_0 H$) applied along the *c*-axis, shown in the upper and lower panels of the inset to Supplemental Fig. S2 respectively. We observe a Lorentz-type positive MR (driven by the cyclical motion of electrons in strong magnetic fields) and an ordinary Hall effect (with positive and negative gradients at high- and low-temperatures, respectively, showing a transition from hole- to electron-like carriers with decreasing temperature). Both these phenomena are as expected for a normal metal such as Ru, meaning that we can attribute any subsequently measured anomalous transport behavior to the Mn$_3$Sn layer alone. In addition, the effects are small, particularly at room temperature, where ρ_{xy} ($\mu_0 H = 8$ T) $= 0.03$ µΩ cm. This, combined with the low thickness of the Ru (as compared with the Mn$_3$Sn films), means that the buffer layer will make a minimum contribution to the overall magnetotransport behavior of the full stack.

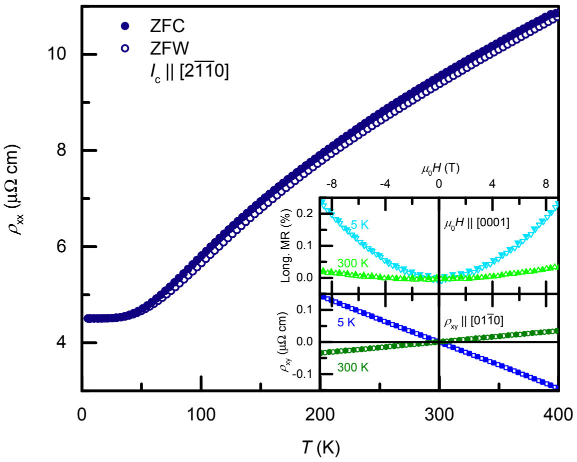

Supplemental FIG. S2 - Magnetotransport for a 5 nm Ru (0001) thin film in the Van der Pauw geometry, with 500 µA current parallel to the in-plane [2$\bar{1}\bar{1}$0] crystallographic direction: Longitudinal resistivity measured as a function of temperature during zero field cooling (closed symbols) and subsequent zero field warming (open symbols). Longitudinal magnetoresistance (upper inset) and Hall resistivity (lower inset) measured at different temperatures as a function of external magnetic field applied out-of-plane. Transverse resistivity was measured along the [01$\bar{1}$0] crystalline axis (closed and open symbols represent down and up field sweeps respectively).

III. THICKNESS DEPENDENCE OF AHE IN Mn$_3$Sn (40$\bar{4}$3) THIN FILMS

To demonstrate the negligible magnetotransport contribution of the Ru layer explicitly, in Supplemental Fig. S3 we plot the Hall effect of MgO (001) substrate / 5 nm Ru buffer / Mn$_3$Sn (40$\bar{4}$3) films of different thicknesses after the subtraction of the ordinary Hall effect background measured from the Ru reference sample, using a parallel resistors model. The resulting Hall effect of the Mn$_3$Sn layer alone does not differ qualitatively, beside the partial removal of a linear background, whilst the minor quantitative change reflects the small role of the Ru buffer in the magnetotransport behavior of the overall multilayer. Here the samples were measured in the Van der Pauw geometry, although the results are in very good agreement with those measured in patterned Hall bar devices (where the contribution from the buffer layer is not routinely subtracted), as reported in the Main Text.

Transverse resistivity was measured at 300 K as a function of magnetic field applied OP for Mn$_3$Sn (40$\bar{4}$3) films of different thicknesses in the range 70 nm down to 30 nm. All films exhibit a large Berry curvature driven anoma-

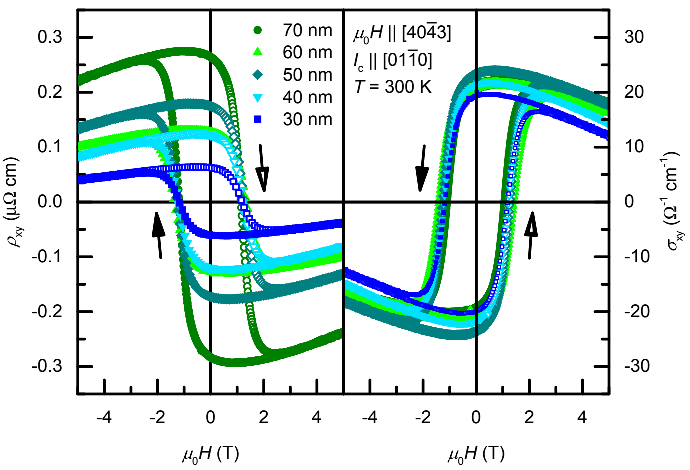

Supplemental FIG. S3 - Hall effect measured at 300 K as a function of external magnetic field applied out-of-plane for different thicknesses of Mn_3Sn (40$\bar{4}$3) films in the Van der Pauw geometry. A background contribution, as recorded from a 5 nm Ru buffer layer reference sample, has been subtracted. Left panel plots transverse resistivity, measured normal to the (0001) crystal plane, with 500 μA current parallel to the [01$\bar{1}$0] in-plane crystallographic direction (closed and open symbols represent down and up field sweeps respectively). Right panel plots the same measurements converted to Hall conductivity, as calculated using the longitudinal resistivity of each film.

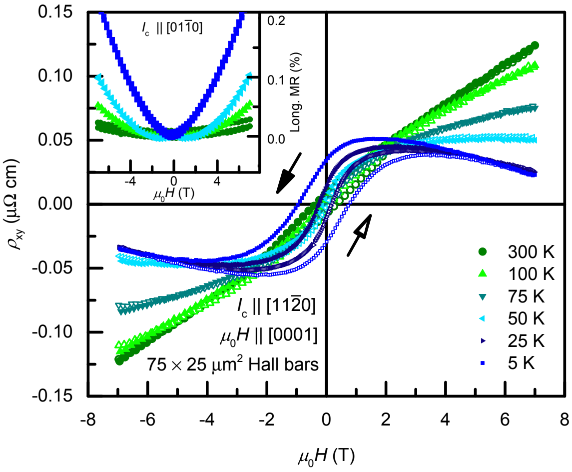

Supplemental FIG. S4 - Hall resistivity measured at different temperatures as a function of external magnetic field applied out-of-plane for a 70 nm Mn_3Sn (0001) film patterned into a 75 × 25 μm^2 Hall bar. Transverse resistivity was measured along the [$\bar{1}$100] crystalline axis, with 500 μA current parallel to the [11$\bar{2}$0] in-plane crystallographic direction (closed and open symbols represent down and up field sweeps respectively). Inset shows longitudinal magnetoresistance, parallel to the [01$\bar{1}$0] crystal direction, measured over the same out-of-plane magnetic field range at different temperatures.

lous Hall effect (AHE), as discussed in the Main Text. Although the magnitude of Hall resistivity decreases as thickness decreases, we otherwise observe no qualitative change in the AHE generated by the topology of the non-collinear antiferromagnetic (AF) structure. In particular, the coercive field, which reflects the reversal of the handedness of the inverse triangular spin texture through a mechanism of chiral domain nucleation and propagation (and is enhanced by the pinning of AF domain walls at crystallite grain boundaries as discussed above), remains the same across the thickness series.

In order to compare this thickness dependence of AHE directly with previous studies, we calculate Hall conductivity ($\sigma_{xy} = \rho_{xy}/\rho_{xx}^2$) for the Mn_3Sn (40$\bar{4}$3) films of different thickness, using their simultaneously measured longitudinal resistivity, as plotted in the right-hand panel of Supplemental Fig. S3. The Hall conductivity remains broadly the same across the thickness series, with a small decrease observed for the 30 nm film, which may reflect a reduction in crystal structure quality at such low thickness. We extract a typical remnant Hall conductivity of σ_{xy} ($\mu_0H = 0$ T) = 21 Ω^{-1}cm^{-1}, which, whilst smaller than that measured for bulk single crystals in Ref. [8] of the Main Text, is larger than the planar Hall effect measured for epitaxial Mn_3Sn films in Main Text Ref. [38], and is comparable to values measured for polycrystalline bulk (Ref. [33]) or thin film (Ref. [35]) samples.

Such large measured values of anomalous Hall conductivity, which persist even at zero magnetic field (thus reflecting the stability of the chiral domain structure even with external magnetic field removed), demonstrate the suitability of these noncollinear AF Mn_3Sn films for topological spintronic applications. Comparison of the transverse and longitudinal conductivities of our thin films confirms that they lie in the regime where intrinsic AHE dominates, comparable to other materials shown to demonstrate Berry curvature driven topological transport properties.

IV. FURTHER MAGNETOTRANSPORT PROPERTIES OF Mn_3Sn (0001) THIN FILMS

Supplemental Fig. S4 shows further temperature dependent measurements of the Hall effect in Mn_3Sn (0001) films. In this case, we measure transverse resistivity as a function of magnetic field applied parallel to the c-axis, for a 75 × 25 μm^2 Hall bar fabricated with its long axis along the $[11\bar{2}0]$ crystallographic direction. In systems with hexagonal structure, the $[11\bar{2}0]$ crystalline axis is distinct from the $[01\bar{1}0]$ direction (as probed in Fig. 3(b) of the Main Text). However, we see that an almost identical Hall effect is measured with current flowing along both crystal directions, with very similar magnitude and temperature dependence.

This can be explained by considering the azimuthal XRD ϕ scans presented in Fig. 1(a) of the Main Text. We observe a six-fold symmetry of the partially IP Mn_3Sn $\{20\bar{2}1\}$ reflections (as opposed to the expected three-fold recurrence), suggesting the hexagonal crystal structure exhibits rotational twinning between basal planes. This rotational twinning of Mn_3Sn will cause magnetotransport to average over crystallographic directions at both 30° and 60° intervals, thus resulting in an identical Hall effect along both the $\langle 01\bar{1}0\rangle$ and $\langle 2\bar{1}\bar{1}0\rangle$ crystalline axes.

The inset of Supplemental Fig. S4 shows longitudinal MR, measured $\parallel$ $[01\bar{1}0]$ with external magnetic field applied $\parallel$ [0001]. We observe an extremely small MR at 300 K, indicating an absence of net magnetization in these AF thin films. As temperature is decreased to 5 K, MR increases as Mn_3Sn transitions into the glassy ferromagnetic (FM) state. This may be the result of increased scattering of charge carriers from the frustrated magnetic moments in the spin glass phase.

V. FURTHER MAGNETOTRANSPORT PROPERTIES OF Mn_3Sn $(40\bar{4}3)$ THIN FILMS

Supplemental Fig. S5 shows further temperature dependent measurements of the Hall effect in 60 nm Mn_3Sn $(40\bar{4}3)$ films. This time, we measure transverse resistivity $\parallel$ $[01\bar{1}0]$, with current applied in a direction partially perpendicular to consecutive (0001) crystal planes (in a geometry orthogonal to that probed in Fig. 4 of the Main Text). However, we observe a very similar magnitude and temperature dependence of Hall effect in both configurations.

This is to be expected, when we consider the four-fold symmetry of crystal grains discussed in the Main Text. A mesoscopic device will consist of multiple crystallites, each of which will have either a $\langle 01\bar{1}0\rangle$ direction, or the *c*-axis, parallel to current flow, depending on which of the four possible cubic axes of the substrate that grain follows. Thus, for a given device, it is not possible to distinguish between the IP $[01\bar{1}0]$ and partially IP [0001] directions across multiple grains. Hall resistivity is averaged over all crystallites, thus resulting in an isotropic Hall effect along both the $\langle 01\bar{1}0\rangle$ and $\langle 0001\rangle$ crystalline axes. Nevertheless, both measurement configurations should yield equally large AHE as predicted in Ref. [7] of the Main Text.

The coercive field is 1.3 T, close to the reversal field of the inverse triangular AF order, indicating the sign of the AHE depends on the chirality of the spin texture. This coercivity is comparable to that reported elsewhere in the literature for Mn_3Sn thin films (for example Refs. [35-37] of the Main Text), but is higher than that measured for bulk single crystals. This can be explained by the structural defects inherent in such thin film samples pinning AF domain wall motion during the reorientation process of the inverse triangular spin texture, and thus indicates the key role played by chiral domains dynamics in determining the magnetotransport behavior of topological antiferromagnets.

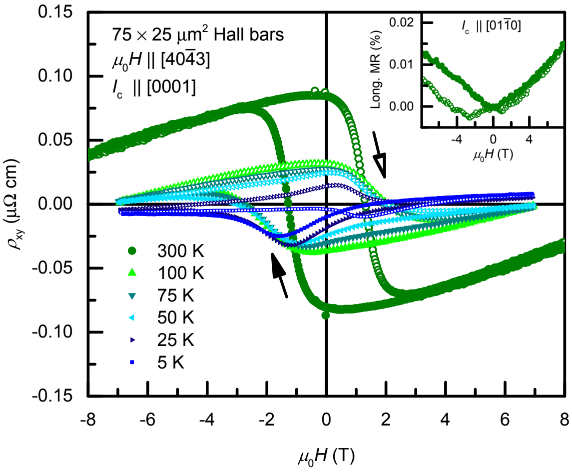

Supplemental FIG. S5 - Hall resistivity measured at different temperatures as a function of external magnetic field applied out-of-plane, for a 60 nm Mn_3Sn $(40\bar{4}3)$ film patterned into a 75 × 25 µm² Hall bar. Transverse resistivity was measured along the $[01\bar{1}0]$ in-plane crystallographic direction, with 500 µA current normal to the (0001) crystal plane (closed and open symbols represent down and up field sweeps respectively). Inset shows longitudinal magnetoresistance, parallel to the $[01\bar{1}0]$ crystal direction, measured over the same out-of-plane magnetic field range at 300 K.

We also note that, as temperature is decreased between 300 K and 50 K, the square shape of the AHE hysteresis loop remains unchanged. There is no evidence of a transition to a helical magnetic phase in these Mn_3Sn $(40\bar{4}3)$ films, as expected for samples that are grown with a slight excess of Mn (see Ref. [28] of the Main Text).

The inset of Supplemental Fig. S5 shows longitudinal MR $\parallel$ $[01\bar{1}0]$. As discussed in the Main Text, we observe an extremely small MR at 300 K (<0.02% at 8 T), reflecting the tiny uncompensated magnetic moment and ruling out ferromagnetism as the origin of the large room temperature AHE observed in these thin films.

Very similar behavior of the Hall effect in Mn_3Sn $(40\bar{4}3)$, specifically a large AHE at room temperature and a transition to THE below 50 K, has been observed across a selection of films with comparable crystal quality

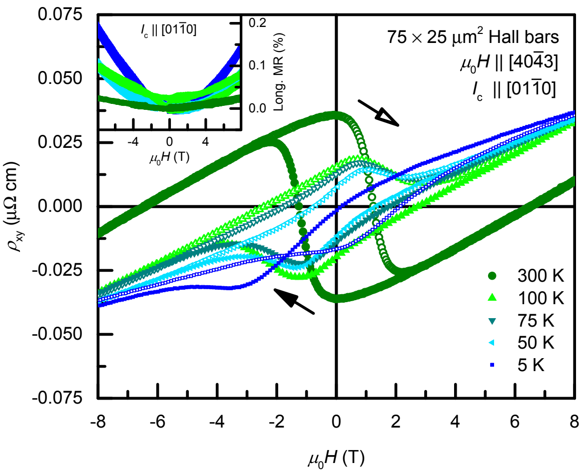

Supplemental FIG. S6 - Hall resistivity measured at different temperatures as a function of external magnetic field applied out-of-plane, for a 30 nm Mn_3Sn $(40\bar{4}3)$ film patterned into a 75 × 25 μm^2 Hall bar. Transverse resistivity was measured normal to the (0001) crystal plane, with 500 μA current parallel to the $[01\bar{1}0]$ in-plane crystallographic direction (closed and open symbols represent down and up field sweeps respectively). Inset shows longitudinal magnetoresistance, parallel to the $[01\bar{1}0]$ crystal direction, measured over the same out-of-plane magnetic field range at different temperatures.

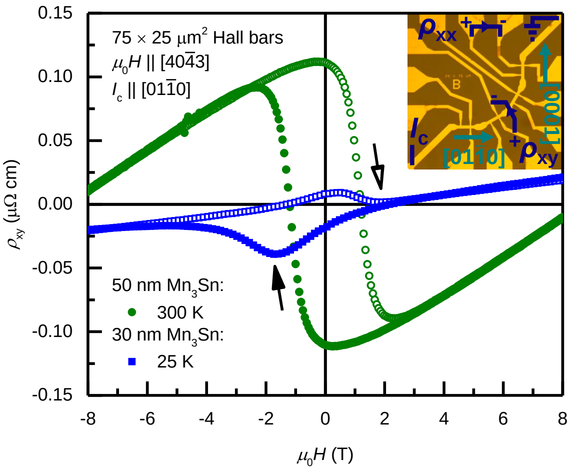

Supplemental FIG. S7 - Hall resistivity measured as a function of external magnetic field applied out-of-plane, at 300 K for a 50 nm Mn_3Sn $(40\bar{4}3)$ film and at 25 K for a 40 nm Mn_3Sn $(40\bar{4}3)$ film, patterned into 75 × 25 μm^2 Hall bars. Transverse resistivity was measured normal to the (0001) crystal plane, with 500 μA current parallel to the $[01\bar{1}0]$ in-plane crystallographic direction (closed and open symbols represent down and up field sweeps respectively). Inset shows optical image of a typical device, with 75 × 25 μm^2 Hall bars fabricated along different crystalline axes and an example measurement geometry indicated.

but different thickness, and grown using an identical technique but in different 'batches'. This gives us confidence that the effects observed are general for this material, and are reproducible.

Temperature dependent magnetotransport properties were studied in such samples of different thicknesses after patterning into Hall bar devices, with the example of a 30 nm Mn_3Sn $(40\bar{4}3)$ film presented in Supplemental Fig. S6. Hall resistivity has a lower magnitude than in thicker films, as discussed above. In addition, Supplemental Fig. S6 shows a steeper linear background in the high magnetic field region. This is because of the lower thickness of the Mn_3Sn film as compared with the Ru buffer layer, whose ordinary Hall contribution has not be subtracted in this case. Nevertheless, the temperature dependence of the Hall effect is in very good agreement with the other samples in the thickness series. This demonstrates that, down to 30 nm, there is little thickness dependence in the magnetotransport properties of Mn_3Sn.

The inset of Supplemental Fig. S6 shows longitudinal MR, measured || $[01\bar{1}0]$ with magnetic field applied OP. Again, we observe a tiny MR at 300 K, reflecting an absence of net magnetization in these Mn_3Sn $(40\bar{4}3)$ films and thus excluding ferromagnetism as the origin of the AHE observed at room temperature. As temperature is decreased to 5 K, MR increases as the material transitions into the glassy FM phase.

A further example is presented in Supplemental Fig. S7. Here, we measure Hall effect at 300 K in a 50 nm Mn_3Sn $(40\bar{4}3)$ film, showing momentum-space Berry curvature driven AHE, and at 25 K in a 40 nm Mn_3Sn $(40\bar{4}3)$ film, showing a real-space Berry curvature driven THE. In the latter case, the sample has been ZFC from 400 K, after saturation in a 9 T external magnetic field.

The inset of Supplemental Fig. S7 shows an optical image of a typical patterned Hall bar, with an example measurement geometry indicated. Devices were fabricated using a combination of electron beam lithography and Ar ion etching, with sizes ranging from 75 × 25 μm^2 down to 3 × 1 μm^2. Different sized Hall bars were, in turn, patterned with their long axis (direction of current flow) along either the $[01\bar{1}0]$ crystallographic axis, or a direction parallel to the IP component of the [0001] c-axis, as well as at 30° intervals in between.

The left-hand panel of Supplemental Fig. S8 shows Hall effect measured at room temperature for a 30 nm Mn_3Sn $(40\bar{4}3)$ film, in 75 × 25 μm^2 Hall bars fabricated along the $[01\bar{1}0]$ crystalline axis, as well as at 30° and at 60°

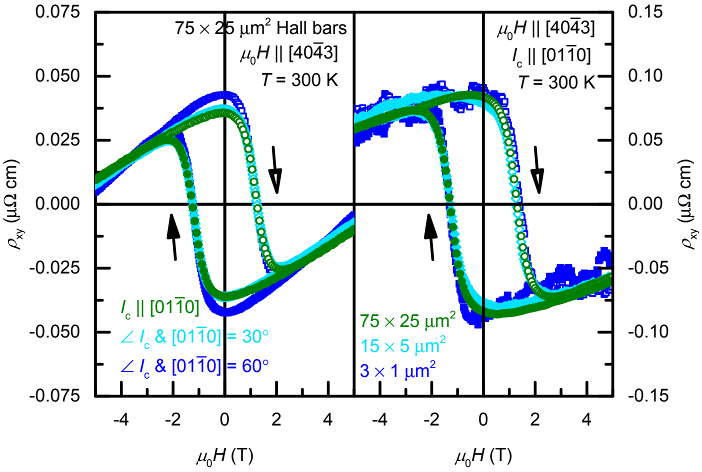

Supplemental FIG. S8 - Hall resistivity measured at 300 K as a function of external magnetic field applied out-of-plane, with 500 μA current along the Hall bar long axis (closed and open symbols represent down and up field sweeps respectively): Left frame shows Hall effect for a 30 nm Mn_3Sn (40$\bar{4}$3) film patterned into 75 × 25 μm² Hall bars directed along 30° intervals to the [01$\bar{1}$0] crystalline axis. Right frame shows Hall effect for a 60 nm Mn_3Sn (40$\bar{4}$3) film patterned into Hall bars of different sizes parallel to the [01$\bar{1}$0] in-plane crystallographic direction.

to this direction. We observe a very similar Hall effect for current flow along all directions. This can be explained by the fact that the weak magnetization in the basal plane of Mn_3Sn, caused by the canting of Mn moments towards the direction joining nearest non-magnetic neighbor atoms, is free to rotate in response to an external magnetic field (as discussed in Ref. [5] of the Main Text). Therefore, regardless of the measurement geometry, external magnetic field will correspondingly orient the chirality of the inverse triangular spin texture, resulting in isotropic AHE with respect to the hexagonal crystal lattice.

Finally, the right-hand panel of Supplemental Fig. S8 shows Hall effect measured at room temperature for a 60 nm Mn_3Sn (40$\bar{4}$3) film, in Hall bars of different dimensions fabricated along the [01$\bar{1}$0] crystallographic axis. Again, an almost identical AHE, of equal magnitude and with the same coercive field, is observed in devices down to 3 × 1 μm² in size. Because we would expect a modification of Hall effect upon approach to measurement of a single domain state, this suggests that the length scale of chiral domains in Mn_3Sn is less than 1 μm, which would indeed be the case if AF domain dimensions are correlated with the size of crystallite grains in the (40$\bar{4}$3) thin films.

ACKNOWLEDGMENTS

We acknowledge Dr Dominik Kriegner for preparation of the Mn_3Sn (40$\bar{4}$3) XRD χ-ϕ pole figure maps. We thank Prof Christian Back for provision of synchrotron beamtime at Helmholtz-Zentrum Berlin on beamline PM2 VEKMAG (under proposal 191-07803), and acknowledge Wolfgang Simeth and Denis Mettus for assistance with measurements. Financial support for the VEKMAG project and for the PM2 VEKMAG beamline are provided by the German Federal Ministry for Education and Research (BMBF 05K10PC2, 05K10WR1, 05K10KE1) and by Helmholtz-Zentrum Berlin, with Steffen Rudorff thanked for technical support. This work was partially funded by ASPIN (EU H2020 FET Open Grant 766566).

4 Conclusion

4.1 Summary

In this thesis, we have studied the physical properties of epitaxial thin films of the noncollinear AFs Mn_3Ir andMn_3Sn. These materials are of interest to the field of AF spintronics, which aims to develop spintronic computational devices using the AF order parameter (thus delivering the advantages of low stray magnetic fields and stability against external perturbations). The particular attractiveness of noncollinear Mn_3X AFs stems from their novel topological properties, arising from the symmetry breaking of their triangular spin texture, which manifest themselves through, for example, magnetotransport phenomena. Such electrical transport may, therefore, provide the large and nonvolatile read-out signals needed to realize applications.

The fabrication of such topological spintronic devices requires these noncollinear AFs to be prepared in thin film form. The results presented in Sections 2.1 and 3.1 detail the growth of films of Mn_3Ir and Mn_3Sn respectively. Thin films were prepared using magnetron sputtering on different single crystalline substrates, with deposition conditions and buffer layers optimized in order to achieve high-quality epitaxial growth and to tune crystallographic texture. In Section 2.1, consisting of the paper J. M. Taylor et al., "Epitaxial growth, structural characterization, and exchange bias of noncollinear antiferromagnetic M_3Ir thin films", *Phys. Rev. Mater.* **3**, 074409 (2019), growth of Mn_3Ir films with both (001) and (111) crystal orientation, with thicknesses ranging from 10 nm down to 3 nm, is reported on MgO (001) or TaN (111) buffered Al_2O_3 (0001) substrates respectively. In Section 3.1, comprised of the paper A. Markou et al., "Noncollinear antiferromagnetic Mn_3Sn films", *Phys. Rev. Mater.* **2**, 051001(R) (2018), growth of *c*-axis oriented Mn_3Sn films on Ru (0001) buffered $Y{:}ZrO_2$ (111) substrates is achieved for the first time.

In both cases, we characterize the crystallographic properties and epitaxial relationships of the thin films by XRD measurements, whilst their thickness is measured using XRR and their roughness determined by AFM. TEM micrographs indicate the crystal structure of the thin films at the nanoscale. In Section 2.1, 10 nm Mn_3Ir (111) films are found to grow fully relaxed, with lattice parameters close to bulk values. The Mn_3Sn (0001) films discussed in Section 3.1 contain stacking plane defects after the first few atomic layers, after which they grow with the basal planes stacked along the OP direction. In both cases, SAED patterns consist of sharp spots, correlated between film and substrate, thus demonstrating heteroepitaxial growth of thin films with single-crystalline quality.

Finally, bilayer stacks were grown with the noncollinear AFs coupled to a 5 nm layer of FM permalloy. Exchange interactions between the FM and AF layers introduce a unidirectional anisotropy to the FM, the EB effect, thus confirming the AF character of the Mn_3X films. The strong internal anisotropies of $\mathrm{Mn_3Ir}$ mean that 10 nm films produce stable exchange anisotropies at room temperature, with exchange bias fields of $-29\,\mathrm{mT}$ achieved. In thinner films, the blocking temperature below which EB begins to occur is suppressed to below room temperature, an effect that was found to depend on the crystalline orientation of $\mathrm{Mn_3Ir}$. Meanwhile, the lower Néel temperature ($T_\mathrm{N} = 420\,\mathrm{K}$) of $\mathrm{Mn_3Sn}$ means that it induces exchange anisotropies in permalloy only at low temperatures.

Following the deposition of high quality thin films of these noncollinear AFs, this thesis went on to explore in more detail the magnetic and electrical transport properties of the $\mathrm{Mn_3Ir}$ and $\mathrm{Mn_3Sn}$ films in the second halves of Parts 2 and 3, respectively. Measurement of the magnetic properties of these thin films using SQUID-VSM proved challenging, primarily due to the small signal from the films themselves and the large background signal produced by the substrates. Nevertheless, in Section 3.2, we succeeded in demonstrating the presence of weak magnetization within the basal plane of $\mathrm{Mn_3Sn}$, as expected due to the canting of moments in its inverse triangular spin structure towards magnetocrystalline easy axes. This moment is reversible by an external magnetic field, corresponding to a change in the handedness of the chiral spin texture.

In order to explore in more detail the magnetism of the Mn_3X thin films, we performed XMCD measurements to probe directly their Mn magnetic moment. In the case of $\mathrm{Mn_3Sn}$, we observed a small uncompensated moment corresponding to that measured using SQUID-VSM, whose value is quantified as $m_\mathrm{s} + m_\mathrm{l} = 0.279\ \mu_\mathrm{B}/\mathrm{f.u.}$ using the XMCD sum rules. As temperature is reduced to 5 K, we observe a significant increase in magnetization directed along the OP direction, in both SQUID-VSM and XMCD, corresponding to the frustration of Mn moments out of the (0001) basal planes as the film transitions to a glassy FM state below 50 K.

$\mathrm{Mn_3Ir}$ (111) films of both 10 nm and 3 nm thicknesses were also measured by XMCD. In the case of the 10 nm thick film, we measure a paramagnetic dependence of moment as a function of magnetic field applied OP, attributed to the forced tilting of Mn spins out of the (111) crystal planes under the influence of a strong external magnetic field. However, for a 3 nm thick film, a small remnant XMCD signal at low temperatures shows a hysteretic behavior in weak applied magnetic fields, with a coercivity of approximate 0.3 T and a remnant moment of $0.02\ \mu_\mathrm{B}/\mathrm{f.u.}$. This demonstrates the presence of a small uncompensated Mn moment in these ultrathin $\mathrm{Mn_3Ir}$ (111) films.

TEM studies show that such 3 nm thick films also show significant IP epitaxial strain. We therefore suggest that modification of exchange interactions brought about by this IP strain act to induce uncompensated moment in ultrathin Mn_3Ir (111) films.

This uncompensated Mn moment is reflected in the magnetotransport properties of the Mn_3Ir (111) thin films reported in Section 2.2, composed of the paper J. M. Taylor et al., "Magnetic and electrical transport signatures of uncompensated moments in epitaxial thin films of the noncollinear antiferromagnet Mn_3Ir", *Appl. Phys. Lett.* **115**, 062403 (2019). Following lithographic patterning of Hall bar devices, transverse resistivity was measured as a function of OP applied magnetic field at different temperatures. In the case of 3 nm Mn_3Ir (111) films, we find a small anomalous-type Hall effect at low temperatures, accompanied by a negative longitudinal magnetoresistance, which we can attribute to the weak magnetization present in these thin films. At higher temperatures, and in the 10 nm Mn_3Ir (111) films, an ordinary Hall effect is observed, i.e. a linear variation in transverse resistivity as a function of external magnetic field. This is as might be expected for a conventional AF. However, in the case of the Mn_3X noncollinear AFs, a novel anomalous Hall conductivity is predicted to be observed, arising from a Berry curvature generated effective field. However, this will only arise should the entire device to be measured demonstrate the same chirality of triangular spin texture throughout. The presence of chiral domains, each with an opposite handedness of AF order, will cause the AHE to cancel across multiple domains. We therefore postulate that the lack of topologically driven AHE in our Mn_3Ir films is due to the presence of many small AF domains, <20 nm in size, which cannot be manipulated by external magnetic fields.

On the other hand, thin films of Mn_3Sn do exhibit a Berry curvature driven AHE. In Section 3.2, we succeed in growing both continuous c-axis oriented Mn_3Sn thin films, but also films with a $(40\bar{4}3)$ texture. In the latter case, the $[2\bar{1}\bar{1}0]$ magnetic easy axis lies partially OP, with the $[01\bar{1}0]$ crystal direction IP. By passing current parallel to this direction, and measuring Hall voltage orthogonal to it, in an IP direction perpendicular to the (0001) basal planes, we measure a large AHE in a conventional Hall geometry with a coercive field of approximately 1.3 T. Measurements in Mn_3Sn $(40\bar{4}3)$ films of different thicknesses reveal a consistently large anomalous Hall conductivity of around $21\,\Omega^{-1}\,\mathrm{cm}^{-1}$. Such an AHE is not observed in (0001) oriented films, where the magnetic field cannot re-orient the uncompensated Mn moment and thus cannot align the entire inverse triangular spin texture into a single chiral domain state.

When cooled to below 50 K, these (0001) oriented films begin to exhibit a conventional AHE. This corresponds to the net magnetization arising as the film transitions into the glassy FM state and Mn moments cant spontaneously out of the basal planes. In the case of $(40\bar{4}3)$ oriented films, where the measurement geometry is insensitive to this conventional AHE, we instead observe a significant THE. The THE results from a noncoplanar and noncollinear spin texture, where nonzero scalar spin chirality leads to electrons acquiring a real-space Berry curvature. The presence of bumps in transverse resistivity close to the coercive field of the Mn_3Sn $(40\bar{4}3)$ films suggests that this THE arises from chiral domain walls. The symmetric polarity of the THE signal with respect to magnetic field leads us to conclude that, whilst the sense of rotations of spins inside the domain wall is reversed for opposite field sweeps, the moment configuration within the domain wall remains the same. As reported in J. M. Taylor et al., "Anomalous and topological Hall effects in epitaxial thin films of the noncollinear antiferromagnet Mn_3Sn", *Phys. Rev. B* **101**, 094404 (2020), the chirality of the domain wall can be controlled by setting the handedness of the inverse triangular spin texture from which it evolves, thus allowing the sign of the resulting THE to be manipulated by different field cooling routines. This also represents an example of a memory effect, which may find potential applications in neuromorphic computing.

4.2 Outlook and future perspectives

Specifically, the THE measured at low temperature 'remembers' the spin texture chirality originally set at room temperature. Furthermore, the magnitude of the THE measured subsequently depends on the previous field-cooling condition. This weighting of the THE could be used to mimic synaptic behavior, potentially allowing Mn_3Sn to find a role in devices performing brain-inspired computing. The efficient implementation of artificial intelligence algorithms on dedicated spintronic hardware is a developing field of research [2–4], in which noncollinear AFs may play a valuable role.

Other future perspectives for the use of Mn_3X in topological spintronic devices also look promising. In this thesis, we report recipes for the growth of thin films of Mn_3Ir and Mn_3Sn, with the high quality crystal structure necessary to demonstrate correlated transport phenomena. This has been achieved through magnetron sputtering, an efficient and widely used deposition technique that is compatible with existing industrial fabrication of microelectronic devices. The growth of thin films of these materials now opens up the possibility to study device physics using noncollinear AFs.

Mn_3Ir has previously been studied in polycrystalline form as an EB material, also used commercially to pin the fixed magnetic electrode in spin valves and MTJs. This is because it offers a number of advantages, such as high Néel temperature and insensitivity to slight compositional variations. These also make Mn_3Ir attractive for other real-world spintronic applications. In our present studies of the crystal structure, magnetic properties, and magnetotransport, we have demonstrated that, in moving from polycrystalline to single crystal thin films, strain plays a major role in determining the behavior of Mn_3Ir as thickness is reduced to the ultrathin regime.

Thus by manipulating strain, one may be able to control the magnetic (and therefore the resulting electrical) properties of Mn_3Ir on demand. Using strain (provided, for example, by piezoelectric substrates), instead of large external magnetic fields or high switching charge currents, to control magnetic elements in an energy efficient way is another area of major focus in contemporary spintronics [109]. Our results therefore demonstrate a path as to how Mn_3Ir may evolve from being merely a passive element of spintronic devices, to playing an active role.

The outlook for Mn_3Sn in topological AF spintronics is even brighter. As noted in the introduction to this thesis, most spintronic phenomena necessarily require thin film structures to utilize them. Here we have demonstrated, for the first time, the growth of thin films of Mn_3Sn. Subsequently, we have proven the possibility to observe Berry curvature driven magnetotransport properties in such epitaxial films, controllable by external magnetic field and temperature. Thus, the stage is now set of explore a range of novel physics in these materials.

The transverse charge currents, spin currents, and spin-polarized charge currents that can be intrinsically generated by Mn_3Sn remain to be fully explored. Specifically, charge-to-spin conversion by the intrinsic SHE in Mn_3Sn thin films could be utilized as a pure spin current source in ST-FMR measurements (see Section 1.2.6) or SOT switching of FM layers (see Section 1.2.1). The disentanglement from this of transverse spin-polarized currents generated by the magnetic SHE can be achieved by measuring their respective even- and odd-dependencies on noncollinear AF structure chirality (see Section 1.2.9). Furthermore, theoretically predicted longitudinal spin-polarized charge currents remain to be discovered experimentally in Mn_3Sn [120].

Exploiting these longitudinal spin-polarized currents, one could now envisage a range of thin film spintronic devices that could be fabricated using our epitaxial Mn_3Sn films substituted in place of conventional FMs, bringing with them all the advantages in performance arising from using a noncollinear AF with large topological transport signatures (see Section 1.2.7). Examples include heterostructures to measure GMR, TMR and optical effects.

To realize such applications, however, will require a more detailed understanding of AF domain nucleation and the motion of chiral domain walls in Mn_3Sn; an interesting avenue of future research. In particular, the current-induced motion of AF domain walls is a necessary first step to achieving complete current-driven switching of Mn_3Sn. Theoretical proposals exist of how spin currents from a FM (in a current-perpendicular-to-plane spin-transfer torque switching geometry) or a heavy metal layer (in a current-in-plane SOT switching mechanism) can reverse the chirality of Mn_3Sn [52].

Alternatively, the internally generated spin-polarized charge currents in Mn_3Sn might produce a spin accumulation capable of directly switching its inverse triangular spin texture. We aim to investigate all these possibilities in future work. Moving beyond manipulation of the handedness of the AF order using external magnetic field alone, potentially even achieving current-induced control of the material's Weyl bandstructure (see Section 1.2.4), will further open up the possible practical applications of *chiralitronics*.

Finally, one key advantage of AFs for spintronics is their dynamics, which lie in the THz frequency range. This potentially allows for picosecond switching of AF spintronic components, orders of magnitude faster than can be achieved in FMs. Therefore, the interaction of THz radiation with AF structures is an exciting direction of future research [49]. We are interested in utilizing THz radiation to excite AF resonance in our Mn_3X films, or potentially using THz pulses to switch chiral spin texture in noncollinear AFs.

List of publications

- A. Markou, J. M. Taylor, J. Gayles, Y. Sun, D. Kriegner, J. Grenzer, W. Schnelle, P. Werner, C. Felser, and S. S. P. Parkin, "Noncollinear antiferromagnetism and spin Hall effect in cubic Weyl $\mathrm{Mn_3Ge}$ thin films", *Submitted* (2020)

- P. K. Sivakumar, B. Göbel, E. Lesne, A. Markou, J. Gidugu, J. M. Taylor, H. Deniz, J. Jena, C. Felser, I. Mertig, and S. S. P. Parkin, "Two topological spin textures hosted in a single tetragonal inverse Heusler thin film", *Under review* (2020)

- J. M. Taylor, A. Markou, E. Lesne, P. K. Sivakumar, C. Luo, F. Radu, P. Werner, C. Felser, and S. S. P. Parkin, "Anomalous and topological Hall effects in epitaxial thin films of the noncollinear antiferromagnet $\mathrm{Mn_3Sn}$", *Phys. Rev. B* **101**, 094404 (2020)

- J. M. Taylor, E. Lesne, A. Markou, F. K. Dejene, P. K. Sivakumar, S. Pöllath, K. G. Rana, N. Kumar, C. Luo, H. Ryll, F. Radu, F. Kronast, P. Werner, C. H. Back, C. Felser, and S. S. P. Parkin, "Magnetic and electrical transport signatures of uncompensated moments in epitaxial thin films of the noncollinear antiferromagnet $\mathrm{Mn_3Ir}$", *Appl. Phys. Lett.* **115**, 062403 (2019)

- J. M. Taylor, E. Lesne, A. Markou, F. K. Dejene, B. Ernst, A. Kalache, K. G. Rana, N. Kumar, P. Werner, C. Felser, and S. S. P. Parkin, "Epitaxial growth, structural characterization, and exchange bias of noncollinear antiferromagnetic $\mathrm{M_3Ir}$ thin films", *Phys. Rev. Mater.* **3**, 074409 (2019)

- A. Markou, J. M. Taylor, A. Kalache, P. Werner, S. S. P. Parkin, and C. Felser, "Noncollinear antiferromagnetic $\mathrm{Mn_3Sn}$ films", *Phys. Rev. Mater.* **2**, 051001(R) (2018)

Curriculum vitae

Personal details

- **Name**: James Mark Taylor
- **Date of birth**: 08.12.1990
- **Place of birth**: Sheffield, UK
- **Nationality**: British
- **Gender**: Male

Contact details

- **Place of residence at time of submittal**: Halle (Saale), Germany
- **Correspondence address at time of submittal**: Max Planck Institute of Microstructure Physics, Weinberg 2, 06120 Halle (Saale), Germany
- **E-mail (persistent)**: james.taylor@mpi-halle.mpg.de

Academic details

- **Academic title at time of submittal**: Master of Physics (MPhys)
- **Subject area of doctoral thesis**: Spintronics, magnetism and magnetic materials, solid state physics

Academic experience

2014–2020	**Doctoral Researcher** at Max Planck Institute of Microstructure Physics (Halle (Saale), Germany)
2014–2017	**Visiting Doctoral Researcher** at Max Planck Institute for Chemical Physics of Solids (Dresden, Germany)

Education

2014–2020	**Doctoral Candidate** at Martin-Luther-University Halle-Wittenberg (Halle (Saale), Germany)
2009–2013	**MPhys (Hons) Physics (2:1)** at Durham University (Durham, UK)
2002–2009	**A-levels in Physics (A), Maths (A) and Chemistry (A)** at Rushcliffe School (Nottingham, UK)

Halle (Saale), 30.09.2020 James M Taylor

Eidesstattliche Erklärung (Statutory declaration)

Hiermit erkläre ich, James M Taylor, die vorliegende Arbeit, *Epitaxial thin films of the noncollinear antiferromagnets* Mn_3Ir *and* Mn_3Sn *for topological spintronic applications*, selbständig und ohne fremde Hilfe verfasst zu haben. Es wurden keine anderen als die von mir angegebenen Quellen und Hilfsmittel benutzt. Die den benutzten Werken wörtlich oder inhaltlich entnommenen Stellen sind als solche kenntlich gemacht worden. Ich erkläre, die Angaben wahrheitsgemäß gemacht, keine vergeblichen Promotionsversuche unternommen und keine Dissertation an einer anderen wissenschaftlichen Einrichtung zur Erlangung eines akademischen Grades eingereicht zu haben. Ich bin weder vorbestraft noch sind gegen mich Ermittlungsverfahren anhängig.

I, James M Taylor, hereby declare that I have written the present work, *Epitaxial thin films of the noncollinear antiferromagnets* Mn_3Ir *and* Mn_3Sn *for topological spintronic applications*, independently and without third-party help. No sources other than those cited by me were used. Elements quoting directly from, or making reference to, such sources have been identified as such. I declare that I have provided this information truthfully, that I have not made any previous unsuccessful attempts at doctoral studies, and that I have not submitted either the current version or another version of this thesis to another academic institution for the purpose of obtaining an academic degree. I do not have any prior criminal convictions, nor am I subject to any preliminary investigations.

Halle (Saale), 30.09.2020 James M Taylor

Acknowledgements

I would like to thank Prof Stuart Parkin for the opportunity to undertake my doctoral studies under his supervision, and for his valuable expertise and guidance during my time at the Max Planck Institute of Microstructure Physics. Here, my gratitude goes to the many other scientists and students, foremost Edouard Lesne, for their advice and encouragement in my development as a scientist: Fasil Kidane Dejene, Kumari Gaurav Rana, Neeraj Kumar, Peter Werner, Hakan Deniz, Holger Meyerheim, Robin Bläsing, Pranava Keerthi Sivakumar, Elisa Yang, Amilcar Bedoya Pinto, Avanindra Kumar Pandeya, Tianping Ma, Bharat Grover, Binoy Krishna Hazra, Banabir Pal, Hao Yang, Jue Huang, Yicheng Guan, Ankit Kumar Sharma, Abhay Kant Srivastava, Jibo Zhang, Jae-Chun Jeon, Andrea Migliorini, Kai-Uwe Demasius, Elena Derunova, Mazhar Ali, Amir Capua, Rana Saha, Bin Cui, Fang Gao, Ajaya Nayak, Ilya Kostanovski and, of course, Jiho Yoon, Alessandro Fumarola and Amine Wahada. For technical assistance, I heartily acknowledge Kai-Uwe Aßmann, Kornelia Sklarek, Martin Gottschalk, Norbet Schammelt, Mike Borrmann and Pierre-Jean Zermattan, as well as the wisdom of Winfried Heichler. For administrative help over the last few years, my thanks go to Antje Paetzold and Simone Jäger.

For the opportunity to undertake part of my studies at the Max Planck Institute for Chemical Physics of Solids, I thank Prof Claudia Felser. In addition, I acknowledge my many friends and collaborators in Dresden: Anastasios Markou, Adel Kalache, Benedikt Ernst, Rolf Stinshoff, Julie Karel, Kai Filsinger, Catherine Rajamathi, Julia Fischer, Carlos Barbosa, Johannes Kroder, Albrech Köhler, Peter Swekis, Dominik Kriegner, Roshnee Sahoo, Kaustuv Manna, Gudrun Auffermann, Walter Schnelle, Yang Zhang, Jakub Železný, Yan Sun, Binghai Yan, Thomas Krüger and Ingrid Rothe.

In the Institute of Physics at the Martin-Luther-University of Halle-Wittenberg, I am lucky enough to have established fruitful, ongoing partnerships with Georg Woltersdorf and Rouven Dreyer.

As part of the cooperation between the Max Planck Institute in Halle and IBM Almaden Research Centre, I am grateful for the support of Yari Ferrante, Andrew Kellock, Weifeng Zhang, See-Hun Yang, Mahesh Samant, Timothy Phung, Panos Filippou and Alberto Lauri.

For valuable assistance during synchrotron beamtimes, I express gratitude to Chen Luo, Simon Pöllath, Hanjo Ryll, Florin Radu and Florian Kronast at BESSY, as well as Stefan Stanescu and Rachid Belkhou at SOLEIL.

I would like to acknowledge a number of external collaborators who have helped along the way to completion of this thesis, including Gernot Güntherodt, Vasile-Dan Hodoroaba, Tobias Kosub and Christian Back.

Finally, I would like to thank Tracy, Mark, Andrew and the rest of my family for their encouragement during the last five years. And last, but by no means least, a big shout-out to the friends, flatmates and fantastic people without whom this would never have happened: Ana, Abraham, Alfred, Alex M, Alex P, Alex S, Andrea, Barbara, Bastien, Ben, Dan, Dom, Farina, Franka, Franzi, Hamid, Henry, Izaak, Jan, Jack, Jez, Joe B, Joe F, Joe G, Joe W, Johann, Johanna, Julia, Kunaal, Karsten, Kerry, Linda, Leonardo, Maik, Markus, Max, Mehrdad, Narwas, Nina, Omar, Sam, Sally, Sandy, Sara, Thalia, Veronika and Younes.